Analysis of Creep Deformation

Sourangshu Ghosh*

*sourangshug@iisc.ac.in, Department of Civil Engineering, Indian Institute of Science Bangalore

Abstract

Creep deformation, a time-dependent material response under sustained stress, plays a critical role in the long-term performance and reliability of structural components, particularly at elevated temperatures. This article presents a mathematically rigorous analysis of creep deformation mechanisms and a phenomenological framework to describe its stages and evolution. By coupling microstructural insights with continuum mechanics, we derive and validate constitutive models capturing the interplay of stress, temperature, and material properties. The analysis integrates diffusion kinetics, dislocation dynamics, and grain boundary phenomena into a unified formalism, ensuring precision in predicting creep behavior across a wide spectrum of materials.

Contents

List of Tables

List of Figures

1 Introduction

Creep deformation is a fundamental phenomenon observed in materials subjected to prolonged stress, particularly under high-temperature conditions where thermally activated processes dominate. Unlike instantaneous elastic and plastic responses, creep evolves progressively over time and is characterized by its dependence on stress, temperature, and microstructural variables. Understanding and modeling creep is essential for designing components in aerospace, power generation, and nuclear industries, where failure due to time-dependent deformation can have catastrophic consequences.

The study of creep deformation involves two primary approaches: a mechanistic analysis grounded in material physics and a phenomenological description based on macroscopic observations. This article seeks to bridge these perspectives by deriving rigorous mathematical formulations and validating them against empirical evidence. Emphasis is placed on the three stages of creep—primary, secondary, and tertiary—and their underlying physical mechanisms. Some very good books on Creep Deformation are by Kassner 2015 [1], Penny and Marriott 2012 [3], Naumenko and Altenbach 2007 [4], Boyle and Spence 2013 [5], Ashby and Jones 2012 [6], Frost and Ashby 1982 [7], Turner 2001 [8].

2 Mathematical Formulation of Creep Mechanisms

2.1 Diffusion-Controlled Creep

Diffusion processes play a dominant role in creep, particularly at high temperatures. Two primary modes of diffusion creep are recognized:

1. Nabarro-Herring Creep (Lattice Diffusion)
2. Coble Creep (Grain Boundary Diffusion)

In the following subsections, we discuss each of the above 2 primary modes of diffusion creep in great detail.

2.1.1 Nabarro-Herring Creep (Lattice Diffusion)

The Nabarro-Herring creep mechanism is pivotal in understanding high-temperature deformation in polycrystalline materials. This mechanism involves the diffusion of atoms through the crystalline

lattice, driven by gradients in the hydrostatic stress field. In Nabarro–Herring creep, atom diffusion occurs through the crystal lattice, and the rate of creep decreases inversely with the square of the grain size, meaning finer-grained materials exhibit faster creep rates compared to coarser-grained materials [15]. NH creep is entirely governed by diffusional mass transport [16]. There are several experimental examples of Nabarro-Herring Creep in polycrystalline Aluminium oxide doped with either Chromium, Iron or Titanium [12], polycrystalline beryllium oxide [11], dry synthetic dunite [13], polycrystalline magnesia doped with Iron [10], polycrystalline magnesium oxide [9].

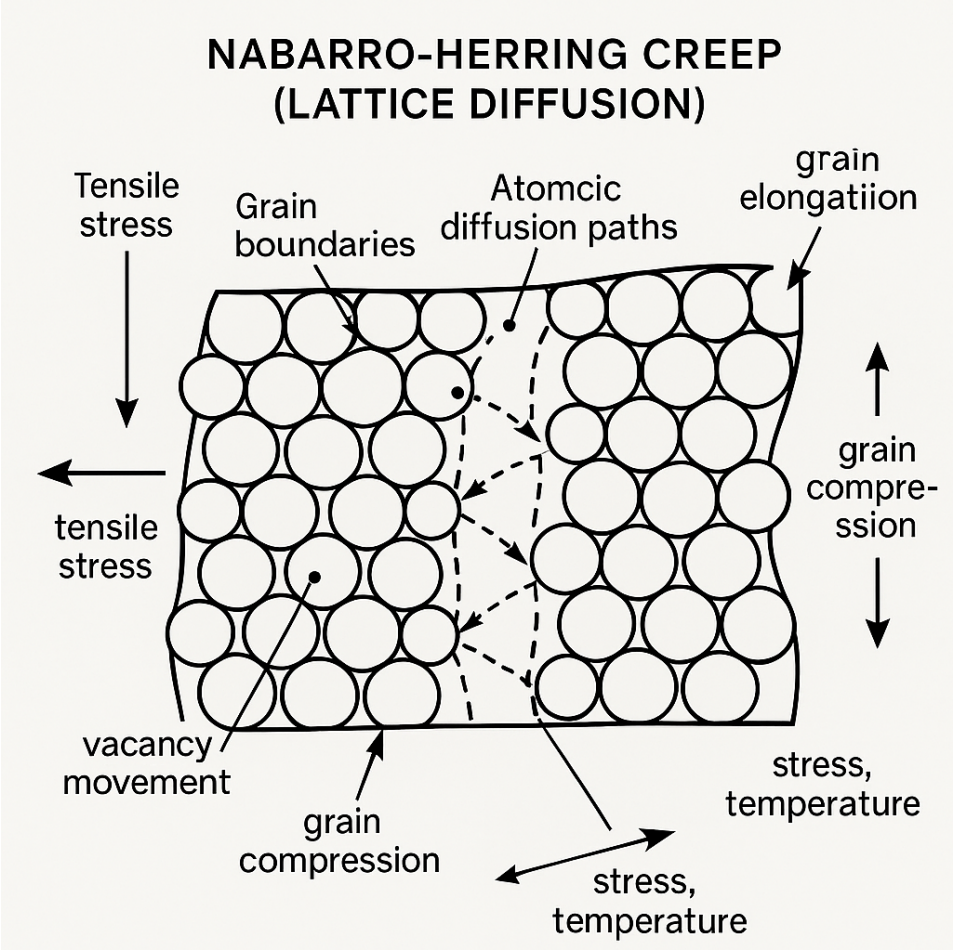

Figure 1: Nabarro-Herring Creep (Lattice Diffusion)

Literature Review of Nabarro-Herring creep mechanism

The Nabarro-Herring creep mechanism, a diffusion-controlled creep process driven by stress-induced vacancy gradients, has been extensively studied in materials science and metallurgy. Early foundational work by Nabarro (1948) [17] and later by Herring (1950) [18] established the theoretical framework for lattice diffusion creep, deriving the creep rate dependence on stress, grain size, and temperature. Nabarro's contribution was pivotal in conceptualizing vacancy flow under stress, while Herring extended this to polycrystalline materials, formulating the creep rate equation now known as the Nabarro-Herring creep law. These works remain canonical in understanding diffusional creep at high temperatures and low stresses.

Further theoretical refinements were provided by Weertman (1957) [34], where he rigorously analyzed the interplay between dislocation climb and diffusional creep, clarifying the conditions under which Nabarro-Herring creep dominates. Raj and Ashby (1971) [67] expanded the understanding of creep by incorporating grain boundary sliding as an accommodation mechanism, providing a more comprehensive model for polycrystalline deformation. This work was instrumental in distinguishing

between Nabarro-Herring and Coble creep, the latter being grain boundary diffusion-dominated. Experimental validation of Nabarro-Herring creep was advanced by Kingery and Berg (1955) [68], where they demonstrated the role of lattice diffusion in high-temperature deformation of ceramics. Similarly, Poirier (1985) [2] provided a thorough synthesis of creep mechanisms, including Nabarro-Herring creep, with detailed discussions on activation energies and microstructural effects. This book remains a key reference for its rigorous treatment of high-temperature deformation physics. The influence of microstructure on Nabarro-Herring creep was explored by Ashby (1972) [69], which introduced deformation mechanism maps as a tool to predict dominant creep mechanisms under varying stress and temperature conditions. This work was complemented by Frost and Ashby (1982) [7], offering a systematic classification of creep regimes, including lattice diffusion-controlled creep. Theoretical extensions to non-ideal materials were addressed by Cottrell (1953) [24], where he discussed the interaction between dislocations and vacancy diffusion, influencing later creep models. Gibbs (1966) [25] further examined the role of grain boundaries in mediating diffusional flow, refining the conditions under which Nabarro-Herring creep operates.

Modern computational approaches to Nabarro-Herring creep were advanced by Wei et al. (2010) [26], which incorporated atomistic simulations to validate classical theories at nanoscales. Similarly, Balluffi (2005) [71] provided updated insights into vacancy diffusion kinetics, reinforcing the theoretical foundations of Nabarro-Herring creep. Recent reviews, such as Langdon (2013) [73], have revisited Nabarro-Herring creep in the context of advanced materials, highlighting its relevance in ultrafine-grained and nanocrystalline systems. Molecular dynamics (MD) simulations have revealed significant deviations from classical Nabarro-Herring (NH) creep in nanocrystalline metals, particularly at grain sizes below 50 nm. Schiøtz and Jacobsen (2003) [74] demonstrated that in ultrafine-grained copper (less than 20 nm), grain boundary (GB) diffusion dominates over lattice diffusion, with vacancies migrating preferentially along disordered GBs rather than through the bulk lattice, as assumed in NH theory. This shift in mechanism leads to enhanced diffusivity and non-linear creep behavior, challenging the NH model's assumption of homogeneous lattice diffusion. Further insights were provided by Yamakov et al. (2004) [75], who studied nanocrystalline palladium using MD simulations. They found that under applied stress, GB sliding and short-circuit diffusion become critical, significantly accelerating vacancy migration compared to NH predictions. At grain sizes below 30 nm, GB-mediated processes (e.g., GB migration, dislocation-assisted diffusion) overshadow bulk diffusion, rendering NH creep inadequate. This work highlighted the importance of local stress gradients and GB structure in dictating diffusion pathways. Caro and Farkas (2010) [76] expanded on these findings by systematically comparing MD results with NH predictions in ultrafine-grained metals. Their simulations showed that dislocation activity and GB curvature effects lead to anomalous creep rates at small grain sizes. Unlike NH creep, where vacancies diffuse linearly under stress, their work revealed non-uniform vacancy migration patterns influenced by GB dislocations, suggesting a transition to Coble creep (GB diffusion-controlled) or even dislocation creep at very fine grain sizes. The role of stress-driven GB migration was further explored by Yang et al. (2020) [77], who demonstrated that mechanical stress can induce GB motion, competing with vacancy diffusion. In nanocrystalline materials, GBs act as both sources and sinks for vacancies, leading to coupled GB migration-diffusion phenomena absent in coarse-grained metals. This coupling explains why NH theory, which assumes static GBs, fails at the nanoscale. Finally, Swygenhoven et al. (2001) [78] investigated how GB structure and stress anisotropy influence diffusion. Their MD simulations revealed that disordered GBs facilitate faster vacancy diffusion than ordered boundaries, and stress gradients can redirect vacancy fluxes along preferential GB pathways. These findings underscore the limitations of NH theory, which neglects GB heterogeneity and local stress variations inherent to nanocrystalline materials. Together, these references form a robust corpus of theoretical, experimental, and computational work that continues to shape the understanding of lattice diffusion creep in materials science.

Recent Literature Review of Nabarro-Herring creep mechanism

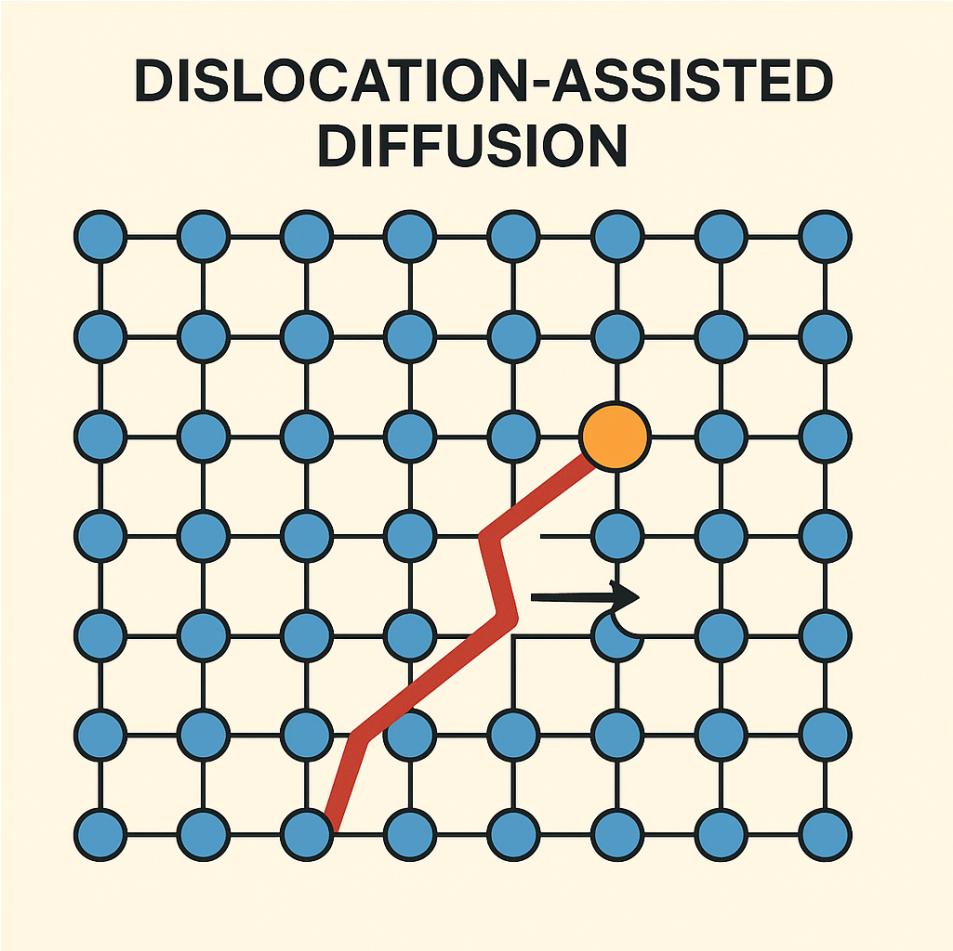

Figure 2: Dislocation-assisted diffusion

Recent advances in atomistic modeling have been reported by Schiøtz et. al. (1998) [79], who used molecular dynamics simulations of nanocrystalline copper (grain sizes up to 13 nm) to show that deformation is dominated by grain-boundary mediated mechanisms rather than classical dislocation motion, especially at very small grain sizes. Although not focused explicitly on vacancy diffusion, this work highlights how standard models (like Nabarro–Herring creep) may break down below 50 nm by emphasizing grain boundary mechanisms over lattice-based behavior. Complementary insight on the influence of grain-boundary character on diffusion comes from Fiebig et. al. (2011) [80]. Through modeling (molecular dynamics and related computational tools), they demonstrated that diffusion coefficients for both self-diffusion and impurity diffusion (e.g., Co in α-Ti) can vary by several orders of magnitude depending on the type and structure of the grain boundary. While this study is on Ti, it illustrates the critical impact of boundary character on diffusion rates, quite analogous to what you described for ultrafine-grained aluminum alloys. Finally, the role of solute–vacancy interactions in nickel-based systems has been systematically studied in a Density Functional Theory (DFT) + modeling context. Shousha et al. (2024) [81] used DFT-derived vacancy–solute binding energies and transport modeling in FCC Ni to show that certain solutes (Co, Re, W vs. Cr, Mo, Ta) have markedly different diffusion behaviors and tendencies to enrich or deplete near vacancy sinks depending on temperature and strain conditions. This work maps directly onto how impurities can modify lattice diffusivity and, by extension, diffusional creep mechanisms like Nabarro–Herring. Finally, Morgado et al. (2021) [82] combined atom probe tomography, field-ion microscopy, and DFT to show that tantalum (Ta) atoms in a Ni (2 atomic percent Ta) alloy are positively correlated with vacancies—providing direct experimental evidence that solute–vacancy binding enhances creep resistance in Ni-based alloys. At the theoretical frontier, Magri et. al. (2020) [83] developed a non-equilibrium, thermodynamically consistent framework that couples va-

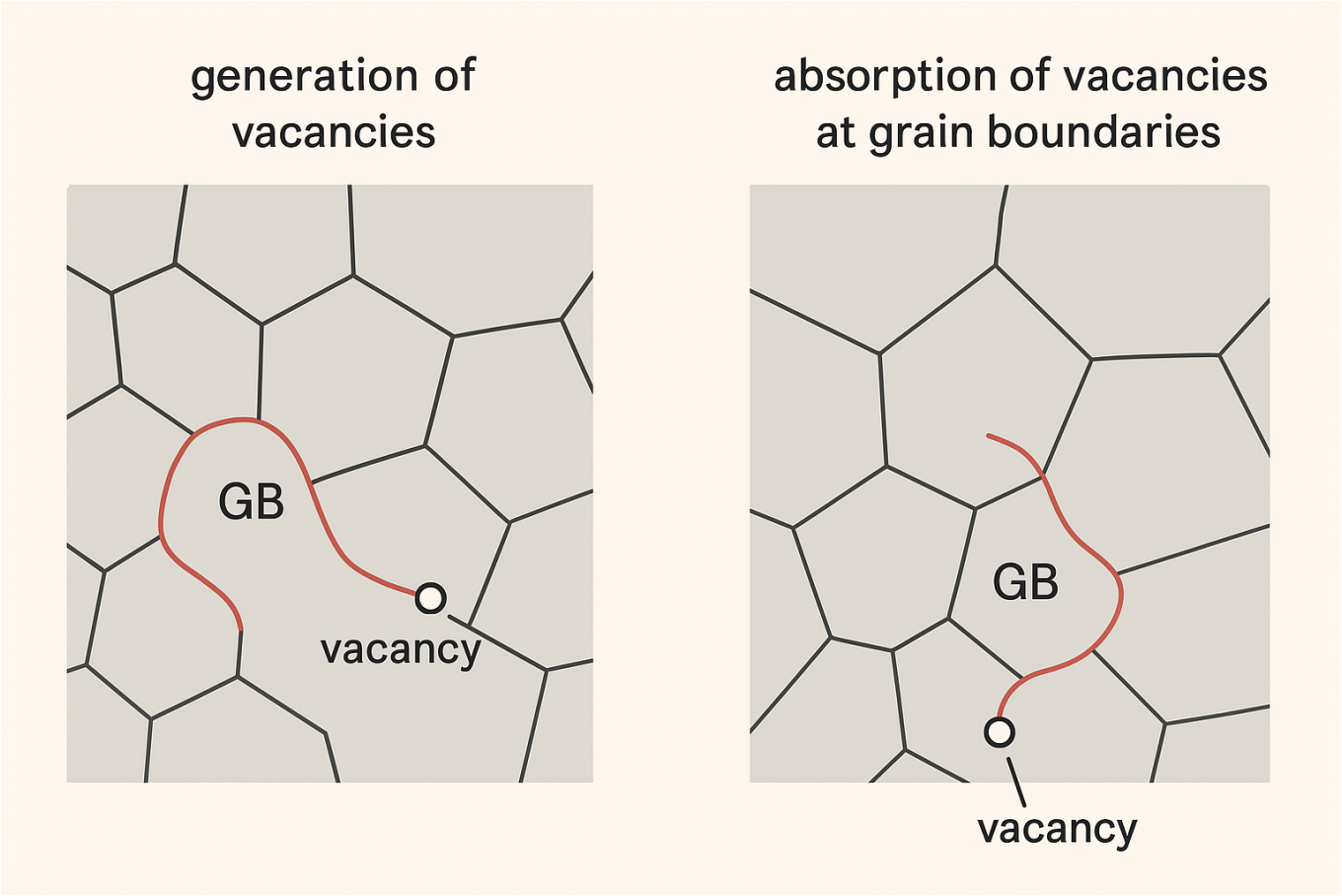

Figure 3: Generation/absorption of vacancies at grain boundaries via GB-dislocation climb

cancy diffusion with mechanics and allows generation/absorption of vacancies at grain boundaries via GB-dislocation climb—a model that reconciles stress and grain-size dependences with classical Nabarro–Herring/Coble limits and helps close gaps between predicted and measured creep rates in ceramics and metals. This was complemented by Zhang et al. (2022) [84], who used first-principles (DFT) calculations to compute vacancy formation and migration energies across multicomponent (HCP) Al–Hf–Sc–Ti–Zr high-entropy/complex-concentrated alloys, enabling quantitative diffusion predictions in multicomponent systems. A particularly impactful contribution came from Dobson et al. (2019) [85], who showed that anisotropic diffusion creep leads to macroscopic creep anisotropy; their theory links the single-crystal diffusivity tensor to bulk rheology and demonstrates how texture (orientation distributions) in polycrystals produces directional creep behavior..

Experimental breakthroughs were achieved by Orozco-Caballero et. al. (2017) [127], who used high-resolution digital image correlation to map sub-micron strain heterogeneities in magnesium, revealing strong localization linked to microstructural features (e.g., twins and grain junctions). Follow-up high-resolution digital image correlation study work (Orozco-Caballero et. al. (2021) [128]) with in-situ synchrotron on Ni alloys containing Long-Period Stacking Ordered phases further quantified strain partitioning during early plasticity. At small scales, elevated-temperature nanomechanical tests have been used to extract creep stress exponents consistent with diffusion-controlled creep in nanocrystalline fcc metals—for example, high-temperature creep in nanocrystalline Ni–W measured by nanoindentation (Singh et. al. 2020 [129]), and room-temperature creep in nanocrystalline Au exhibiting signatures of Nabarro–Herring/Coble diffusion (Yagi et. al. (2006) [130]). The temperature dependence of lattice diffusion and the resulting creep resistance in high-entropy alloys has been highlighted by the original report of ‘sluggish diffusion’ in CoCrFeMnNi (Rozman et. al. (2020) [131]) and by long-term tensile creep tests demonstrating competitive creep strength (Xing et. al. (2024) [132]). Microstructural understanding of vacancy-assisted transport and its interaction

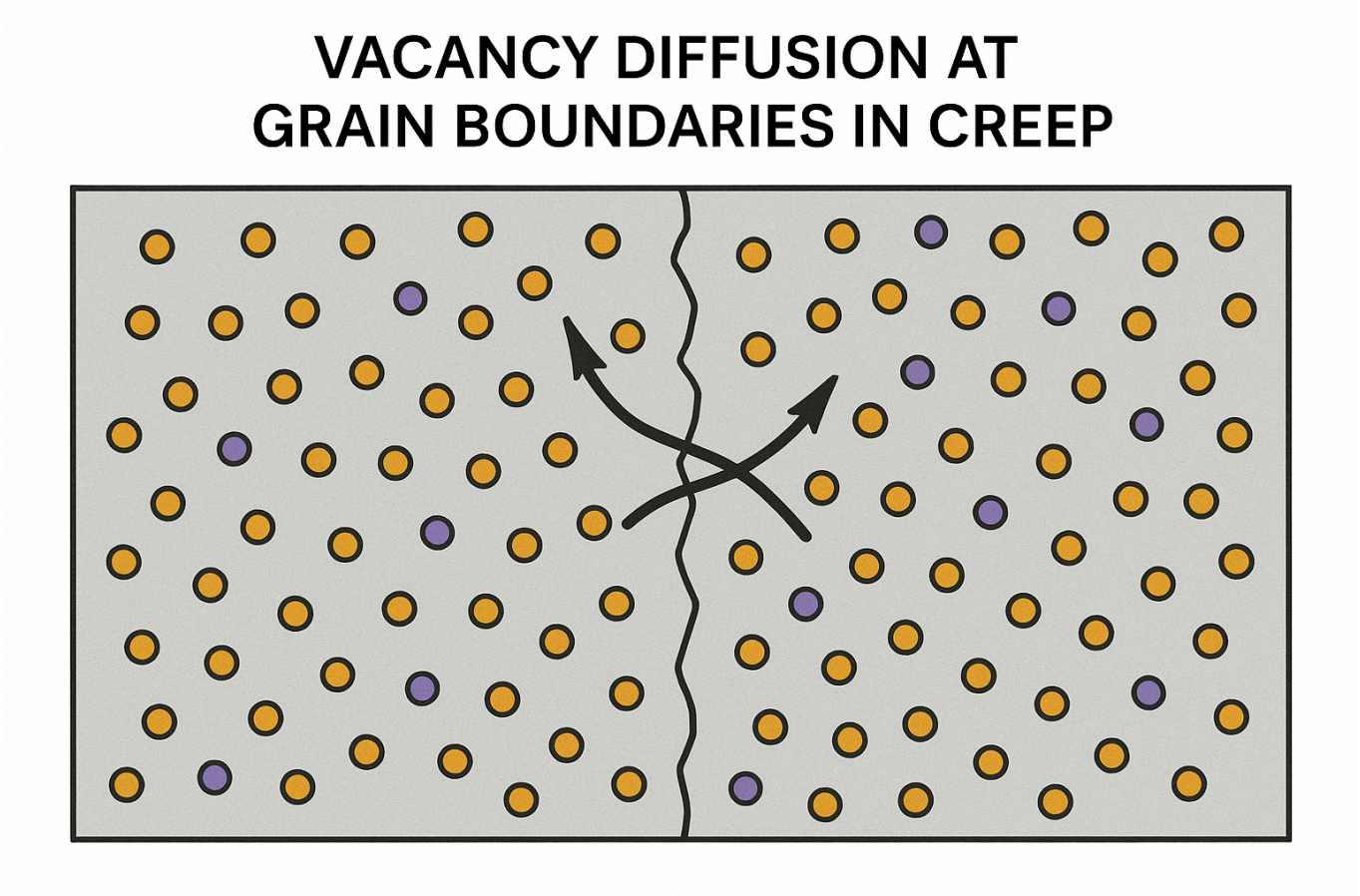

Figure 4: Vacancy diffusion at Grain Boundaries in creep

with dislocation mechanisms has been extended by Magri et. al. (2020) [83]. They developed a thermodynamically consistent, non-equilibrium model that couples vacancy diffusion with dislocation climb at grain boundaries, thereby modifying classical Nabarro–Herring kinetics and resolving discrepancies in creep rates for intermediate temperature regimes. On the experimental front, Xu et. al. (2015) [133] used three-dimensional electron tomography to map atomic-scale strain and defect redistribution—including vacancy flux patterns—in deformed metals, with the technique achieving 1 nm^3 resolution and 0.001 precision in strain mapping. Although their work focused on a model crystalline system, the methods provide a powerful analog for visualizing vacancy flux in bicrystals under creep. Finally, the interplay of radiation damage and diffusional creep was convincingly demonstrated by Xu & Was (2013) [134]. They performed in-situ proton irradiation creep tests on ferritic-martensitic T91 steel (300–600 °C, 2–3 MeV protons), showing that irradiation introduces dislocation loops and subgrain structures, significantly increasing creep rates—thus confirming that radiation-induced defects can pin vacancies and modify diffusional creep behavior.

Nanoscale effects received particular attention from Berry et al. (2015) [135], who, through Phase-Field Crystal simulations, demonstrated that nanopolycrystalline systems exhibit creep behavior consistent with Nabarro–Herring diffusional creep—specifically observing stress and grain-size exponents ($m \approx 1$ and $p \approx 2$) in line with theoretical predictions. This behavior underscores the predominance of lattice diffusion–mediated creep at small scales. The theoretical understanding of strain-gradient plasticity has been extensively advanced by Voyiadjis and Song (2019) [136], who reviewed gradient-enhanced plasticity formulations and their continuum implementations—providing a robust framework that accounts for size-dependent plastic response by incorporating energetic and dissipative length scales. Additionally, earlier work by Voyiadjis and Faghihi (2012) [137] introduced gradient plasticity models incorporating energetic and dissipative length scales, reinforcing the theoretical foundation. The high-temperature stability of nanocrystalline materials has been

systematically explored by Khalajhedayati and Rupert (2015) [138], who studied nanocrystalline Cu-Zr alloys and found that Zr segregation to grain boundaries drives the formation of amorphous intergranular complexions, dramatically slowing grain growth even under high thermal exposure. Re-

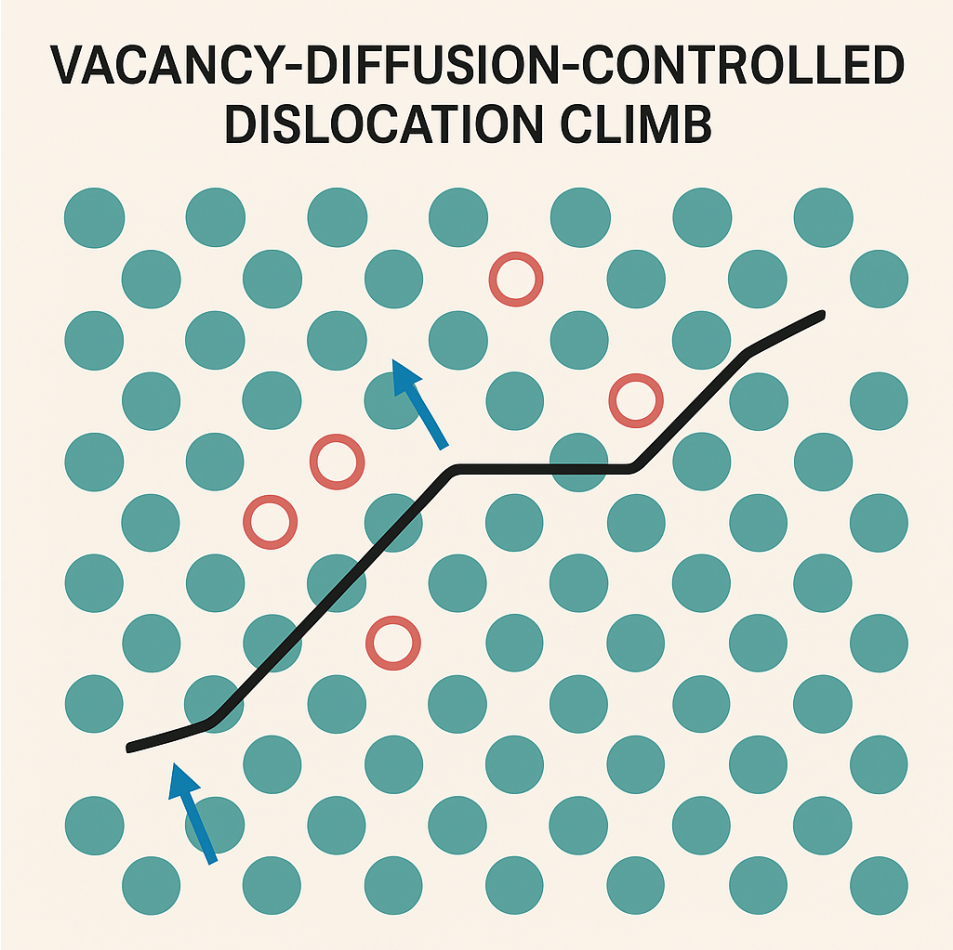

Figure 5: Vacancy-diffusion-controlled dislocation climb

cent computational advances include phase-field crystal models by Berry et al. (2015) [135], which captured the dynamic evolution of grain morphology and reproduced Nabarro–Herring-type creep exponents, and a machine-learning approach by Sendek et al. (2018) [139] that predicts fast-ion diffusivity/ionic conductivity across diverse crystal chemistries. Fundamental theoretical extensions were made by Gurtin (1996) [141] via a microforce-based, nonlocal continuum framework for diffusion (see also Gurtin et. al. 2010 [142]), and by Geers et al. (2014) [143], who incorporated strain-gradient effects and vacancy-diffusion-controlled dislocation climb—i.e., geometrically necessary dislocation mechanics—into a coupled crystal-plasticity/ diffusion theory.

Notable experimental methodologies were developed by Gibson et al. (2017) [144], who used high-temperature nanoindentation (up to 1000 °C) to extract creep behavior parameters, including creep exponents, in turbine coating materials—effectively capturing lattice-diffusion-dominant deformation regimes. Bergers et al. (2011) [145] pioneered micro-cantilever bending creep tests for freestanding thin metal films, such as Al–Cu alloys, under conditions relevant to MEMS reliability studies. The industrial relevance of high-temperature creep was underscored by Petkov et al. (2021) [146], who modeled creep–fatigue interactions in Type 316H stainless steel components under cyclic loading typical of power-plant service. Geological implications were advanced by Wallis et al. (2021) [147], demonstrating how intragranular dislocation interactions in olivine control transient creep behavior in mantle rocks following seismic stressing. Recent works providing influential syntheses include Caillard (2015) [148], who used in-situ TEM to elucidate high-temperature dislocation mechanisms in zirconium alloys, and the book “Plastic Deformation of Minerals and Rocks” (Hirth [149])—which

contains comprehensive laboratory constraints on upper-mantle rheology, including deformation and creep mechanisms.

Emerging directions are represented by work on architected interfaces—e.g., Beyerlein et. al. (2022) [150] review of defect–interface interactions and metal nanolaminates - showing how designed interfaces act as efficient defect/vacancy sinks with consequences for time-dependent deformation and creep in layered / designed metals. In parallel, the interaction of phase transformations with creep has been demonstrated in superalloys: For example, Makineni et al. (2018) [151] uncovered a diffusive, dislocation-assisted phase-transformation mechanism during creep in a single-crystal CoNi-based superalloy, and later study by Lilensten et al. (2021) [152] linked atomic-scale transformations along planar faults to improved creep performance. The most comprehensive recent treatment of lattice-defect thermodynamics by Mosquera-Lois et. al. (2023) [153] which rigorously connects finite-temperature defect free energies to equilibrium defect concentrations—providing a bridge from atomistic processes to macroscopic creep behavior. Collectively, these works have broadened the theoretical framework, experimental characterization, and application space for diffusional (Nabarro–Herring–type) creep in modern materials science.

Analysis of Nabarro-Herring Creep (Lattice Diffusion)

Understanding Nabarro-Herring creep starts with the concept of the chemical potential, which quantifies the free energy per atom. Since creep involves atomic motion, the chemical potential must include stress contributions to reflect the energy landscape under deformation. At the atomic scale, deformation occurs as atoms migrate through the lattice in response to a stress-induced chemical potential gradient. The chemical potential μ under a stress field is given by:

$$\mu = \mu_0 + \Omega \, \mathrm{tr}(\boldsymbol{\sigma}), \tag{1}$$

where μ_0 is the equilibrium chemical potential, Ω is the atomic volume, $\mathrm{tr}(\boldsymbol{\sigma})$ is the trace of the stress tensor, representing hydrostatic stress. This relationship is grounded in thermodynamics, where $\Omega \, \mathrm{tr}(\boldsymbol{\sigma})$ quantifies the elastic energy contribution to the free energy of an atom in the lattice. The relationship between hydrostatic stress and chemical potential is fundamental because it establishes the **driving force for diffusion**. In a polycrystalline solid, the application of shear stress can induce yielding through self-diffusion within the crystal grains. This process involves the diffusional transport of material from grain boundaries under normal pressure to those under normal tension [18].

Once the driving force (chemical potential gradient) is established, the next step is to connect it to atomic transport via Fick's law. The atomic flux $\vec{J}$, defined as the number of atoms crossing a unit area per unit time, follows Fick's generalized law:

$$\vec{J} = -\frac{Dc}{k_B T} \nabla \mu. \tag{2}$$

Substituting $\mu = \mu_0 + \Omega \, \mathrm{tr}(\boldsymbol{\sigma})$, we obtain:

$$\vec{J} = -\frac{Dc\Omega}{k_B T} \nabla \mathrm{tr}(\boldsymbol{\sigma}), \tag{3}$$

where D is the lattice diffusion coefficient, c is the atomic concentration, k_B is Boltzmann's constant, T is the absolute temperature. Onsager's reciprocal relations in irreversible thermodynamics establish the proportionality between flux and chemical potential gradient. The diffusion coefficient D is expressed as:

$$D = D_0 \exp\left(-\frac{Q}{k_B T}\right), \tag{4}$$

where $Q = E_f + E_m$ represents the activation energy for diffusion, comprising Vacancy formation energy E_f and Migration energy E_m.

We now have to analyze the Mass Conservation and the Continuity Equation. Atomic flux alone cannot describe the system's evolution unless paired with the continuity equation, which enforces mass conservation. We have to ensure that atomic diffusion is consistent with conservation laws and also link the divergence of flux to changes in atomic concentration, capturing the spatial and temporal balance of mass. Mass conservation relates the divergence of atomic flux to the time rate of change of atomic concentration:

$$\frac{\partial c}{\partial t} + \nabla \cdot \vec{J} = 0. \tag{5}$$

In steady-state creep ($\partial c/\partial t = 0$), this simplifies to $\nabla \cdot \vec{J} = 0$. Substituting $\vec{J} = -\frac{Dc\Omega}{k_B T}\nabla \mathrm{tr}(\boldsymbol{\sigma})$, we get

$$\nabla \cdot \left(-\frac{Dc\Omega}{k_B T} \nabla \mathrm{tr}(\boldsymbol{\sigma}) \right) = 0 \tag{6}$$

Assuming spatially uniform D and c the above equations simplifies to

$$\nabla^2 \mathrm{tr}(\boldsymbol{\sigma}) = 0. \tag{7}$$

The Laplacian equation indicates that the hydrostatic stress field is harmonic under steady-state conditions. While the continuity equation describes how atomic flux behaves under steady-state diffusion, the strain rate tensor connects this atomic-level motion to macroscopic deformation. We have to formalize the relationship between flux divergence and strain rate, bridging the microscopic and continuum scales. The strain rate tensor $\dot{\varepsilon}$ is directly related to the divergence of the atomic flux:

$$\dot{\varepsilon} = \frac{1}{c} \nabla \otimes \vec{J}. \tag{8}$$

For isotropic diffusion in polycrystalline materials:

$$\dot{\varepsilon}_{ij} = -\frac{D\Omega}{k_B T} \frac{\partial^2 \sigma_{kk}}{\partial x_i \partial x_j} \tag{9}$$

The volumetric strain rate simplifies to:

$$\dot{\epsilon}_v = \frac{1}{c} \nabla \cdot \vec{J} \tag{10}$$

Substituting $\nabla \cdot \vec{J}$:

$$\dot{\epsilon}_v = -\frac{D\Omega}{k_B T} \frac{\nabla^2 \mathrm{tr}(\boldsymbol{\sigma})}{c} \tag{11}$$

In terms of the grain size d, the strain rate becomes:

$$\dot{\epsilon}_v \propto \frac{D\Omega\sigma}{k_B T d^2} \tag{12}$$

Note that here the d^{-2} dependence reflects the inverse-square scaling of diffusion pathways within grains. Every physical process must comply with the second law of thermodynamics. We have to quantify the irreversibility of creep through the entropy production rate and demonstrate that Nabarro-Herring creep generates entropy, ensuring thermodynamic consistency. The entropy production rate $\dot{S}$ quantifies the irreversibility of Nabarro-Herring creep shall be

$$\dot{S} = \int_V \frac{\vec{J} \cdot \nabla \mu}{T} \, dV \tag{13}$$

Substituting $\vec{J} = -\frac{Dc\Omega}{k_B T} \nabla \mathrm{tr}(\boldsymbol{\sigma})$:

$$\dot{S} = \int_V \frac{Dc\Omega^2}{T k_B T^2} \left(\nabla \mathrm{tr}(\boldsymbol{\sigma}) \right)^2 \, dV \tag{14}$$

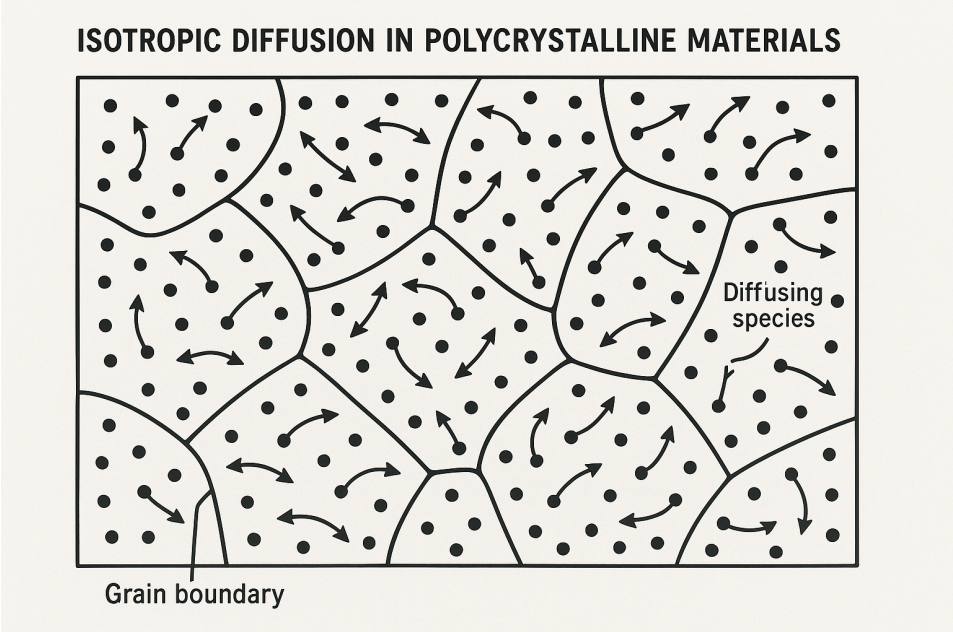

Figure 6: Isotropic diffusion in polycrystalline materials

Positive entropy production ensures compliance with the second law of thermodynamics. Here the diffusion coefficient D integrates atomic-scale processes, including:

$$D = a^2 \nu \exp\left(-\frac{Q}{k_B T}\right) \tag{15}$$

where a is the atomic jump distance, and ν is the vibrational frequency. The characteristic diffusion length d governs the creep rate: $\dot{\varepsilon} \propto \frac{1}{d^2}$. For polycrystalline aggregates, we have:

$$\dot{\varepsilon} = A \frac{\sigma D \Omega}{k_B T d^2} \tag{16}$$

where A accounts for grain geometry and crystal anisotropy. Doing the Comparison with Other Mechanisms: The strain rate due to lattice diffusion is given by:

Mechanism	Diffusion Path	Strain Rate Dependence	Grain Size Scaling
Nabarro-Herring	Lattice diffusion	$\dot{\varepsilon} \propto \frac{\sigma}{d^2}$	d^{-2}
Coble Creep	Grain boundary	$\dot{\varepsilon} \propto \frac{\sigma}{d^3}$	d^{-3}

Table 1: Comparison of Creep Mechanisms

$$\dot{\varepsilon}_{\mathrm{NH}} = A_1 \frac{\sigma}{d^2} \exp\left(-\frac{Q_d}{RT}\right) \tag{17}$$

where $\dot{\varepsilon}_{\mathrm{NH}}$ is the strain rate, σ is the applied stress, d is the grain size, Q_d is the activation energy for diffusion, R is the universal gas constant, T is the absolute temperature, and A_1 is a material-dependent constant. Phase Field Crystal simulations successfully modeled nanopolycrystalline systems, demonstrating theoretical agreement in both creep stress and grain size exponents [14].

2.1.2 Coble Creep (Grain Boundary Diffusion)

Coble creep is a diffusional deformation mechanism occurring in fine-grained polycrystalline materials at elevated temperatures. This creep was first observed by Coble in 1963 [22]. It arises due

to the stress-driven redistribution of material through grain boundary diffusion, leading to strain accommodation. The deformation behavior of polycrystalline materials at elevated temperatures is governed by creep mechanisms that depend on microstructural parameters such as grain size and diffusional pathways. Among these mechanisms, *Coble creep* dominates in materials with fine grain sizes, where grain boundary diffusion is the primary mode of atomic transport. Coble creep and pressure solution plays an important role in the deformation of polymineralic rocks [47] [48].

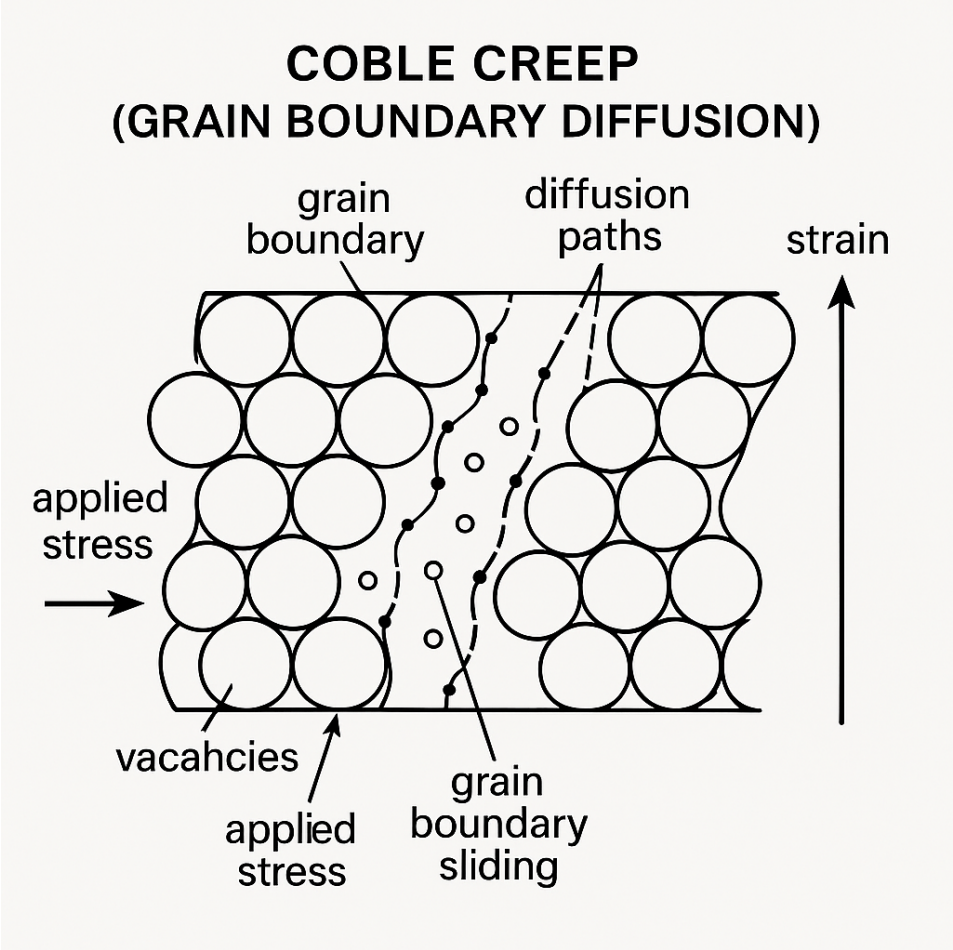

Figure 7: Coble Creep (Grain Boundary Diffusion)

Literature Review of Coble Creep (Grain Boundary Diffusion)

The modern understanding of grain-boundary diffusion creep begins with Coble (1963) [22], who derived the now-classic creep law in which the strain rate depends linearly on stress and inversely on the cube of the grain size, showing that grain-boundary diffusion controls creep in fine-grained materials. Around the same time, Paladino and Coble (1963) [154] provided experimental confirmation in ceramics that grain boundaries dominate high-temperature transport, offering essential support for Coble's theory.

Building on this, Raj and Ashby (1971) [67] demonstrated how grain-boundary sliding must be accommodated by diffusion and showed that at small grain sizes and low stresses, boundary diffusion provides the accommodation mechanism. Ashby and Verrall (1973) [155] refined this with a core–mantle model of sliding, distinguishing conditions where Coble creep dominates over Nabarro–Herring creep. Experimental criteria for recognizing diffusional creep were clarified by Langdon (1994) [156], who emphasized the stress exponent of 1 and the grain-size exponent of 3, while Langdon (2006) [72] later reviewed decades of work on grain-boundary sliding, highlighting how GB diffusion underlies fine-grained creep. The framework was consolidated by major texts such as Frost and Ashby

(1982) [7], which mapped the stress–temperature–grain-size regimes of Coble creep, Poirier (1985) [2], which gave rigorous derivations of diffusional creep. Yokogawa et. al. (1989) [157] and Shewmon (2016) [158] compiled diffusion data for boundaries that underpin rate laws. Theoretical treatments by Ghahremani (1980) [159] modeled stress fields created by diffusion-accommodated sliding, while experimental observations by Ruano and Sherby (1982) [160] confirmed Coble-type behavior at low stresses. A comprehensive review of boundary diffusion data by Lessing and Gordon (1977) [161] supplied quantitative parameters, and Wakai et. al. (2005) [162] estimated rates of densification and creep in polycrystals, clarifying the conditions where boundary diffusion dominates.

The link between Coble creep and fracture was made clear by Nix (1988) [163], who showed that creep cavities grow by grain-boundary diffusion. Later, Kassner and Pérez-Prado (2000) [164] reviewed creep broadly, distinguishing diffusional from dislocation mechanisms, while experiments by Mohamed and Langdon (1974) [165] and Langdon (1977) [167] showed how diffusional creep regimes emerge at fine grains and low stresses. Mohamed and Li (2001) [168] further reviewed superplastic flow, identifying the conditions where GB diffusion controls accommodation. The role of second phases was clarified by Atkinson (1988) [169], who showed how particles that pin boundaries alter Coble rates. In Earth sciences, Herwegh and Jenni (2001) [170] quantified how grain-boundary networks provide diffusion pathways, and Hirth and Kohlstedt (2003) [171] synthesized flow laws for olivine, showing where Coble creep dominates. More recently, Wang et al. (2020) [172] reviewed rock viscosity, highlighting $m \approx 3$ regimes consistent with GB diffusion, while Tasaka et al. (2017) [173] [174] experimentally demonstrated diffusion creep in plagioclase. Hansen et al. (2011) [176] constrained low-temperature flow of olivine, and Goldsby and Kohlstedt (2001) [177] identified the grain-size and stress exponents for ice consistent with Coble behavior, building on their earlier direct evidence of GBS in ice (Goldsby and Kohlstedt (1997) [178]). These works established that Coble creep is active not just in ceramics and metals but also in rocks and ice.

Syntheses by Bürgmann and Dresen (2008) [179] emphasized that Coble creep is important in the lower crust and upper mantle. Earlier, Mocellin and Kingery (1980) [180] had shown in fine-grained alumina that GB diffusion controls creep, with marker-line studies by Chokshi (1990) [181] confirming sliding accommodated by diffusion. Later work on oxygen and aluminum diffusion in alumina by Heuer (2008) [182] refined the kinetic inputs to Coble laws, while investigations of (Co,Mg)O by Dimos (1988) [183] showed grain-size sensitive creep matching boundary diffusion control. Review by Gifkins (1968) [184] had already established how Nabarro–Herring and Coble regimes could be separated. Other probes included noise studies in aluminum by Koch (1985) [185], where activation energies matched GB diffusion, and transient creep studies by Raj (1975) [186] showing how elastic strains evolve into diffusional flow. The connection between Coble creep and cavitation was drawn by Raj and Ashby (1975) [187], who modeled void growth by GB diffusion, with later reviews (Kassner and Hayes (2003) [188] & Meixner et. al. (2022) [189]) consolidating this picture. Small-angle neutron scattering studies by Fuller (1984) [190] directly quantified creep cavities formed under Coble-controlled conditions.

Theoretical extensions such as those by polycrystal models by Kim (2003) [191] predicted creep rates for elongated grains where GB diffusion and sliding interact. At the nanometer scale, PhD work by Wang (2010) [192] and Brassard (2003) [193] showed that nanocrystalline Ni and Cu undergo room-temperature creep controlled by GB diffusion. Simulation studies by Schiotz (1998) [194] confirmed that below 20 nm, grain-boundary-mediated processes dominate, while more recent efforts in grain-boundary complexion engineering by Khalajhedayati & Rupert (2015) [138] and Zhang (2022) [196] demonstrated that chemical doping can suppress Coble creep by reducing GB diffusivity. Finally, modern textbooks by Carter and Norton (2007) [197], Meyers and Chawla (2008) [198], and Kassner (2015) [1] consolidated this knowledge for broad use. In Earth sciences, reviews of mantle rheology (Hirth & Kohlstedf (2003) [171]) and work on ice creep (Goldsby & Kohlstedt (2001) [177]) reinforced that grain-boundary diffusion creep is a universal mechanism across different materials.

Even summaries in sources like Wikipedia today rest on this robust body of literature, consistently distinguishing the cubic grain-size dependence of Coble creep from the quadratic dependence of Nabarro–Herring creep.

Analysis of Coble Creep (Grain Boundary Diffusion)

The initiation of Coble creep is fundamentally driven by stress-induced gradients in chemical potential. Understanding these gradients requires a rigorous formulation of the thermodynamic forces acting on atoms. We need to establish the connection between external stress and the chemical potential gradients that drive diffusion. The chemical potential μ of an atom in the presence of stress is expressed as:

$$\mu = \mu_0 + \Omega\sigma \tag{18}$$

where μ_0 is the reference chemical potential in the absence of stress, Ω is the atomic volume, σ is the applied stress. The gradient of the chemical potential along a grain boundary is given by:

$$\frac{\partial \mu}{\partial x} = \Omega \frac{\partial \sigma}{\partial x} \tag{19}$$

where x is the spatial coordinate along the grain boundary. The atomic flux J, which quantifies the rate of diffusion, is governed by Fick's first law:

$$J = -D_b \frac{\partial C}{\partial x} \tag{20}$$

where D_b is the grain boundary diffusion coefficient, and C is the concentration of atoms. Using the Boltzmann relation for atomic concentration:

$$C = C_0 \exp\left(\frac{\mu}{kT}\right) \tag{21}$$

where k is Boltzmann's constant and T is the absolute temperature, the gradient of concentration becomes:

$$\frac{\partial C}{\partial x} = \frac{C_0}{kT} \exp\left(\frac{\mu}{kT}\right) \frac{\partial \mu}{\partial x} \tag{22}$$

Substituting Eq. (2) into Eq. (5), we have:

$$\frac{\partial C}{\partial x} = \frac{C_0 \Omega}{kT} \frac{\partial \sigma}{\partial x} \tag{23}$$

Finally, substituting Eq. (6) into Eq. (3), the atomic flux is expressed as:

$$J = -\frac{D_b C_0 \Omega \sigma}{kT} \tag{24}$$

This equation forms the foundation for connecting atomic diffusion to macroscopic deformation. To describe macroscopic deformation, it is essential to relate the atomic flux derived above to the volumetric transport of material and, ultimately, to the strain rate. We need to bridge the microscopic and macroscopic descriptions of the deformation process. The volumetric transport rate per unit area of grain boundary is given by:

$$\dot{V} = J\Omega \tag{25}$$

where $\dot{V}$ is the volumetric transport rate, and Ω is the atomic volume. For a cubic grain with side length d, the strain rate $\dot{\varepsilon}$ is proportional to the volumetric transport rate scaled by the geometric factor of the grain:

$$\dot{\varepsilon} = \frac{\delta}{d^3} \dot{V} \tag{26}$$

where δ is the effective thickness of the grain boundary. Substituting Eq. (8) into Eq. (9), we have:

$$\dot{\varepsilon} = \frac{\delta}{d^3} J\Omega \tag{27}$$

Using the flux expression from Eq. (7), the strain rate becomes:

$$\dot{\varepsilon} = \frac{\delta}{d^3} \frac{D_b C_0 \Omega^2 \sigma}{kT} \tag{28}$$

This equation explicitly connects the strain rate to grain size, stress, and temperature, providing a macroscopic description of Coble creep.

To predict the behavior of materials undergoing Coble creep, it is crucial to understand how the strain rate depends on fundamental parameters such as temperature, grain size, and stress. We have to derive these dependencies and explores their implications. The grain boundary diffusion coefficient D_b is temperature-dependent and follows an Arrhenius-type relationship:

$$D_b = D_0 \exp\left(-\frac{Q_b}{RT}\right) \tag{29}$$

where D_0 is the pre-exponential factor, Q_b is the activation energy for grain boundary diffusion, and R is the universal gas constant. Substituting Eq. (12) into Eq. (11), the strain rate becomes:

$$\dot{\varepsilon} = \frac{\delta}{d^3} \frac{D_0 \Omega^2 \sigma}{kT} \exp\left(-\frac{Q_b}{RT}\right) \tag{30}$$

This equation highlights the exponential sensitivity of the strain rate to temperature, dominated by the activation energy Q_b. The cubic dependence on grain size is evident in Eq. (11). Smaller grain sizes increase the strain rate significantly:

$$\dot{\varepsilon} \propto \frac{1}{d^3} \tag{31}$$

The linear dependence of strain rate on applied stress σ reflects the direct influence of external loading:

$$\dot{\varepsilon} \propto \sigma \tag{32}$$

In fine-grained materials, grain boundary diffusion dominates, and the strain rate is expressed as:

$$\dot{\varepsilon}_{\mathrm{C}} = A_2 \frac{\sigma}{d^3} \exp\left(-\frac{Q_g}{RT}\right) \tag{33}$$

where Q_g is the activation energy for grain boundary diffusion, and A_2 is another material constant.

These mechanisms emphasize the inverse dependence of creep rate on grain size, highlighting the significance of microstructural engineering in creep-resistant materials. To identify the dominant mechanism in a material, researchers often analyze the relationship between grain size and strain rate. By altering the grain size and observing its impact on the strain rate, they can calculate the value of n and determine whether Coble creep or Nabarro–Herring creep prevails [21].

2.2 Dislocation Creep

Creep deformation in crystalline materials under sustained stress at elevated temperatures is a key phenomenon in the study of material durability and performance. Dislocation creep, a mechanism central to plastic deformation in crystalline solids, arises from the thermally activated motion of dislocations under stress. Among various creep mechanisms, dislocation creep dominates in metals and alloys, where plastic deformation is driven by the glide and climb of dislocations. The rigorous

description of the mechanics of Dislocation Creep is given by Blum and Eisenlohr [49]. The phenomena of Dislocation Creep have been seen in Quartz Aggregates [50], Mg-Al-Zn Alloys [51], Calcite [52]. Predicting this behavior necessitates a mathematical formulation that connects the atomic-scale motion of dislocations to macroscopic deformation. To construct a mathematically rigorous framework, it is essential to begin with the precise dynamics governing the motion of dislocations. We now establish the equations of motion for dislocations under applied stress and thermal conditions.

The motion of a dislocation is determined by balancing the applied force per unit length with resistive forces. For a dislocation segment, the applied force is given by:

$$F_{\text{applied}} = \tau b \tag{34}$$

where τ is the resolved shear stress and b is the magnitude of the Burgers vector. The resistive force is proportional to the dislocation velocity v_d, with a drag coefficient B:

$$F_{\text{drag}} = B v_d \tag{35}$$

By Newton's second law, the balance of forces yields:

$$\tau b = B v_d \implies v_d = \frac{\tau b}{B} \tag{36}$$

The drag coefficient B encapsulates resistance due to lattice interactions, which are thermally dependent. It is expressed as:

$$B = B_0 \exp\left(-\frac{Q}{k_B T}\right) \tag{37}$$

where B_0 is a reference drag coefficient, Q is the activation energy, k_B is Boltzmann's constant, T is the absolute temperature. Substituting Eq. (4) into Eq. (3), the velocity becomes:

$$v_d = \frac{\tau b}{B_0} \exp\left(-\frac{Q}{k_B T}\right) \tag{38}$$

The dislocation density ρ, representing the number of dislocations per unit volume, is a dynamic quantity influenced by stress-driven multiplication and mutual annihilation. A rigorous formulation of its evolution is critical for understanding how microscopic dynamics influence macroscopic deformation. The rate of change of dislocation density is expressed as:

$$\frac{d\rho}{dt} = \alpha \frac{\tau}{b} v_d - \beta \rho^2 \tag{39}$$

where α is a constant representing the efficiency of stress-driven multiplication, β is a coefficient for annihilation due to dislocation interactions. Substituting v_d from Eq. (5):

$$\frac{d\rho}{dt} = \alpha \frac{\tau^2 b}{B_0} \exp\left(-\frac{Q}{k_B T}\right) - \beta \rho^2 \tag{40}$$

This nonlinear equation captures the competing mechanisms of dislocation multiplication and annihilation, incorporating stress and temperature dependencies. To connect the microscopic behavior of dislocations to macroscopic deformation, the strain rate must be rigorously derived as a function of dislocation density and motion. The plastic strain rate $\dot{\epsilon}_p$ arises from the collective motion of dislocations:

$$\dot{\epsilon}_p = \rho b v_d \tag{41}$$

Substituting v_d from Eq. (5):

$$\dot{\epsilon}_p = \rho b \frac{\tau b}{B_0} \exp\left(-\frac{Q}{k_B T}\right) \tag{42}$$

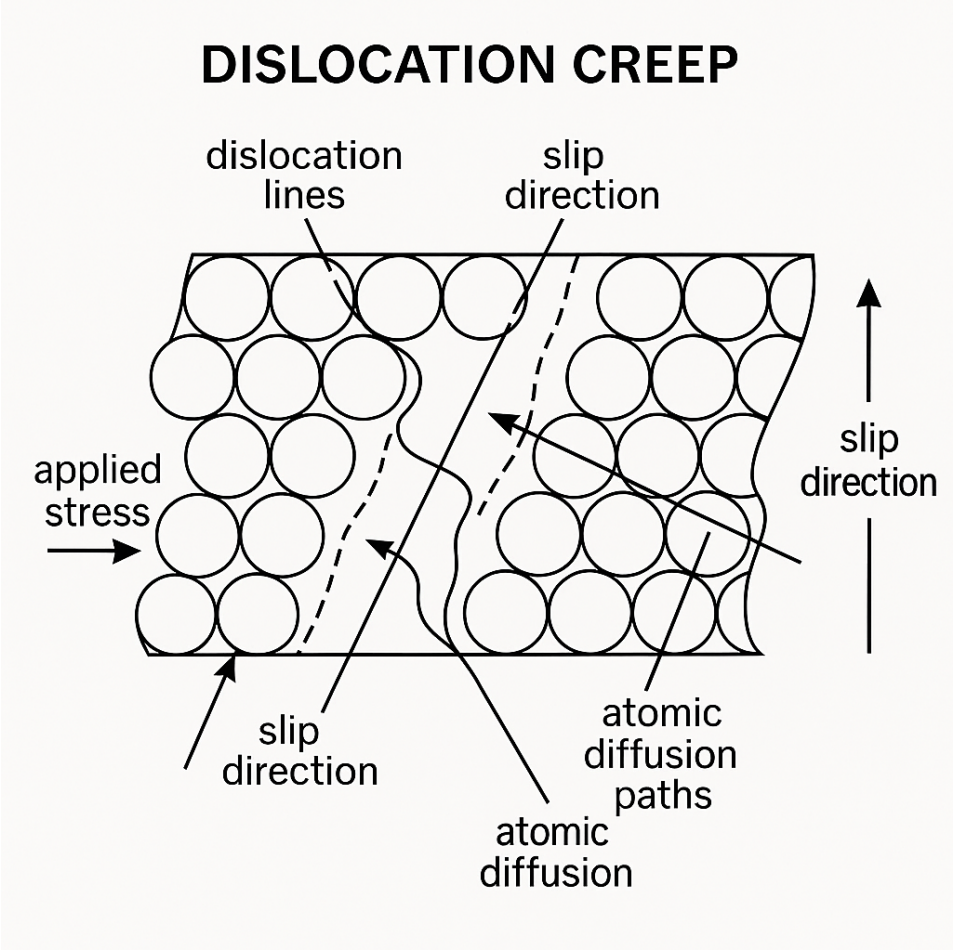

Figure 8: Dislocation Creep

Simplifying further:

$$\dot{\epsilon}_p = \rho \frac{\tau b^2}{B_0} \exp\left(-\frac{Q}{k_B T}\right) \tag{43}$$

In practical scenarios, dislocation creep often stabilizes into a steady-state regime where dislocation density and strain rate reach equilibrium. We now derive the steady-state conditions and their implications. At steady state, $\frac{d\rho}{dt} = 0$. Setting Eq. (7) to zero:

$$\alpha \frac{\tau^2 b}{B_0} \exp\left(-\frac{Q}{k_B T}\right) = \beta \rho^2 \tag{44}$$

Solving for ρ:

$$\rho_{\text{ss}} = \sqrt{\frac{\alpha \tau^2 b}{\beta B_0} \exp\left(-\frac{Q}{k_B T}\right)} \tag{45}$$

The Steady-State Strain Rate can be get by substituting ρ_{ss} into Eq. (10):

$$\dot{\epsilon}_{\text{ss}} = \sqrt{\frac{\alpha \tau^2 b}{\beta B_0} \exp\left(-\frac{Q}{k_B T}\right)} \frac{\tau b^2}{B_0} \exp\left(-\frac{Q}{k_B T}\right) \tag{46}$$

Simplifying:

$$\dot{\epsilon}_{\text{ss}} = \frac{\alpha b^3}{\beta B_0^2} \tau^3 \exp\left(-\frac{2Q}{k_B T}\right) \tag{47}$$

This equation rigorously describes the steady-state strain rate, explicitly linking it to stress, temperature, and material parameters. At higher stresses, creep deformation is governed by the motion

of dislocations through the lattice. The strain rate for dislocation creep is commonly modeled as:

$$\dot{\varepsilon}_{\mathrm{d}} = B\sigma^n \exp\left(-\frac{Q_c}{RT}\right) \tag{48}$$

where B is a pre-exponential factor, n is the stress exponent, typically between 3 and 8, Q_c is the activation energy for dislocation motion. The stress exponent n provides insight into the dominant mechanism, with higher values indicating greater sensitivity to applied stress. The derived equations must be contextualized within material science and engineering applications. We now evaluate the physical implications of the results and their relevance to material performance.

1. **Stress Sensitivity:** The cubic dependence of $\dot{\epsilon}_{\mathrm{ss}}$ on τ highlights the nonlinear impact of stress on dislocation creep. Stress sensitivity in dislocation creep refers to the mathematical and physical relationship between the applied differential stress, σ, and the resulting steady-state strain rate, $\dot{\varepsilon}$, in materials undergoing deformation at high temperatures and low to moderate stresses, where dislocation motion is the dominant mechanism. This relationship is described by a power-law equation, $\dot{\varepsilon} = A\sigma^n \exp\left(-\frac{Q}{RT}\right)$ where A encapsulates material-specific constants such as dislocation density and grain size, Q is the activation energy required for creep processes, R is the universal gas constant, T is the absolute temperature, and n is the stress exponent, which characterizes the stress sensitivity of the deformation process. The term σ^n signifies the nonlinear dependence of the strain rate on stress, with the stress exponent n reflecting the dominant dislocation mechanisms. A smaller n, typically near 3, indicates that dislocation creep is governed primarily by climb processes, where the rate-limiting step involves vacancy diffusion that enables dislocations to bypass obstacles. In contrast, larger values of n, often exceeding 5, suggest that glide-controlled mechanisms dominate, where dislocations overcome stronger obstacles such as precipitates or other dislocations, requiring higher stresses to sustain significant deformation. The stress exponent can be rigorously derived from experimental data by examining the logarithmic relationship between $\dot{\varepsilon}$ and σ, specifically by differentiating $\ln \dot{\varepsilon}$ with respect to $\ln \sigma$, yielding $n = \frac{\partial \ln \dot{\varepsilon}}{\partial \ln \sigma}$. This procedure highlights the sensitivity of the strain rate to variations in stress, with a higher n signifying a more pronounced influence of stress on deformation kinetics. The exponential term $\exp\left(-\frac{Q}{RT}\right)$ further incorporates the thermal activation of atomic processes, underscoring the role of temperature in facilitating dislocation motion through enhanced diffusion. Stress sensitivity thus provides profound insights into the interplay of stress, temperature, and microstructural factors, enabling predictive modeling of material behavior under high-temperature conditions and informing the design of alloys and geological models where dislocation creep mechanisms predominate.

2. **Thermal Effects:** The exponential temperature dependence underscores the dominance of thermally activated mechanisms in governing creep behavior. Thermal effects in dislocation creep refer to the profound influence of temperature on the mechanisms that govern the movement of dislocations and, consequently, the rate of creep deformation. Dislocation creep is a thermally activated process, meaning that an increase in temperature facilitates the atomic and microstructural processes required for dislocation motion. These processes are captured mathematically in the creep equation $\dot{\varepsilon} = A\sigma^n \exp\left(-\frac{Q}{RT}\right)$ where $\dot{\varepsilon}$ is the steady-state strain rate, A is a material-specific constant, σ is the applied differential stress, n is the stress exponent, Q is the activation energy for the creep process, R is the universal gas constant, and T is the absolute temperature. The exponential term $\exp\left(-\frac{Q}{RT}\right)$ explicitly describes the thermal activation of the creep process. At low temperatures, the exponential factor significantly suppresses the strain rate because the energy available thermally is insufficient to overcome the barriers associated with dislocation motion, such as lattice resistance, pinning at obstacles, or vacancy formation. Conversely, as temperature increases, the thermal energy becomes comparable to or exceeds the activation energy Q, facilitating dislocation climb and glide.

   Dislocation climb, in particular, is a diffusion-controlled process, where atoms or vacancies

must migrate to or away from dislocations for them to bypass obstacles. The rate of atomic diffusion is strongly temperature-dependent and typically follows an Arrhenius relationship, which is directly reflected in the $\exp\left(-\frac{Q}{RT}\right)$ term. The activation energy Q is a critical parameter that depends on the dominant diffusion mechanism in the material. For instance, in pure metals, Q is often associated with self-diffusion, whereas in alloys or complex materials, it may reflect vacancy diffusion through solute-rich regions. The temperature dependency is so significant that even slight changes in T can result in orders-of-magnitude variations in $\dot{\varepsilon}$. Moreover, at very high temperatures approaching the melting point of a material, the mobility of dislocations becomes exceptionally high due to enhanced diffusion, leading to faster creep rates. However, if the temperature becomes excessively high, other deformation mechanisms, such as diffusional creep or grain boundary sliding, may become more dominant than dislocation creep. In summary, thermal effects in dislocation creep control the rate at which dislocations overcome obstacles via thermally activated mechanisms such as climb and glide. The temperature dependence, encapsulated in the Arrhenius-type term $\exp\left(-\frac{Q}{RT}\right)$, highlights the critical role of thermal energy in facilitating the microstructural processes that drive dislocation motion. Understanding these effects is essential for predicting and mitigating high-temperature deformation in engineering materials.

3. **Implications for Material Design:** The implications of dislocation creep for material design are fundamentally rooted in the quantitative relationship between strain rate, applied stress, and temperature, encapsulated in the constitutive equation $\dot{\varepsilon} = A\sigma^n \exp\left(-\frac{Q}{RT}\right)$. This equation reveals that the steady-state strain rate, $\dot{\varepsilon}$, is exponentially sensitive to the activation energy Q, inversely proportional to temperature T, and nonlinearly dependent on the applied stress σ through the stress exponent n. The precise interplay of these parameters highlights critical pathways for designing materials that resist dislocation creep under high-temperature and high-stress conditions. One of the most significant factors is the activation energy Q, which represents the energy barrier for thermally activated dislocation mechanisms such as climb and glide. Increasing Q through microstructural engineering—such as the introduction of solute atoms, precipitates, or dispersoids—creates barriers that hinder dislocation mobility, thereby reducing the strain rate exponentially. These obstacles can also influence the stress dependence characterized by n, with materials designed to promote a higher effective stress exponent being more resistant to small increments in applied stress.

   The pre-exponential factor A and its relation to the material's microstructure further illustrate the intricacy of design strategies. This parameter reflects the density and mobility of dislocations, which are heavily influenced by grain size, dislocation substructures, and precipitate distribution. Grain size, in particular, governs the Hall-Petch effect, where finer grains reduce dislocation mobility through grain boundary strengthening. However, at high temperatures, fine grains may encourage grain boundary sliding or diffusional creep mechanisms, necessitating an optimal grain size tailored to the specific temperature and stress regime. Precipitates, often introduced through precipitation hardening, provide long-range elastic fields that impede dislocation motion. The coherency, size, and spacing of these precipitates are critical; too small or incoherent precipitates may lose effectiveness at elevated temperatures, while excessive precipitate coarsening can degrade mechanical properties over time.

   Another central consideration in material design is the effect of solid solution strengthening, where alloying elements create local lattice distortions that interact with dislocations, increasing the stress required for motion. The solute-dislocation interaction becomes particularly significant for dislocation climb, a diffusion-controlled process essential for bypassing obstacles. This interaction underscores the importance of the diffusivity term implicit in the exponential factor $\exp\left(-\frac{Q}{RT}\right)$, where Q often correlates with the self-diffusion or vacancy diffusion energy of the host lattice or secondary phases. Furthermore, the temperature-dependent

exponential term underscores the dominance of thermal stability. Materials that retain their microstructural integrity, such as stable precipitates or low-diffusivity phases, exhibit superior performance at elevated temperatures. For example, nickel-based superalloys, employed in turbine blades, achieve remarkable creep resistance through the optimization of Q and A via careful alloying and processing to stabilize the γ'-phase precipitates and suppress diffusional degradation.

Additionally, environmental considerations, such as oxidation or corrosion, interact synergistically with creep mechanisms, exacerbating deformation through surface or grain boundary degradation. The application of protective coatings or the incorporation of oxidation-resistant alloying elements can mitigate these effects. In totality, the design of creep-resistant materials involves a multi-faceted optimization of the parameters A, Q, n, and T through advanced microstructural engineering, alloy development, and environmental control. This rigorous approach, grounded in the mathematical formalism of dislocation dynamics and thermal activation theory, enables the creation of materials capable of withstanding extreme service conditions, ensuring structural integrity and prolonged lifespans in critical applications. This framework provides predictive tools for designing materials with enhanced creep resistance by optimizing parameters such as α, β and Q.

2.3 Grain Boundary Sliding

Grain boundary sliding contributes significantly to creep in fine-grained polycrystals. This mechanism, often coupled with diffusion, facilitates accommodation of plastic deformation without substantial microstructural changes. Adams and Murray [91] in 1962 first observed Grain boundary scattering in NaCl and MgO bicrystals. Grain boundary scattering has also been observed for other systems like octachloropropane using in situ techniques [88], Zn-Al alloys using electron microscopy [92]. Grain Boundary Sliding (GBS) is an intricate deformation mechanism essential to the behavior of polycrystalline materials under elevated temperatures. Grain Boundary Sliding refers to the relative tangential motion of grains across their boundaries under applied stress, often driven by applied stresses under high-temperature conditions. In polycrystalline materials, this happens when external stress is applied, and the homologous temperature rises above roughly 0.4 [64]. Grain boundary sliding can be categorized into two primary types: Rachinger sliding [65][16] and Lifshitz sliding [66]. The shape of the boundary plays a significant role in influencing both the extent and speed of grain boundary sliding [67]. Grain boundaries tend to exhibit a wavy appearance during creep at high temperatures. Such boundaries can be represented mathematically by a sinusoidal curve defined by its wavelength λ and amplitude h. High λ/h ratios can hinder diffusional flow, potentially resulting in the formation of diffusional voids that ultimately cause creep fracture [70] [67]. A substantial portion of strain is attributed to grain boundary sliding, particularly in fine-grained materials and at elevated temperatures. Lifshitz grain boundary sliding accounts for approximately 50-60 percentage of the strain in Nabarro–Herring diffusion creep [72], and it is the main contributor to ceramic failure at high temperatures due to the formation of glassy phases at their grain boundaries [87]. For polycrystalline grains to slide relative to each other, there must be simultaneous mechanisms that allow for this movement without the grains overlapping, which would be physically impossible [88]. The primary mechanisms by which materials can accommodate deformation at the microscopic level are:

1. **Dislocation Movement** [89]: Dislocations are line defects within the crystal lattice that move under stress, contributing significantly to plastic deformation. Dislocation movement occurs through processes such as **glide** and **climb**. **Glide** refers to the motion of dislocations along specific crystallographic planes, driven by shear stress, allowing for deformation by sliding of atomic planes relative to each other. This sliding is characterized by a decrease in elastic energy, making the material more ductile. **Climb**, on the other hand, is the process where dislocations move out of their glide planes by the absorption or emission of vacancies. This movement can

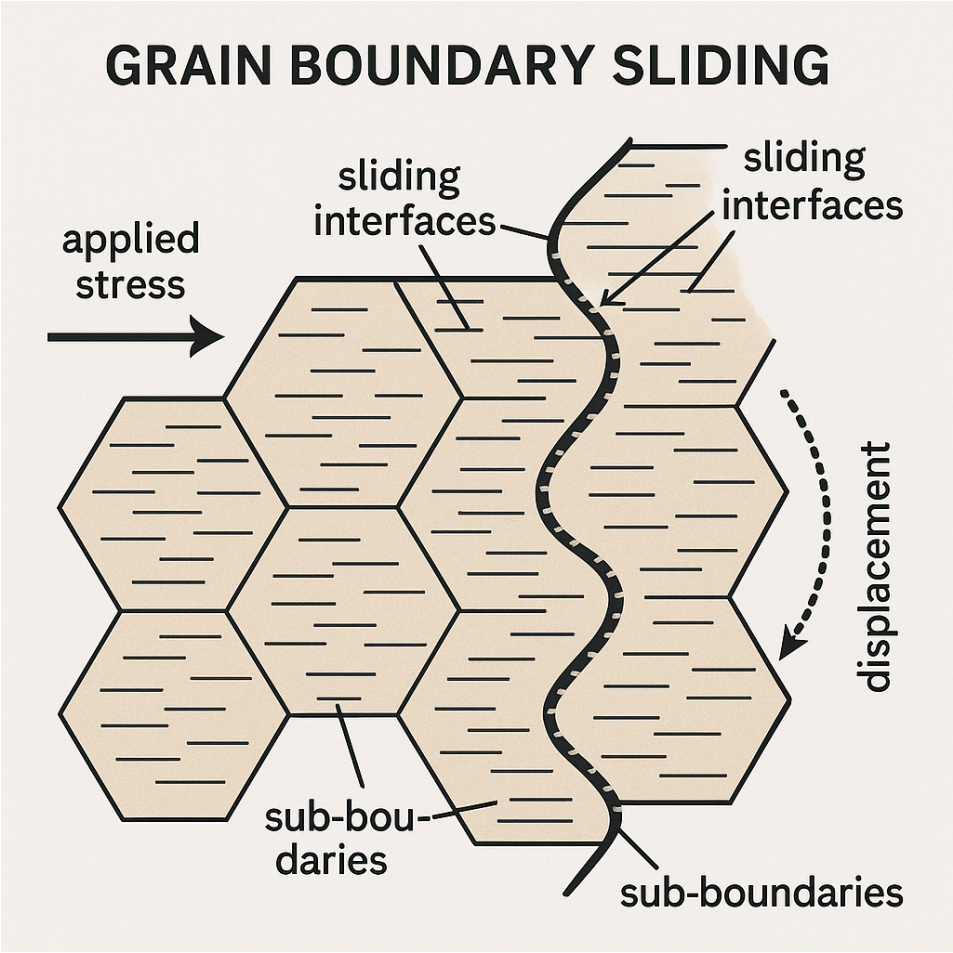

Figure 9: Grain Boundary Sliding

relieve local stress fields more directly, allowing dislocations to reconfigure and reduce their energy, thereby accommodating deformation more effectively. The combination of glide and climb mechanisms allows for continuous strain accommodation, maintaining structural integrity under stress.

2. **Elastic Distortion** [67]: **Elastic deformation** is the reversible change in shape of the grains within a material when subjected to small deformations. In this mechanism, the grains themselves can deform elastically, meaning the atoms within the grains move under stress but return to their original positions once the stress is removed. This elastic response is crucial for accommodating small strains without permanent deformation. When a material undergoes small deformations, the grains can distort elastically, which not only absorbs the applied stress but also permits the recovery of energy without the accumulation of dislocations. This mechanism helps in distributing the stress more evenly across the material, preventing localized plastic deformation and crack initiation, thereby maintaining compatibility and preventing failure.

3. **Diffusional Accommodation** [67]: **Diffusional creep** is a critical mechanism for accommodating plastic deformation, especially at elevated temperatures. In diffusional accommodation, atoms or vacancies migrate through the grain boundaries or within the grains themselves. This diffusion process allows for the redistribution of material, helping to relieve stress by moving atoms to areas where the material is more compressed. The movement can occur along grain boundaries where atomic mobility is enhanced due to the reduced energy barrier compared to intra-grain diffusion. This redistribution enables the material to deform more uniformly and adapt to stress by adjusting its microstructure without permanent change in the lattice. This diffusional process can effectively increase the material's ductility, enabling it to handle higher strains before failure.

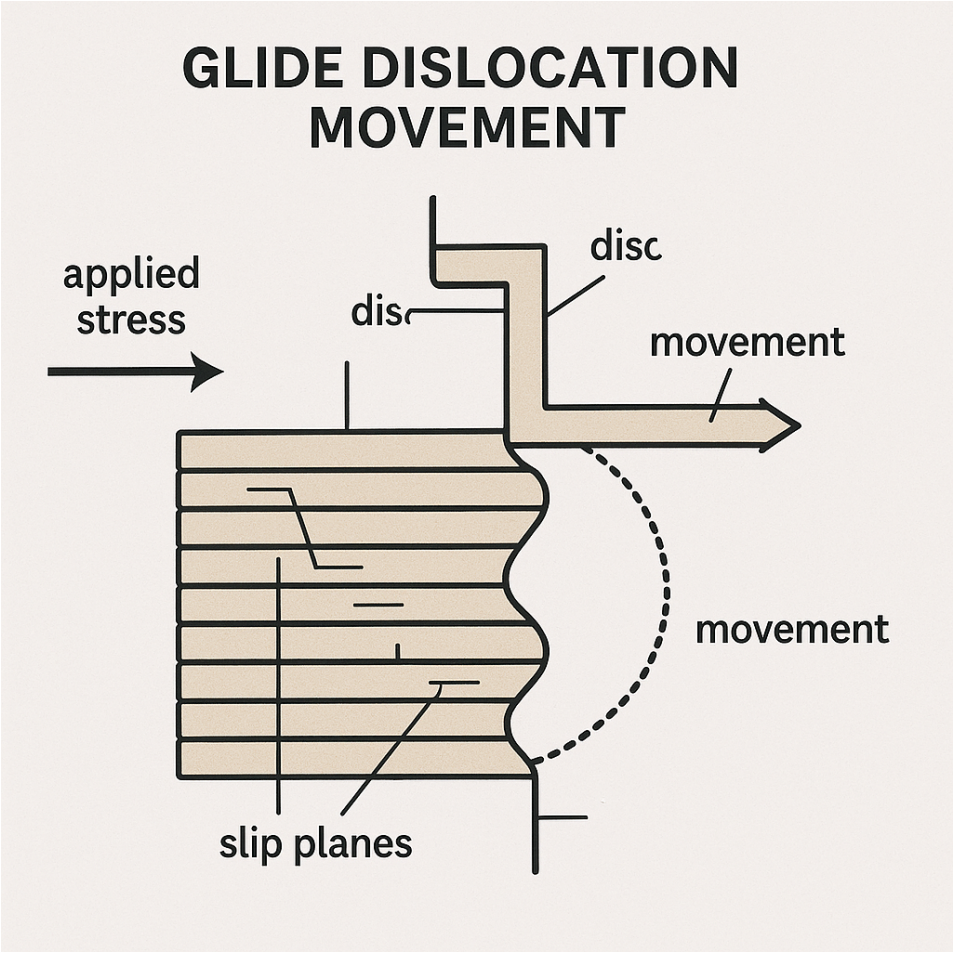

Figure 10: Glide Dislocation Movement

Each of these mechanisms—dislocation movement, elastic distortion, and diffusional accommodation—plays a crucial role in the accommodation of plastic deformation. They operate on different timescales and at different scales within the material, each contributing to the overall ductility and strength of the material. Dislocations manage localized deformation through dislocation glide and climb, elastic distortion ensures recoverable strains in the grains, and diffusional accommodation allows for stress relaxation via atomic movement. These processes are not mutually exclusive but rather interdependent, acting in concert to enable a material to deform compatibly under applied stress, thus maintaining its structural integrity and preventing catastrophic failure. The Grain Boundary Sliding's role in accommodating strain mismatches, influencing creep, and dictating microstructural evolution makes it a cornerstone of deformation mechanics. The minimum creep rate for diffusion can be expressed as [90]:

$$\dot{\epsilon}_s = \frac{ADGb}{kT}\left(\frac{b}{d}\right)^p\left(\frac{\sigma}{G}\right)^n$$

Grain boundaries serve as the loci of relative motion and must be precisely represented as two-dimensional manifolds embedded in the three-dimensional bulk material. This geometric description provides the foundation for all subsequent kinematic and mechanical formulations. Let $S \subset \mathbb{R}^3$ denote a grain boundary, parameterized by the coordinates $(u, v) \in \mathcal{D} \subset \mathbb{R}^2$. The position vector is:

$$\vec{r}(u, v) = x(u, v)\vec{e}_1 + y(u, v)\vec{e}_2 + z(u, v)\vec{e}_3 \tag{49}$$

where $\{\vec{e}_i\}_{i=1}^3$ form an orthonormal basis. The tangent vectors to S are:

$$\vec{t}_u = \frac{\partial \vec{r}}{\partial u}, \quad \vec{t}_v = \frac{\partial \vec{r}}{\partial v} \tag{50}$$

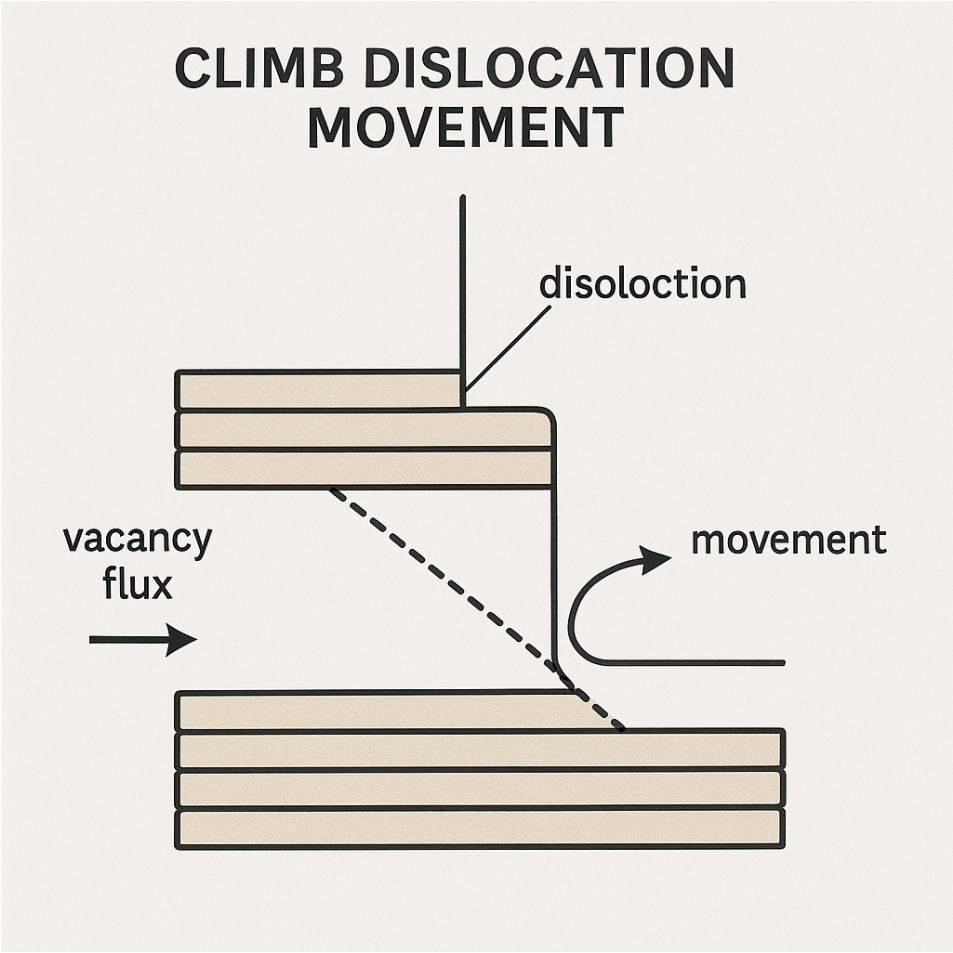

Figure 11: Climb Dislocation Movement

The unit normal vector $\vec{n}$ is:

$$\vec{n} = \frac{\vec{t}_u \times \vec{t}_v}{\|\vec{t}_u \times \vec{t}_v\|} \tag{51}$$

The metric tensor $\mathbf{g}$ encodes the intrinsic geometry of the surface:

$$\mathbf{g} = \begin{bmatrix} \vec{t}_u \cdot \vec{t}_u & \vec{t}_u \cdot \vec{t}_v \\ \vec{t}_v \cdot \vec{t}_u & \vec{t}_v \cdot \vec{t}_v \end{bmatrix} \tag{52}$$

The infinitesimal area element on S is:

$$\mathrm{d}A = \|\vec{t}_u \times \vec{t}_v\| \, \mathrm{d}u \, \mathrm{d}v \tag{53}$$

Kinematics forms the basis for describing the motion of material points on either side of the grain boundary. A rigorous derivation of relative velocity, sliding displacement, and compatibility conditions is essential for a complete understanding of GBS. The relative velocity between two adjacent grains, G_1 and G_2, at any point on S is:

$$\vec{v}_{\mathrm{rel}} = \vec{v}_1 - \vec{v}_2 \tag{54}$$

where $\vec{v}_1$ and $\vec{v}_2$ are the velocity fields of G_1 and G_2, respectively. The tangential component of $\vec{v}_{\mathrm{rel}}$, representing the sliding velocity, is:

$$\vec{v}_s = (\vec{I} - \vec{n} \otimes \vec{n}) \cdot \vec{v}_{\mathrm{rel}} \tag{55}$$

where $\vec{I}$ is the identity tensor, and $\vec{n} \otimes \vec{n}$ represents the dyadic product projecting along the normal direction. The sliding displacement $\vec{\delta}_s$ over a time interval $[0, t]$ is:

$$\vec{\delta}_s = \int_0^t \vec{v}_s \, \mathrm{d}\tau \tag{56}$$

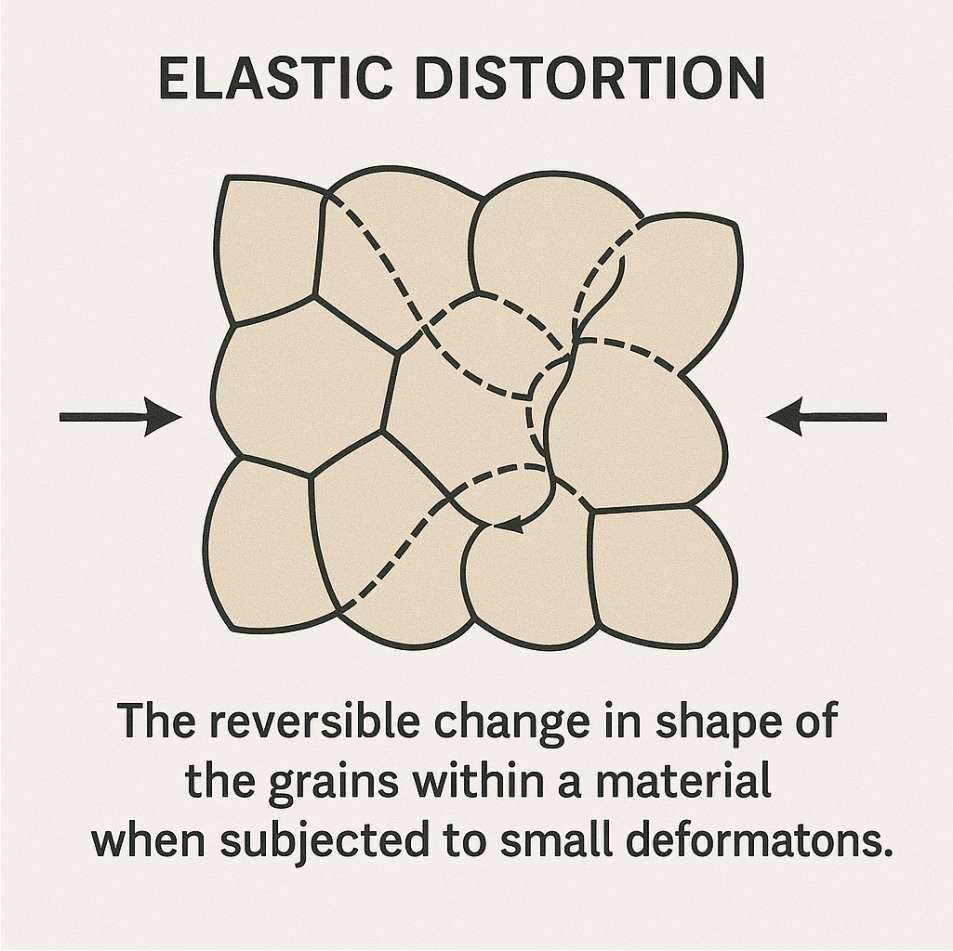

Figure 12: Elastic Distortion

The total strain rate tensor $\dot{\boldsymbol{\varepsilon}}$ is decomposed as:

$$\dot{\boldsymbol{\varepsilon}} = \dot{\boldsymbol{\varepsilon}}_{\text{bulk}} + \dot{\boldsymbol{\varepsilon}}_{\text{GBS}} \tag{57}$$

where $\dot{\boldsymbol{\varepsilon}}_{\text{bulk}}$ accounts for bulk deformation, and $\dot{\boldsymbol{\varepsilon}}_{\text{GBS}}$ is the contribution from GBS. The forces driving GBS are derived from the stress distribution at the grain boundary. A rigorous formulation of traction vectors and their tangential components is required to quantify these driving forces. The traction vector $\vec{t}$ at the grain boundary is: $\vec{t} = \boldsymbol{\sigma} \cdot \vec{n}$ where $\boldsymbol{\sigma}$ is the Cauchy stress tensor. The tangential component of $\vec{t}$, responsible for driving sliding, is:

$$\vec{t}_{\text{tan}} = (\vec{I} - \vec{n} \otimes \vec{n}) \cdot \vec{t} \tag{58}$$

Equilibrium at the grain boundary requires $\int_S \vec{t}\,\mathrm{d}A = 0$ where $\mathrm{d}A$ is the differential surface area. Constitutive relations connect the tangential traction to the sliding velocity, enabling quantitative predictions of GBS behavior. The tangential sliding velocity is proportional to the tangential traction:

$$\vec{v}_s = \frac{1}{\eta}\vec{t}_{\text{tan}} \tag{59}$$

where η is the grain boundary viscosity. The rate of energy dissipation per unit area is:

$$\dot{W}_{\text{diss}} = \vec{t}_{\text{tan}} \cdot \vec{v}_s = \frac{\|\vec{t}_{\text{tan}}\|^2}{\eta} \tag{60}$$

The validity of the GBS framework is contingent upon compliance with thermodynamic laws. This section evaluates entropy production and ensures adherence to the second law of thermodynamics. The entropy production rate per unit area is:

$$\dot{S} = \frac{\dot{W}_{\text{diss}}}{T} = \frac{\|\vec{t}_{\text{tan}}\|^2}{\eta T} \tag{61}$$

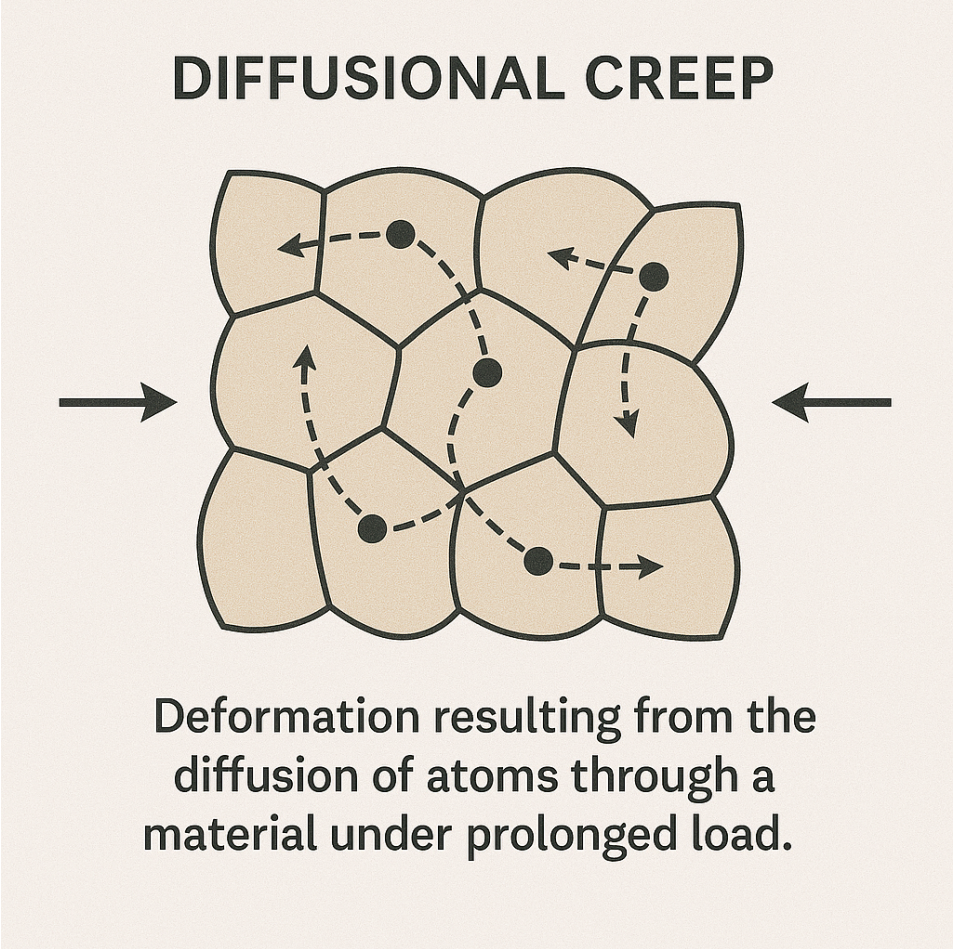

Figure 13: Diffusional creep

where T is the absolute temperature. The Clausius-Duhem inequality imposes:

$$\dot{S} \geq 0 \implies \eta > 0 \tag{62}$$

GBS contributes significantly to the macroscopic creep behavior of polycrystals. This section integrates GBS into the broader context of creep mechanics. The total creep strain rate is $\dot{\varepsilon}_{\text{creep}} = \dot{\varepsilon}_{\text{bulk}} + \dot{\varepsilon}_{\text{GBS}}$. Grain boundary sliding strain rate ($\dot{\epsilon}_{\text{GBS}}$) depends on grain size (d) for the following reasons:

1. **Role of Grain Boundaries**: Grain boundary sliding occurs along grain boundaries, and the density of grain boundaries increases as the grain size decreases. The number of grain boundaries per unit volume scales inversely with the grain size, $\sim 1/d$. A higher grain boundary density means there are more locations where sliding can occur, which increases the contribution of GBS to the overall strain rate.

2. **Diffusion Mechanisms**: Grain boundary sliding is often accommodated by diffusion, either along grain boundaries or through the bulk. Smaller grains shorten the diffusion path between boundaries, facilitating faster accommodation of sliding. The diffusion time scales inversely with d, further enhancing the rate of grain boundary sliding for smaller grains.

3. **Stress Distribution and Sliding**: For a given applied stress, smaller grains experience higher stress concentrations at the grain boundaries due to reduced grain size. This enhanced stress at the boundaries promotes sliding, leading to faster strain accumulation in smaller grains.

The GBS strain rate scales inversely with grain size d:

$$\dot{\varepsilon}_{\text{GBS}} \propto \frac{\tau}{\eta d} \tag{63}$$

where τ is the applied shear stress. The complexity of solving the governing equations necessitates numerical techniques for realistic applications. This section formulates a computational approach for analyzing GBS. The sliding velocity field is iteratively solved using:

$$\vec{v}_s^{(k+1)} = \vec{v}_s^{(k)} - \alpha \nabla(\dot{W}_{\text{diss}}) \tag{64}$$

where α is a relaxation parameter.

2.3.1 Nanomaterials

Nano-crystalline materials, consisting of grains typically less than 100 nanometers in size, exhibit unique mechanical behaviors due to their microstructural features. The fine-grained nature of these materials significantly enhances their mechanical properties by suppressing lattice creep, a thermally activated deformation process that occurs at relatively low temperatures. Lattice creep is primarily driven by the motion of dislocations — line defects within the crystal structure that facilitate plastic deformation. In nano-crystalline materials, the high density of grain boundaries acts as a barrier to dislocation motion, effectively blocking their movement and diffusion. This occurs because the dislocations encounter these grain boundaries as obstacles that prevent their glide and cross-slip — essential mechanisms for dislocation movement. The suppression of lattice creep in nano-crystalline materials can be quantitatively described using the Hall-Petch relationship:

$$\sigma_y = \sigma_0 + \frac{k}{\sqrt{d}},$$

where σ_y is the yield strength, σ_0 is the frictional stress, k is the strengthening coefficient, and d is the grain size. The relationship highlights how reducing the grain size increases the strength of the material due to the increased barrier provided by grain boundaries to dislocation movement. However, as the temperature increases, the behavior of nano-crystalline materials changes drastically. At high temperatures, the probability of grain boundary sliding increases significantly. Grain boundary sliding refers to the relative displacement of adjacent grains along their boundaries without significant dislocation movement within the grains themselves. This process becomes more probable because the thermal energy available at high temperatures facilitates atomic-level diffusion across grain boundaries. The activation energy for grain boundary sliding, Q, plays a crucial role in determining the likelihood of this process. Mathematically, the probability (P) of grain boundary sliding can be described by the Arrhenius equation:

$$P = \exp\left(-\frac{Q}{k_B T}\right),$$

where Q is the activation energy for grain boundary sliding, k_B is the Boltzmann constant, T is the absolute temperature, and P is the probability of sliding. As temperature increases, Q becomes smaller and more accessible to thermal activation, leading to a higher probability of grain boundary sliding. This sliding mechanism results in enhanced plastic deformation, which is detrimental to the mechanical properties of nano-crystalline materials at high temperatures. The increased grain boundary sliding disrupts the suppression of lattice creep and causes significant degradation in strength and stiffness of the material [93].

2.3.2 Application to High-Strength Steel and Tungsten filaments

The important application of high-strength steel within contemporary engineering practice is indicative of its exceptional mechanical properties and its critical role in supporting advanced construction technologies. To establish a robust engineering foundation for real-world applications, the precise modeling of high-strength steel is indispensable. This modeling process requires an in-depth understanding of key material parameters, including the elastic modulus, yield strength, Poisson's ratio, and specific heat capacity, which are essential for defining the intrinsic mechanical, thermal, and

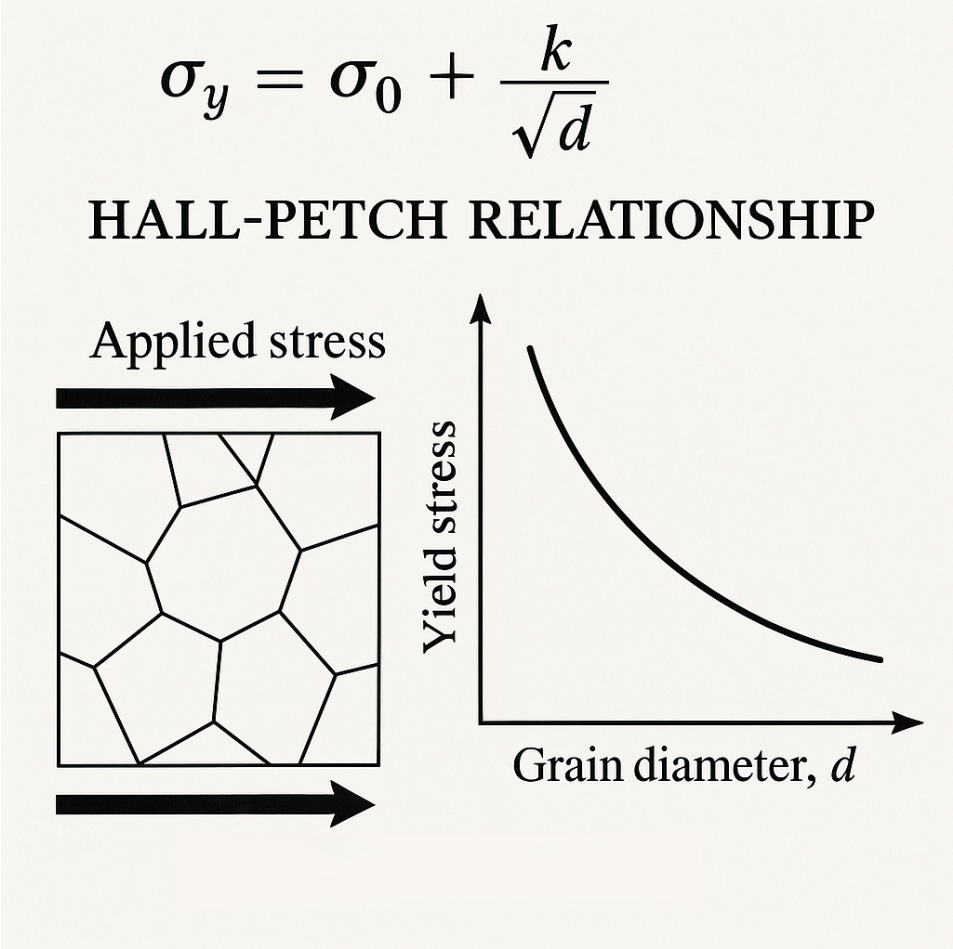

Figure 14: Hall-Petch Relationship

phase behaviors of the material.

By integrating these critical parameters across two distinct temperatures, we can perform a meticulous thermodynamic analysis to derive the Gibbs free energy (GBS energy) of high-strength steel as a function of temperature. The Gibbs free energy is a fundamental thermodynamic potential that quantitatively describes the system's potential for reversible work at a given temperature and pressure, reflecting the balance of enthalpy, entropy, and temperature-dependent internal energy transformations. This thermodynamic quantity provides a comprehensive framework for understanding the material's phase stability, structural transformations, and response to thermal loads. From this Gibbs free energy-temperature relationship, the yield strength of high-strength steel can be derived as a temperature-dependent property. Yield strength, which defines the stress at which the material begins to plastically deform, is a critical indicator of its load-bearing capacity and its suitability for structural applications exposed to varying thermal environments. The ability to model yield strength as a function of temperature enables engineers to predict and optimize the material's mechanical performance across a wide range of operating conditions, ensuring its reliability and safety in practical engineering applications [94].

Tungsten filaments, widely used in incandescent lamps and electron tubes, are exposed to extreme conditions involving high temperatures and mechanical stresses. These conditions necessitate a thorough understanding of the material's deformation mechanisms, especially grain boundary sliding. Grain boundary sliding is a significant deformation mechanism that plays a crucial role in maintaining the mechanical properties of tungsten filaments under such conditions. This process involves the relative movement of grains along their boundaries, facilitated by atomic-scale diffusion, which in turn affects the material's fatigue resistance, thermal stability, and overall durability.

The applications of Grain Boundary Sliding to Tungesten filaments is given very rigorously in the following works [96], [97], and [98].

- **High-Temperature Structural Stability and Atomic Mobility**:
  - Tungsten filaments operate at temperatures around 2000°C, where the material's mechanical properties are governed by grain boundary sliding.
  - At these temperatures, the atomic interactions at grain boundaries are critically important for accommodating deformation.
  - Grain boundary sliding involves the migration of vacancies and interstitial atoms through the grain boundary, facilitated by increased thermal energy promoting atomic diffusion.
  - The atomic-scale mechanism maintains the structural integrity of tungsten filaments under prolonged thermal exposure.
- **Micromechanical Mechanisms of Grain Boundary Sliding**:
  - The sliding of grains across their boundaries involves the activation of localized stress fields within the grain boundary regions.
  - These stress fields are a consequence of the anisotropic distribution of atomic interactions along the boundary.
  - The process follows an Arrhenius-type relationship for the sliding velocity v dependent on temperature:
    $$v \sim \exp\left(-\frac{Q}{RT}\right),$$
    where Q is the activation energy for sliding, R is the universal gas constant, and T is the absolute temperature.
  - The rate of grain boundary sliding in tungsten is influenced by impurity content and their segregation to grain boundaries, which alters the activation energy for sliding.
- **Enhancement of Fatigue Resistance**:
  - Grain boundary sliding significantly enhances the fatigue resistance of tungsten filaments.
  - The process allows for efficient stress redistribution during cyclic loading, mitigating the formation of dislocation pile-ups and microcracks.
  - The redistribution of stresses through grain boundary sliding reduces the likelihood of fatigue failure under thermal cycling conditions.
- **Thermal Management and Stress Relaxation**:
  - Grain boundary sliding plays a pivotal role in thermal management within tungsten filaments.
  - The sliding mechanism accommodates thermal expansion mismatches between adjacent grains, preventing the development of thermal gradients that could lead to stress concentrations and microcracking.
  - Stress relaxation provided by grain boundary sliding is crucial for preventing the accumulation of stress-induced defects such as dislocation tangles and microcracks.
- **Microstructural Optimization**:
  - The effectiveness of grain boundary sliding in tungsten filaments is closely tied to the material's microstructural characteristics.
  - Key factors include grain size, grain boundary misorientation, and impurity content.

- Smaller grain sizes enhance grain boundary sliding by increasing the volume fraction of grain boundaries relative to the total volume.
- Low-angle grain boundaries, characterized by high dislocation densities, are particularly conducive to sliding due to the lower activation energy for atomic diffusion.
- The presence of impurities such as oxygen, carbon, or metal alloying elements can significantly affect the grain boundary properties, influencing the sliding behavior.

In summary, grain boundary sliding is a vital deformation mechanism that significantly influences the high-temperature mechanical properties of tungsten filaments. The integration of experimental observations, advanced computational simulations, and theoretical models provides a rigorous scientific framework for understanding and optimizing grain boundary sliding in tungsten filaments. This understanding enables the design of tungsten filaments with improved fatigue resistance, thermal management, and durability under extreme conditions, ensuring their reliability in applications such as incandescent lamps and electron tubes.

2.3.3 Superplastic forming (SPF) technique

The superplastic forming (SPF) technique is an advanced material deformation process in which metals and alloys are subjected to extreme strains well beyond their yield stress. This technique facilitates the fabrication of intricate, lightweight structures with high geometric fidelity. The mechanism enabling this phenomenon is grain boundary sliding (GBS), a process that is governed by the combined actions of dislocation slip, creep, and diffusional processes. These processes occur at elevated temperatures where the material's microstructural characteristics allow for a substantial increase in the deformation capacity. Dislocation slip is the motion of dislocations—linear defects within the crystal lattice—across grain boundaries, enabling localized plastic deformation. This movement allows the material to elongate substantially without fracturing. Dislocation slip occurs due to the application of shear stress, which facilitates the sliding of dislocations through the crystal lattice, thereby accommodating plastic strain. Creep, particularly diffusional creep, involves the thermally activated movement of atoms over long distances within the material, driven by a reduction in the activation energy for diffusion at elevated temperatures. This process is crucial for accommodating the grain boundary sliding by enabling a redistribution of atomic sites across grain boundaries, thereby facilitating the sliding of grains relative to one another.

Grain boundary sliding is a key mechanism in SPF, where adjacent grains are capable of sliding past each other, accommodating large deformations while maintaining structural integrity. This sliding minimizes the development of localized stress concentrations within grains, which is a common precursor to failure in conventional forming processes. The diffusional aspect of creep promotes the exchange of atoms across grain boundaries, thus enhancing the grain boundary sliding process. The synergy of dislocation slip, diffusional creep, and grain boundary sliding underpins the extraordinary deformability of materials in SPF, allowing for the elongation and thinning required to form complex shapes without fracture. This process is particularly effective at elevated temperatures, where diffusional creep is significantly enhanced, and deformation rates are exceedingly low. Therefore, SPF is a critical technique for producing components in advanced engineering applications, such as in the aerospace and automotive industries, where weight savings, material efficiency, and performance under high-stress conditions are paramount. The interplay between dislocation slip, diffusional creep, and grain boundary sliding is fundamental to the exceptional material properties achieved in superplastic forming, making it a uniquely powerful process for manufacturing lightweight, high-strength structures.

The behavior of commercial fine-grained Al-Mg alloys under superplastic deformation, focusing on the influence of Mg content and its associated microstructural features [95]:

1. **Unusually Weak Grain Boundary Sliding (GBS)**: During the initial stage of superplastic deformation in commercial fine-grained Al-Mg alloys, grain boundary sliding (GBS) is observed to be unusually weak. This phenomenon is due to the presence of a complex microstructure, where the grain boundaries are not easily activated for sliding. The resistance to GBS is primarily due to the strengthening precipitates within the grains and along the grain boundaries, which hinder dislocation movement and grain boundary mobility. These precipitates serve as barriers to dislocation glide and grain boundary motion, creating a high-energy configuration that requires significant strain energy for activation [95].

2. **Tensile Test and Grain Elongation**: A tensile test was conducted to evaluate the superplastic properties, where grains elongated significantly along the tensile direction to a range of 50% to 70%. This substantial elongation indicates effective plastic strain accommodation through GBS, which is crucial for the material's superplasticity. The tensile test quantifies the material's ability to elongate without fracturing, which is a hallmark of superplasticity. The deformation mechanism in this context involves the cooperative action of grain boundary sliding, dislocation movement, and the formation of subgrains, all of which contribute to the observed strain [95].

3. **Increased Precipitation Depletion Zone Fractions**: Increased Mg content leads to the formation of larger precipitation depletion zones within the grains. These zones are regions devoid of precipitates, effectively weakening the grain boundaries by reducing the pinning force on dislocations. As Mg content increases, the volume fraction of these depletion zones becomes more significant, which facilitates grain boundary sliding by lowering the energy barrier for sliding at these boundaries. The depletion zones act as initiation sites for GBS, making the grain boundaries more compliant to sliding during deformation. The quantitative relationship between Mg content and the size of these depletion zones can be described by the empirical increase in their volume fraction, leading to an enhanced ability of the material to undergo GBS [95].

4. **Particle Segregation on Longitudinal Grain Boundaries**: The segregation of particles along the longitudinal grain boundaries is a crucial factor enhancing GBS. With higher Mg content, these particles, which are typically Mg-rich phases, segregate at the grain boundaries. The presence of these particles reduces the grain boundary strength, creating lubricated interfaces that are easier to slide. The particle segregation provides a lower friction interface along the grain boundaries, significantly lowering the activation energy required for GBS. The quantitative description of this phenomenon can be derived from the increased particle volume fraction, which correlates directly with the increased Mg content [95].

5. **Dislocation Activity and Subgrains**: Dislocation activity within the grains plays a pivotal role in the deformation mechanism. As Mg content increases, there is an increased density of dislocations and subgrains. These subgrains are small, misoriented regions formed by dislocations within the grains, which reduce the overall resistance to deformation. The dislocation activity within the grains leads to the formation of these subgrains, which in turn facilitate GBS by reducing the grain boundary friction. The formation of subgrains is a quantitative indicator of the enhanced plasticity of the alloy, as they reduce the internal stress and energy associated with dislocation interactions. The density of subgrains and the mobility of dislocations are critical for achieving higher elongations during superplastic deformation [95].

6. **Mg Content and Grain Size Stability**: Increasing the Mg content from 4.8% to 6.5–7.6% significantly aids grain size stability during increased temperature processes. The higher Mg content stabilizes the grain boundaries, preventing excessive grain coarsening at elevated temperatures. This stabilization is crucial for maintaining superplastic properties, as finer grains are more conducive to GBS. The Mg content helps in pinning the grain boundaries by forming Mg-rich particles within the matrix, which limit grain boundary mobility and

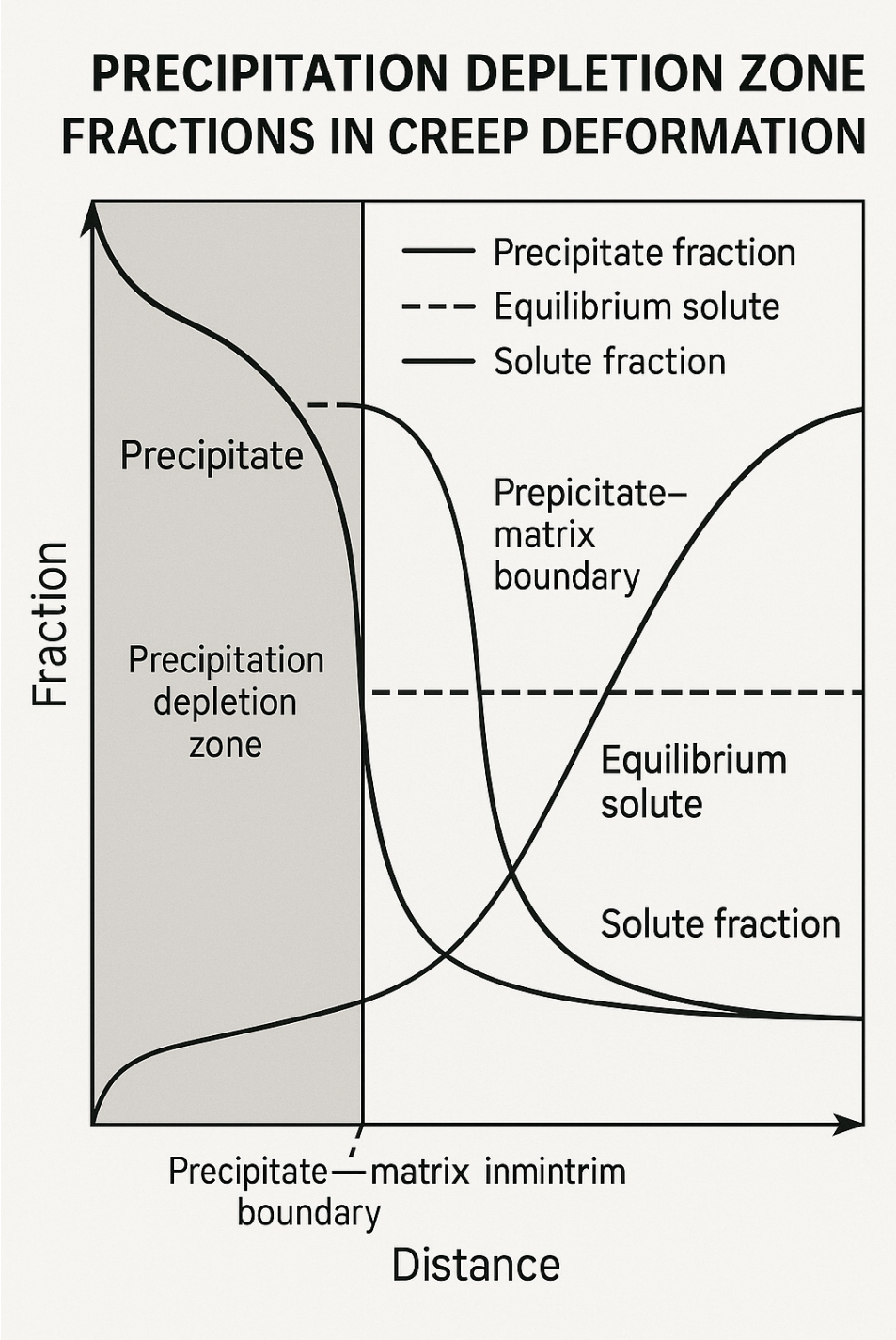

Figure 15: Precipitation Depletion Zone

prevent grain growth. The relationship between Mg content and grain size stability can be quantitatively described by the reduction in grain growth rate with increasing Mg content [95].

7. **Simplified Grain Boundary Sliding (GBS) and Reduced Diffusion Creep**: The increased Mg content simplifies GBS by providing a more lubricated grain boundary interface. This lubrication effect reduces the resistance to grain boundary sliding, which is a primary mechanism for superplastic deformation. Additionally, the higher Mg content reduces the contribution of diffusion creep to deformation. Diffusion creep is a mechanism where atomic diffusion occurs along the grain boundaries to accommodate deformation. As Mg content increases, the alloy becomes less reliant on diffusion creep, as the grain boundaries are already weakened by Mg segregation and depletion zones, reducing the need for atomic diffusion. The decreased diffusion creep contribution can be quantitatively described by the reduced activa-

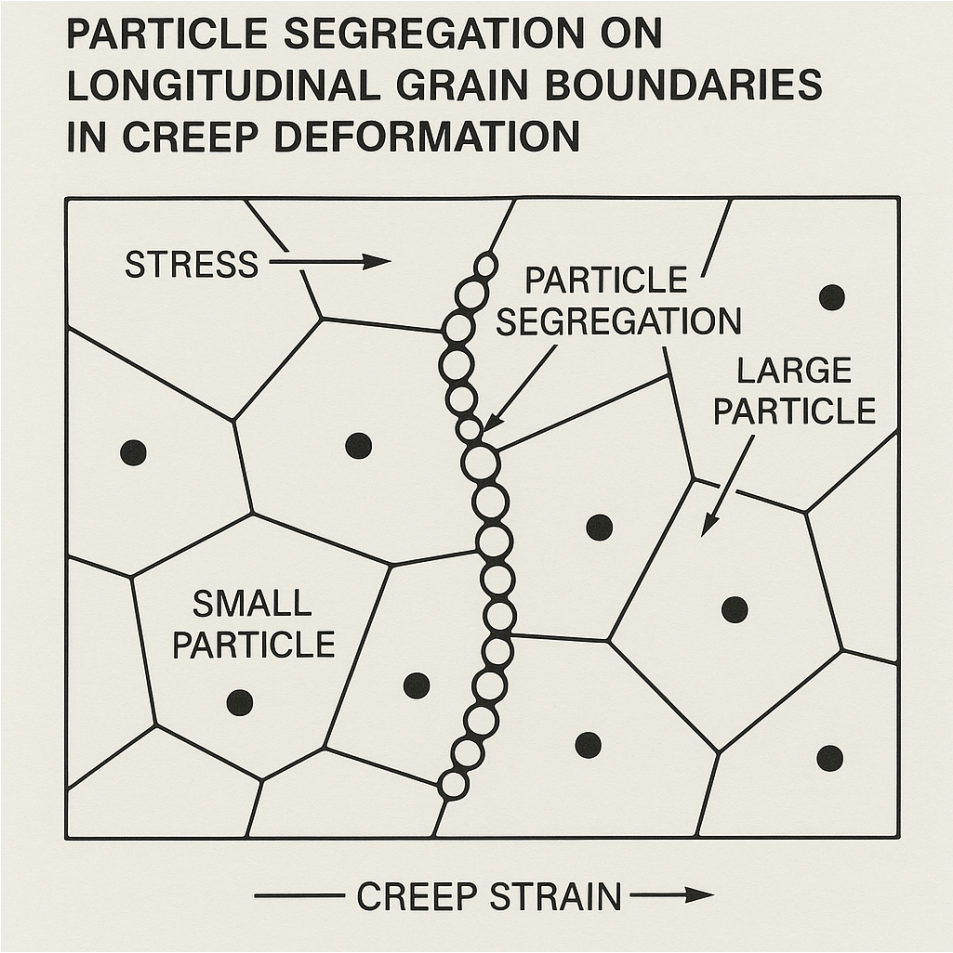

Figure 16: Particle Segregation on Longitudinal Grain Boundaries

tion energy for deformation and the corresponding decrease in the diffusion coefficients at high temperatures [95].

8. **Increased Failure Strain**: The modification of Mg content leads to a significant increase in the material's failure strain from 300% to 430%. This increase is a direct result of the enhanced GBS, reduced diffusion creep contribution, and the improved microstructural stability due to higher Mg content. The increased failure strain quantifies the alloy's ability to sustain higher levels of deformation without fracture. The quantitative measure of failure strain can be linked to the increased volume fractions of precipitation depletion zones, the enhanced particle segregation, and the higher density of dislocations and subgrains. These factors collectively contribute to a more ductile and superplastic material, capable of large elongations during deformation [95].

2.4 Solute Drag Creep

Solute drag creep is a deformation mechanism occurring predominantly in materials at high temperatures and low stresses, characterized by the resistance to dislocation motion caused by solute atoms in the lattice. This resistance is a result of the elastic and diffusive interaction between dislocations and solute atoms. The understanding of solute drag creep is deeply rooted in diffusion theory, elasticity, and the dynamics of dislocation motion, as captured through mathematical models. At the core of solute drag creep is the coupling between the motion of dislocations and the diffusion of solute atoms. Dislocations, being line defects, generate stress fields within the crystal lattice. A solute atom in the lattice experiences a potential energy E_{int} due to these stress fields. The interaction

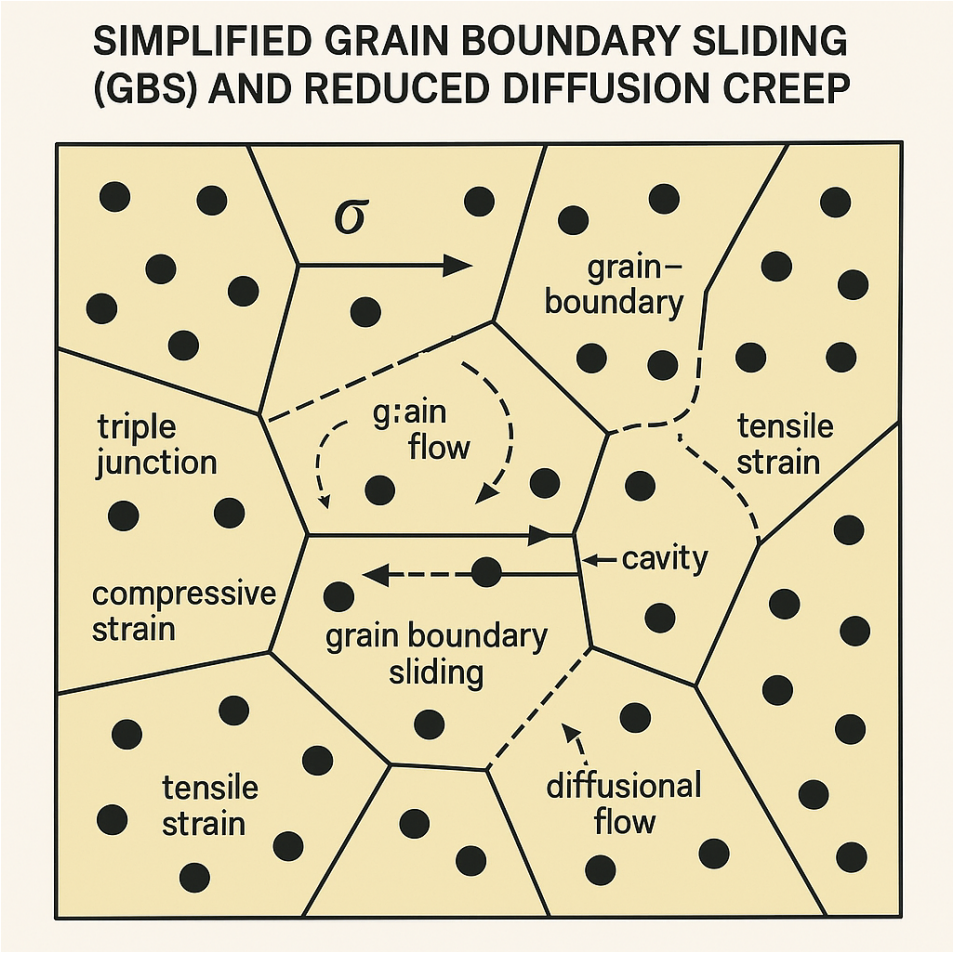

Figure 17: Simplified Grain Boundary Sliding and Reduced Diffusion Creep

energy can be expressed as:

$$E_{\text{int}} = \frac{1}{2} \int_V \sigma_{ij}\, \epsilon_{ij}\, dV \tag{65}$$

where σ_{ij} is the stress field due to the dislocation, ϵ_{ij} is the strain induced by the solute atom, and V is the interaction volume. This energy creates a preferential segregation of solute atoms around the dislocation core, forming what is called a Cottrell atmosphere. The drag force F_{drag} experienced by a dislocation moving through this solute field is given by:

$$F_{\text{drag}} = \int_S \sigma_{ij}\, b_j\, dS \tag{66}$$

where b_j is the Burgers vector, and S is the area swept by the dislocation. This force depends on the relative velocities of the solute atoms (via diffusion) and the dislocation. Cottrell and Jaswon [23] describe the maximum force (per unit length) that the solute atom atmosphere can exert on the dislocation.

$$\frac{F_{\max}}{L} = \frac{C_0 \beta^2}{bkT} \tag{67}$$

The amount of drag exerted by the solute atoms on the dislocation is influenced by their diffusivity in the metal at the given temperature; a higher diffusivity leads to lower drag, while a lower diffusivity results in higher drag. The dislocation glide velocity can be roughly estimated using a power law of the given form.

$$v = B\sigma^{*m} B = B_0 \exp\left(\frac{-Q_{\text{g}}}{RT}\right) \tag{68}$$

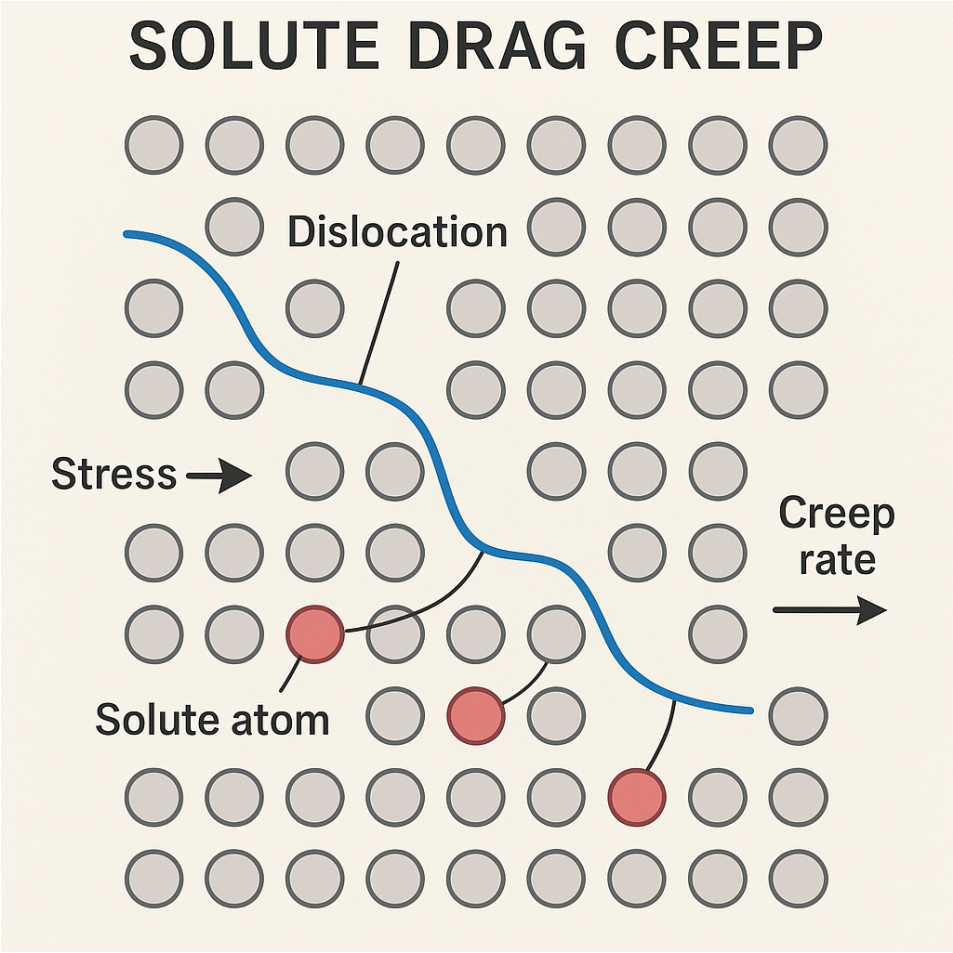

Figure 18: Solute Drag Creep

Cottrell and Jaswon [23] derived the parameter B in the above equation based on the relative atomic size misfit ϵ_a of solutes to describe the interaction between solute atoms and dislocations.

$$B = \frac{9kT}{MG^2b^4 \ln \frac{r2}{r1}} \cdot \frac{D_{\text{sol}}}{\varepsilon_{\text{a}}^2 c_0} \tag{69}$$

The velocity of a dislocation under an applied stress σ is a critical parameter in creep. In the presence of solute drag, this velocity is governed by:

$$v_d = \frac{\sigma - \sigma_{\text{drag}}}{B_d} \tag{70}$$

where B_d is the drag coefficient, and σ_{drag} is the solute drag stress. The drag coefficient B_d is proportional to the solute concentration C_s and the diffusion coefficient D:

$$B_d = \frac{k_B T}{D} \cdot C_s \tag{71}$$

where k_B is Boltzmann's constant, and T is the absolute temperature. The drag stress σ_{drag} arises from the redistribution of solute atoms during dislocation motion. For a steady-state creep condition, it can be approximated by:

$$\sigma_{\text{drag}} = \frac{\Delta G_s}{b\rho} \tag{72}$$

where ΔG_s is the change in Gibbs free energy due to solute redistribution, and ρ is the dislocation density. The steady-state creep rate $\dot{\epsilon}$ is linked to the dislocation velocity v_d and the dislocation density ρ $\dot{\epsilon} = b\, v_d\, \rho$. Substituting v_d, the creep rate becomes:

$$\dot{\epsilon} = b\, \rho\, \frac{\sigma - \sigma_{\text{drag}}}{B_d} \tag{73}$$

In solute drag creep, the activation energy for creep Q includes contributions from both lattice diffusion and solute-dislocation interaction energy. The creep rate can therefore be expressed in an Arrhenius form:

$$\dot{\epsilon} = A \cdot \sigma^n \cdot \exp\left(-\frac{Q}{k_B T}\right) \tag{74}$$

where A is a pre-exponential factor, n is the stress exponent, and Q is the activation energy for creep. For solute drag creep, n typically ranges from 3 to 5. The interaction between dislocations and solute atoms is mediated by diffusion. The solute diffusivity D is given by:

$$D = D_0 \exp\left(-\frac{Q_D}{k_B T}\right) \tag{75}$$

where D_0 is the pre-exponential factor for diffusion, and Q_D is the activation energy for diffusion. The redistribution of solute atoms around a dislocation moving at velocity v_d is governed by the continuity equation:

$$\frac{\partial C_s}{\partial t} + \nabla \cdot (C_s \, \vec{v}_d) = D \nabla^2 C_s \tag{76}$$

This equation highlights the dynamic equilibrium between solute diffusion and the motion of dislocations. The drag stress σ_{drag} depends on the thermodynamic driving force for solute redistribution. This force is proportional to the gradient of the chemical potential μ:

$$\vec{F}_{\text{drag}} = -C_s \nabla \mu \tag{77}$$

The chemical potential μ for solute atoms in the stress field of a dislocation is given by:

$$\mu = \mu_0 + \Omega \sigma \tag{78}$$

where μ_0 is the chemical potential in the absence of stress, and Ω is the atomic volume. The creep rate is sensitive to the solute concentration C_s, dislocation density ρ, and temperature T. For solute drag creep, the scaling relationship is:

$$\dot{\epsilon} \propto C_s \cdot \frac{\sigma}{\rho} \cdot \exp\left(-\frac{Q}{k_B T}\right) \tag{79}$$

At high temperatures, where solute diffusivity is significant, the creep rate exhibits a strong temperature dependence due to the exponential term. Conversely, at lower temperatures, solute drag effects diminish as diffusion becomes sluggish. The solutes are drawn to the stress fields around dislocations and help alleviate the elastic stress fields of existing dislocations, thereby becoming bound to the dislocations. The Cottrell atmosphere [31] defines the solute concentration C at a distance r from a dislocation.

$$C_r = C_0 \exp\left(-\frac{\beta \sin\theta}{rKT}\right) \tag{80}$$

In summary, solute drag creep is governed by the interaction of solute atoms with dislocations, mediated by diffusion and elastic interactions. The interplay of these factors determines the drag stress, dislocation velocity, and ultimately the creep rate. The numerous equations provided here illustrate the fundamental mechanisms and their quantitative dependencies, reinforcing the theoretical foundation of solute drag creep with extreme mathematical rigor.

2.4.1 Portevin–Le Chatelier effect

The Portevin–Le Chatelier effect [24][27][28][29][30] is a special phenomenon that can occur over a limited strain rate in solute drag creep. The Portevin–Le Chatelier (PLC) effect is characterized by serrated yielding or "jerky flow" observed in the stress–strain curve of certain alloys during plastic deformation. During a tensile test, instead of a smooth, continuous increase in stress with strain, the PLC effect produces a series of abrupt drops in stress, resulting in a serrated or saw-tooth pattern on the stress–strain graph. Types of Serrations are:

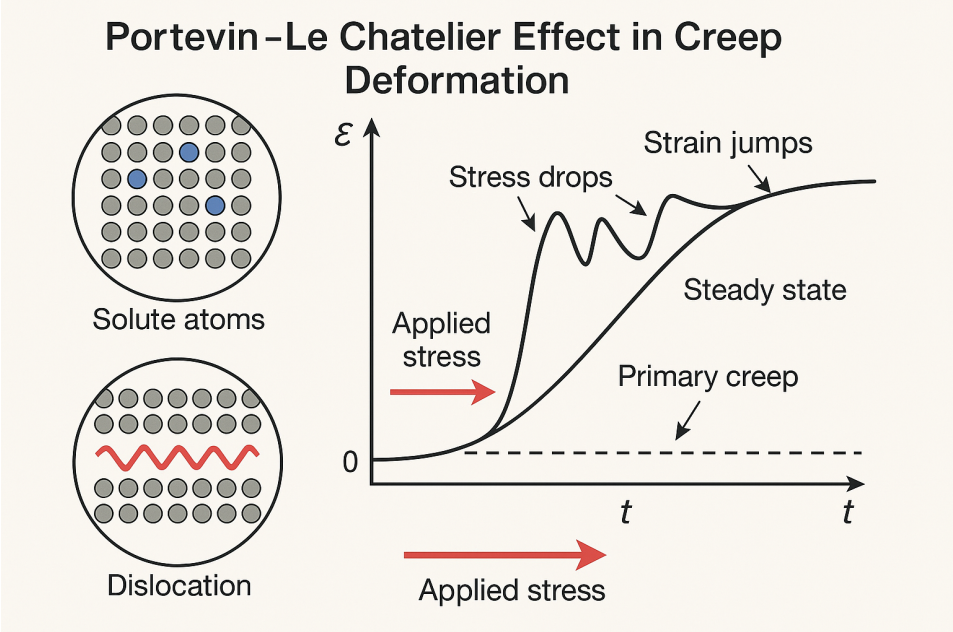

Figure 19: Portevin–Le Chatelier effect in Creep Deformation

1. **Type A**: Regular, propagating bands with large, periodic serrations.
2. **Type B**: Hopping bands with smaller, more frequent serrations.
3. **Type C**: Static bands with large, irregular, and chaotic serrations

This phenomenon is closely associated with dynamic strain aging, where the interaction between moving dislocations and diffusing solute atoms leads to intermittent, localized plastic deformation bands. This effect can be explained in 3 points as follows:

- **Dislocation-Solute Interaction**: When the applied stress becomes sufficiently large, dislocations—imperfections within the crystal structure—are able to break away from solute atoms. This happens because the dislocation velocity increases with the applied stress, making it easier for dislocations to move past solute atoms.
- **Stress Dynamics**: After dislocations break away from solute atoms, the stress initially decreases, and the dislocation velocity also decreases. During this period, solute atoms can approach and reattach to the previously departed dislocations, leading to an increase in local stress. This reattachment happens because the solute atoms have a tendency to obstruct dislocation movement.
- **Repetitive Stress Behavior**: The process of dislocations moving away and then being obstructed by solute atoms can repeat, creating a cyclic pattern of local stress maxima and minima. These repetitions of stress maxima and minima are characteristic of solute drag creep. The cyclic nature indicates a dynamic interaction between dislocations and solute atoms under stress, which can be observed experimentally in the form of fluctuating stress levels in the material.

2.5 Dislocation Climb-Glide Creep

Dislocation climb-glide creep is a deformation mechanism that combines two primary dislocation behaviors—*glide* and *climb*—to allow plastic deformation under high temperatures and applied stress. The Dislocation climb-glide creep is rigorously examined in the works of Heald and Harbottle [32] and Mansur [33]. The full understanding of this mechanism requires a detailed theoretical framework and supporting equations that describe the underlying processes. The first component, **dislocation**

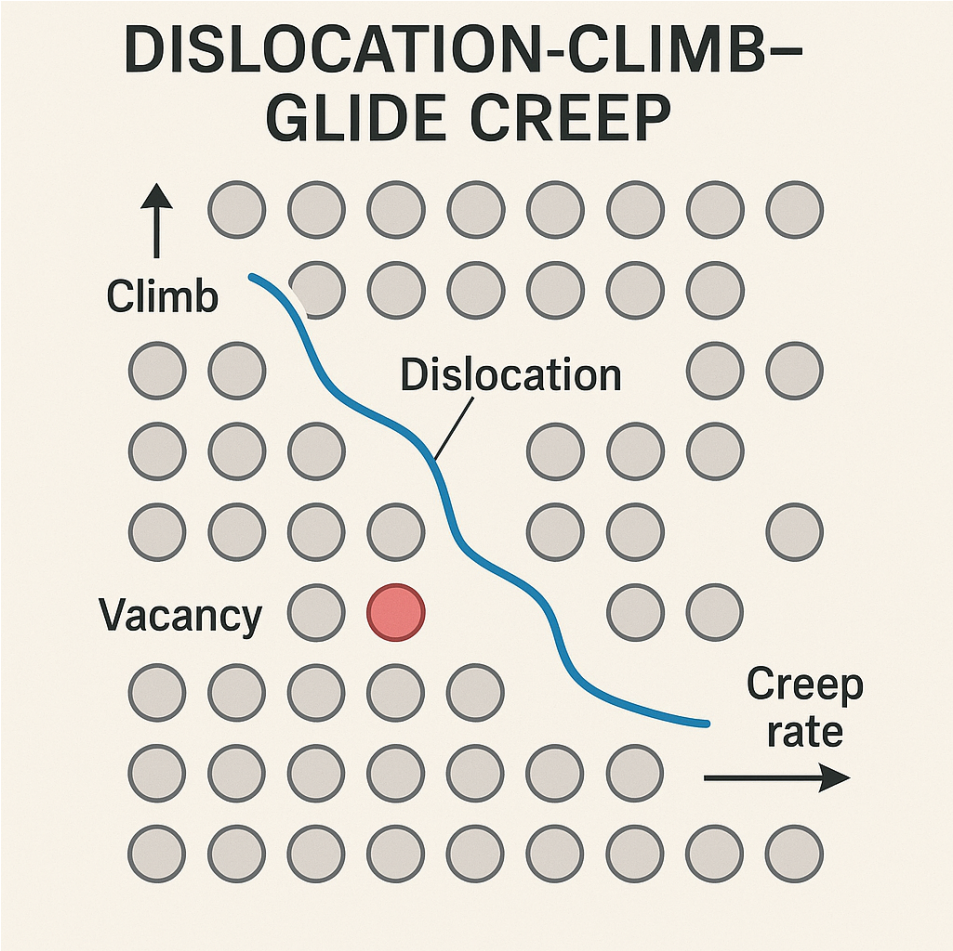

Figure 20: Dislocation Climb-Glide Creep

glide, occurs when dislocations move within their slip planes due to an applied shear stress. The driving force for glide is the resolved shear stress, τ, which acts on the dislocation line. The equation for the force per unit length on the dislocation is:

$$f = \tau b \tag{81}$$

where b is the Burgers vector representing the magnitude and direction of lattice distortion. The velocity of dislocation motion due to glide, v_g, can be expressed as:

$$v_g = m\tau b \tag{82}$$

where m is the mobility of the dislocation in the slip plane. The contribution of glide to the strain rate is given by:

$$\dot{\epsilon}_{\text{glide}} = \rho b v_g = \rho b^2 m\tau \tag{83}$$

where ρ is the dislocation density. However, glide alone cannot sustain deformation when obstacles impede the dislocation motion. This brings us to the second component, **dislocation climb**, which allows dislocations to move out of their slip planes by interacting with vacancies. Climb is governed by the diffusion of vacancies, which is a thermally activated process. The diffusion flux of vacancies, J_v, is described by Fick's first law:

$$J_v = -D_v \nabla c_v \tag{84}$$

where D_v is the diffusion coefficient of vacancies, and c_v is the vacancy concentration. The diffusion coefficient follows the Arrhenius equation:

$$D_v = D_0 \exp\left(-\frac{Q}{k_B T}\right) \tag{85}$$

where D_0 is the pre-exponential factor, Q is the activation energy for vacancy diffusion, k_B is Boltzmann's constant, and T is the absolute temperature. The rate of climb is proportional to the vacancy flux and the Burgers vector:

$$v_c = \frac{J_v b}{\rho} \tag{86}$$

and the climb contribution to the strain rate is:

$$\dot{\epsilon}_{\text{climb}} = \frac{\rho b v_c}{L} \tag{87}$$

where L is the average spacing between dislocations. The total creep rate is the sum of the contributions from climb and glide:

$$\dot{\epsilon} = \dot{\epsilon}_{\text{climb}} + \dot{\epsilon}_{\text{glide}} \tag{88}$$

or explicitly:

$$\dot{\epsilon} = \frac{\rho b^2 D_v \sigma}{k_B T} + \rho b^2 m \tau \tag{89}$$

Dislocation climb is driven by the stress field around the dislocation, which affects the chemical potential of vacancies. The chemical potential, μ_v, for vacancies near a dislocation is:

$$\mu_v = \mu_0 + \Omega \sigma \tag{90}$$

where μ_0 is the chemical potential in the absence of stress, Ω is the atomic volume, and σ is the normal stress component acting on the dislocation. The flux of vacancies toward or away from the dislocation alters its position. The climb velocity, v_c, is determined by the balance of vacancy flux and the stress acting on the dislocation:

$$v_c = \frac{\sigma b}{k_B T} D_v \tag{91}$$

The strain rate due to climb is then:

$$\dot{\epsilon}_{\text{climb}} = \rho b v_c = \frac{\rho b^2 \sigma}{k_B T} D_v \tag{92}$$

At high temperatures, climb becomes increasingly significant because the diffusion coefficient D_v increases exponentially with temperature. This exponential dependence explains why creep rates increase so dramatically with temperature, following the equation:

$$\dot{\epsilon} = A \sigma^n \exp\left(-\frac{Q}{k_B T}\right) \tag{93}$$

The energy barriers associated with climb and glide dictate the dominant deformation mechanism. For glide, the critical stress τ_c to overcome obstacles is:

$$\tau_c = \frac{Gb}{L} \tag{94}$$

where G is the shear modulus, and L is the mean obstacle spacing. If $\tau < \tau_c$, climb becomes essential to bypass the obstacles. The climb process is further influenced by the elastic interactions between dislocations. The stress field of a dislocation is described by:

$$\sigma_{ij} = \frac{Gb}{2\pi(1-\nu)} \frac{x_i x_j}{(x_k x_k)^2} \tag{95}$$

where x_i represents the coordinates relative to the dislocation line, G is the shear modulus, and ν is Poisson's ratio. This stress field alters the vacancy concentration near the dislocation, driving the diffusion required for climb. The climb-glide mechanism becomes evident in steady-state creep,

where the strain rate remains constant due to a balance between dislocation generation, annihilation, and climb-assisted bypassing of obstacles. Experimental observations using transmission electron microscopy (TEM) confirm the presence of climb features, such as jogs and kinks, which indicate out-of-plane dislocation motion. The rate of creep deformation can be expressed as:

$$\frac{\mathrm{d}\varepsilon}{\mathrm{d}t} = \frac{A_{\mathrm{CG}} D_{\mathrm{L}}}{\sqrt{M}} \left(\frac{\sigma\Omega}{kT}\right)^{4.5} \tag{96}$$

In this equation, A_{CG} represents parameters associated with the geometry of the dislocation loops, D_{L} denotes the diffusivity of atoms within the lattice, and M is the density of dislocation sources per unit volume. The applied stress is given by σ, while Ω is the atomic volume. The exponent 4.5 characterizes the stress dependence of dislocation climb-glide creep under the assumption that M remains unaffected by stress. This exponent has been shown to align with a substantial body of experimental observations.

In summary, dislocation climb-glide creep is a thermally activated process that relies on the diffusion of vacancies to enable out-of-plane dislocation motion, coupled with in-plane glide driven by applied stress. The interplay between these mechanisms is mathematically governed by diffusion equations, vacancy flux, and the stress dependence of dislocation motion, providing a comprehensive framework for understanding high-temperature deformation in crystalline materials. The explicit equations underscore the physical processes that dominate under varying temperature and stress conditions, offering insights into the design of creep-resistant materials.

2.6 Harper-Dorn Creep

At low stress levels, Harper–Dorn creep occurs as a dislocation mechanism driven by climb and has been identified in materials such as aluminum, lead, and tin, as well as in nonmetallic substances like ceramics and ice. Based on the earlier works done by Weertman [34] and Mott [35], Harper and Dorn first discovered this creep deformation in 1957 [36]. This creep deformation is dislocation-motion dependent [37][39]. The rate of Harper–Dorn creep is determined by vacancy diffusion to and from dislocations, as indicated by the volumetric activation energy, which drives climb-controlled dislocation motion [40] [2]. Other creep mechanisms generally dominate over Harper–Dorn creep, causing it to remain unnoticeable in the majority of systems. The behavior of Harper–Dorn creep is represented by an empirical relationship:

$$\frac{\mathrm{d}\varepsilon}{\mathrm{d}t} = \rho_0 \frac{D_{\mathrm{v}} G b^3}{kT} \left(\frac{\sigma_{\mathrm{s}}^n}{G}\right) \tag{97}$$

In the above equation, b is the Burgers vector, D_v is the diffusivity of the material, ρ_0 is the dislocation density (Here, the dislocation density is unaffected by the applied stress and remains constant, which is not the case in other creep mechanisms [37]), G is the shear modulus. The stress exponent n ranges from 1 to 3 [41]. There is emerging experimental evidence pointing to the stress exponent being around 2 [45] [42] [43]. The fundamental steady-state strain rate in Harper–Dorn creep is governed by the linear stress dependence, given by:

$$\dot{\varepsilon} = A \frac{D}{kT} \frac{\sigma}{G}. \tag{98}$$

This relation combines the effects of stress (σ), temperature (T), and material constants into a single proportionality. Breaking this down further requires an understanding of the factors influencing D, G, and σ. The diffusion coefficient, D, governs the mobility of vacancies in the material, essential for dislocation climb. Its dependence on temperature is expressed as:

$$D = D_0 \exp\left(-\frac{Q}{RT}\right), \tag{99}$$

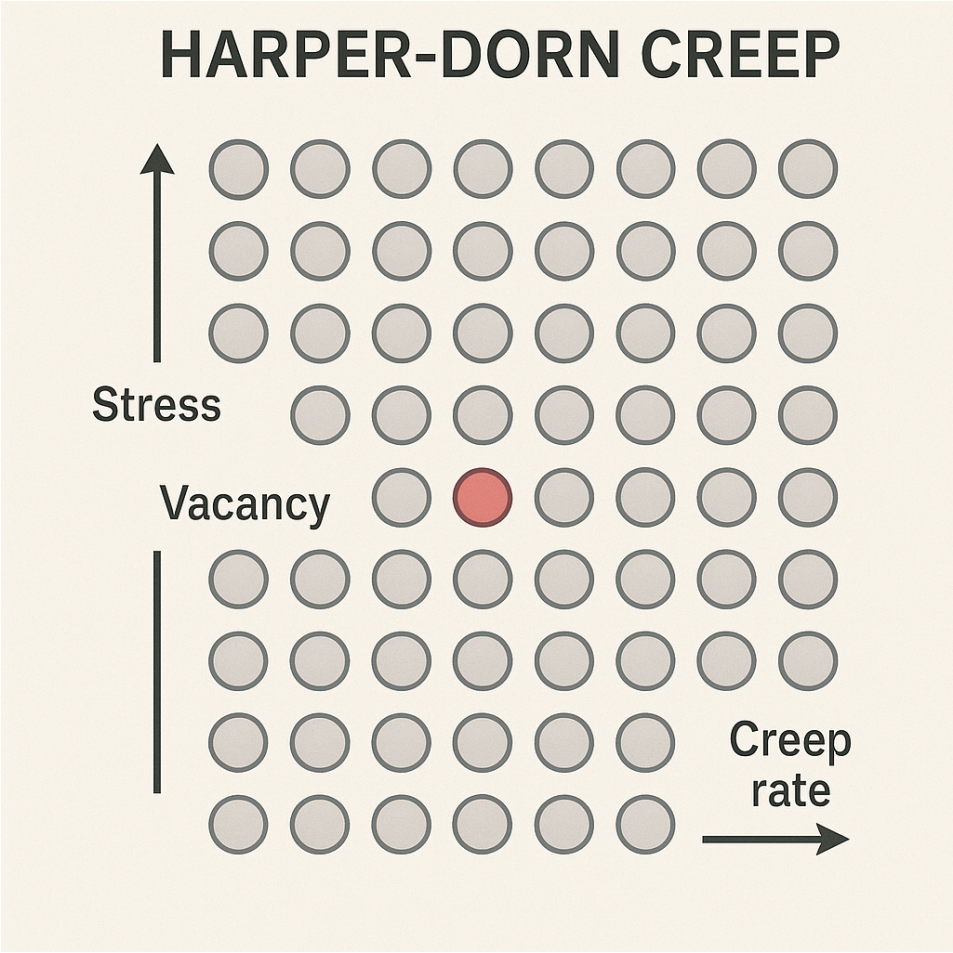

Figure 21: Harper-Dorn Creep

where D_0 is the pre-exponential factor for diffusion, Q is the activation energy for diffusion, R is the universal gas constant, and T is the absolute temperature. Substituting D into the strain rate equation reveals the temperature sensitivity of Harper–Dorn creep:

$$\dot{\varepsilon} = A\frac{D_0}{kT}\exp\left(-\frac{Q}{RT}\right)\frac{\sigma}{G}. \tag{100}$$

Dislocation climb, a key process in Harper–Dorn creep, is controlled by the balance of vacancy flux at the dislocation core. The velocity of a climbing dislocation, v_{climb}, is related to the stress σ by:

$$v_{\text{climb}} = \frac{bD}{kT}\sigma, \tag{101}$$

where b is the Burgers vector. The strain rate is then proportional to v_{climb} and the dislocation density ρ_d, yielding:

$$\dot{\varepsilon} = \rho_d b v_{\text{climb}} = \rho_d b\frac{bD}{kT}\sigma. \tag{102}$$

In Harper–Dorn creep, the dislocation density ρ_d remains low and stable, typically on the order of $10^{10}\,\text{m}^{-2}$ or less. The average spacing between dislocations, Λ, is related to ρ_d as:

$$\Lambda = \frac{1}{\sqrt{\rho_d}} \tag{103}$$

Substituting Λ into the strain rate equation provides:

$$\dot{\varepsilon} = B\frac{bD}{\Lambda^2} = BbD\rho_d \tag{104}$$

where B is a geometric factor dependent on the dislocation arrangement. The shear modulus, G, decreases with increasing temperature. This relationship is approximately linear for many materials at high homologous temperatures and can be expressed as:

$$G(T) = G_0 \left(1 - \alpha \frac{T}{T_m}\right) \tag{105}$$

where G_0 is the shear modulus at absolute zero, α is a material-specific coefficient, and T_m is the melting temperature. The temperature dependence of G further influences the strain rate:

$$\dot{\varepsilon} = A \frac{D_0}{kT} \exp\left(-\frac{Q}{RT}\right) \frac{\sigma}{G_0 \left(1 - \alpha \frac{T}{T_m}\right)} \tag{106}$$

At low stresses, the glide of dislocations is negligible compared to climb. The force per unit length on a dislocation due to the applied stress σ is:

$$f = \sigma b \tag{107}$$

The climb velocity v_{climb} is proportional to this force and the diffusion coefficient:

$$v_{\text{climb}} = \frac{D}{kT} f = \frac{D}{kT} \sigma b \tag{108}$$

The strain rate, being proportional to v_{climb}, inherits this linear stress dependence. The importance of high homologous temperatures in Harper–Dorn creep is reflected in the activation energy for diffusion, Q. For $T/T_m \geq 0.5$, significant vacancy mobility enables dislocation climb. The strain rate is extremely sensitive to T, as evidenced by:

$$\dot{\varepsilon} \propto \exp\left(-\frac{Q}{RT}\right) \tag{109}$$

which amplifies exponentially with small increases in T. The linear dependence of $\dot{\varepsilon}$ on σ is experimentally confirmed by plotting $\log(\dot{\varepsilon})$ against $\log(\sigma)$, which yields a slope of unity:

$$\log(\dot{\varepsilon}) = \log(A) + \log\left(\frac{D}{kT} \frac{1}{G}\right) + \log(\sigma) \tag{110}$$

This linearity differentiates Harper–Dorn creep from other mechanisms, such as power-law creep, where $\dot{\varepsilon} \propto \sigma^n$ with $n > 1$.

The Harper–Dorn creep mechanism is mathematically and physically characterized by its linear stress dependence, dominance of vacancy diffusion, and temperature sensitivity. The strain rate equation encapsulates multiple interdependent variables—diffusion coefficient, dislocation density, and stress—each contributing to the overall deformation mechanism. By incorporating the temperature dependence of D and G, along with the microstructural stability of ρ_d, Harper–Dorn creep emerges as a regime where minimal dislocation activity results in steady-state deformation, governed entirely by diffusion and high-temperature physics. According to Blum and Maier [44], the experimental data supporting Harper–Dorn creep is not entirely persuasive. They further suggested that 99.99 percentage pure aluminum does not satisfy the required condition for Harper–Dorn creep, and the steady-state stress exponent n for the creep rate is invariably greater than 1. Ginter et al. [45] later demonstrated that Harper–Dorn creep is achievable in aluminum with 99.9995 percentage purity but absent in aluminum with 99.99 percentage purity. Additionally, they also discovered that the creep curves in the ultra-high-purity material displayed periodic and regular accelerations. According to Ginter et al. [46], the creep behavior transitions from following a stress exponent of $n = 1$ to exhibiting evidence of a stress exponent greater than $n = 2$ when strains exceed 0.1 during testing.

2.7 Sequential and Parallel Process in Creep

Creep, the time-dependent deformation of materials under constant stress at elevated temperatures, arises from thermally activated processes that manifest through intricate material responses. The distinction between **sequential** and **parallel** processes in creep lies in the interplay of mechanisms that contribute to deformation. While the sequential process emphasizes the evolution of mechanisms over time, the parallel process underscores the simultaneous operation of various deformation modes. Both approaches are essential to a comprehensive understanding of creep, requiring detailed

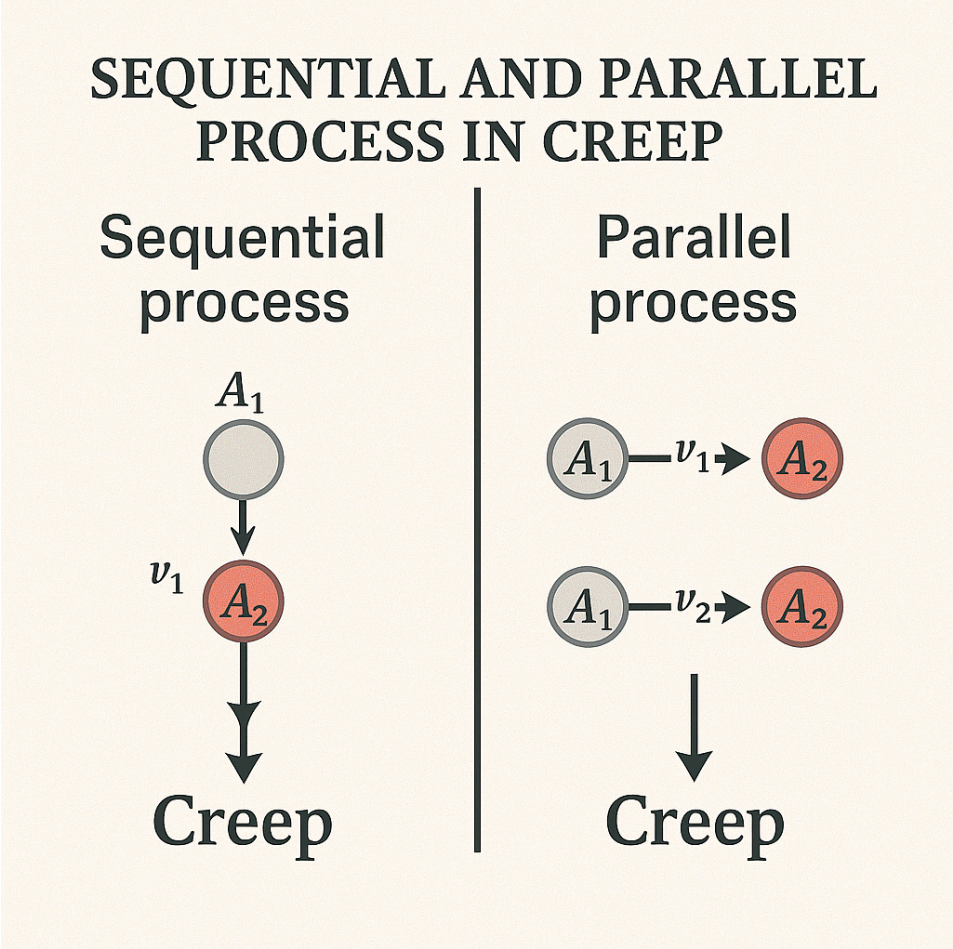

Figure 22: Sequential and Parallel Process in Creep

consideration of thermodynamic, kinetic, and microstructural factors. In the sequential process, the creep behavior unfolds in a series of stages: primary, secondary, and tertiary creep. These stages represent the chronological dominance of specific deformation mechanisms. Initially, during primary creep, the material experiences a decreasing strain rate due to strain hardening. The dislocations generated during deformation interact with each other and with obstacles such as precipitates and grain boundaries, increasing the resistance to further plastic deformation. The thermodynamics of this stage involve the interplay of stored elastic energy and dissipative mechanisms. The energy barrier for dislocation motion is modulated by the applied stress, with the strain rate described by exponential or power-law relations involving the stress exponent and material constants. The microstructural evolution is characterized by an increase in dislocation density and rearrangement, reflecting the growing resistance to plastic flow.

Secondary creep, often referred to as steady-state creep, emerges when a dynamic equilibrium is established between strain hardening and recovery processes. In this stage, recovery mechanisms such as dislocation climb and annihilation balance the production of dislocations, resulting in a constant strain rate. This stage is critical for predicting long-term material performance, as it often

dominates the material's lifespan under constant stress. The steady-state strain rate adheres to an Arrhenius relationship, where the activation energy encapsulates the energy barrier for dislocation motion or diffusion processes, depending on the dominant mechanism. At the microstructural level, the material forms stable subgrain structures, whose size inversely correlates with the applied stress, indicating a balance between the driving force for dislocation activity and the recovery kinetics. The final stage, tertiary creep, marks the onset of material instability and damage accumulation. During this phase, the strain rate accelerates due to the interplay of necking, grain boundary void nucleation, and microcrack propagation. Thermodynamically, the material transitions into a state where the energy dissipated through deformation exceeds the material's capacity for internal stabilization, ultimately culminating in failure. The time to rupture in tertiary creep can be estimated using empirical and mechanistic models, which capture the accelerating strain rate as a function of stress, temperature, and material properties. In contrast, the parallel process in creep considers the simultaneous contribution of multiple deformation mechanisms, each governed by its own kinetics and thermodynamics. For instance, dislocation creep, diffusion creep, and grain boundary sliding can act concurrently, with their relative contributions determined by stress, temperature, and microstructural parameters such as grain size. Dislocation creep dominates at high stresses, where dislocation glide and climb are facilitated by thermal energy. The mathematical description of this mechanism involves power-law relationships, with the strain rate proportional to the stress raised to an exponent that reflects the sensitivity of the mechanism to stress.

Diffusion creep, on the other hand, prevails at lower stresses and is driven by the diffusion of atoms through the lattice or along grain boundaries. Nabarro-Herring creep, associated with lattice diffusion, and Coble creep, governed by grain boundary diffusion, are the primary modes of diffusion-controlled deformation. The strain rate for diffusion creep is inversely proportional to the grain size, emphasizing the critical role of microstructural refinement in enhancing creep resistance. Grain boundary sliding, a distinct mechanism often complementary to diffusion creep, involves the relative motion of grains facilitated by atomic diffusion or dislocation activity at the boundaries. The contribution of grain boundary sliding is significant in materials with fine-grained microstructures, where the increased boundary area amplifies this effect. The mathematical framework for the parallel process involves the superposition of strain rates from each active mechanism. The total strain rate is expressed as the sum of contributions from dislocation creep, diffusion creep, and grain boundary sliding. This additive model captures the complexity of real-world creep, where multiple mechanisms interact in a non-linear and stress-dependent manner. Thermodynamically, the simultaneous operation of these mechanisms reflects the material's attempt to minimize its free energy under applied stress, with each mechanism contributing to the overall entropy production rate. Comparing the sequential and parallel processes highlights their complementary nature. The sequential process provides a time-resolved view of creep, ideal for understanding the progression of deformation in long-term applications. The parallel process, on the other hand, offers insight into the simultaneous operation of mechanisms, crucial for microstructural design and optimization. Both approaches are rooted in the fundamental principles of materials science, leveraging the interplay of mechanics, thermodynamics, and microstructural physics to describe and predict creep behavior with scientific and mathematical rigor. This dual perspective allows engineers and scientists to design materials and predict their performance under complex loading conditions, ensuring safety and reliability in high-temperature applications.

Ghosh (2024) [57] derived the expressions for fundamental differential operators—namely the gradient, divergence, and curl—as well as the vector gradient of a vector field within curvilinear coordinate systems. This work significantly enhances clarity on the application of the del operator in non-Cartesian contexts, laying a robust foundation for advanced analytical and computational treatments of vector calculus in complex geometries.

3 Phenomenological Description of Creep

3.1 Stages of Creep

Creep deformation is typically divided into three distinct stages, each characterized by unique strain-time behavior:

1. Primary Creep
2. Secondary Creep
3. Tertiary Creep

In the following subsections, we discuss each of the above 3 distinct stages of Creep in great detail.

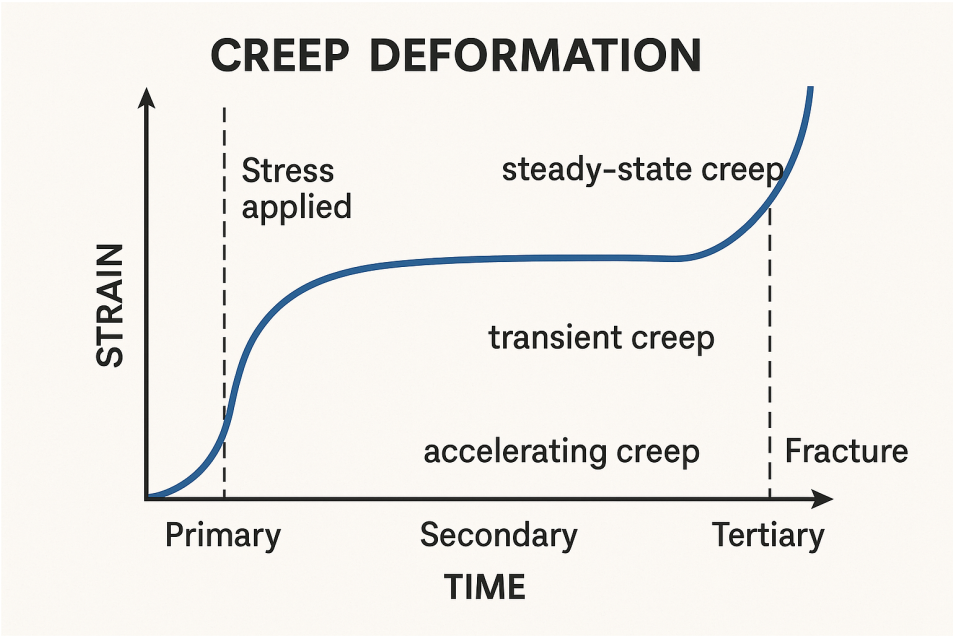

Figure 23: 3 Stages of Creep

3.1.1 Primary Creep

Primary creep, or transient creep, occurs under a constant stress $\boldsymbol{\sigma}$ and elevated temperature T. The deformation is a time-dependent process governed by:

1. **Stress-induced deformation (via dislocation glide, climb, and diffusion):** Stress-induced deformation in primary creep involves the movement of dislocations within the crystal lattice, facilitated by mechanisms such as glide, climb, and diffusion, in response to an applied stress. During this initial stage of creep, the strain rate decreases over time as the material adjusts to the applied load. Dislocation glide occurs when dislocations move along specific crystallographic planes under shear stress, allowing plastic deformation. However, at elevated temperatures, obstacles such as other dislocations, impurities, or grain boundaries can impede glide, requiring additional mechanisms to continue deformation. Dislocation climb becomes active under these conditions, where atoms diffuse around obstacles, enabling dislocations to move out of their glide planes. Diffusion also plays a role in redistributing atoms to accommodate stress concentrations, further facilitating deformation. These combined mechanisms allow the material to deform plastically while redistributing stress, leading to a reduction in strain rate as the material undergoes work hardening. Stress-induced deformation during primary creep is critical in establishing the microstructural changes that influence the material's subsequent behavior in the steady-state (secondary) creep phase.

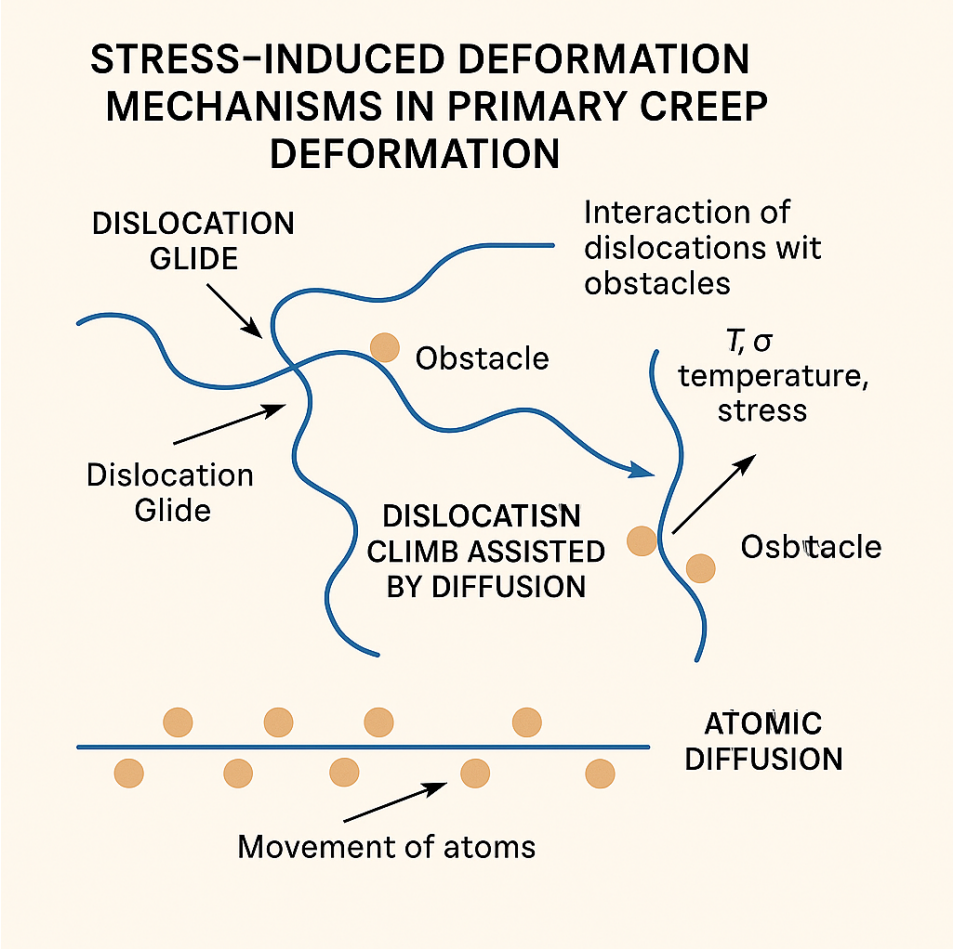

Figure 24: Stress-induced Deformation in Primary Creep

2. **Strain hardening (increased material resistance due to evolving dislocation interactions):** Strain hardening in primary creep refers to the progressive increase in a material's resistance to deformation due to the accumulation and interaction of dislocations as the material is subjected to sustained stress. During primary creep, the material initially deforms at a relatively high strain rate, but as dislocations are generated and move through the crystal lattice, they interact with each other and with other obstacles such as grain boundaries or second-phase particles. These interactions create a tangled network of dislocations that impede further dislocation motion, increasing the material's strength and reducing the rate of deformation over time. This process of strain hardening counteracts the applied stress, leading to a gradual decrease in the creep strain rate characteristic of the primary creep stage. The extent of strain hardening depends on factors such as the material's composition, temperature, and microstructure. Strain hardening is essential for establishing the microstructural framework that influences the material's transition to the steady-state deformation observed in secondary creep, where a balance between hardening and recovery mechanisms is achieved.

3. **Microstructural recovery (dynamic reorganization of internal defects):** Microstructural recovery in primary creep is the process by which the internal defects within a material, such as dislocations, dynamically reorganize and reduce their energy state under sustained stress and elevated temperatures. As the material deforms during the initial stages of creep, dislocations are generated and accumulate, leading to localized stress concentrations. However, at elevated temperatures, the enhanced atomic mobility allows for mechanisms such as dislocation annihilation, rearrangement, and the formation of lower-energy configurations. These processes help to alleviate the internal stresses caused by dislocation interactions, partially offsetting the effects of strain hardening. Microstructural recovery contributes to the gradual decrease in strain rate observed in primary creep, as it counterbalances the increasing resis-

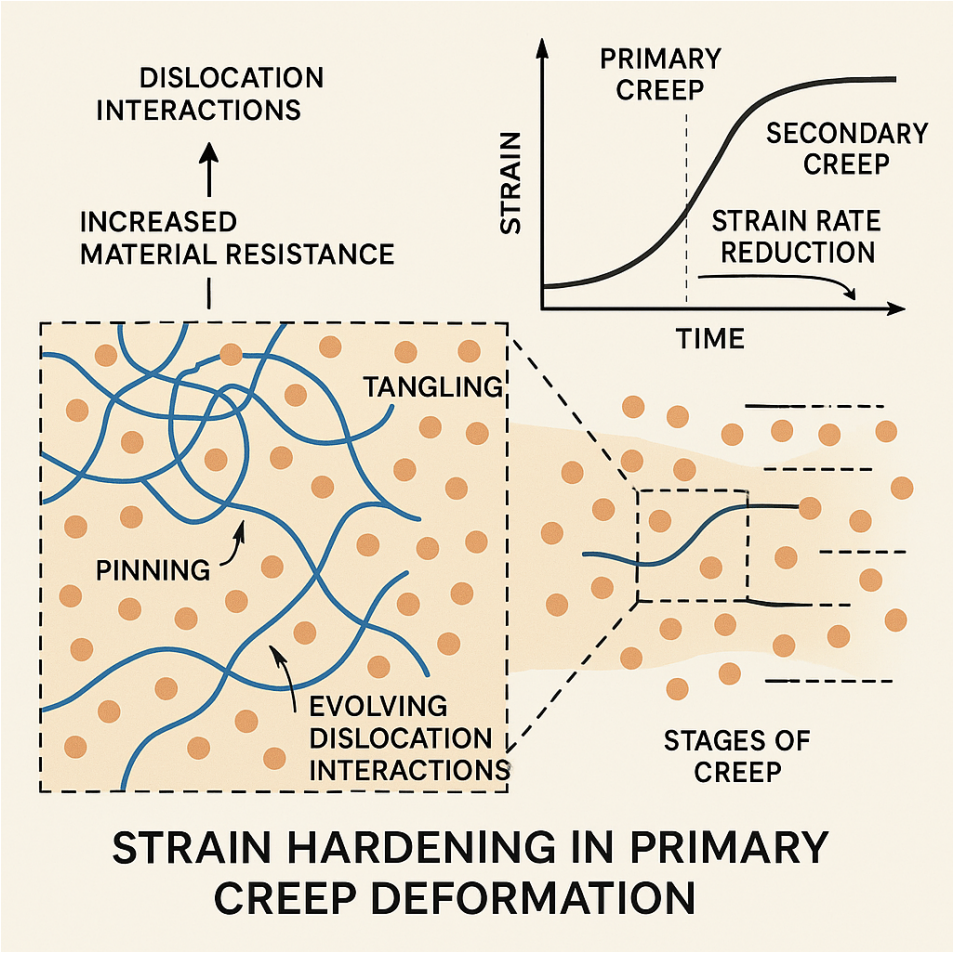

Figure 25: Strain Hardening in Primary Creep

tance to deformation caused by dislocation tangling and interaction. The degree of recovery depends on factors such as the applied stress, temperature, and material properties, and it plays a crucial role in determining how the material transitions from the primary to the secondary creep stage, where a steady-state strain rate is achieved through a balance between recovery and hardening mechanisms.

This interplay results in a strain rate $\dot{\varepsilon}(t)$ that decreases with time. To model this rigorously, the deformation is expressed as:

$$\boldsymbol{\varepsilon}(t) = \boldsymbol{\varepsilon}_{\text{elastic}} + \boldsymbol{\varepsilon}_{\text{plastic}} + \boldsymbol{\varepsilon}_{\text{thermal}} \tag{111}$$

For primary creep, we focus on $\boldsymbol{\varepsilon}_{\text{plastic}}$, which dominates the time-dependent response. Under the framework of continuum mechanics, the strain tensor $\boldsymbol{\varepsilon}$ is decomposed as: $\boldsymbol{\varepsilon} = \frac{1}{2}\left(\nabla \boldsymbol{u} + (\nabla \boldsymbol{u})^T\right)$, where $\boldsymbol{u}$ is the displacement field. For small deformations, the creep strain rate tensor $\dot{\boldsymbol{\varepsilon}}_{\text{creep}}$ satisfies $\dot{\boldsymbol{\varepsilon}}_{\text{creep}} = \frac{\partial \boldsymbol{\varepsilon}_{\text{creep}}}{\partial t}$ The primary creep response is governed by a constitutive equation linking $\dot{\boldsymbol{\varepsilon}}_{\text{creep}}$ to the stress tensor $\boldsymbol{\sigma}$:

$$\dot{\boldsymbol{\varepsilon}}_{\text{creep}} = \mathcal{F}(\boldsymbol{\sigma}, T, \boldsymbol{\kappa}, t) \tag{112}$$

where $\mathcal{F}$ is a material-specific function dependent on $\boldsymbol{\sigma}$ is the Cauchy stress tensor, T is the Absolute temperature, $\boldsymbol{\kappa}$ is the Set of internal variables (e.g., dislocation density, hardening parameters), and t is the Time. The transient creep strain rate is directly tied to the motion and evolution of dislocations. The dislocation density ρ evolves with time according to:

$$\frac{d\rho}{dt} = K_1 \frac{\sigma}{G} - K_2 \rho \tag{113}$$

where K_1 is the Proportionality constant for dislocation multiplication, K_2 is the Recovery constant due to dislocation annihilation, σ is the Applied stress (scalar equivalent of $\boldsymbol{\sigma}$), G is the Shear modulus. The strain rate due to dislocation motion is $\dot{\varepsilon}_{\text{creep}} = \rho b v$ where b is the Burgers vector magnitude

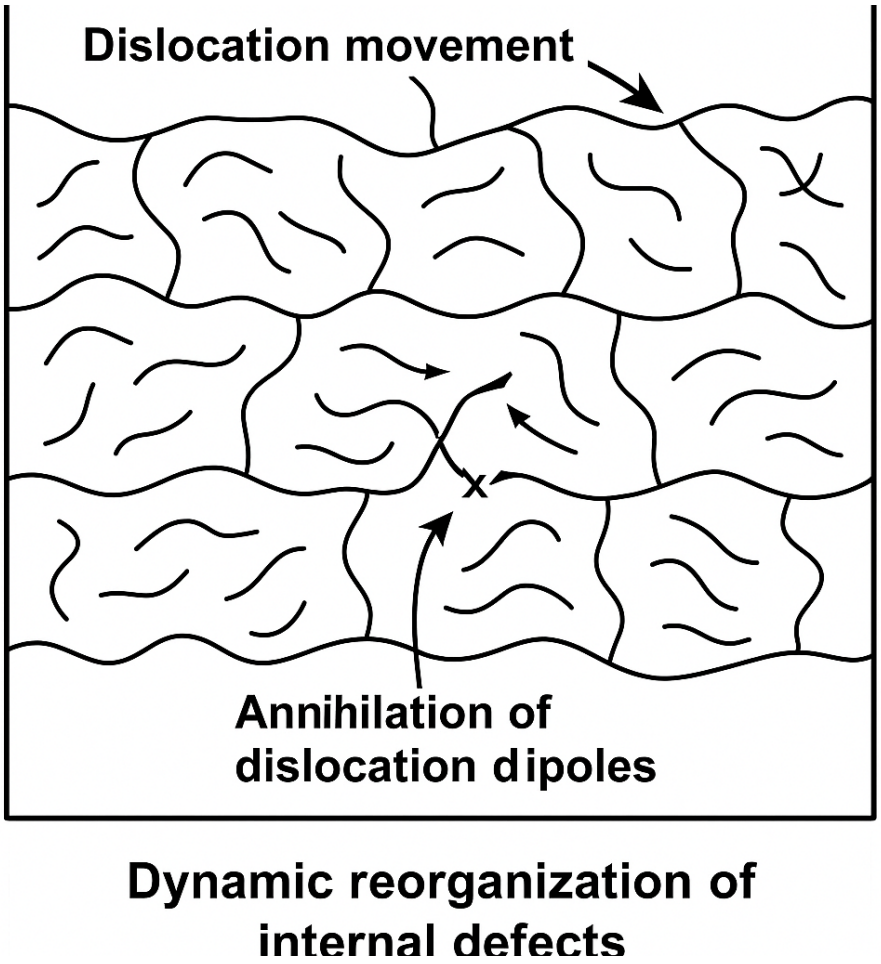

Figure 26: Microstructural Recovery in Primary Creep

and v is the Average dislocation velocity. The velocity v is modeled using thermally activated theory $v = v_0 e^{-\frac{\Delta G}{k_B T}}$ where v_0 is the Pre-exponential velocity factor, ΔG is the Activation energy for dislocation motion, k_B is the Boltzmann constant, T is the Absolute temperature. Substituting for v, the strain rate becomes:

$$\dot{\varepsilon}_{\text{creep}} = \rho b v_0 e^{-\frac{\Delta G}{k_B T}} \tag{114}$$

During primary creep, the resistance to deformation increases due to strain hardening, represented by an internal variable κ. The evolution of κ is governed by:

$$\frac{d\kappa}{dt} = H(\boldsymbol{\sigma}, \kappa) - R(\kappa) \tag{115}$$

where: $H(\boldsymbol{\sigma}, \kappa)$: Hardening rate, increasing with stress, $R(\kappa)$: Recovery rate, decreasing with dislocation annihilation. The strain rate tensor is then expressed as:

$$\dot{\boldsymbol{\varepsilon}}_{\text{creep}} = \frac{1}{E}\boldsymbol{\sigma} \cdot \Phi(\kappa, T) \tag{116}$$

where $\Phi(\kappa, T)$ incorporates temperature and hardening effects. Using thermodynamic principles, the Helmholtz free energy ψ is expressed as:

$$\psi = \psi_{\text{elastic}}(\boldsymbol{\varepsilon}_{\text{elastic}}) + \psi_{\text{plastic}}(\boldsymbol{\kappa}) \tag{117}$$

where ψ_{plastic} captures the energy stored in the evolving microstructure. The dissipation inequality imposes:

$$\boldsymbol{\sigma} : \dot{\boldsymbol{\varepsilon}}_{\text{plastic}} - \frac{\partial \psi_{\text{plastic}}}{\partial \boldsymbol{\kappa}} \cdot \dot{\boldsymbol{\kappa}} \geq 0 \tag{118}$$

This ensures thermodynamic consistency during creep deformation. By integrating the strain rate tensor over time, we obtain the total primary creep strain:

$$\boldsymbol{\varepsilon}_{\text{creep}}(t) = \int_0^t \dot{\boldsymbol{\varepsilon}}_{\text{creep}}(t')\, dt' \tag{119}$$

with $\dot{\boldsymbol{\varepsilon}}_{\text{creep}}(t')$ derived from the full constitutive model. A general solution is:

$$\boldsymbol{\varepsilon}_{\text{creep}}(t) = \boldsymbol{\varepsilon}_0 + \frac{\boldsymbol{\sigma}}{\eta}\left(1 - e^{-\beta t}\right) \tag{120}$$

where $\boldsymbol{\varepsilon}_0$: Initial elastic strain, η: Effective viscosity, β: Time constant related to strain hardening.

Parameters such as K_1, K_2, β, and ΔG are experimentally calibrated using creep tests. Advanced numerical methods, including **finite element analysis (FEA)**, are employed to solve the governing equations over complex geometries. FEA simulations use the above constitutive models to compute the Time-dependent strain fields $\boldsymbol{\varepsilon}(t)$, Stress redistribution $\boldsymbol{\sigma}(t)$, Evolution of microstructural variables $\kappa(t), \rho(t)$. Primary creep is a thermomechanically driven phenomenon with time-dependent strain evolution. Its rigorous description integrates tensorial mechanics, thermodynamic principles, and dislocation dynamics into a unified framework. The mathematical formulation captures the transient interplay of strain hardening and recovery, providing a predictive model for high-temperature material behavior. This depth of understanding is crucial for designing components in high-stress, high-temperature environments. Initial rapid deformation due to strain hardening, followed by a gradual decrease in strain rate. Mathematically, the strain rate is modeled as:

$$\dot{\varepsilon}(t) = \dot{\varepsilon}_0 e^{-\beta t} \tag{121}$$

where β is a hardening parameter.

3.1.2 Secondary Creep

Secondary creep, or the steady-state creep stage, is a defining phenomenon in materials science and continuum mechanics, representing a period of time-dependent, irreversible deformation under constant stress and elevated temperature. Unlike primary creep, characterized by decelerating strain rates, and tertiary creep, marked by accelerating strain rates due to material degradation, secondary creep exhibits a nearly constant strain rate ($\dot{\varepsilon}_s$) that arises from an equilibrium of competing microstructural mechanisms. Secondary creep is vital in the design and analysis of materials exposed to prolonged stresses, such as in high-temperature power plants, aerospace components, and nuclear reactors. Its theoretical understanding integrates thermodynamics, microstructural mechanics, and continuum modeling.

Secondary creep reflects a *non-equilibrium thermodynamic steady-state*, where the system achieves a dynamic balance between energy dissipation and internal resistance to deformation. The strain rate during secondary creep is driven by the dissipation of mechanical work ($\sigma\dot{\varepsilon}$), which manifests as heat and internal energy changes. According to the second law of thermodynamics, the entropy production rate must remain positive and constant in this steady-state regime:

$$\dot{S}_{\text{prod}} = \frac{\sigma \dot{\varepsilon}_s}{T} \tag{122}$$

where: σ is the applied stress, $\dot{\varepsilon}_s$ is the steady-state strain rate, T is the absolute temperature. The constancy of $\dot{S}_{\text{prod}}$ during secondary creep indicates a stable thermodynamic state, ensuring long-term predictability of material behavior. The nearly constant strain rate in secondary creep arises from a balance between:

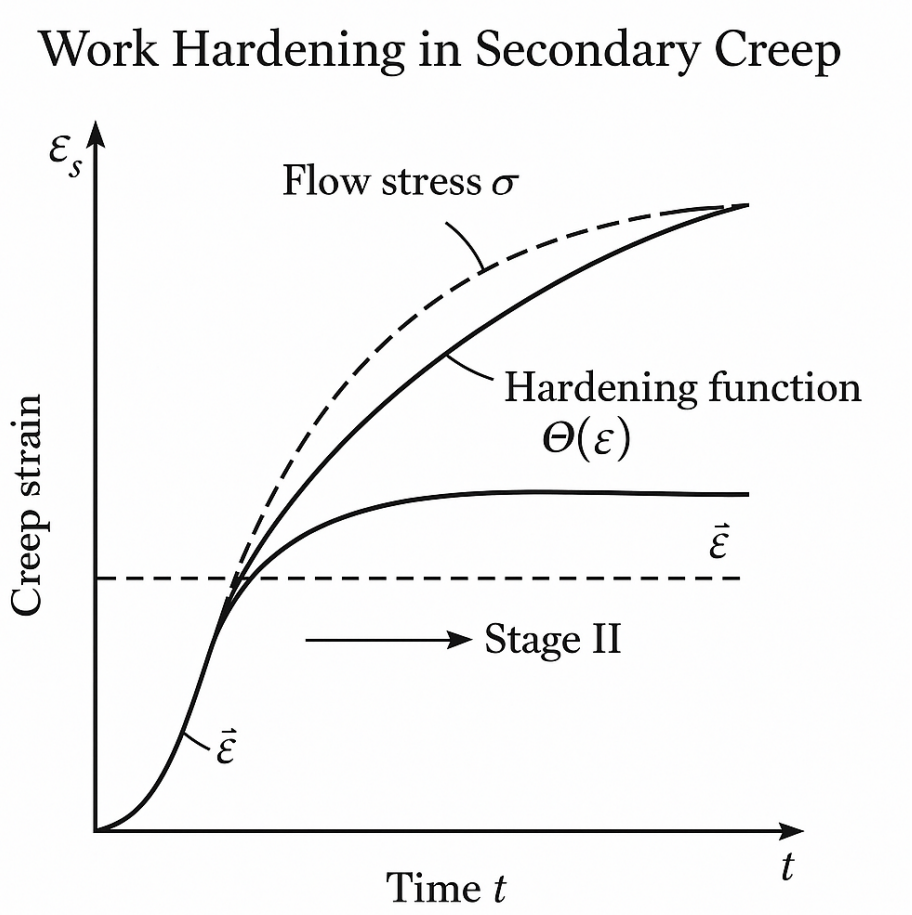

Figure 27: Work Hardening in Secondary Creep

1. **Work Hardening**: Work hardening in secondary creep refers to the process by which a material becomes progressively stronger and more resistant to deformation as dislocations accumulate and interact within the crystal structure during plastic deformation. In the secondary creep stage, the strain rate reaches a steady state due to a dynamic balance between work hardening and recovery mechanisms. As the material deforms under sustained stress, dislocations are generated and move through the crystal lattice. These dislocations interact with each other, forming tangles and networks that create barriers to further dislocation motion, thereby increasing the material's strength. This phenomenon is known as work hardening and contributes to the deceleration of the strain rate that characterizes the transition from primary to secondary creep. However, at the elevated temperatures typical of creep conditions, recovery processes, such as dislocation annihilation and rearrangement, also occur, mitigating the effects of work hardening. The balance between these opposing mechanisms maintains the steady strain rate observed in secondary creep. Work hardening plays a crucial role in the material's ability to sustain long-term deformation under high-temperature and high-stress conditions, influencing its overall creep resistance and structural integrity.

2. **Dynamic Recovery**: Dynamic recovery in secondary creep is the process by which a material undergoing sustained deformation at high temperatures continuously relieves internal stress through the rearrangement and annihilation of dislocations. During secondary creep, the material reaches a steady-state strain rate due to a balance between work hardening, which increases the material's resistance to deformation, and dynamic recovery, which counteracts it. As dislocations are generated and move through the crystal lattice under stress, interactions between them create localized regions of high stress and energy. At elevated temperatures, atomic mobility increases, allowing dislocations to rearrange into lower-energy configurations or to annihilate through mechanisms such as climb or cross-slip. This recovery process reduces

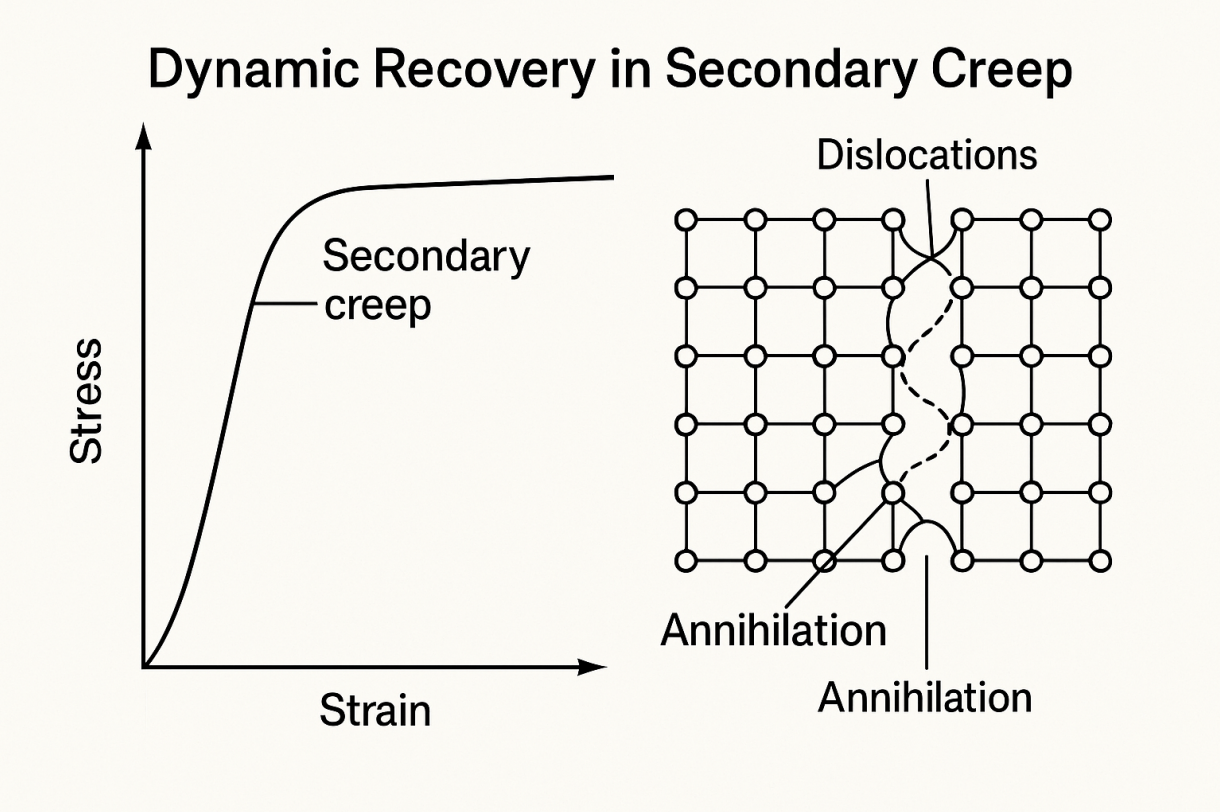

Figure 28: Dynamic Recovery in Secondary Creep

the overall dislocation density and alleviates the internal stress, enabling the material to continue deforming without a significant increase in resistance. Dynamic recovery is particularly important in materials with high-temperature ductility, as it helps to stabilize the creep rate during the secondary stage, preventing rapid strain rate escalation. It is a key factor in determining a material's long-term performance under high-stress, high-temperature conditions, as it influences the material's ability to accommodate plastic deformation without accumulating excessive damage.

The interplay of these mechanisms results in a dynamic equilibrium where the rate of dislocation generation equals the rate of dislocation annihilation. Mathematically, this equilibrium can be expressed as:

$$\frac{d\rho}{dt} = k_1\dot{\varepsilon}_s - k_2\rho^2 = 0 \tag{123}$$

where ρ is the dislocation density, k_1 and k_2 are material constants. At steady-state, the dislocation density stabilizes, leading to a constant creep rate. Dislocations are linear defects that govern plastic deformation. During secondary creep, dislocation climb (motion perpendicular to the slip plane) becomes critical, as it allows dislocations to bypass obstacles. This process is diffusion-controlled and highly temperature-dependent, explaining the Arrhenius-type relationship for creep rate:

$$\dot{\varepsilon}_s \propto \exp\left(-\frac{Q_c}{RT}\right) \tag{124}$$

where Q_c is the activation energy for dislocation climb. At lower stresses and smaller grain sizes, atomic diffusion dominates. This diffusion can occur:

1. **Through the lattice (Nabarro-Herring creep)**: Atoms migrate through the bulk of the grains.

2. **Along grain boundaries (Coble creep)**: Atomic motion is concentrated at grain boundaries, particularly in fine-grained materials.

Both mechanisms contribute to the elongation of grains along the stress axis and are sensitive to grain size (d). For example, in Coble creep: $\dot{\varepsilon}_s \propto \frac{1}{d^3}$. The steady-state creep rate ($\dot{\varepsilon}_s$) typically follows a *power-law relationship* with the applied stress (σ): $\dot{\varepsilon}_s = A\sigma^n$ where A is a material constant, n is the stress exponent. The value of n reflects the dominant creep mechanism:

- $n \approx 1$: Diffusion creep (linear relationship with stress).
- $n \approx 3 - 8$: Dislocation creep (nonlinear relationship with stress).

The thermal activation of creep mechanisms introduces an exponential dependence on temperature, leading to the *Arrhenius relationship*:

$$\dot{\varepsilon}_s = A\sigma^n \exp\left(-\frac{Q}{RT}\right) \tag{125}$$

where Q is the activation energy associated with the dominant creep mechanism. The higher the temperature, the greater the atomic mobility and dislocation activity, resulting in increased creep rates.

Secondary creep can be modeled as a nonlinear viscous flow, where the material behaves like a fluid with stress-dependent viscosity. This behavior is captured by constitutive models that describe the steady-state deformation rate in terms of the applied stress and material properties. To unify the effects of stress and temperature, the Zener-Hollomon parameter (Z) is often introduced:

$$Z = \dot{\varepsilon}_s \exp\left(\frac{Q}{RT}\right). \tag{126}$$

This parameter consolidates the temperature and stress dependencies, providing a robust framework for creep analysis across different materials and conditions. The steady-state stage where strain rate remains constant due to a balance between strain hardening and recovery. The strain rate is expressed as:

$$\dot{\varepsilon}_{\text{ss}} = C\sigma^n \exp\left(-\frac{Q_c}{RT}\right), \tag{127}$$

with C being an empirically determined material constant. Despite its designation as a steady-state process, secondary creep involves continuous microstructural evolution:

- **Dislocation Networks**: Dislocation networks in secondary creep represent the stabilized structure of dislocations that form within a material under sustained stress and temperature during the steady-state phase of creep. In secondary creep, the material experiences a constant strain rate, which arises from a balance between the processes of dislocation generation, motion, and annihilation. Dislocations are line defects in the crystal lattice that serve as carriers of plastic deformation, and their density increases as deformation progresses. As the dislocations move and interact, they form tangles and networks, which act as barriers to further dislocation motion. These networks stabilize the creep rate by hindering the free movement of dislocations, requiring additional stress to drive further deformation. The formation and evolution of dislocation networks depend on the material's microstructure, stress level, and temperature, with higher temperatures allowing dislocations to rearrange into more stable configurations. These networks are crucial in controlling the mechanical behavior of materials during secondary creep, as they dictate the material's resistance to deformation and its ability to sustain steady-state operation under prolonged service conditions.
- **Grain Boundary Sliding**: Grain boundary sliding in secondary creep is a deformation mechanism that occurs when grains within a polycrystalline material slide relative to each other along their boundaries under the influence of sustained stress and elevated temperatures. This

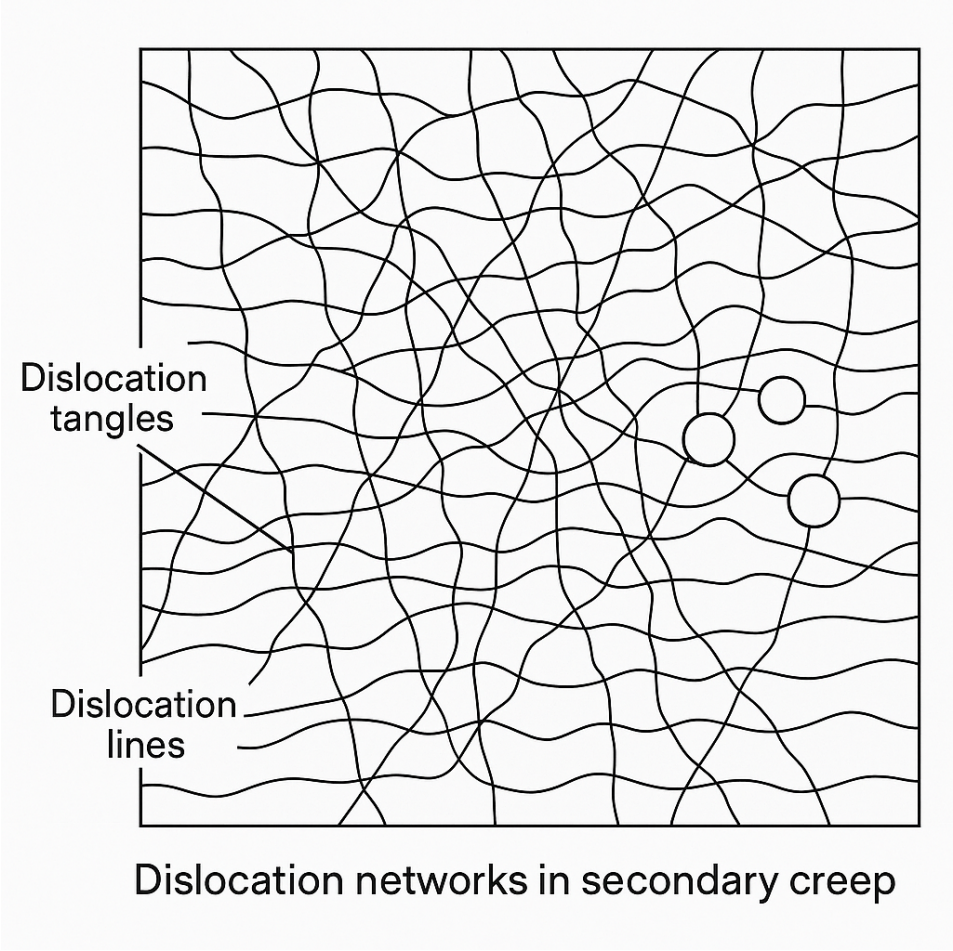

Figure 29: Dislocation Networks in Secondary Creep

sliding accommodates plastic deformation and contributes to the steady-state strain rate characteristic of secondary creep. Unlike primary creep, where strain rate decreases over time, secondary creep achieves a balance between deformation mechanisms such as dislocation movement and grain boundary sliding. Grain boundary sliding in this phase typically occurs in a more controlled manner, facilitated by diffusion processes and the mobility of atoms at elevated temperatures. It is particularly prominent in materials with fine grains, where the increased number of grain boundaries provides more pathways for sliding. However, to maintain continuity at the boundaries, deformation is often accompanied by localized adjustments, such as the formation of voids or dislocation activity, which can evolve into more significant damage over time. Grain boundary sliding is a key factor in determining the creep resistance of materials, especially in high-temperature applications, as it plays a role in controlling the overall strain rate and contributes to the material's ability to sustain loads during long-term service.

These mechanisms ensure that while the macroscopic strain rate remains constant, the material's internal structure is far from static. The long duration and predictability of secondary creep make it a critical consideration in the design of components subjected to high-temperature environments:

- **Aerospace**: Turbine blades must resist deformation over thousands of hours of operation.
- **Power Plants**: Steam generators and pressure vessels must maintain structural integrity under sustained loads.
- **Nuclear Reactors**: Materials must withstand radiation damage in addition to creep stresses.

The Monkman-Grant relationship, which relates the rupture time (t_f) to the steady-state creep rate, provides a practical tool for predicting material lifespan:

$$t_f \cdot \dot{\varepsilon}_s^m = \text{constant} \tag{128}$$

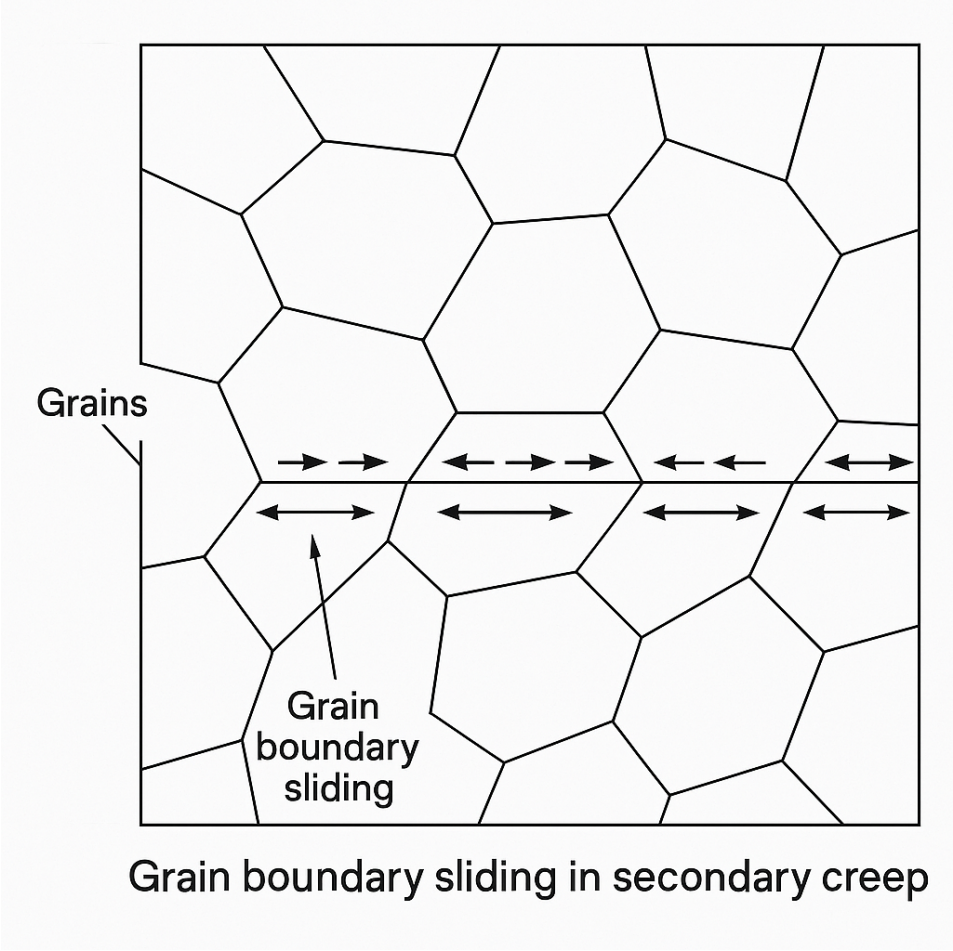

Figure 30: Grain Boundary Sliding in Secondary Creep

where m is a material constant. Secondary creep is a complex yet stable regime of material deformation, governed by a dynamic equilibrium of thermally activated processes. Its theoretical framework integrates thermodynamic principles, microstructural mechanics, and continuum modeling, offering profound insights into the behavior of materials under prolonged stress and temperature. The interplay of mechanisms such as dislocation climb, diffusion, and grain boundary sliding underscores the multi-scale nature of secondary creep, bridging atomic-level processes with macroscopic deformation. Understanding secondary creep is indispensable for the design of resilient, high-performance materials across a spectrum of engineering applications.

3.1.3 Tertiary Creep

Tertiary creep is the final and most critical phase of the creep process, where material deformation accelerates exponentially due to compounded microstructural damage mechanisms. This stage is pivotal for predicting material failure under long-term loading conditions, especially in high-temperature environments such as power plants, aerospace structures, and nuclear reactors. Tertiary creep represents the transition from stable deformation to material rupture. The defining characteristic of this phase is an exponentially accelerating strain rate, attributed to progressive material degradation, including:

1. **Void Nucleation and Growth:** Void nucleation and growth in tertiary creep is a critical phenomenon that plays a significant role in the eventual failure of materials subjected to prolonged high stress and elevated temperatures. During the tertiary stage of creep, the strain rate accelerates rapidly as the material undergoes microstructural degradation. This degradation is driven by the formation and evolution of microscopic cavities, or voids, which nucleate at stress

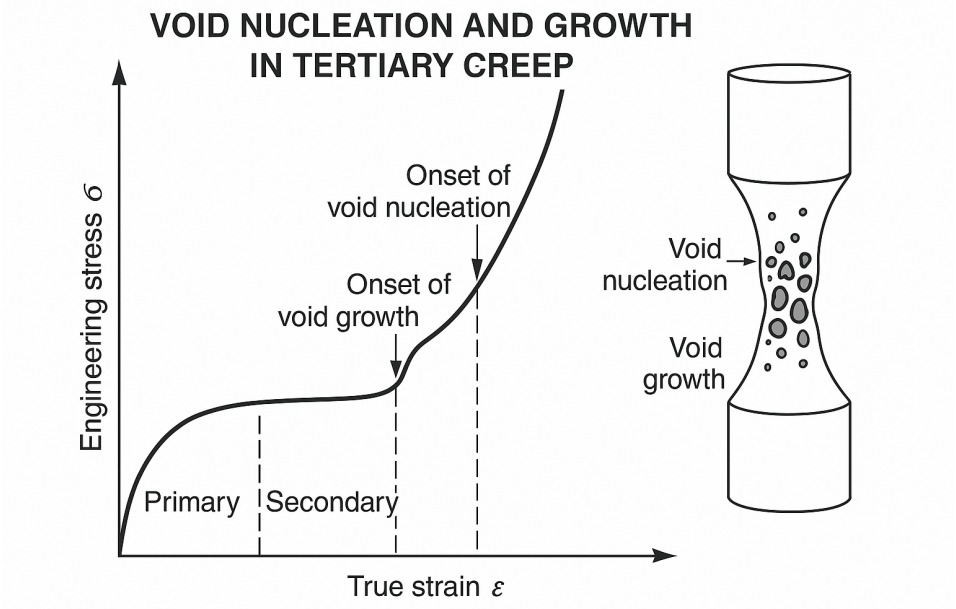

Figure 31: Void Nucleation and Growth in Tertiary Creep

concentration sites. These sites often include grain boundaries, second-phase particles, inclusions, or areas with high dislocation density. The initiation of voids is influenced by factors such as the stress distribution, material microstructure, and temperature. Once nucleated, the voids grow due to mechanisms like atomic diffusion away from the void surfaces and localized plastic deformation around the cavities. Elevated temperatures enhance atomic mobility, facilitating the diffusion process, while high stresses accelerate plastic deformation, further enlarging the voids. As the voids expand, they begin to coalesce, linking together to form microcracks. This coalescence significantly reduces the effective cross-sectional area of the material, causing an exponential increase in strain rate during tertiary creep. Ultimately, the material fails through mechanisms such as ductile fracture or intergranular cracking, depending on the temperature and stress conditions. Understanding the interplay of void nucleation, growth, and coalescence is crucial for predicting material failure and designing components capable of withstanding the demands of high-temperature, high-stress environments.

2. **Microcrack Formation:** Microcrack formation in tertiary creep is a critical process that contributes to the accelerated degradation and eventual failure of materials under prolonged stress and elevated temperatures. During tertiary creep, the material experiences an increased strain rate driven by the accumulation of damage at the microstructural level. This damage begins with the nucleation and growth of voids, which eventually coalesce to form microcracks. These microcracks typically originate at regions of stress concentration, such as grain boundaries, inclusions, or second-phase particles, where the local stress exceeds the material's capacity to deform plastically. The growth of microcracks is facilitated by mechanisms such as localized plastic deformation and atomic diffusion, both of which are enhanced at high temperatures. As these cracks propagate, they reduce the effective load-bearing cross-sectional area of the material, leading to a further increase in strain rate. The interaction and linkage of microcracks create a network of weakened zones that accelerate material failure. Ultimately, this progression leads to macroscopic cracking and fracture, marking the final stage of tertiary creep. Understanding microcrack formation is essential for predicting the lifespan of materials and preventing catastrophic failure in applications where sustained high-stress and temperature conditions are prevalent.

3. **Grain Boundary Sliding:** Grain boundary sliding in tertiary creep is a deformation mechanism that occurs as grains within a material slide past one another along their boundaries

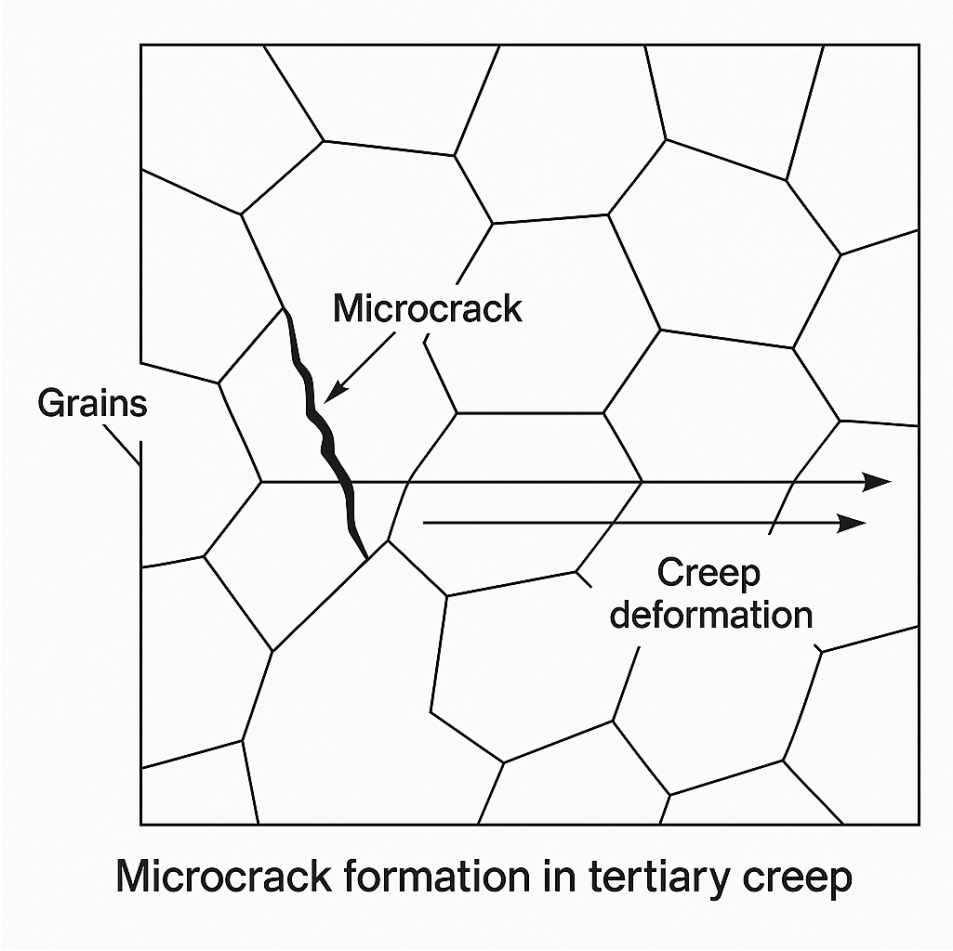

Figure 32: Microcrack Formation in Tertiary Creep

under the influence of sustained stress and elevated temperatures. This process is a significant contributor to the accelerated strain rate observed during tertiary creep, as it facilitates the redistribution of stress and accommodates plastic deformation. Grain boundaries, being regions of atomic misalignment, serve as preferred pathways for sliding due to their relatively lower resistance compared to the grain interiors. At high temperatures, the atomic mobility increases, enabling the grains to slide more easily while maintaining the overall structural integrity of the material. However, this sliding is not uniform and often leads to the nucleation of voids or microcracks at triple junctions or regions where the boundaries are irregular. These defects grow and coalesce, accelerating the onset of failure. Grain boundary sliding is particularly prominent in materials with fine grains and weak boundary strength, and its extent is influenced by factors such as temperature, stress level, and the presence of impurities or secondary phases. This mechanism is critical in determining the creep resistance and long-term reliability of materials exposed to high-temperature environments, such as in power plants, turbines, and aerospace applications.

4. **Necking and Localization:** Necking and localization in tertiary creep are phenomena that signify the final stages of deformation leading to material failure under sustained stress and high temperatures. Necking refers to the progressive reduction in cross-sectional area at a specific region of a material, which concentrates stress and accelerates the deformation in that localized area. This stress concentration creates a feedback loop where the localized thinning of the material increases the strain rate, further intensifying the deformation in that region. As the neck forms, the material's ability to carry the applied load diminishes, and the deformation becomes highly localized, often accompanied by microstructural damage such as void formation, microcrack development, and grain boundary sliding. These processes collectively exacerbate the localization of strain, leading to catastrophic failure through ductile fracture or

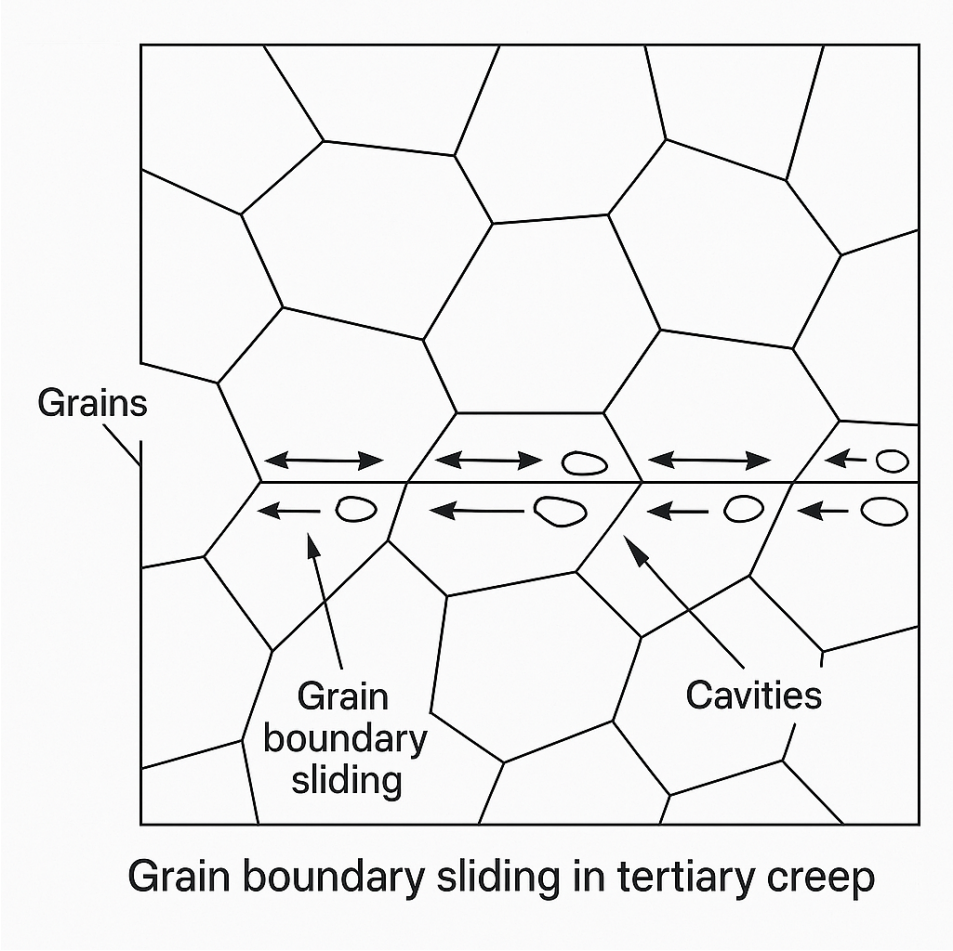

Figure 33: Grain Boundary Sliding in Tertiary Creep

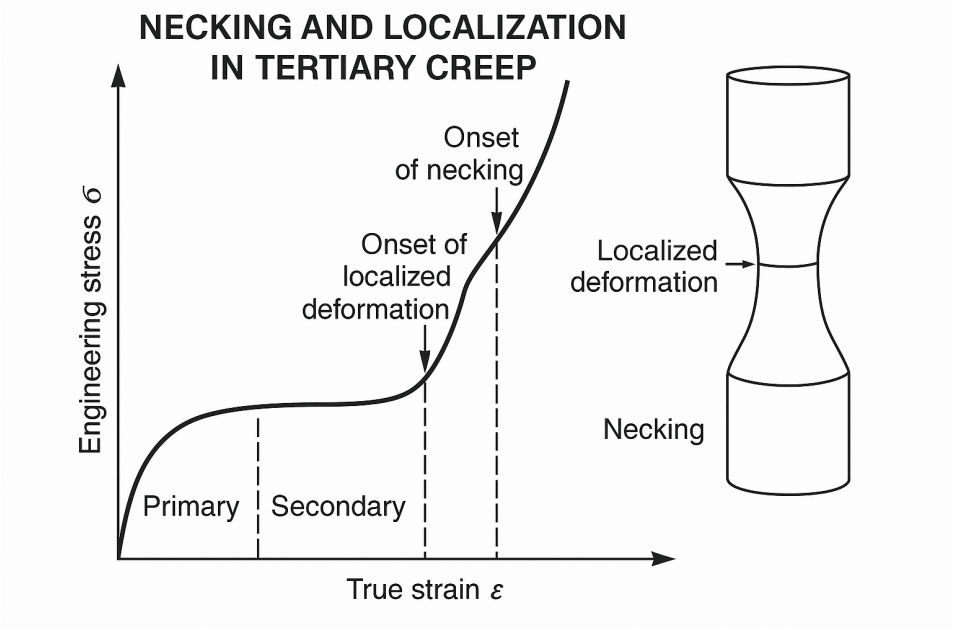

Figure 34: Necking and Localization in Tertiary Creep

intergranular cracking. Necking and localization are influenced by factors such as the material's ductility, the applied stress, and the operating temperature. These phenomena are critical to understanding the mechanical behavior of materials during tertiary creep, as they dictate the ultimate failure mechanism and limit the material's service life in high-stress, high-temperature applications.

A rigorous treatment of tertiary creep necessitates describing the strain rate $\dot{\varepsilon}$ as a function of stress, temperature, time, and damage. The generalized equation is:

$$\dot{\varepsilon} = f(\sigma, T, t, D) \tag{129}$$

where D is the damage variable ($0 \leq D \leq 1$), representing accumulated material degradation. Expanding f, we include stress and temperature dependencies:

$$\dot{\varepsilon} = A\sigma^n \exp\left(-\frac{Q}{RT}\right)(1-D)^p \tag{130}$$

where A is the Material constant, n is the Stress exponent, Q is the Activation energy for creep, R: Universal gas constant, T is the Absolute temperature, p is the Damage exponent. This form integrates the effects of stress, thermal activation, and damage softening. The damage variable D evolves with time as material degradation progresses. A typical phenomenological model for damage evolution is:

$$\frac{dD}{dt} = C\sigma^m(1-D)^r \tag{131}$$

where C is the Material constant, m is the Stress exponent for damage evolution, r is the Exponent controlling the nonlinearity of damage accumulation. Integrating this equation provides $D(t)$, which can then be used to compute the strain rate. As damage accumulates, the effective stress σ_{eff} increases due to the reduction in load-bearing area:

$$\sigma_{\text{eff}} = \frac{\sigma}{1-D}. \tag{132}$$

The strain rate is then recalculated using σ_{eff}, creating a feedback loop that accelerates deformation:

$$\dot{\varepsilon} = A\left(\frac{\sigma}{1-D}\right)^n \exp\left(-\frac{Q}{RT}\right) \tag{133}$$

Void growth under hydrostatic stress σ_h is governed by diffusion-driven mechanisms. The growth rate of a void radius a is given by:

$$\frac{da}{dt} = \frac{A\sigma_h\Omega}{kT}\ln\left(\frac{\sigma_h}{\sigma_c}\right), \tag{134}$$

where Ω is the Atomic volume, k is the Boltzmann constant, σ_c is the Critical stress for void growth. Grain boundary sliding contributes to strain through diffusion and dislocation motion. The strain rate due to sliding is:

$$\dot{\varepsilon}_{\text{gb}} = \frac{\delta b\sigma}{kT}\exp\left(-\frac{Q_b}{RT}\right), \tag{135}$$

where: b is the Burgers vector, δ is the Grain boundary thickness, Q_b is the Activation energy for boundary sliding. Tertiary creep is inherently an irreversible process associated with entropy production. The entropy generation rate $\dot{S}_{\text{prod}}$ is related to mechanical dissipation:

$$\dot{S}_{\text{prod}} = \frac{\sigma\dot{\varepsilon}}{T}. \tag{136}$$

As the strain rate accelerates, $\dot{S}_{\text{prod}}$ increases, indicating the system's approach to a critical failure state. The total energy dissipated during tertiary creep is:

$$W_{\text{diss}} = \int_0^{t_f} \sigma\dot{\varepsilon}\, dt \tag{137}$$

where t_f is the time to failure. This energy is partitioned into **Stored Energy** contributing to dislocation structures and **Dissipated Energy** associated with damage and heat generation. The Monkman-Grant relationship links the minimum creep rate $\dot{\varepsilon}_{\min}$ to the time to failure t_f:

$$\dot{\varepsilon}_{\min} t_f^k = M \tag{138}$$

where k and M are material-specific constants. For tertiary creep, this relationship is modified to account for accelerating strain rates. By integrating the strain rate equation over the tertiary phase, the total strain $\varepsilon_{\text{tertiary}}$ and time to failure can be estimated:

$$t_f = \int_0^{\varepsilon_f} \frac{1}{\dot{\varepsilon}} \, d\varepsilon \tag{139}$$

where ε_f is the strain at failure. At the atomic level, dislocation motion and vacancy diffusion dominate. The diffusivity D_{diff} at temperature T is:

$$D_{\text{diff}} = D_0 \exp\left(-\frac{Q_{\text{diff}}}{RT}\right) \tag{140}$$

where D_0 is the pre-exponential factor and Q_{diff} is the activation energy for diffusion. At the microscale, void growth and crack propagation are modeled by fracture mechanics principles. The growth rate of a crack of length a under stress intensity K is:

$$\frac{da}{dt} = CK^m \tag{141}$$

where C and m are empirical constants. At the macroscale, continuum damage mechanics provides a comprehensive framework for modeling creep deformation. The total creep strain is:

$$\varepsilon_{\text{total}} = \varepsilon_{\text{primary}} + \varepsilon_{\text{secondary}} + \varepsilon_{\text{tertiary}} \tag{142}$$

Self-consistent models treat the material as a heterogeneous medium, where individual grains or phases deform based on their local environment. These models integrate grain boundary sliding, void growth, and dislocation motion to predict macroscopic behavior. The accelerating strain rate in tertiary creep can be analyzed as a dynamic instability. Stability criteria involve examining the eigenvalues of the material's constitutive equations under perturbation.

Tertiary creep embodies the terminal stage of material deformation under prolonged stress and temperature, characterized by a synergistic interaction of microstructural damage, thermodynamic irreversibility, and mechanical instability. This description combines advanced equations with deep theoretical insights, offering a holistic view of the phenomenon. Such rigorous modeling is critical for predicting failure and designing materials with enhanced creep resistance. Accelerated deformation leading to failure, driven by microstructural degradation such as void formation and necking. The strain rate in this stage is modeled as:

$$\dot{\varepsilon}_{\text{ter}}(t) = \dot{\varepsilon}_f e^{\alpha t}, \tag{143}$$

where α characterizes the rate of degradation.

3.2 Constitutive Models

Several phenomenological models have been proposed to describe creep behavior:

3.2.1 Norton-Bailey Law

The **Norton-Bailey Law** describes the steady-state creep behavior of materials under constant stress and elevated temperatures, where the material's deformation is time-dependent yet stabilized by a dynamic equilibrium of competing mechanisms. This phenomenological law integrates principles from thermodynamics, continuum mechanics, and microstructural physics to relate macroscopic strain rates to stress and temperature. The Norton-Bailey Law is expressed as:

$$\dot{\epsilon}_c = A\sigma^n \exp\left(-\frac{Q}{RT}\right) \tag{144}$$

The law applies to the **secondary creep regime**, where:

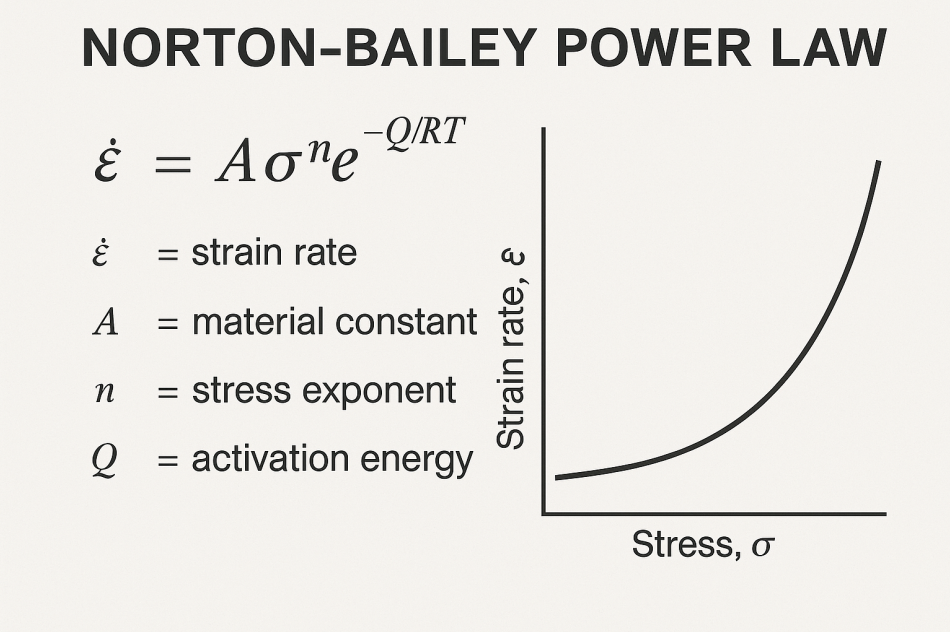

Figure 35: Norton-Bailey Law

- The creep strain rate is constant over time ($\dot{\epsilon}_c = \text{constant}$).
- Work hardening and recovery mechanisms reach equilibrium, balancing the opposing effects of dislocation generation and annihilation.

The steady-state condition can be seen as the minimum of a thermodynamic potential, where the material minimizes its free energy under the constraints of applied stress and thermal activation. Creep deformation is inherently governed by the principles of nonequilibrium thermodynamics. The **Driving Forces and Fluxes** are the applied stress σ which is the thermodynamic driving force and the creep strain rate $\dot{\epsilon}_c$ which is the corresponding flux, proportional to the force in the linear-response regime. Regarding the **Entropy Production**, Deformation is an irreversible process characterized by positive entropy production. The second law of thermodynamics imposes:

$$\frac{\mathrm{d}S}{\mathrm{d}t} \geq 0 \tag{145}$$

where S is the system entropy. The strain rate contributes to this entropy generation through plastic work dissipation. The temperature dependence of $\dot{\epsilon}_c$ reflects the probability of thermally activated processes $\exp\left(-\frac{Q}{RT}\right)$ where Q is the activation energy, representing the barrier to atomic or dislocation motion. The stress exponent n reflects the sensitivity of the creep strain rate to applied stress:

$$n = \frac{\partial \ln \dot{\epsilon}_c}{\partial \ln \sigma} \tag{146}$$

The Interpretation of n is:

- $\mathbf{n = 1}$: Indicates diffusional creep, where strain is governed by atomic diffusion under a stress gradient.
- $\mathbf{n > 3}$: Suggests dislocation creep, where the rate-controlling step involves thermally activated dislocation climb or glide.

Regarding the Microscopic Basis for Stress Dependence, For diffusional creep, the stress gradient drives atomic or vacancy fluxes, whereas for dislocation creep, the applied stress modifies the energy landscape of dislocation motion:

$$\tau_{\text{effective}} = \tau_{\text{applied}} - \tau_{\text{back}} \tag{147}$$

where $\tau_{\text{effective}}$ is the resolved shear stress driving dislocations, and τ_{back} accounts for resistance from obstacles. The material-specific factor A encapsulates the influence of microstructure, including **Grain Size (d):**

$$\dot{\epsilon}_c \propto d^{-p} \tag{148}$$

where $p = 2$ for Nabarro-Herring creep and $p = 3$ for Coble creep. For **Dislocation Density (ρ_d):**

$$\dot{\epsilon}_c \propto \rho_d^{-1/2} \tag{149}$$

For **Precipitate Distribution**, Coherent or incoherent precipitates impede dislocation motion, contributing to hardening. Precipitates, which are second-phase particles formed within a parent matrix during processes like heat treatment or aging, play a critical role in impeding dislocation motion and contributing to hardening. Their spatial distribution, whether uniform or localized, determines the degree of interaction with dislocations. A uniform distribution ensures consistent resistance to dislocation motion, whereas localized distributions may lead to uneven strengthening. The hardening effect is influenced by the volume fraction of precipitates and the spacing between them, with smaller spacing providing greater resistance. Precipitates can be classified as coherent or incoherent based on their lattice relationship with the surrounding matrix. Coherent precipitates maintain lattice continuity with the matrix, resulting in elastic strain fields due to differences in lattice parameters. These strain fields interact with dislocations, requiring additional energy for the dislocations to pass through or shear the precipitate. This process contributes to hardening through mechanisms like the cutting of coherent precipitates, which depends on their size, elastic modulus, and interfacial energy. In contrast, incoherent precipitates, which lack lattice continuity with the matrix, create distinct interfaces that act as strong obstacles to dislocation motion. Dislocations are forced to bypass these obstacles via the Orowan mechanism, where they bow around the precipitates and leave behind dislocation loops. This bypassing process requires a stress proportional to the shear modulus of the matrix, the magnitude of the Burgers vector, and the spacing between the precipitates. The resistance to dislocation motion caused by precipitates directly increases the mate-

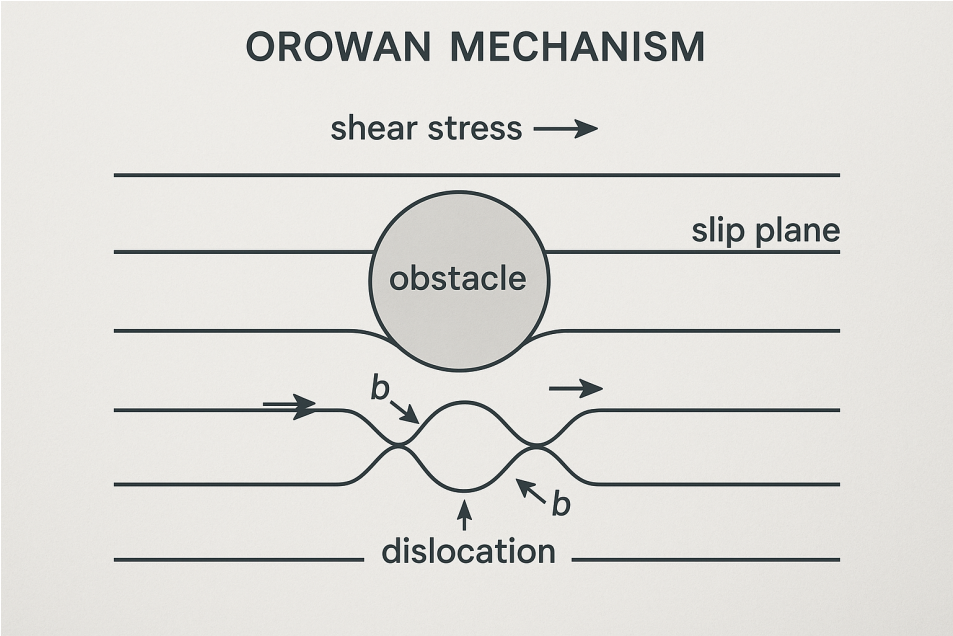

Figure 36: Orowan Mechanism

rial's yield strength. Coherent precipitates harden the material by distorting the surrounding lattice and interacting elastically with dislocations, while incoherent precipitates act as physical barriers that dislocations must bypass. The critical resolved shear stress for dislocation motion reflects these contributions, with terms accounting for lattice friction, dislocation-dislocation interactions, and the strengthening effect of precipitates. Thus, precipitates—whether coherent or incoherent—provide

significant barriers to dislocation motion, enhancing the material's resistance to plastic deformation and contributing substantially to hardening. Diffusional creep occurs via the movement of atoms or vacancies in response to a stress gradient:

$$D = D_0 \exp\left(-\frac{Q_D}{RT}\right) \tag{150}$$

Dislocation creep involves:

$$v_d \propto \sigma^m \exp\left(-\frac{Q}{RT}\right) \tag{151}$$

where m reflects the stress sensitivity. For multiaxial loading, the effective stress σ_{eff} replaces the uniaxial stress σ:

$$\sigma_{\text{eff}} = \sqrt{\frac{3}{2}\mathbf{S} : \mathbf{S}} \tag{152}$$

where $\mathbf{S}$ is the deviatoric stress tensor. The Determination of Parameters **Stress Exponent (n)** and **Activation Energy (Q)** shall be:

$$n = \frac{\partial \ln \dot{\epsilon}_c}{\partial \ln \sigma}, \quad Q = -R\frac{\partial \ln \dot{\epsilon}_c}{\partial (1/T)} \tag{153}$$

Pre-Exponential Factor (A): Found by substituting experimental data into the Norton-Bailey equation. The Norton-Bailey Law has limitations:

- It does not account for transient or tertiary creep.
- Its parameters must be experimentally calibrated.
- Microstructural degradation is not explicitly included.

Extensions include incorporating time-dependent terms and coupling with microstructural models. The Norton-Bailey Law integrates thermodynamic principles, microstructural mechanisms, and mathematical formalism to describe steady-state creep. Its utility in engineering design and material science is vast, offering a framework for predicting long-term deformation. Therefore the The **Norton-Bailey Law** is wildly used due to its simplicity and applicability.

3.2.2 Time-Hardening Model

The **Time-Hardening Model** represents a phenomenologically derived, physically motivated constitutive framework for describing creep deformation, where the material's time-dependent inelastic strain evolves explicitly with respect to elapsed time under applied stress. This model arises from principles of continuum mechanics, thermodynamics, and material science, emphasizing the explicit decoupling of time effects from strain hardening, thus providing a robust approach for certain material behaviors. The Time-Hardening Model is predicated upon the following fundamental assumptions:

1. **Material Homogeneity and Isotropy:** The material is considered homogeneous and isotropic at the macroscopic scale, ensuring that the creep behavior depends only on stress magnitude σ and time t, not on directionality.
2. **Time-Driven Evolution:** The primary driver of inelastic strain is time elapsed under stress, decoupled from the total strain magnitude.
3. **Stress-Dependent Strain Rate:** Creep strain rate scales with the applied stress according to a power-law relationship, reflecting dominant dislocation-based mechanisms.

The fundamental constitutive equation for creep strain rate is:

$$\dot{\epsilon}^c = A\sigma^n t^m \tag{154}$$

where A, n, and m are constants determined by the material properties and operating conditions (e.g., temperature). The Time-Hardening Model adheres to the framework of thermodynamically consistent material behavior: **Helmholtz Free Energy Density (Ψ)** which represents the energy stored elastically within the material and evolves with creep strain ϵ^c and **Dissipation Potential (Φ)** which governs the irreversible energy dissipation during creep deformation. The entropy production rate $\dot{S}$ in creep deformation is expressed as:

$$\dot{S} = \sigma\dot{\epsilon}^c \geq 0 \tag{155}$$

ensuring compliance with the second law of thermodynamics. Under the principles of continuum mechanics, the total strain tensor $\boldsymbol{\epsilon}$ is partitioned into elastic $\boldsymbol{\epsilon}^e$, plastic $\boldsymbol{\epsilon}^p$, and creep $\boldsymbol{\epsilon}^c$ components:

$$\boldsymbol{\epsilon} = \boldsymbol{\epsilon}^e + \boldsymbol{\epsilon}^p + \boldsymbol{\epsilon}^c \tag{156}$$

For time-dependent processes, the creep component $\boldsymbol{\epsilon}^c(t)$ evolves independently of plastic strain, driven by:

$$\dot{\boldsymbol{\epsilon}}^c = A(\|\boldsymbol{\sigma}\|)^n t^m \frac{\boldsymbol{\sigma}}{\|\boldsymbol{\sigma}\|} \tag{157}$$

where $\|\boldsymbol{\sigma}\|$ is the von Mises equivalent stress. To compute the accumulated creep strain $\epsilon^c(t)$, the constitutive equation is integrated over time $[0, t]$:

$$\epsilon^c(t) = \int_0^t \dot{\epsilon}^c \, dt = \int_0^t A\sigma^n t^m \, dt. \tag{158}$$

For the General Case ($m \neq -1$), Performing the integration for $m \neq -1$ yields:

$$\epsilon^c(t) = \frac{A\sigma^n}{m+1} t^{m+1}. \tag{159}$$

For the Singular Case ($m = -1$), the integral becomes logarithmic:

$$\epsilon^c(t) = A\sigma^n \ln(t). \tag{160}$$

Regarding Regularization for $t \to 0$, we have to address singularities as $t \to 0$ for $m \geq 0$, hence a small time offset t_0 is introduced:

$$\dot{\epsilon}^c = A\sigma^n (t + t_0)^m, \tag{161}$$

ensuring bounded creep strain rates during the initial transient phase. The stress and time exponents n and m are empirically determined and correspond to specific creep mechanisms:

1. **Dislocation Creep:** Dominated by dislocation climb and glide. Characterized by n in the range 3–10 and $m \approx 0$.

2. **Diffusional Creep:** Includes Nabarro-Herring (bulk diffusion) and Coble (grain boundary diffusion) mechanisms. Typically exhibits $n \approx 1$ and $m = 0$.

3. **Grain Boundary Sliding:** Common in polycrystalline materials. Results in moderate n and m, dependent on grain size.

The temperature dependence of A is captured by the Arrhenius relation:

$$A = A_0 \exp\left(-\frac{Q}{RT}\right), \tag{162}$$

where Q is the activation energy for the dominant creep mechanism, R is the universal gas constant, and T is the absolute temperature. For practical applications, Q is experimentally calibrated, often lying in the range of 100–400 kJ/mol for metallic systems. Numerical solutions of the Time-Hardening Model involve discretizing time and solving for creep strain incrementally. The creep strain increment over a small time step Δt is:

$$\Delta\epsilon^c = A\sigma^n \left(t_i^m \Delta t + \frac{m}{m+1} \Delta t^{m+1} \right), \tag{163}$$

ensuring stability for small Δt. Regarding Coupling with Finite Element Analysis (FEA), creep strains are incorporated into the deformation gradient tensor $\boldsymbol{F}$, iteratively updating the stress distribution:

$$\boldsymbol{F} = \boldsymbol{F}^e \cdot \boldsymbol{F}^c, \tag{164}$$

where $\boldsymbol{F}^c$ accounts for creep deformations. Regarding Validation and Experimental Correlation, we have the **Constant-Load Tests** which extracts A, n, m by fitting creep strain-time data and **Multi-Axial Testing** which validates the tensorial extension of the model under complex loading. Nonlinear regression is employed to minimize the error:

$$E = \sum_{i=1}^{N} \left(\epsilon^c_{\text{exp},i} - \epsilon^c_{\text{model},i} \right)^2. \tag{165}$$

Unified creep models combine time and strain hardening:

$$\dot{\epsilon}^c = A\sigma^n (\epsilon^c)^p t^m, \tag{166}$$

encompassing broader material behavior. The Time-Hardening Model is integrated with damage mechanics:

$$\dot{\epsilon}^c = A\sigma^n t^m (1-\omega), \tag{167}$$

where ω is a scalar damage variable. The Applications are **Nuclear Reactors** where there is Long-term creep in pressure vessels and piping, **Aerospace Components** like High-temperature turbine blades, **Energy Systems** like Boiler tubes and heat exchangers.

3.2.3 Strain-Hardening Model

Strain hardening refers to the increased resistance of a material to plastic deformation with continued straining. It is a manifestation of irreversible microstructural changes, primarily associated with dislocation interactions in crystalline materials. At the macroscopic scale, strain hardening alters the stress-strain curve, transitioning from the elastic regime into the strain-hardening regime. The phenomenon can be mathematically described as:

$$\sigma = \sigma_y(\kappa), \tag{168}$$

where σ is the applied stress, $\sigma_y(\kappa)$ is the evolving yield stress dependent on the internal state variable κ, which characterizes the material's hardening state. The strain-hardening process adheres to the principles of *thermodynamic consistency*, ensuring energy conservation and dissipation. The response involves a coupling between elasticity, plasticity, and microstructure evolution. Strain-hardening models must satisfy the *first and second laws of thermodynamics*, which are expressed as follows. Regarding, the Energy Balance (First Law) the total power input is balanced by the rate of change in internal energy U and dissipation $\mathcal{D}$:

$$\dot{W}_{\text{ext}} = \frac{d}{dt}(U) + \mathcal{D}, \tag{169}$$

where $\mathcal{D} \geq 0$ ensures compliance with the second law. The Helmholtz free energy Ψ is a potential function dependent on state variables:

$$\Psi = \Psi(\varepsilon^e, \kappa), \tag{170}$$

where ε^e is the elastic strain tensor, κ represents a set of internal variables associated with hardening (e.g., dislocation density ρ). The stress tensor σ and thermodynamic conjugate forces X are obtained as:

$$\sigma = \frac{\partial \Psi}{\partial \varepsilon^e}, \quad X = -\frac{\partial \Psi}{\partial \kappa}. \tag{171}$$

The dissipation rate is given by:

$$\mathcal{D} = \sigma : \dot{\varepsilon}^p - \sum_i X_i \dot{\kappa}_i \geq 0, \tag{172}$$

where X_i are generalized thermodynamic forces, and $\dot{\kappa}_i$ are rates of change of the internal variables κ_i. This inequality constrains the constitutive laws for plastic flow and hardening. The boundary between elastic and plastic deformation is defined by the yield function $f(\sigma, \kappa)$:

$$f(\sigma, \kappa) \leq 0, \tag{173}$$

where $f = 0$ represents the yield surface. The evolution of κ due to strain hardening causes the yield surface to expand or translate in stress space. The plastic strain rate $\dot{\varepsilon}^p$ is derived using the flow rule:

$$\dot{\varepsilon}^p = \lambda \frac{\partial f}{\partial \sigma}, \tag{174}$$

where $\lambda \geq 0$ is the plastic multiplier. The consistency condition ensures the stress state remains on the yield surface during plastic deformation:

$$\dot{f} = \frac{\partial f}{\partial \sigma} : \dot{\sigma} + \frac{\partial f}{\partial \kappa} \cdot \dot{\kappa} = 0. \tag{175}$$

The internal variable κ evolves according to hardening laws that account for isotropic, kinematic, or combined effects.

The isotropic hardening model is a fundamental concept in the strain-hardening behavior of materials, particularly metals, during plastic deformation. In this model, the yield surface of the material expands uniformly in all directions in stress space as plastic deformation progresses, reflecting an increase in the material's yield strength. This expansion is associated with an increase in dislocation density, which enhances the resistance to dislocation motion throughout the material. Isotropic hardening assumes that the material remains homogeneous and that the hardening effect is independent of the loading direction. As a result, the material's ability to withstand additional stress increases equally in all directions, without any change in its shape or orientation of the yield surface. This model effectively captures the phenomenon of work hardening, where the material becomes stronger and less ductile with continued plastic deformation. It is widely used in computational plasticity and constitutive modeling to describe the behavior of materials under monotonic loading conditions, providing a simplified yet powerful framework for understanding and predicting plastic deformation in isotropic materials. The isotropic hardening model describes uniform expansion of the yield surface:

$$\sigma_y = \sigma_0 + H\kappa, \tag{176}$$

where H is the isotropic hardening modulus, and κ is often the equivalent plastic strain:

$$\kappa = \int_0^t \|\dot{\varepsilon}^p\| \, dt, \quad \|\dot{\varepsilon}^p\| = \sqrt{\frac{2}{3}\dot{\varepsilon}^p : \dot{\varepsilon}^p}. \tag{177}$$

Kinematic hardening is a strain-hardening model used to describe the behavior of materials undergoing plastic deformation, particularly under cyclic or non-monotonic loading conditions. Unlike isotropic hardening, where the yield surface expands uniformly, kinematic hardening involves the translation of the yield surface in stress space without any change in its size or shape. This translation reflects the Bauschinger effect, where the material exhibits a reduced yield strength upon

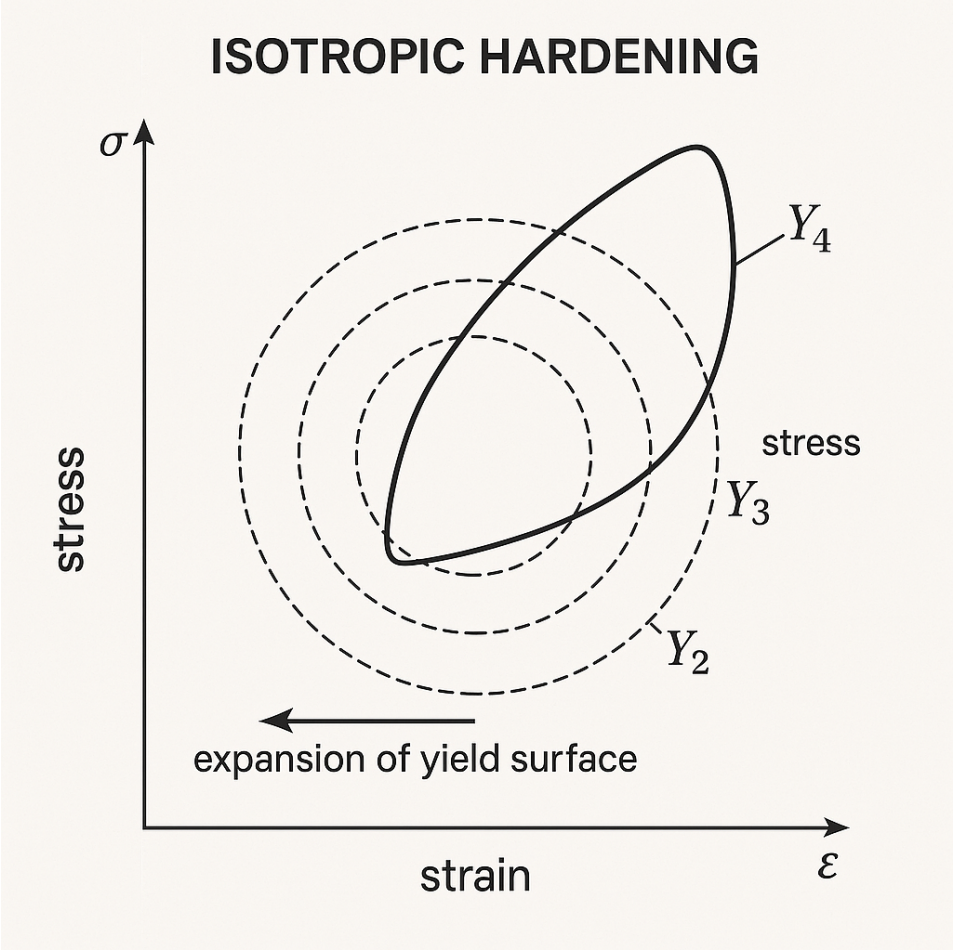

Figure 37: Isotropic Hardening Model

reversal of the loading direction due to the residual internal stresses generated during prior deformation. Kinematic hardening captures the movement of dislocations and the evolution of back stress, which represents the internal resistance to plastic deformation caused by these dislocations. As the material undergoes cyclic loading, the shifting yield surface allows for an accurate representation of the hysteresis loops and the progressive accumulation of plastic strain. This model is widely applied in simulations of material behavior in applications involving repeated or complex loading paths, as it provides a more realistic depiction of the directional nature of strain hardening and the asymmetry in material response under tension and compression. Kinematic hardening accounts for translation of the yield surface, modeled by the evolution of the backstress tensor α:

$$\dot{\alpha} = C\dot{\varepsilon}^p - \gamma\alpha, \tag{178}$$

where C and γ are material parameters related to the rate of hardening and dynamic recovery. Combined hardening combines isotropic and kinematic contributions:

$$f(\sigma, \alpha, \kappa) = \|\sigma - \alpha\| - \sigma_y(\kappa). \tag{179}$$

Dislocations are the primary carriers of plastic deformation in crystalline materials. Strain hardening arises from dislocation interactions, governed by the following mechanisms. Plastic deformation increases dislocation density ρ according to:

$$\dot{\rho} = K_1\rho\dot{\varepsilon}^p - K_2\rho^2, \tag{180}$$

where K_1 and K_2 are material constants representing multiplication and annihilation rates, respectively. Forest dislocations refer to immobile or sessile dislocations within a crystalline material that act as obstacles to the movement of mobile dislocations during deformation. These dislocations are

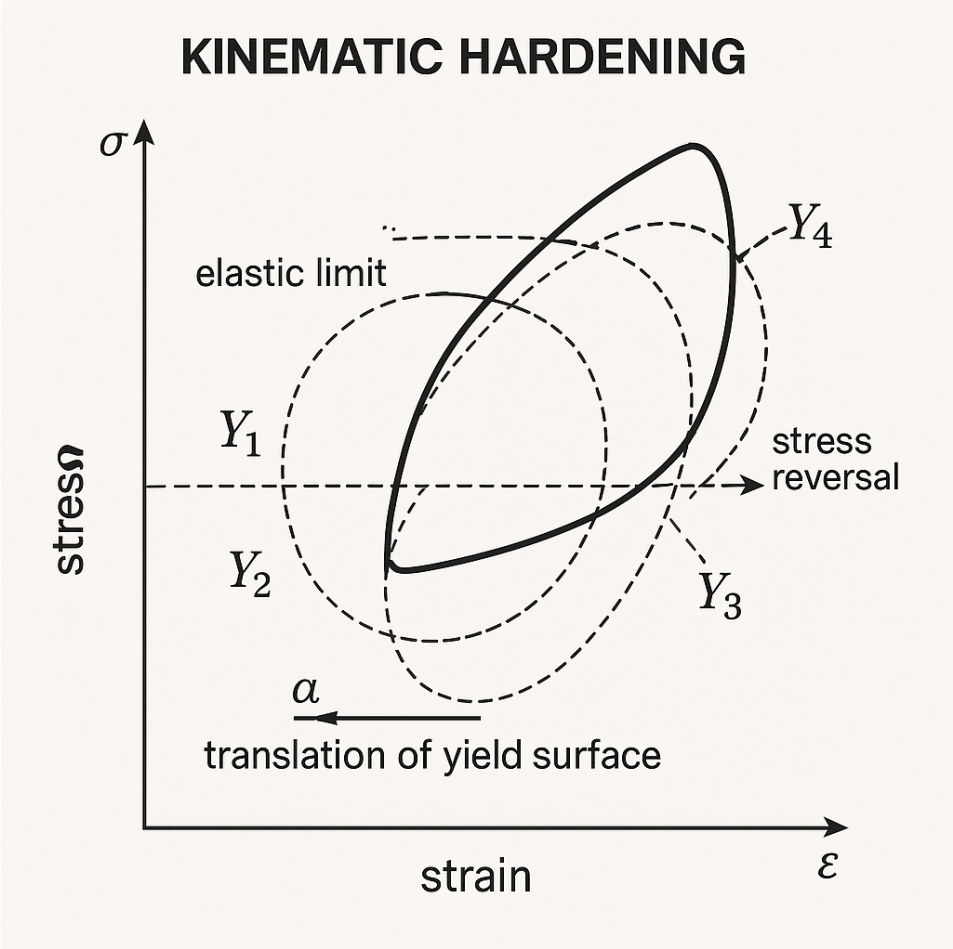

Figure 38: Kinematic Hardening Model

typically formed during prior deformation or thermal processes, and their density increases as plastic deformation progresses. As mobile dislocations move through the crystal lattice under an applied stress, they encounter forest dislocations that impede their motion. The interaction between mobile dislocations and forest dislocations occurs primarily through their stress fields, which can produce attractive or repulsive forces, making it more difficult for the mobile dislocations to proceed. To bypass these obstacles, mobile dislocations may need to undergo processes such as cross-slip or climb, which require additional energy.

In the strain-hardening model, this interaction plays a pivotal role in increasing the resistance to dislocation motion, leading to the phenomenon of work hardening. As deformation continues, the density of dislocations in the material increases, and the average spacing between dislocations decreases. This higher density, described by the Taylor relationship, results in a critical resolved shear stress that is proportional to the square root of the dislocation density. Consequently, the material requires progressively higher stresses for further plastic deformation. Additionally, the pile-up of mobile dislocations against forest dislocations can create localized stress concentrations, which may activate new slip systems and further enhance the dislocation density. These interactions collectively strengthen the material, reducing its ductility while increasing its hardness and resistance to further deformation. Thus, forest dislocations are fundamental to the strain-hardening process and provide a key mechanism for explaining the strengthening behavior of metals and alloys under mechanical strain. Dislocations interact with immobile "forest" dislocations, increasing resistance to motion. The flow stress τ scales as:

$$\tau = \tau_0 + \alpha \mu b \sqrt{\rho}, \tag{181}$$

where μ is the shear modulus, b is the Burgers vector, α is a material constant. Dynamic recovery mechanisms, such as dislocation climb and cross-slip, counteract strain hardening, leading to satura-

tion in the hardening rate. The stress-strain relationship in strain-hardening materials often follows a power-law behavior:

$$\sigma = K\varepsilon^n, \tag{182}$$

where K is the Strength coefficient and n is the Strain-hardening exponent. Strain-hardening behavior is incorporated into finite element models through:

1. *Return-Mapping Algorithms*: Enforcing plastic consistency conditions numerically. Return-mapping algorithms represent the backbone of incremental-iterative schemes for solving nonlinear problems in computational inelasticity. Their goal is to project the trial stress state back onto the admissible stress manifold (e.g., yield surface) while ensuring thermodynamic consistency, stability, and accuracy. This requires robust formulations, iterative solution strategies, and advanced integration schemes. The foundation of computational mechanics begins with the principle of virtual work. For a deformable body, the internal and external virtual work must balance:

$$\int_\Omega \boldsymbol{\sigma} : \delta\boldsymbol{\varepsilon}\, d\Omega = \int_\Omega \mathbf{b} \cdot \delta\mathbf{u}\, d\Omega + \int_{\Gamma_t} \bar{\mathbf{t}} \cdot \delta\mathbf{u}\, d\Gamma, \tag{183}$$

where $\boldsymbol{\sigma}$ is the Cauchy stress tensor, $\delta\boldsymbol{\varepsilon}$ is the virtual strain tensor, $\mathbf{b}$ is the body force, $\bar{\mathbf{t}}$ is the traction on boundary Γ_t, $\mathbf{u}$ is the displacement vector. Plasticity models govern the constitutive behavior $\boldsymbol{\sigma} = \boldsymbol{\sigma}(\boldsymbol{\varepsilon}, \boldsymbol{\varepsilon}^p, \kappa)$. Plasticity models must satisfy thermodynamic laws, including:

   (a) **First Law (Energy Balance):**

$$\dot{U} = P^{\text{ext}} - P^{\text{int}}, \tag{184}$$

   where U is internal energy, P^{ext} is external power, and P^{int} is internal dissipation.

   (b) **Second Law (Clausius-Duhem Inequality):** The dissipation potential $\mathcal{D} \geq 0$:

$$\mathcal{D} = \boldsymbol{\sigma} : \dot{\boldsymbol{\varepsilon}} - \dot{\psi} - \mathbf{h} \cdot \dot{\kappa} \geq 0, \tag{185}$$

   where ψ is the Helmholtz free energy, and $\mathbf{h}$ is the thermodynamic force conjugate to κ.

We now have to analyze the Constitutive Relations. The general structure of the constitutive relations for strain-hardening plasticity includes **Elastic Stress-Strain Law** which states that

$$\boldsymbol{\sigma} = \mathbf{C} : (\boldsymbol{\varepsilon} - \boldsymbol{\varepsilon}^p), \tag{186}$$

where $\mathbf{C}$ is the elastic stiffness tensor. The **Yield Function** states that

$$f(\boldsymbol{\sigma}, \kappa) = \phi(\boldsymbol{\sigma}) - R(\kappa) \leq 0, \tag{187}$$

where $\phi(\boldsymbol{\sigma})$ is the stress measure, and $R(\kappa)$ is the hardening parameter. The **Flow Rule** states that

$$\dot{\boldsymbol{\varepsilon}}^p = \dot{\lambda}\frac{\partial g}{\partial \boldsymbol{\sigma}}, \tag{188}$$

with g as the plastic potential. The **Hardening Law** states that

$$\dot{\kappa} = \dot{\lambda} H, \tag{189}$$

where H is the hardening modulus. The return-mapping algorithm resolves the incremental evolution of stresses and internal variables within the framework of strain-hardening plasticity. It is composed of the **elastic predictor** and **plastic corrector** steps. The elastic predictor step assumes no plastic deformation occurs within a load increment:

$$\boldsymbol{\sigma}_{\text{trial}} = \boldsymbol{\sigma}_n + \mathbf{C} : \Delta\boldsymbol{\varepsilon}. \tag{190}$$

The trial stress is evaluated against the yield function:

$$f_{\text{trial}} = \phi(\boldsymbol{\sigma}_{\text{trial}}) - R(\kappa_n). \tag{191}$$

- If $f_{\text{trial}} \leq 0$, the material remains elastic.
- If $f_{\text{trial}} > 0$, plastic correction is required.

We now state the Plastic Corrector step. The plastic corrector step enforces the yield condition:

$$f(\boldsymbol{\sigma}_{n+1}, \kappa_{n+1}) = 0. \tag{192}$$

Regarding the Consistency Condition, The yield function is linearized using Taylor expansion:

$$f^{(k+1)} \approx f^{(k)} + \frac{\partial f}{\partial \boldsymbol{\sigma}} : \Delta\boldsymbol{\sigma} + \frac{\partial f}{\partial \kappa}\Delta\kappa = 0. \tag{193}$$

We now need to do Stress Correction. The stress update is obtained by projecting $\boldsymbol{\sigma}_{\text{trial}}$ onto the yield surface:

$$\boldsymbol{\sigma}_{n+1} = \boldsymbol{\sigma}_{\text{trial}} - \mathbf{C}_{\text{plastic}} : \Delta\boldsymbol{\varepsilon}^p, \tag{194}$$

where $\mathbf{C}_{\text{plastic}}$ is the plastic tangent operator. We have to do Numerical Integration of Hardening Variables. The hardening parameter κ_{n+1} evolves according to:

$$\kappa_{n+1} = \kappa_n + H\Delta\lambda, \tag{195}$$

where $\Delta\lambda$ is determined from the consistency condition. Regarding Radial Return-Mapping for von Mises Plasticity, For von Mises plasticity with isotropic hardening, we first compute the equivalent stress:

$$\sigma_{\text{eq}} = \sqrt{\frac{3}{2}\mathbf{s} : \mathbf{s}}, \tag{196}$$

where $\mathbf{s} = \boldsymbol{\sigma} - \frac{1}{3}\text{tr}(\boldsymbol{\sigma})\mathbf{I}$. We then solve for the plastic multiplier $\Delta\lambda$:

$$f = \sigma_{\text{eq}} - \sigma_y(\kappa) = 0. \tag{197}$$

We then update the stress and internal variables:

$$\mathbf{s}_{n+1} = \mathbf{s}_{\text{trial}} - 2G\Delta\lambda\frac{\mathbf{s}_{\text{trial}}}{\sigma_{\text{eq,trial}}}, \tag{198}$$

$$\kappa_{n+1} = \kappa_n + \sqrt{\frac{2}{3}}\Delta\lambda. \tag{199}$$

For Thermodynamic Consistency, The return-mapping algorithm must satisfy the dissipation inequality:

$$\mathcal{D} = \boldsymbol{\sigma} : \dot{\boldsymbol{\varepsilon}}^p - \dot{\psi} \geq 0. \tag{200}$$

For **Algorithmic Tangent Moduli**, The consistent tangent operator is derived from the linearization of the constitutive equations to ensure quadratic convergence:

$$\mathbf{C}_{\text{alg}} = \frac{\partial\boldsymbol{\sigma}}{\partial\boldsymbol{\varepsilon}}. \tag{201}$$

Regarding **Viscoplastic Extensions**, Viscoplasticity incorporates rate dependence:

$$\dot{\lambda} = \left\langle \frac{f}{\eta} \right\rangle^n \tag{202}$$

requiring regularization of the yield surface. In **Large Deformation Framework**, for large strains, multiplicative decomposition and logarithmic strain measures replace additive frameworks.

2. *Incremental Formulation*: Computing stress and strain increments iteratively. The incremental formulation in the strain hardening model is a mathematically rigorous framework employed to describe the evolution of stresses and strains in a material undergoing plastic deformation, where the material's resistance to further deformation increases due to strain hardening. This formulation is rooted in the decomposition of the total strain tensor, $\boldsymbol{\varepsilon}$, into its elastic and plastic components, such that $\boldsymbol{\varepsilon} = \boldsymbol{\varepsilon}^e + \boldsymbol{\varepsilon}^p$, where $\boldsymbol{\varepsilon}^e$ represents the recoverable elastic strain and $\boldsymbol{\varepsilon}^p$ signifies the irrecoverable plastic strain. The governing equations are derived incrementally, acknowledging the fact that material deformation is typically path-dependent in the plastic regime. The incremental stress-strain relationship is derived from the generalized Hooke's law for elastic behavior, modified to account for plastic deformation. This relationship is expressed as

$$d\boldsymbol{\sigma} = \mathbf{C}^e : (d\boldsymbol{\varepsilon} - d\boldsymbol{\varepsilon}^p), \tag{203}$$

where $d\boldsymbol{\sigma}$ is the increment in the Cauchy stress tensor, $\mathbf{C}^e$ is the fourth-order elastic stiffness tensor, $d\boldsymbol{\varepsilon}$ is the total strain increment, and $d\boldsymbol{\varepsilon}^p$ is the plastic strain increment. The plastic strain increment, $d\boldsymbol{\varepsilon}^p$, is determined using an associated flow rule derived from the yield function, f, which characterizes the boundary between elastic and plastic behavior in stress space. Mathematically, the plastic strain increment is expressed as

$$d\boldsymbol{\varepsilon}^p = \dot{\lambda} \frac{\partial f}{\partial \boldsymbol{\sigma}}, \tag{204}$$

where $\dot{\lambda}$ is a scalar plastic multiplier determined by enforcing the consistency condition, and $\frac{\partial f}{\partial \boldsymbol{\sigma}}$ defines the direction of plastic flow. The strain hardening behavior of the material is incorporated through the evolution of the yield surface, which depends on internal state variables such as the accumulated plastic strain. A typical hardening law relates the current yield stress, k, to the effective plastic strain, $\bar{\varepsilon}^p$, via a hardening modulus, H. For isotropic hardening, this relationship can be expressed as

$$k = k_0 + H\bar{\varepsilon}^p, \tag{205}$$

where k_0 is the initial yield stress and

$$\bar{\varepsilon}^p = \int_0^t \sqrt{\frac{2}{3}\dot{\boldsymbol{\varepsilon}}^p : \dot{\boldsymbol{\varepsilon}}^p}\, dt \tag{206}$$

quantifies the accumulated plastic deformation. This formulation ensures that the yield surface expands uniformly in stress space as plastic deformation progresses, reflecting the material's increased resistance to plastic flow. The yield function, $f(\boldsymbol{\sigma}, k)$, is updated incrementally to account for the evolving yield stress. In the von Mises yield criterion, for example, the function takes the form

$$f(\boldsymbol{\sigma}, k) = \|\boldsymbol{\sigma}^{\text{dev}}\| - \sqrt{\frac{2}{3}}k, \tag{207}$$

where $\boldsymbol{\sigma}^{\text{dev}}$ is the deviatoric component of the stress tensor, and k is the current yield stress. When plasticity occurs, the stress state must satisfy the consistency condition $f(\boldsymbol{\sigma}, k) = 0$, which is enforced using numerical methods. If the stress state violates this condition, a return mapping algorithm is employed to project the stress back onto the updated yield surface. This ensures that the solution remains consistent with the yield criterion while incorporating the effects of strain hardening.

The numerical implementation of the incremental formulation involves solving a set of coupled nonlinear equations iteratively, often using methods such as Newton-Raphson. The computational framework requires updating the stress tensor, plastic strain tensor, and internal state variables incrementally within each load or time step. This approach ensures a rigorous treatment of the path-dependent nature of plastic deformation, accounting for the interplay between

elastic recovery, plastic flow, and strain hardening. Through this mathematically rigorous and systematic formulation, the incremental strain hardening model enables accurate simulations of material behavior under complex loading conditions.

The stress update involves solving the coupled system:

$$\Delta\sigma = C^e : \Delta\varepsilon^e, \tag{208}$$

$$\Delta\varepsilon^e = \Delta\varepsilon - \Delta\varepsilon^p, \tag{209}$$

$$\Delta\kappa = h(\Delta\varepsilon^p), \tag{210}$$

where C^e is the elastic stiffness tensor and h is the hardening law. For Experimental Validation, we need **Stress-Strain Curves** which provides data for determining hardening parameters, **Cyclic Tests** where we isolate isotropic and kinematic components, and *Microscopy* where Techniques like transmission electron microscopy (TEM) reveal dislocation structures.

4 Plasticity models of Creep Deformation

4.1 Introduction

Creep deformation is a manifestly **time-dependent permanent deformation** that occurs when a material is subjected to a sustained stress at elevated temperature. In the small-strain regime the total infinitesimal strain tensor is decomposed into an elastic part and an inelastic part; for the class of plasticity-based creep models this inelastic part is identified with plastic (viscoplastic/creep) flow. Thus one writes, for the Cauchy strain tensor,

$$\boldsymbol{\varepsilon}(t) = \boldsymbol{\varepsilon}^e(t) + \boldsymbol{\varepsilon}^p(t),$$

where $\boldsymbol{\varepsilon}^e$ is the recoverable elastic strain and $\boldsymbol{\varepsilon}^p$ is the permanent (plastic/creep) strain. The rate form, which is central to constitutive modelling of creep, is

$$\dot{\boldsymbol{\varepsilon}} = \dot{\boldsymbol{\varepsilon}}^{\,e} + \dot{\boldsymbol{\varepsilon}}^{\,p}.$$

A thermodynamically consistent constitutive framework begins with a free-energy density $\psi = \psi(\boldsymbol{\varepsilon}^e, \boldsymbol{\alpha}, T)$ depending on the elastic strain, internal state variables $\boldsymbol{\alpha}$ (e.g. dislocation density, backstress, damage), and temperature T. The Clausius–Duhem inequality (mechanical form) in isothermal form (or with explicit thermal terms suppressed for clarity) requires non-negative dissipation:

$$\mathcal{D} \;=\; \boldsymbol{\sigma} : \dot{\boldsymbol{\varepsilon}} - \rho\,\dot{\psi} \;\geq\; 0,$$

where $\boldsymbol{\sigma}$ is the Cauchy stress tensor and ρ is mass density. Using the constitutive identification of stress from the free energy,

$$\boldsymbol{\sigma} \;=\; \rho\,\frac{\partial\psi}{\partial\boldsymbol{\varepsilon}^e},$$

and the additive decomposition of strain rates, the dissipation reduces to the inelastic contribution

$$\mathcal{D} \;=\; \boldsymbol{\sigma} : \dot{\boldsymbol{\varepsilon}}^{\,p} - \rho\,\frac{\partial\psi}{\partial\boldsymbol{\alpha}} \cdot \dot{\boldsymbol{\alpha}} \;\geq\; 0,$$

which enforces admissible evolution equations for $\dot{\boldsymbol{\varepsilon}}^{\,p}$ and $\dot{\boldsymbol{\alpha}}$. This inequality is the starting point for deriving flow rules from a dissipation potential or an overstress function and guarantees thermodynamic admissibility of any proposed creep law.

Classical plasticity concepts are carried over into the creep regime by introducing a scalar effective stress measure and a driving force for plastic flow. Let $q(\boldsymbol{\sigma})$ denote an equivalent (e.g. von

Mises) stress and let $f(q, \boldsymbol{\alpha}, T)$ be a generalized yield or flow function. For rate-independent plasticity one enforces $f \leq 0$ and normality; in rate-dependent (viscoplastic/creep) models the flow rate is a function of the overstress f or of the stress directly. A generic viscoplastic flow rule can be written in the rate form

$$\dot{\boldsymbol{\varepsilon}}^{\,p} \;=\; \Gamma\big(q(\boldsymbol{\sigma}), \boldsymbol{\alpha}, T\big)\, \frac{\partial q}{\partial \boldsymbol{\sigma}},$$

where the scalar mobility $\Gamma \geq 0$ encodes the time-dependent kinetics (thermally activated rates, diffusion controls, etc.) and $\partial q/\partial \boldsymbol{\sigma}$ gives the flow direction (associated flow if q is used, or non-associated if another potential is chosen). Thermodynamic consistency requires Γ to produce non-negative $\mathcal{D}$.

A frequently used and experimentally validated form for high-temperature creep is the power-law Norton relation, which is naturally interpreted as a viscoplastic flow law:

$$\dot{\varepsilon}^{\,p}_{\mathrm{eq}} \;=\; A(T)\, q(\boldsymbol{\sigma})^{\,n}, \qquad A(T) = A_0 \exp\big(-Q/(RT)\big),$$

where $\dot{\varepsilon}^{\,p}_{\mathrm{eq}}$ is the equivalent creep strain rate, n is the stress exponent, Q is an activation energy, R is the gas constant and A_0 a pre-exponential factor. Embedding this scalar relation into tensorial flow via

$$\dot{\boldsymbol{\varepsilon}}^{\,p} \;=\; \dot{\varepsilon}^{\,p}_{\mathrm{eq}}\, \frac{\partial q}{\partial \boldsymbol{\sigma}}$$

yields a full viscoplastic constitutive law consistent with the dissipation inequality when the flow direction is chosen appropriately.

A microstructural bridge to plasticity is given by the Orowan relation which links plastic strain rate to dislocation kinematics:

$$\dot{\varepsilon}^{\,p}_{\mathrm{eq}} \;=\; \rho_m\, b\, v_d,$$

where ρ_m is the mobile dislocation density, b is the Burgers vector magnitude, and v_d is the mean dislocation velocity. Thermally activated glide/climb models give v_d as an Arrhenius-type or sinh-type function of stress and temperature; for example a simple activated form is

$$v_d \;=\; v_0 \exp\big(-\Delta G(\tau)/(k_B T)\big),$$

with $\Delta G(\tau)$ the stress-dependent activation barrier and τ the resolved shear stress. Combining these relations and models for the evolution of ρ_m (hardening by multiplication and recovery by annihilation, e.g. $\dot{\rho}_m = K_1 \sqrt{\rho_m}\, \dot{\varepsilon}^{\,p}_{\mathrm{eq}} - K_2 \rho_m$) yields mesoscale evolution equations whose steady-state balance gives power-law dependence of $\dot{\varepsilon}^{\,p}_{\mathrm{eq}}$ on stress, thereby rationalizing the Norton form from dislocation plasticity and recovery kinetics.

Finally, plasticity-based creep models naturally accommodate multi-stage creep and coupling to damage by introducing internal variables for hardening, kinematic backstress, and scalar damage $D \in [0, 1)$. A representative coupled set is

$$\begin{aligned}
\dot{\boldsymbol{\varepsilon}}^{\,p} \;&=\; \Gamma\big(q(\boldsymbol{\sigma}, \boldsymbol{\alpha}), \boldsymbol{\alpha}, T\big)\, \frac{\partial q}{\partial \boldsymbol{\sigma}}, \\
\dot{\boldsymbol{\alpha}} \;&=\; \mathcal{H}\big(\boldsymbol{\alpha}, \dot{\boldsymbol{\varepsilon}}^{\,p}, T\big), \\
\dot{D} \;&=\; \mathcal{R}\big(D, q(\boldsymbol{\sigma}), \dot{\boldsymbol{\varepsilon}}^{\,p}\big),
\end{aligned}$$

with the constitutive functions $\mathcal{H}$, $\mathcal{R}$ chosen to satisfy $\mathcal{D} \geq 0$. This structure permits rigorous modelling of primary (transient) creep through evolving $\boldsymbol{\alpha}$, steady secondary creep when $\dot{\boldsymbol{\alpha}} = 0$, and tertiary creep/rupture through accelerating damage $\dot{D}$. Collectively these equations show that plasticity principles — flow rules, hardening/recovery kinetics, and thermodynamic dissipation constraints — are essential and sufficient building blocks for mathematically rigorous models of creep deformation.

Ghosh (2025) [140] presented a mathematically rigorous continuum plasticity framework enriched with gradient terms to capture nonlocal effects in beam deformation. The model remains rate-independent, preserving classical yield and hardening behavior, while the inclusion of gradient-enhanced variables facilitates the representation of size-dependent behavior and mitigates localization issues commonly encountered in standard plasticity theories. By formulating the governing equations specifically for Euler–Bernoulli beam kinematics, the study delivers a tractable yet robust methodology for problems where gradient effects play a critical role in plastic deformation. Ghosh (2025) [118] developed a thermodynamically consistent and geometrically exact constitutive framework for rate-dependent plasticity within the scope of Euler–Bernoulli beam theory. The model rigorously integrates rate-dependent plastic flow into beam kinematics, thereby enabling accurate representation of size effects and time-dependent plastic deformation under large strains and elevated temperatures. Comprehensive derivations of the constitutive relations, alongside numerical illustrations, showcase the robustness of the proposed model for capturing complex creep-like responses in slender structures.

4.2 Fundamentals of Plasticity and Creep

Plastic deformation in the small-strain regime is classically decomposed additively into elastic and plastic parts; this kinematic split underpins rate forms of constitutive laws for creep when strains remain small:

$$\boldsymbol{\varepsilon} = \boldsymbol{\varepsilon}^e + \boldsymbol{\varepsilon}^p, \qquad \dot{\boldsymbol{\varepsilon}} = \dot{\boldsymbol{\varepsilon}}^{\,e} + \dot{\boldsymbol{\varepsilon}}^{\,p},$$

with elastic response given (for hyperelastic or linear elastic materials) by

$$\boldsymbol{\sigma} = \mathbb{C} : \boldsymbol{\varepsilon}^e,$$

where $\mathbb{C}$ is the fourth-order elasticity tensor (isotropic form $\mathbb{C}_{ijkl} = \lambda\delta_{ij}\delta_{kl} + 2\mu\delta_{ik}\delta_{jl}$ when isotropy is assumed). In finite strain kinematics the appropriate multiplicative decomposition is

$$\mathbf{F} = \mathbf{F}^e\mathbf{F}^p,$$

with $\mathbf{F}$ the deformation gradient and $\mathbf{F}^p$ the plastic part; objective measures of stress and strain must then be used (e.g. Kirchhoff stress and elastic logarithmic strain) in the constitutive statements that follow.

Yielding and the initiation of irreversible (plastic/creep) flow are described by a yield or flow function f defined on stress, internal variables $\boldsymbol{\alpha}$, and temperature T. Typical effective stress measures are the von Mises (J_2) equivalent and Tresca equivalent:

$$q_{\mathrm{vM}}(\boldsymbol{\sigma}) = \sqrt{\tfrac{3}{2}\,\mathbf{s} : \mathbf{s}}, \qquad \mathbf{s} = \boldsymbol{\sigma} - \tfrac{1}{3}(\operatorname{tr}\boldsymbol{\sigma})\mathbf{I},$$

$$f(\boldsymbol{\sigma}, \boldsymbol{\alpha}, T) = q(\boldsymbol{\sigma}) - \sigma_y(\boldsymbol{\alpha}, T) \le 0,$$

with σ_y the current (possibly evolving) yield strength. For rate-independent plasticity the Kuhn–Tucker conditions and consistency condition hold:

$$\dot{\gamma} \ge 0, \qquad f \le 0, \qquad \dot{\gamma} f = 0, \qquad \dot{f} = 0 \text{ if } \dot{\gamma} > 0,$$

where $\dot{\gamma}$ is the plastic multiplier; associated flow assumes

$$\dot{\boldsymbol{\varepsilon}}^{\,p} = \dot{\gamma}\,\frac{\partial f}{\partial \boldsymbol{\sigma}}.$$

Hardening is introduced by internal variables with explicit evolution laws; common forms include isotropic hardening $R(\alpha)$ and kinematic backstress $\mathbf{X}$:

$$\sigma_y(\boldsymbol{\alpha}, T) = \sigma_{y0} + R(\alpha), \qquad f = q(\boldsymbol{\sigma} - \mathbf{X}) - \sigma_{y0} - R(\alpha).$$

Representative evolution equations (small strain) are

$$\dot{\alpha} = h(\alpha, \dot{\gamma}), \qquad \dot{\mathbf{X}} = c\,\dot{\boldsymbol{\varepsilon}}^{\,p} - \gamma_\infty\,\mathbf{X}\,\dot{\gamma},$$

where h models isotropic hardening/recovery kinetics and the Armstrong–Frederick style form above models nonlinear kinematic hardening; parameter choices determine transient (primary) response and steady (secondary) flow behavior. A thermodynamically consistent framework follows from a free-energy density $\psi(\boldsymbol{\varepsilon}^e, \boldsymbol{\alpha}, T)$ and the Clausius–Duhem inequality. With ρ mass density the mechanical dissipation must satisfy

$$\mathcal{D} = \boldsymbol{\sigma} : \dot{\boldsymbol{\varepsilon}} - \rho\,\dot{\psi} \geq 0,$$

which, using $\boldsymbol{\sigma} = \rho\,\partial\psi/\partial\boldsymbol{\varepsilon}^e$ and the strain split, gives the reduced dissipation

$$\mathcal{D} = \boldsymbol{\sigma} : \dot{\boldsymbol{\varepsilon}}^{\,p} - \rho\frac{\partial\psi}{\partial\boldsymbol{\alpha}} \cdot \dot{\boldsymbol{\alpha}} \geq 0.$$

Imposing an additive decomposition of dissipation into contributions from flow and internal variable evolution yields flow rules and evolution laws that guarantee nonnegative dissipation (e.g. via a dissipation potential Φ or overstress function).

Rate-dependent (viscoplastic/creep) laws replace the yield-surface complementarity by kinetic relations that permit $f > 0$ (overstress) or directly relate stress to plastic strain rate. A generic associative viscoplastic flow may be written

$$\dot{\boldsymbol{\varepsilon}}^{\,p} = \Gamma\big(f(\boldsymbol{\sigma}, \boldsymbol{\alpha}, T)\big)\,\frac{\partial f}{\partial \boldsymbol{\sigma}}, \qquad \Gamma \geq 0,$$

with common specific choices producing Norton (power-law) creep and Perzyna type overstress models. The scalar Norton law for the equivalent creep strain rate is

$$\dot{\varepsilon}^{\,p}_{\mathrm{eq}} = A(T)\,q(\boldsymbol{\sigma})^{\,n}, \qquad A(T) = A_0\exp\big(-Q/(RT)\big),$$

where n is the stress exponent, Q the activation energy, R the gas constant, and A_0 a pre-exponential constant; embedding into tensorial flow yields

$$\dot{\boldsymbol{\varepsilon}}^{\,p} = \dot{\varepsilon}^{\,p}_{\mathrm{eq}}\,\frac{\partial q}{\partial \boldsymbol{\sigma}}.$$

Creep phenomenology is classically partitioned into three stages whose mathematical description is captured through evolution equations for hardening/recovery and damage. A simple phenomenological representation of primary (transient) and secondary (steady) creep uses

$$\dot{\varepsilon}_{\mathrm{cr}}(t) = B\,\sigma^n\,\varepsilon_{\mathrm{cr}}(t)^p + C\,\sigma^m\,t^r,$$

or, more commonly for primary→secondary behavior, a strain-hardening ordinary differential equation

$$\dot{\varepsilon}_{\mathrm{cr}} = K\sigma^n - \alpha(\varepsilon_{\mathrm{cr}})\,\dot{\varepsilon}_{\mathrm{cr}},$$

with $\alpha(\varepsilon_{\mathrm{cr}})$ describing hardening recovery so that transient decrease in $\dot{\varepsilon}_{\mathrm{cr}}$ occurs until a steady state $\dot{\varepsilon}^{\infty}_{\mathrm{cr}}$ satisfying hardening = recovery is reached. Tertiary creep is modelled by coupling a scalar damage variable $D \in [0, 1)$ whose growth accelerates strain rate; a common Kachanov–Rabotnov form is

$$\dot{D} = g(D)\,\big(\sigma_{\mathrm{eff}}\big)^p, \qquad \sigma_{\mathrm{eff}} = (1 - D)^{-1}\,q(\boldsymbol{\sigma}),$$

and the effective area reduction produces accelerating creep and eventual rupture when $D \to 1$.

Microstructurally informed relations bridge dislocation kinetics and diffusional mechanisms with continuum creep laws. The Orowan relation links mobile dislocation activity to plastic strain rate:

$$\dot{\varepsilon}^{p}_{\mathrm{eq}} = \rho_m \, b \, v_d,$$

with ρ_m the mobile dislocation density, b the Burgers vector and v_d the mean dislocation velocity. Thermally activated glide/climb gives

$$v_d = v_0 \exp\Big(- \frac{\Delta G(\tau)}{k_B T} \Big),$$

with $\Delta G(\tau)$ a stress-dependent activation barrier (e.g. $\Delta G(\tau) = \Delta F\big(1-(\tau/\tau_c)^{p}\big)^{q}$), which combined with evolution laws for ρ_m (multiplication and annihilation terms such as $\dot{\rho}_m = C_1\sqrt{\rho_m}\,\dot{\varepsilon}^{p}_{\mathrm{eq}} - C_2\rho_m$) yields, at steady state, power-law relations of Norton type and temperature dependence consistent with Arrhenius factors. Diffusional (diffusion-controlled) creep mechanisms produce different scaling with grain size and stress: Nabarro–Herring (lattice diffusion) and Coble (grain-boundary diffusion) give respectively

$$\dot{\varepsilon}_{\mathrm{NH}} \propto \frac{D_L \, \sigma}{G \, a^2}\,, \qquad \dot{\varepsilon}_{\mathrm{Coble}} \propto \frac{D_{GB} \, \sigma}{G \, a^3}\,,$$

where D_L and D_{GB} are lattice and grain-boundary diffusion coefficients, G the shear modulus, and a the grain size; these expressions demonstrate the inverse grain-size dependence and linear stress scaling characteristic of diffusion creep and are reconciled with continuum viscoplastic formulations by recognizing the distinct kinetic origin of Γ in the generic flow rule.

Finally, constitutive models used in computational practice combine the above ingredients into unified viscoplastic–damage frameworks. A compact representation is

$$\begin{aligned}
&\dot{\boldsymbol{\varepsilon}} = \mathbb{C}^{-1} : \dot{\boldsymbol{\sigma}} + \dot{\boldsymbol{\varepsilon}}^{\,p},\\
&\dot{\boldsymbol{\varepsilon}}^{\,p} = \Gamma\big(q(\boldsymbol{\sigma},\boldsymbol{\alpha},T), D\big)\,\frac{\partial q}{\partial \boldsymbol{\sigma}},\\
&\dot{\boldsymbol{\alpha}} = \mathcal{H}(\boldsymbol{\alpha}, \dot{\boldsymbol{\varepsilon}}^{\,p}, T), \qquad \dot{D} = \mathcal{R}(D, q, \dot{\boldsymbol{\varepsilon}}^{\,p}),
\end{aligned}$$

with $\Gamma, \mathcal{H}, \mathcal{R}$ chosen to satisfy $\mathcal{D} \geq 0$ (Clausius–Duhem) and calibrated to experiments; this structure furnishes a rigorous mathematical and thermodynamic foundation for modeling primary, secondary and tertiary creep within a plasticity framework.

4.3 Classical Creep Models and Their Plasticity Basis

The classical phenomenological creep laws are succinctly expressed as relations between the (equivalent) creep strain rate $\dot{\varepsilon}_{\mathrm{cr}}$, the stress σ (or an equivalent stress measure $q(\boldsymbol{\sigma})$), time t, and internal state variables $\boldsymbol{\alpha}$. The simplest empirical representations are the time-hardening and strain-hardening forms. The time-hardening law is written as

$$\varepsilon_{\mathrm{cr}}(t) = A \, \sigma^{n} \, t^{m},$$

with $A, n, m > 0$ material constants; differentiating gives the rate form

$$\dot{\varepsilon}_{\mathrm{cr}}(t) = A \, \sigma^{n} \, m \, t^{\,m-1}.$$

This form captures primary creep through the time exponent m (for $0 < m < 1$ the rate decays with time), and admits a closed-form integrated expression for total creep strain under constant stress. The strain-hardening (or strain-dependent) representation posits a rate law of the form

$$\dot{\varepsilon}_{\mathrm{cr}} = B \, \sigma^{n} \, \varepsilon^{p}_{\mathrm{cr}},$$

where p controls how accumulated creep strain modulates the instantaneous rate; this ODE structure can model either transient acceleration or deceleration depending on the sign and magnitude of p and is commonly used to represent self-accelerating or saturating behaviour by appropriate choice of p and initial condition.

A widely used, experimentally supported and physically interpretable relation for steady (secondary) creep is Norton's power law:

$$\dot{\varepsilon}_{\mathrm{cr}} = A(T)\,\sigma^{n}, \qquad A(T) = A_0 \exp\Big(-\frac{Q}{RT}\Big),$$

where n is the stress exponent, Q the activation energy, R the universal gas constant, and A_0 a pre-exponential constant. Norton's law is most valid in stress–temperature regimes where dislocation climb or glide mechanisms produce a power-law sensitivity; the Arrhenius factor in $A(T)$ encodes thermally activated kinetics. Embedding Norton's scalar law into a tensorial viscoplastic flow for an equivalent stress $q(\boldsymbol{\sigma})$ yields

$$\dot{\boldsymbol{\varepsilon}}^{\,p} = A(T)\,q(\boldsymbol{\sigma})^{\,n}\,\frac{\partial q}{\partial \boldsymbol{\sigma}},$$

which ensures that the tensorial flow direction is aligned with the chosen equivalent stress measure and that the scalar Norton rate is recovered by taking the appropriate norm. A microstructural justification of power-law behaviour is obtained from dislocation kinematics via the Orowan relation

$$\dot{\varepsilon}^{\,p}_{\mathrm{eq}} = \rho_m\, b\, v_d,$$

where ρ_m is the mobile dislocation density, b the Burgers vector magnitude, and v_d the average dislocation velocity. If dislocation motion is thermally activated over barriers with a stress-dependent activation energy $\Delta G(\tau)$, then a generic Arrhenius (or sinh) form for the velocity is

$$v_d = v_0\,\sinh\Big(\frac{\tau}{\tau_0}\Big)\,\exp\Big(-\frac{\Delta F}{k_B T}\Big) \quad \text{or} \quad v_d = v_0 \exp\Big(-\frac{\Delta G(\tau)}{k_B T}\Big),$$

with τ the resolved shear stress and $\Delta G(\tau)$ often modelled as $\Delta G(\tau) = \Delta F\big(1-(\tau/\tau_c)^{p}\big)^{q}$. Combining these relations with an evolution law for ρ_m that includes multiplication proportional to plastic activity and recovery (annihilation) terms,

$$\dot{\rho}_m = C_1\sqrt{\rho_m}\,\dot{\varepsilon}^{\,p}_{\mathrm{eq}} - C_2\,\rho_m,$$

and seeking a steady state $\dot{\rho}_m = 0$ yields $\rho_m \propto \dot{\varepsilon}^{\,p\,2}_{\mathrm{eq}}$ (under simplifying assumptions). Substituting back into Orowan then produces, after algebraic elimination, a power-law dependence $\dot{\varepsilon}^{\,p}_{\mathrm{eq}} \propto \tau^{\,n}$ with a stress exponent n that emerges from the stress sensitivity of v_d and the ρ_m closure; thus Norton's law can be rationalized as a mesoscale steady-state balance of multiplication and recovery of dislocations coupled to thermally activated mobility.

In many materials and stress/temperature regimes a threshold stress σ_0 or a sinh-type law provides a better fit than a pure power law. The threshold-adjusted power law and sinh law read respectively

$$\dot{\varepsilon}_{\mathrm{cr}} = A(T)\,(\sigma-\sigma_0)^{\,n}, \qquad \dot{\varepsilon}_{\mathrm{cr}} = B(T)\,\sinh\Big(\frac{\sigma}{\sigma_1}\Big)^{m},$$

where σ_0 accounts for obstacles that must be surmounted before significant creep ensues, and the sinh form captures both low-stress linear and high-stress power-law asymptotes (via the small-argument and large-argument behaviour of sinh) and is derivable from activated glide models with symmetric forward/backward rates. To represent the three classical creep stages and transition between transient and steady regimes, phenomenological models couple Norton-type steady laws with hardening/recovery kinetics. A compact representative set is

$$\dot{\varepsilon}_{\mathrm{cr}} = A(T)\,\sigma^{n} + H(\varepsilon_{\mathrm{cr}}, T)\,, \qquad \dot{\alpha} = h(\alpha, \dot{\varepsilon}_{\mathrm{cr}}, T),$$

or, equivalently, a strain-hardening ODE

$$\dot{\varepsilon}_{\mathrm{cr}} = K\sigma^n - \alpha(\varepsilon_{\mathrm{cr}})\,\dot{\varepsilon}_{\mathrm{cr}},$$

where $\alpha(\varepsilon_{\mathrm{cr}})$ models the instantaneous recovery/hardening state (e.g. dynamic recovery decreasing mobile dislocation density) so that primary creep is captured by transient reduction in $\dot{\varepsilon}_{\mathrm{cr}}$ and secondary creep by the fixed point solving $K\sigma^n = \alpha(\varepsilon_{\mathrm{cr}}^{\infty})\dot{\varepsilon}_{\mathrm{cr}}^{\infty}$.

Damage coupling and tertiary creep are often represented by scalar damage $D \in [0,1)$ modifying the load-carrying cross-section or stiffness. The Kachanov–Rabotnov style coupling appears as

$$\dot{\varepsilon}_{\mathrm{cr}} = A(T)\left((1-D)^{-1}q(\boldsymbol{\sigma})\right)^n, \qquad \dot{D} = R\big(D, \dot{\varepsilon}_{\mathrm{cr}}, q(\boldsymbol{\sigma})\big),$$

for example with $\dot{D} = B_D(1-D)^{-\beta}\,\dot{\varepsilon}_{\mathrm{cr}}^{\gamma}$, which yields positive feedback: increasing D raises the effective stress $(1-D)^{-1}q$, accelerating $\dot{\varepsilon}_{\mathrm{cr}}$ and leading to rupture when $D \to 1$. The Monkman–Grant empirical relation linking minimum creep rate and rupture time is often used in life prediction:

$$\dot{\varepsilon}_{\min}\, t_r^m = C_{MG},$$

with m and C_{MG} determined experimentally; such relations can be recovered approximately from coupled damage-creep ODE systems under simplifying assumptions. Multi-mechanism creep is represented by additive or multiplicative rule combinations reflecting parallel or serial operative processes. An additive decomposition of rates due to dislocation (power-law) and diffusional mechanisms is

$$\dot{\varepsilon}_{\mathrm{cr}} = \dot{\varepsilon}_{\mathrm{disl}} + \dot{\varepsilon}_{\mathrm{diff}} = A_d(T)\,\sigma^{n_d} + A_{NH}(T)\,\frac{\sigma}{a^2} + A_C(T)\,\frac{\sigma}{a^3},$$

where the Nabarro–Herring and Coble contributions scale as σa^{-2} and σa^{-3} respectively (with a the grain size), demonstrating how grain size and temperature select the dominant mechanism. Thermodynamic admissibility of such combined laws is ensured if each contribution is dissipative (nonnegative product of driving force and rate) so that the total dissipation $\mathcal{D} = \boldsymbol{\sigma} : \dot{\boldsymbol{\varepsilon}}^{\,p} - \rho\partial_{\boldsymbol{\alpha}}\psi\cdot\dot{\boldsymbol{\alpha}} \geq 0$ is satisfied termwise.

Finally, constitutive identification and calibration proceed by fitting the above models to creep tests (constant stress, stepped stress, constant load/uniaxial and multiaxial experiments) and extracting parameters $A(T), n, Q, \sigma_0$, as well as kinetics parameters in $\dot{\rho}_m$ and damage laws; model selection is guided by physical mechanism maps (stress vs. $1/T$ regimes), microstructural scales (grain size, precipitates) and the need for predictive coupling to plasticity and damage in structural analyses.

4.4 Unified Viscoplastic Models

A unified viscoplastic framework treats creep as rate-dependent plastic flow by replacing the rate-independent yield/consistency complementarity with kinetic relations driven by an overstress or by a dissipation potential; the kinematic basis in small strains is the additive decomposition

$$\boldsymbol{\varepsilon} = \boldsymbol{\varepsilon}^e + \boldsymbol{\varepsilon}^p, \qquad \dot{\boldsymbol{\varepsilon}} = \dot{\boldsymbol{\varepsilon}}^{\,e} + \dot{\boldsymbol{\varepsilon}}^{\,p},$$

with elastic constitutive law $\boldsymbol{\sigma} = \mathbb{C} : \boldsymbol{\varepsilon}^e$. Introduce an effective (equivalent) stress measure $q(\boldsymbol{\sigma}, \mathbf{X})$ (e.g. $q = \sqrt{\frac{3}{2}\mathbf{s} : \mathbf{s}}$ with $\mathbf{s} = \boldsymbol{\sigma} - \frac{1}{3}\operatorname{tr}(\boldsymbol{\sigma})\mathbf{I}$ or shifted by a backstress $\mathbf{X}$) and a scalar flow potential or overstress function $f(q, \alpha, T)$ such that viscoplastic flow is governed by a nonnegative mobility Γ:

$$\dot{\boldsymbol{\varepsilon}}^{\,p} = \Gamma\big(f(q(\boldsymbol{\sigma}, \mathbf{X}), \alpha, T)\big)\,\frac{\partial q}{\partial \boldsymbol{\sigma}}, \qquad \Gamma \geq 0.$$

Thermodynamic admissibility is enforced by the Clausius–Duhem inequality; with free energy $\psi(\boldsymbol{\varepsilon}^e, \alpha, T)$ and $\boldsymbol{\sigma} = \rho\partial_{\boldsymbol{\varepsilon}^e}\psi$ the dissipation reduces to

$$\mathcal{D} = \boldsymbol{\sigma} : \dot{\boldsymbol{\varepsilon}}^{\,p} - \rho\frac{\partial \psi}{\partial \alpha}\dot{\alpha} \geq 0.$$

A constructive route enforces $\dot{\boldsymbol{\varepsilon}}^{\,p} = \partial_{\boldsymbol{\sigma}}\Phi(\boldsymbol{\sigma}, \alpha, T)$ with a convex dissipation potential Φ in $\boldsymbol{\sigma}$ (or dual potential in flow rates), which guarantees $\mathcal{D} = \boldsymbol{\sigma} : \partial_{\boldsymbol{\sigma}}\Phi - \rho\partial_{\alpha}\psi\dot{\alpha} \geq 0$ provided the internal-variable evolution is chosen consistent with a nonnegative internal dissipation term.

The Perzyna overstress model is a canonical unified viscoplastic example: define a yield function $f(\boldsymbol{\sigma}, \boldsymbol{\alpha})$ and write the viscoplastic multiplier $\dot{\gamma}$ as a function of the overstress

$$\dot{\gamma} = \frac{1}{\eta(T)}\Big\langle \frac{f(\boldsymbol{\sigma}, \boldsymbol{\alpha})}{\sigma_0} \Big\rangle^{m}, \qquad \dot{\boldsymbol{\varepsilon}}^{\,p} = \dot{\gamma}\,\frac{\partial f}{\partial \boldsymbol{\sigma}},$$

where $\langle\cdot\rangle$ is the Macauley bracket, $\eta(T)$ a viscosity parameter, σ_0 a reference stress and $m \geq 1$ a rate exponent. Norton's law is recovered for $f \propto q$ and suitable choice of η (or letting $m = n$ and absorbing constants), i.e.

$$\dot{\varepsilon}^{\,p}_{\mathrm{eq}} = A(T)\, q^{\,n} \quad \Longleftrightarrow \quad \dot{\gamma} = \frac{1}{\eta} q^{\,n}.$$

An alternative regularization is the Duvaut–Lions viscoplasticity which enforces stress relaxation towards an elastic–perfectly plastic projection $\mathrm{Proj}_{Y}(\boldsymbol{\sigma})$ on a time scale τ:

$$\dot{\boldsymbol{\sigma}} = \mathbb{C} : \big(\dot{\boldsymbol{\varepsilon}} - \dot{\boldsymbol{\varepsilon}}^{\,p}\big), \qquad \mathbb{T} := \boldsymbol{\sigma} + \tau\dot{\boldsymbol{\sigma}}, \qquad \mathrm{Proj}_{Y}(\mathbb{T}) = \boldsymbol{\sigma},$$

or equivalently the evolution law

$$\tau\dot{\boldsymbol{\sigma}} + \boldsymbol{\sigma} = \boldsymbol{\sigma}_{\text{el-pl}}(\boldsymbol{\varepsilon}),$$

which yields rate-dependent responses and can be shown to be equivalent to a Perzyna law for particular choices of projection and τ.

Unified phenomenological models (Bodner–Partom, Bodner–Partom–Laird family) introduce internal (isotropic) state variables Z (resistance) and possibly kinematic backstress $\mathbf{X}$, with empirical kinetic equations coupling stress, equivalent plastic strain ε_p and strain rate. A compact Bodner–Partom style form for the equivalent rate is

$$\dot{\varepsilon}^{\,p}_{\mathrm{eq}} = A\left(\frac{q - \chi(Z)}{1 + B\varepsilon_p}\right)^{n},$$

with evolution laws

$$\dot{Z} = h_1(Z, \dot{\varepsilon}^{\,p}_{\mathrm{eq}}), \qquad \dot{\chi} = h_2(\chi, \dot{\varepsilon}^{\,p}_{\mathrm{eq}}),$$

where B captures strain-dependent softening/hardening and $\chi(Z)$ shifts the effective driving stress. Calibrated kinetic forms for h_1, h_2 reproduce primary→secondary creep transitions by balancing hardening (increasing Z) and recovery (decreasing Z). The Chaboche unified viscoplastic model couples a nonlinear kinematic hardening law with a Perzyna-type viscous flow; choose yield function

$$f(\boldsymbol{\sigma}, \mathbf{X}, R) = q(\boldsymbol{\sigma} - \mathbf{X}) - R,$$

with isotropic hardening R and backstress $\mathbf{X}$. The flow and hardening evolution read

$$\dot{\boldsymbol{\varepsilon}}^{\,p} = \dot{\gamma}\,\frac{\partial q}{\partial \boldsymbol{\sigma}}, \qquad \dot{\gamma} = \frac{1}{\eta}\left\langle \frac{f}{k} \right\rangle^{m},$$

$$\dot{R} = b\big(R_{\infty}(R) - R\big)\dot{\gamma}, \qquad \dot{\mathbf{X}} = \sum_{i=1}^{N} \big(c_i\dot{\boldsymbol{\varepsilon}}^{\,p} - \gamma_i \mathbf{X}_i\dot{\gamma}\big),$$

where $\mathbf{X} = \sum_i \mathbf{X}_i$ and the Armstrong–Frederick type term $c_i\dot{\boldsymbol{\varepsilon}}^{\,p} - \gamma_i\mathbf{X}_i\dot{\gamma}$ models nonlinear kinematic hardening and dynamic recovery; this structure captures ratchetting, cyclic creep and transient creep via internal variable kinetics. Microstructure-informed unified models embed physically motivated

evolution laws (e.g. for mobile dislocation density ρ_m) into the viscoplastic mobility Γ. For example combining Orowan with multiplication–recovery kinetics gives

$$\dot{\varepsilon}^{\,p}_{\mathrm{eq}} = \rho_m b v_d(\tau, T), \qquad \dot{\rho}_m = K_1\sqrt{\rho_m}\,\dot{\varepsilon}^{\,p}_{\mathrm{eq}} - K_2\rho_m,$$

whose steady state yields $\rho_m \propto (\dot{\varepsilon}^{\,p}_{\mathrm{eq}})^2$ and, after eliminating ρ_m, a power-law $\dot{\varepsilon}^{\,p}_{\mathrm{eq}} \propto \tau^n$ consistent with Norton, but with explicit temperature and microstructure dependence encoded in v_d and K_i.

For finite strains the unified viscoplastic framework uses the multiplicative decomposition $\mathbf{F} = \mathbf{F}^e\mathbf{F}^p$ and objective measures (Kirchhoff stress $\boldsymbol{\tau}$, elastic left Cauchy–Green $\mathbf{b}^e$), and writes the flow in intermediate configuration as

$$\mathbf{L}^p = (\dot{\mathbf{F}}^p)\mathbf{F}^{p-1}, \qquad \mathbf{d}^p = \operatorname{sym}\mathbf{L}^p, \qquad \mathbf{d}^p = \Gamma\big(f(\mathbf{M},\alpha)\big)\frac{\partial f}{\partial \mathbf{M}},$$

with $\mathbf{M}$ the Mandel stress; thermodynamic consistency requires the dissipation per unit reference volume $\mathcal{D} = \mathbf{M} : \mathbf{d}^p - \rho_0\partial_\alpha\psi\dot{\alpha} \geq 0$. Numerical integration of unified viscoplastic laws generally employs implicit backward Euler schemes for stability; for Perzyna/Chaboche type models with flow direction $\mathbf{n} = \partial q/\partial\boldsymbol{\sigma}$ the semi-discrete update under strain increment $\Delta\boldsymbol{\varepsilon}$ yields an elastic predictor $\boldsymbol{\sigma}^{\mathrm{trial}} = \mathbb{C} : (\boldsymbol{\varepsilon}^{n+1} - \boldsymbol{\varepsilon}^{p,n})$ and the corrector solves for $\Delta\gamma$ from the nonlinear scalar equation

$$\Delta\gamma = \Delta t\;\Gamma\Big(f\big(\boldsymbol{\sigma}^{\mathrm{trial}} - \Delta\gamma\,\mathbb{C} : \mathbf{n}, \alpha^n + \Delta\alpha\big)\Big),$$

with $\Delta\alpha$ given by implicit evolution; the consistent tangent modulus used in Newton–Raphson iterations is

$$\mathbb{C}_{\mathrm{tan}} = \mathbb{C} - \frac{\mathbb{C} : (\mathbf{n}\otimes\mathbf{n}) : \mathbb{C}\;\Delta t\;\Gamma'}{1 + \Delta t\;\Gamma'\,\mathbb{C} : (\mathbf{n}\otimes\mathbf{n})},$$

where $\Gamma' = \partial\Gamma/\partial f \cdot \partial f/\partial q \cdot (\partial q/\partial\boldsymbol{\sigma} : \mathbb{C} : \mathbf{n})$ (symbolic form) and the denominator enforces algorithmic consistency; this structure yields quadratic convergence when solved with Newton schemes.

Unified viscoplastic models therefore present a hierarchy: (i) purely phenomenological Perzyna/Duvaut–Lions regularizations that recover Norton behaviour as a special case, (ii) phenomenological internal-variable models (Bodner–Partom, Chaboche) that couple isotropic/kinematic hardening with viscous flow to capture primary/secondary/tertiary creep, and (iii) microstructure-based closures embedding dislocation/diffusion kinetics into the mobility Γ. Each class is constrained by thermodynamics via the Clausius–Duhem inequality and is implemented numerically with implicit schemes and consistent tangents to ensure stability and convergence in structural analyses.

4.5 Crystal Plasticity Models of Creep

Crystal-plasticity provides a rigorous microscale constitutive description of creep by resolving plastic flow on individual crystallographic slip systems and coupling slip kinetics, dislocation population dynamics and diffusion-controlled mechanisms to produce the macroscopic time-dependent plastic response. At finite strains the kinematic basis is the multiplicative decomposition of the deformation gradient into elastic and plastic parts,

$$\mathbf{F} = \mathbf{F}^e\mathbf{F}^p,$$

with the plastic part $\mathbf{F}^p$ mapping the reference lattice to an intermediate (stress-free) configuration and the elastic part $\mathbf{F}^e$ accommodating lattice stretch/rotation; the plastic velocity gradient in the intermediate configuration is

$$\mathbf{L}^p = (\dot{\mathbf{F}}^p)\mathbf{F}^{p-1}, \qquad \mathbf{d}^p = \tfrac{1}{2}\big(\mathbf{L}^p + \mathbf{L}^{pT}\big),$$

so that the macroscopic (symmetric) plastic strain rate is obtained from $\mathbf{d}^p$ after push-forward/pull-back as required for the chosen stress measure.

Plastic flow is decomposed over the set of crystallographic slip systems $\{\alpha\}$ by expressing the plastic velocity gradient as a sum of slip contributions,

$$\mathbf{L}^p = \sum_\alpha \dot\gamma^\alpha \, \mathbf{s}^\alpha \otimes \mathbf{m}^\alpha,$$

where $\mathbf{s}^\alpha$ is the unit slip direction, $\mathbf{m}^\alpha$ the unit slip plane normal (both defined in the appropriate configuration) and $\dot\gamma^\alpha$ the shear (slip) rate on system α. The resolved shear (Schmid) stress driving slip is

$$\tau^\alpha = \mathbf{s}^\alpha \cdot \boldsymbol{\sigma} \cdot \mathbf{m}^\alpha$$

(in small-strain / Cauchy stress form) or, in the intermediate configuration appropriate for finite strains, with the Mandel stress $\mathbf{M}$,

$$\tau^\alpha = \mathbf{M} : \mathbf{P}^\alpha, \qquad \mathbf{P}^\alpha = \tfrac{1}{2}\big(\mathbf{s}^\alpha \otimes \mathbf{m}^\alpha + \mathbf{m}^\alpha \otimes \mathbf{s}^\alpha\big),$$

so that slip kinetics are consistently defined with respect to crystal orientation and objective stress measures.

Slip-system kinetics (constitutive laws for $\dot\gamma^\alpha$) are chosen to capture glide, climb and thermally activated processes observed in creep. Common forms are the phenomenological power law and the thermally activated (Arrhenius / sinh) laws:

$$\dot\gamma^\alpha = \dot\gamma_0^\alpha \left\langle \frac{|\tau^\alpha| - \tau_c^\alpha}{\tau_0^\alpha} \right\rangle^{n^\alpha} \operatorname{sign}(\tau^\alpha),$$

$$\dot\gamma^\alpha = \dot\gamma_0^\alpha \, \exp\!\Big(-\frac{\Delta G^\alpha(\tau^\alpha)}{k_B T}\Big) \operatorname{sign}(\tau^\alpha),$$

$$\text{(or)} \qquad \dot\gamma^\alpha = \dot\gamma_0^\alpha \, \sinh\!\Big(\frac{\tau^\alpha}{\tau_1^\alpha}\Big)^{m^\alpha} \exp\!\Big(-\frac{Q^\alpha}{k_B T}\Big),$$

where τ_c^α is the current critical resolved shear stress (CRSS) on system α, n^α, m^α rate exponents, $\Delta G^\alpha(\tau)$ a stress-dependent activation barrier, Q^α an activation energy, k_B Boltzmann's constant, and $\dot\gamma_0^\alpha$ a reference rate. The choice of the barrier function $\Delta G^\alpha(\tau)$ (e.g. $\Delta G = \Delta F(1-(|\tau|/\tau_p)^p)^q$) determines low- and high-stress asymptotics and connects microscale obstacle overcoming to macroscopic rate sensitivity. Microstructural state evolution closes the system through dislocation population and hardening laws. Mobile and forest dislocation densities $\rho_m^\alpha, \rho_f^\alpha$ on each system satisfy kinetics such as

$$\dot\rho_m^\alpha = A_1^\alpha \sqrt{\rho^\alpha}\,|\dot\gamma^\alpha| - A_2^\alpha \rho_m^\alpha + A_3^\alpha \, \Phi(\{\dot\gamma^\beta\}),$$

with multiplication proportional to plastic activity, recovery (annihilation) proportional to ρ_m^α, and cross-system interaction Φ. The CRSS is related to dislocation structure via Taylor-type relations and latent hardening:

$$\tau_c^\alpha = \alpha_{\mathrm{T}}\, \mu\, b \sqrt{\sum_\beta a^{\alpha\beta} \rho^\beta}, \qquad \dot\tau_c^\alpha = \sum_\beta h^{\alpha\beta}\,|\dot\gamma^\beta|,$$

where μ is the shear modulus, b Burgers vector magnitude, $a^{\alpha\beta}$ interaction coefficients, α_T a constant, and $h^{\alpha\beta}$ the hardening/latent-hardening matrix; dynamic recovery can be modelled by adding $-r^\alpha \tau_c^\alpha$ terms to $\dot\tau_c^\alpha$.

High-temperature creep requires explicit representation of climb and diffusion. Dislocation climb velocity v_{cl}^α (which controls through Orowan the slip rate) is diffusion-limited and can be expressed schematically as

$$v_{\mathrm{cl}}^\alpha \;\approx\; \frac{D_v\, \Omega}{k_B T}\, \frac{\tau_\perp^\alpha}{\ell^\alpha},$$

where D_v is the vacancy diffusion coefficient, Ω the atomic volume, $\tau_\perp^\alpha$ the non-Schmid normal stress driving climb, and ℓ^α an effective capture length; the slip rate then follows Orowan per system,

$$\dot{\gamma}^\alpha = \rho_m^\alpha \, b \, v^\alpha, \qquad v^\alpha \sim v_{\text{glide}}^\alpha + v_{\text{cl}}^\alpha,$$

so that climb-controlled kinetics inherit Arrhenius temperature dependence through $D_v(T)$ and yield stress/grain-size controlled rate laws (e.g. power-law creep when climb mobility scales as $\tau^p \exp(-Q/k_B T)$). Grain-boundary processes and grain-boundary sliding (GBS) are incorporated as additional inelastic degrees of freedom that must be compatible with intragranular slip via accommodation fields. A compact continuum representation for GBS rate $\dot{\gamma}_{GB}$ is

$$\dot{\gamma}_{GB} = B_{GB} \, a^{-r} \, \tau_{GB}^s \exp\Big(- \frac{Q_{GB}}{k_B T} \Big),$$

with grain size a, viscosity coefficient B_{GB}, exponents r, s determined by diffusion/control mechanism, and τ_{GB} the tangential traction; the total inelastic deformation is the sum of intragranular slip and intergranular sliding contributions, and compatibility is enforced by geometric compatibility equations and accommodation slip rates computed from local stress and orientation. Thermodynamic admissibility is enforced at the slip-system level by the dissipation inequality: the rate of mechanical dissipation per unit current volume is the sum of shear work on all systems and internal variable storage rates,

$$\mathcal{D} = \sum_\alpha \tau^\alpha \dot{\gamma}^\alpha - \dot{\Psi}(\{\rho^\alpha\}, \ldots) \geq 0,$$

which for isothermal evolution reduces to the requirement $\sum_\alpha \tau^\alpha \dot{\gamma}^\alpha \geq 0$ when the free energy Ψ depends only on internal variables whose evolution is specified consistently; convex dissipation potentials at the system level yield flow laws that automatically satisfy this inequality.

Homogenization of crystal-plastic kinetics yields macroscopic creep laws: the macroscopic plastic strain rate is the volume or orientation average of the symmetric part of slip contributions,

$$\dot{\bar{\boldsymbol{\varepsilon}}}^p = \frac{1}{V} \int_V \sum_\alpha \dot{\gamma}^\alpha(\mathbf{x}) \, \mathrm{sym}(\mathbf{s}^\alpha \otimes \mathbf{m}^\alpha) \, \mathrm{d}V$$

(or, for a single crystal, $\dot{\boldsymbol{\varepsilon}}^p = \sum_\alpha \dot{\gamma}^\alpha \, \mathrm{sym}(\mathbf{s}^\alpha \otimes \mathbf{m}^\alpha)$). If slip rates scale with resolved shear stress as $\dot{\gamma}^\alpha \propto (\tau^\alpha)^{p_\alpha}$ and if dislocation structure or density introduces an additional stress-sensitivity $\rho^\alpha \propto (\tau^\alpha)^{q_\alpha}$, then the effective macroscopic stress exponent emerges as the sum of microscale sensitivities,

$$\dot{\varepsilon}_{\text{macro}} \propto \sum_\alpha (\tau^\alpha)^{p_\alpha + q_\alpha} \quad \Rightarrow \quad \dot{\varepsilon}_{\text{macro}} \propto \sigma^n, \qquad n \approx p_{\text{eff}} + q_{\text{eff}},$$

providing a clear mechanistic pathway from slip-level kinetics and dislocation scaling laws to Norton-type power laws observed experimentally. Numerical implementation integrates the slip ODEs and plastic flow multiplicatively: discretely update $\mathbf{F}^p$ by

$$\mathbf{F}_{n+1}^p = \exp\Big(\Delta t \sum_\alpha \Delta\gamma^\alpha \, \mathbf{s}^\alpha \otimes \mathbf{m}^\alpha \Big) \mathbf{F}_n^p,$$

solve the nonlinear algebraic system for slip increments $\{\Delta\gamma^\alpha\}$ arising from implicit time discretization of the kinetic laws and internal variable evolution, and construct a consistent tangent operator by linearization of the return map to ensure quadratic convergence of Newton iterations in finite-element contexts.

Taken together, crystal-plasticity models for creep deliver a mathematically rigorous, thermodynamically consistent, orientation- and mechanism-resolved framework: slip-level kinetics (glide, climb, thermally activated barrier overcoming), dislocation population dynamics (multiplication, recovery, latent interactions), and grain-boundary processes (sliding, diffusion accommodation) are coupled through objective kinematics and homogenized to produce predictive macroscopic creep laws and their temperature, stress and microstructure dependencies.

4.6 Coupled Creep-Plasticity-Damage Models

A coupled creep–plasticity–damage continuum is founded on an additive small-strain kinematics with an internal scalar damage variable $D \in [0, 1)$ that degrades the material stiffness and modifies the driving stresses for inelastic flow; the kinematic split is

$$\boldsymbol{\varepsilon} = \boldsymbol{\varepsilon}^e + \boldsymbol{\varepsilon}^p, \qquad \dot{\boldsymbol{\varepsilon}} = \dot{\boldsymbol{\varepsilon}}^{\,e} + \dot{\boldsymbol{\varepsilon}}^{\,p}.$$

Introduce a Helmholtz free-energy density per unit mass that depends on elastic strain, internal plasticity variables $\boldsymbol{\alpha}$ and the damage D:

$$\psi = \psi(\boldsymbol{\varepsilon}^e, \boldsymbol{\alpha}, D, T).$$

A common and convenient ansatz for isotropic stiffness degradation is multiplicative degradation of the elastic stored energy,

$$\psi(\boldsymbol{\varepsilon}^e, \boldsymbol{\alpha}, D) = (1 - D)\, \psi_0(\boldsymbol{\varepsilon}^e, \boldsymbol{\alpha}) + \psi_{\text{int}}(\boldsymbol{\alpha}) + \psi_D(D)$$

with $\psi_0 = \frac{1}{2}\boldsymbol{\varepsilon}^e : \mathbb{C} : \boldsymbol{\varepsilon}^e$ for linear elasticity, ψ_{int} internal energy of plastic internal variables, and ψ_D a possibly small energetic penalty for damage nucleation. The constitutive stress follows from the elastic part of the free energy (for isothermal conditions and with ρ absorbed into ψ notation):

$$\boldsymbol{\sigma} = \rho \frac{\partial \psi}{\partial \boldsymbol{\varepsilon}^e} = (1 - D)\, \mathbb{C} : \boldsymbol{\varepsilon}^e.$$

Thus damage reduces stiffness and increases the effective stress acting on the intact portion of material when the macroscopic applied stress is fixed.

Impose the Clausius–Duhem inequality in reduced (isothermal) form:

$$\mathcal{D} = \boldsymbol{\sigma} : \dot{\boldsymbol{\varepsilon}} - \rho \dot{\psi} \geq 0.$$

Using $\dot{\boldsymbol{\varepsilon}} = \dot{\boldsymbol{\varepsilon}}^{\,e} + \dot{\boldsymbol{\varepsilon}}^{\,p}$ and the constitutive relation for $\boldsymbol{\sigma}$ yields the reduced dissipation

$$\mathcal{D} = \boldsymbol{\sigma} : \dot{\boldsymbol{\varepsilon}}^{\,p} - \rho \frac{\partial \psi}{\partial \boldsymbol{\alpha}} \cdot \dot{\boldsymbol{\alpha}} - \rho \frac{\partial \psi}{\partial D} \dot{D} \geq 0.$$

Define the thermodynamic driving force (damage energy release rate)

$$Y \;=\; -\rho \frac{\partial \psi}{\partial D} \;=\; \tfrac{1}{2}\, \boldsymbol{\varepsilon}^e : \mathbb{C} : \boldsymbol{\varepsilon}^e - \rho \psi'_D(D) - \cdots,$$

so that the damage contribution to dissipation appears as $Y\dot{D}$ (note sign convention chosen so $Y \geq 0$ tends to promote damage growth when $\dot{D} \geq 0$) and the dissipation inequality becomes

$$\mathcal{D} = \boldsymbol{\sigma} : \dot{\boldsymbol{\varepsilon}}^{\,p} - \rho \frac{\partial \psi}{\partial \boldsymbol{\alpha}} \cdot \dot{\boldsymbol{\alpha}} + Y \dot{D} \geq 0.$$

A thermodynamically admissible split of dissipation is obtained by prescribing dissipative constitutive laws for plastic flow and for damage growth separately. Let $q(\boldsymbol{\sigma}, \boldsymbol{\alpha})$ be an equivalent stress (e.g. von Mises shifted by backstress). A generic viscous/plastic flow rule that respects the dissipation is

$$\dot{\boldsymbol{\varepsilon}}^{\,p} = \Gamma\big(q(\boldsymbol{\sigma}, \boldsymbol{\alpha}), D, T\big)\, \frac{\partial q}{\partial \boldsymbol{\sigma}}, \qquad \Gamma \geq 0,$$

which contributes $\boldsymbol{\sigma} : \dot{\boldsymbol{\varepsilon}}^{\,p} = \Gamma\, q$ to the dissipation (since $\partial q / \partial \boldsymbol{\sigma} : \boldsymbol{\sigma} = q$ for typical choices of q); to ensure $\mathcal{D} \geq 0$ the damage evolution law must satisfy $Y\dot{D} \geq -(\boldsymbol{\sigma} : \dot{\boldsymbol{\varepsilon}}^{\,p} - \rho \partial_{\boldsymbol{\alpha}} \psi \cdot \dot{\boldsymbol{\alpha}})$, and a natural choice is to make each term non-negative independently.

Commonly used damage evolution laws are driven by an effective stress measure σ_{eff} that accounts for area reduction or stiffness loss:

$$\sigma_{\text{eff}} = \frac{q(\boldsymbol{\sigma})}{1-D},$$

and Kachanov–Rabotnov type kinetics prescribe

$$\dot{D} = h\big(\sigma_{\text{eff}}, \dot{\varepsilon}^{p}_{\text{eq}}, D, T\big) \geq 0,$$

with canonical forms

$$\dot{D} = B\left(\sigma_{\text{eff}}\right)^{m} \quad \text{or} \quad \dot{D} = B_D\,(1-D)^{-\beta}\,\dot{\varepsilon}^{p\,\gamma}_{\text{eq}},$$

where B, B_D, m, β, γ are nonnegative material parameters; substituting $\sigma_{\text{eff}} = (1-D)^{-1}q$ shows the positive feedback mechanism: damage growth increases σ_{eff}, accelerating $\dot{D}$ and $\dot{\varepsilon}^{\,p}$. A frequently used coupled example for creep modelling couples Norton-type viscoplasticity with Kachanov–Rabotnov damage:

$$\dot{\varepsilon}^{p}_{\text{eq}} = A(T)\left((1-D)^{-1}q(\boldsymbol{\sigma})\right)^{n}, \qquad \dot{D} = B(T)\left((1-D)^{-1}q(\boldsymbol{\sigma})\right)^{m},$$

which transparently satisfies $\boldsymbol{\sigma} : \dot{\boldsymbol{\varepsilon}}^{\,p} = (1-D)^{-1}q\,\dot{\varepsilon}^{p}_{\text{eq}} \geq 0$ and produces tertiary creep as $D \to 1$. Calibration of exponents n, m and prefactors A, B is performed from creep-rupture and minimum-creep-rate data. To prevent pathological localization and mesh sensitivity and to represent nonlocal microstructural length scales, gradient damage regularization augments the free energy with a damage gradient term:

$$\psi_D(D, \nabla D) = \psi_D^{\text{loc}}(D) + \tfrac{1}{2}\,a_\ell^2\,|\nabla D|^2,$$

leading to the Euler–Lagrange damage balance (static or rate form)

$$Y - a_\ell^2 \Delta D = \mathcal{G}(D, \dot{D}, \ldots),$$

or written variationally from total potential minimization. Here a_ℓ is a material length scale and the Laplacian term supplies nonlocal energetic resistance to damage localization and mathematical well-posedness. Damage mechanics also couples to kinematic/isotropic hardening through internal variables: let $\boldsymbol{\alpha}$ include isotropic resistance R and kinematic backstress $\mathbf{X}$ with evolutions

$$\dot{R} = h_R(R, \dot{\varepsilon}^{p}_{\text{eq}}, T) - r_R(D)R, \qquad \dot{\mathbf{X}} = h_X(\mathbf{X}, \dot{\boldsymbol{\varepsilon}}^{\,p}, T) - r_X(D)\mathbf{X},$$

where the recovery terms $r_R(D), r_X(D)$ can increase with damage to model softening of hardening capacity as microstructure degrades; these couplings modify the flow driving force $f(q(\boldsymbol{\sigma}-\mathbf{X}), R, D)$ used in Γ.

For numerical implementation one collects the coupled system to solve incrementally (implicit backward Euler recommended):

$$\begin{aligned}
&\boldsymbol{\sigma}^{n+1} = (1 - D^{n+1})\,\mathbb{C} : (\boldsymbol{\varepsilon}^{n+1} - \boldsymbol{\varepsilon}^{p,n+1}),\\
&\dot{\boldsymbol{\varepsilon}}^{\,p} = \Gamma\big(f(\boldsymbol{\sigma}, \boldsymbol{\alpha}, D)\big)\partial_{\boldsymbol{\sigma}} q,\\
&\dot{\boldsymbol{\alpha}} = \mathcal{H}(\boldsymbol{\alpha}, \dot{\boldsymbol{\varepsilon}}^{\,p}, D), \qquad \dot{D} = \mathcal{R}(D, q, \dot{\boldsymbol{\varepsilon}}^{\,p}),
\end{aligned}$$

and the local nonlinear solve for increments $\Delta\gamma, \Delta\boldsymbol{\alpha}, \Delta D$ follows from the implicit discrete residuals; the consistent tangent modulus used in global equilibrium iterations is obtained by linearizing the stress update with respect to $\Delta\boldsymbol{\varepsilon}$, producing

$$\mathbb{C}_{\text{tan}} = \frac{\partial \boldsymbol{\sigma}^{n+1}}{\partial \boldsymbol{\varepsilon}^{\,n+1}} = (1-D)\left[\mathbb{C} - \mathbb{C} : \mathbf{P} : \mathbb{C}\right] - \mathbb{C} : \boldsymbol{\varepsilon}^{e} \otimes \frac{\partial D}{\partial \boldsymbol{\varepsilon}},$$

where $\mathbf{P}$ gathers contributions from plastic corrector directions and $\partial D/\partial\boldsymbol{\varepsilon}$ arises if damage is strain-driven; computing $\mathbb{C}_{\text{tan}}$ consistently is essential for quadratic convergence. From an engineering life-prediction viewpoint, coupled models yield empirically observed relations: for the coupled ODE

system $\dot{\varepsilon}_{\min} = A(\sigma_{\text{eff}})^n,\ \dot{D} = B(\sigma_{\text{eff}})^m$ one can integrate under constant stress to obtain approximate rupture time scaling; eliminating time gives a Monkman–Grant type relation

$$\dot{\varepsilon}_{\min}\, t_r^{\,p} \approx \text{const},$$

with exponent p related to the ratio m/n under the assumed kinetics and damage criterion for rupture $D(t_r) = D_c$.

In summary, coupled creep–plasticity–damage models are constructed by (i) embedding damage into the free energy (and hence the stress), (ii) defining thermodynamically admissible flow laws for plasticity and evolution laws for internal variables, (iii) prescribing damage kinetics driven by the energy release rate Y or effective stress measures, and (iv) regularizing with gradient terms or nonlocal integrals to ensure well-posedness and objective representation of localization; the Clausius–Duhem inequality provides the central constraint guaranteeing nonnegative dissipation and thus admissible couplings.

4.7 Numerical Implementation

The numerical implementation of creep–plasticity constitutive laws is built on (i) time discretization of rate equations (implicit backward-Euler preferred for stability), (ii) local (material-point) nonlinear solves for plastic/internal variable increments, and (iii) consistent linearization (algorithmic tangent) for global Newton iterations in finite-element equilibrium. For small strains with additive split $\boldsymbol{\varepsilon} = \boldsymbol{\varepsilon}^e + \boldsymbol{\varepsilon}^p$ and elastic law $\boldsymbol{\sigma} = \mathbb{C} : (\boldsymbol{\varepsilon} - \boldsymbol{\varepsilon}^p)$, the incremental (backward-Euler) update over $[t_n, t_{n+1}]$ with $\Delta t = t_{n+1} - t_n$ reads (trial elastic predictor)

$$\boldsymbol{\sigma}^{\text{trial}} = \mathbb{C} : \big(\boldsymbol{\varepsilon}^{n+1} - \boldsymbol{\varepsilon}^{p,n}\big).$$

The corrector solves for the plastic multiplier increment $\Delta\gamma$ (or for vector of slip increments $\{\Delta\gamma^\alpha\}$) from the implicit flow law

$$\Delta\boldsymbol{\varepsilon}^p \;=\; \Delta\gamma\,\mathbf{n}, \qquad \Delta\gamma = \Delta t\;\Gamma\big(f(\boldsymbol{\sigma}^{n+1}, \boldsymbol{\alpha}^{n+1}, D^{n+1})\big),$$

with $\mathbf{n} = \partial q/\partial\boldsymbol{\sigma}$ and the updated stress

$$\boldsymbol{\sigma}^{n+1} = \mathbb{C} : \big(\boldsymbol{\varepsilon}^{n+1} - \boldsymbol{\varepsilon}^{p,n} - \Delta\gamma\,\mathbf{n}\big).$$

Substitute to obtain the scalar (or small system) nonlinear residual for $\Delta\gamma$:

$$R(\Delta\gamma) \;=\; \Delta\gamma - \Delta t\;\Gamma\Big(f\big(\mathbb{C} : (\boldsymbol{\varepsilon}^{n+1} - \boldsymbol{\varepsilon}^{p,n} - \Delta\gamma\mathbf{n}),\ \boldsymbol{\alpha}^n + \Delta\boldsymbol{\alpha},\ D^n + \Delta D\big)\Big) = 0,$$

where $\Delta\boldsymbol{\alpha}, \Delta D$ are given by their implicit evolution laws $\Delta\boldsymbol{\alpha} = \Delta t\,\mathcal{H}(\boldsymbol{\alpha}^{n+1}, \dot{\boldsymbol{\varepsilon}}^{p,n+1})$, $\Delta D = \Delta t\,\mathcal{R}(D^{n+1}, q^{n+1}, \dot{\boldsymbol{\varepsilon}}$
Solve $R(\Delta\gamma) = 0$ by local Newton iterations:

$$\Delta\gamma^{(k+1)} = \Delta\gamma^{(k)} - \big[\,\partial_{\Delta\gamma} R(\Delta\gamma^{(k)})\,\big]^{-1} R(\Delta\gamma^{(k)}),$$

with derivative

$$\partial_{\Delta\gamma} R = 1 + \Delta t\,\Gamma'(f)\,\Big(\partial_f f\Big)\,\Big(\mathbb{C} : (\mathbf{n}\otimes\mathbf{n})\Big),$$

where $\Gamma' = \partial\Gamma/\partial f$ and $\partial_f f = \partial f/\partial q \cdot (\partial q/\partial\boldsymbol{\sigma} : \mathbb{C} : -\mathbf{n})$ evaluated consistently (symbolically shown); include contributions from $\partial\Delta\boldsymbol{\alpha}/\partial\Delta\gamma$ and $\partial\Delta D/\partial\Delta\gamma$ when internal variables are fully coupled (implicit treatment). The consistent algorithmic tangent (material Jacobian) $\mathbb{C}_{\text{tan}} = \partial\boldsymbol{\sigma}^{n+1}/\partial\boldsymbol{\varepsilon}^{n+1}$ required for global Newton solves is obtained by differentiating the stress corrector under the solved $\Delta\gamma$ (implicit function theorem). For the scalar-$\Delta\gamma$ case one obtains

$$\mathbb{C}_{\text{tan}} \;=\; \mathbb{C} - \frac{\mathbb{C} : (\mathbf{n}\otimes\mathbf{n}) : \mathbb{C}}{1 + \Delta t\,\Gamma'\,\big(\partial_f f\big)\,\mathbb{C} : (\mathbf{n}\otimes\mathbf{n})}\;\Delta t\,\Gamma',$$

or compactly

$$\mathbb{C}_{\tan} = \mathbb{C} - \frac{\mathbb{C} : \mathbf{A} : \mathbb{C}}{S}, \qquad \mathbf{A} = \Delta t\, \Gamma' \, \mathbf{n} \otimes \mathbf{n}, \qquad S = 1 + \Delta t\, \Gamma' \, \mathbb{C} : (\mathbf{n} \otimes \mathbf{n}).$$

When internal variables are coupled, the tangent requires inversion of the local Jacobian system that couples $\Delta\gamma, \Delta\boldsymbol{\alpha}, \Delta D$; write the local residual vector $\mathbf{R}_\ell(\Delta\mathbf{y}) = \mathbf{0}$ with $\Delta\mathbf{y} = [\Delta\gamma, \Delta\boldsymbol{\alpha}, \Delta D]^T$ and obtain

$$\frac{\partial \Delta\mathbf{y}}{\partial \boldsymbol{\varepsilon}^{n+1}} = -\big(\partial_{\Delta\mathbf{y}} \mathbf{R}_\ell\big)^{-1} \partial_{\boldsymbol{\varepsilon}^{n+1}} \mathbf{R}_\ell,$$

then

$$\mathbb{C}_{\tan} = \mathbb{C} : \Big(\mathbf{I} - \partial_{\Delta\mathbf{y}} \boldsymbol{\varepsilon}^p \, \frac{\partial \Delta\mathbf{y}}{\partial \boldsymbol{\varepsilon}^{n+1}}\Big),$$

ensuring exact linearization and quadratic convergence of the global Newton method when assembled into the finite element stiffness matrix $\mathbf{K} = \int_\Omega \mathbf{B}^T \mathbb{C}_{\tan} \mathbf{B}\, dV$. For Perzyna or Norton-type flow with analytic $\Gamma(f)$ a closed form for Γ' is available; for Duvaut–Lions regularization implement the differential relaxation by solving (implicit) the stress evolution

$$\tau \frac{\boldsymbol{\sigma}^{n+1} - \boldsymbol{\sigma}^n}{\Delta t} + \boldsymbol{\sigma}^{n+1} = \boldsymbol{\sigma}^{n+1}_{\text{proj}},$$

where $\boldsymbol{\sigma}^{n+1}_{\text{proj}}$ is the elastic–plastic projection (return mapping) evaluated at t_{n+1}; algebraic elimination yields an effective $\mathbb{C}_{\tan}$ similar to the Perzyna form with time scale τ.

In finite-strain multiplicative frameworks $\mathbf{F} = \mathbf{F}^e \mathbf{F}^p$ the update uses exponential maps to preserve $\det \mathbf{F}^p > 0$. Integrate the plastic flow in the intermediate configuration via

$$\mathbf{F}^p_{n+1} = \exp\Big(\Delta t\, \mathbf{L}^p_{n+1}\Big) \mathbf{F}^p_n, \qquad \mathbf{L}^p_{n+1} = \sum_\alpha \dot\gamma^{\alpha, n+1} \, \mathbf{s}^\alpha \otimes \mathbf{m}^\alpha,$$

and update elastic strain measures (e.g. $\mathbf{b}^e = \mathbf{F}^e \mathbf{F}^{eT}$) followed by objective stress $\mathbf{M}$ evaluations. The consistent tangent in finite strain is the fourth-order linearization $\mathbb{C}_{\tan} = \partial \mathbf{P}^{n+1} / \partial \mathbf{F}^{n+1}$ (or its spatial counterpart), obtained by differentiating the push-forward/pull-back operations and the exponential map; algorithmic differentiation or symbolic linearization of the exponential map (via Baker–Campbell–Hausdorff truncation or exact series) is required for exact consistent tangent. Coupled damage or additional internal variables are solved in a monolithic local Newton system for robustness, or via a staggered scheme when computational cost demands splitting. Monolithic implicit treatment defines local residuals

$$\mathbf{R}_\ell(\Delta\mathbf{y}) = \begin{bmatrix} \Delta\gamma - \Delta t\, \Gamma(f(\boldsymbol{\sigma}^{n+1}, \boldsymbol{\alpha}^{n+1}, D^{n+1})) \\ \Delta\boldsymbol{\alpha} - \Delta t\, \mathcal{H}(\boldsymbol{\alpha}^{n+1}, \dot{\boldsymbol{\varepsilon}}^{p,n+1}) \\ \Delta D - \Delta t\, \mathcal{R}(D^{n+1}, q^{n+1}, \dot{\boldsymbol{\varepsilon}}^{p,n+1}) \end{bmatrix} = \mathbf{0},$$

solve by Newton with Jacobian $\partial_{\Delta\mathbf{y}} \mathbf{R}_\ell$, and compute $\mathbb{C}_{\tan}$ from the implicit sensitivities as above. Staggered schemes (solve plasticity with fixed D then update D) reduce local algebraic size but require sub-iterations or reduced time step sizes to maintain stability and accuracy. Global finite-element equilibrium solves the weak form residual

$$\mathbf{R}_g(\mathbf{u}) = \int_\Omega \mathbf{B}^T \boldsymbol{\sigma}(\mathbf{u})\, dV - \mathbf{F}_{\text{ext}} = \mathbf{0},$$

and Newton updates $\delta\mathbf{u} = -\mathbf{K}^{-1} \mathbf{R}_g$ with $\mathbf{K} = \partial \mathbf{R}_g / \partial \mathbf{u} = \int_\Omega \mathbf{B}^T \mathbb{C}_{\tan} \mathbf{B}\, dV$. Line search or trust-region globalization may be used when large steps or strong softening (damage) cause loss of quadratic convergence. Adaptive time stepping controls accuracy and computational effort. Use embedded

error estimation by comparing a single implicit step with two half steps (local temporal Richardson estimate) and require

$$\mathrm{err} = \frac{\|\boldsymbol{\sigma}^{\Delta t} - \boldsymbol{\sigma}^{\Delta t/2 + \Delta t/2}\|}{\|\boldsymbol{\sigma}^{\Delta t/2 + \Delta t/2}\| + \varepsilon_{\mathrm{tol}}} \le \mathrm{tol},$$

adapt $\Delta t \leftarrow \Delta t \cdot \big(\mathrm{tol}/\mathrm{err}\big)^{1/(p+1)}$ for scheme order p (backward-Euler $p = 1$), and enforce limits to resolve rapid tertiary acceleration (damage) or rate changes in Γ.

Practical implementation notes expressed mathematically: ensure $\partial_{\Delta \mathbf{y}} \mathbf{R}_\ell$ is well-conditioned (regularize Γ' near zero by small viscous regularization), enforce yield floor by Macauley brackets $\langle \cdot \rangle$ in residuals, and include consistent numerical limits for exponentials to avoid overflow in Arrhenius/sinh laws. For parallel FE solves assemble $\mathbf{K}$ and $\mathbf{R}_g$ with domain decomposition; the local solves are independent and ideally vectorized for efficiency:

$$\forall \text{ Gauss points } i: \quad \Delta \mathbf{y}_i \leftarrow \mathrm{NewtonSolve}\big(\mathbf{R}_\ell^i, \partial_{\Delta \mathbf{y}} \mathbf{R}_\ell^i\big), \qquad \mathbb{C}_{\mathrm{tan}}^i \leftarrow \mathrm{Linearize}(\Delta \mathbf{y}_i).$$

In summary, rigorous and robust numerical implementation requires implicit (A-stability) time integration, monolithic local Newton solves for coupled inelastic/damage kinetics, exact consistent linearization for $\mathbb{C}_{\mathrm{tan}}$ (or carefully derived approximate tangents when justified), adaptive time stepping governed by local error estimates, and careful handling of finite-strain exponential updates; these steps produce a provably convergent Newton scheme at the global level when the local Jacobians and consistent tangents are correctly assembled.

4.8 Case Studies and Applications

4.8.1 Turbine blades — single-crystal high-temperature creep–plasticity

Single-crystal turbine blades are modeled by crystal-plasticity with rate-dependent slip and anisotropic elasticity. In the finite-strain multiplicative framework the local update solves

$$\mathbf{F} = \mathbf{F}^e \mathbf{F}^p, \qquad \mathbf{L}^p = \sum_\alpha \dot{\gamma}^\alpha \, \mathbf{s}^\alpha \otimes \mathbf{m}^\alpha,$$

with slip kinetics on system α

$$\dot{\gamma}^\alpha = \dot{\gamma}_0^\alpha \exp\Big(- \frac{\Delta G^\alpha(\tau^\alpha)}{k_B T} \Big) \operatorname{sign}(\tau^\alpha), \qquad \tau^\alpha = \mathbf{M} : \mathbf{P}^\alpha,$$

and elastic stress in the intermediate configuration given by the Mandel stress $\mathbf{M} = \mathbf{F}^{eT} \mathbf{S} \mathbf{F}^e$ (with $\mathbf{S}$ the second Piola–Kirchhoff stress from $\psi(\mathbf{C}^e)$). Numerical blade analysis imposes equilibrium and thermal boundary conditions,

$$\mathrm{Div}\, \boldsymbol{\sigma} + \mathbf{b} = \mathbf{0}, \qquad \boldsymbol{\sigma} = (1 - D)\, \mathcal{F}(\mathbf{F}^e),$$

with rotation/inertia terms for centrifugal loading when relevant. Life prediction couples creep strain accumulation to a rupture criterion: use a damage variable D with kinetics

$$\dot{D} = B(T) \big((1 - D)^{-1} q(\boldsymbol{\sigma}) \big)^m,$$

and rupture time t_r defined by $D(t_r) = D_c$. Calibration uses high-temperature single-crystal creep tests to determine $\dot{\gamma}_0^\alpha, \Delta G^\alpha$ and $B(T), m$.

4.8.2 Reactor pressure vessels and main vessels — continuum viscoplastic–damage at component scale

Large pressure-containing structures operate in regimes where creep, plasticity and damage interact over long times. The governing BVP is

$$\operatorname{Div}\boldsymbol{\sigma} + \rho\mathbf{g} = \mathbf{0}, \qquad \boldsymbol{\sigma} = (1-D)\,\mathbb{C} : (\boldsymbol{\varepsilon} - \boldsymbol{\varepsilon}^{p}),$$

with viscoplastic flow

$$\dot{\boldsymbol{\varepsilon}}^{\,p} = \Gamma\big(q(\boldsymbol{\sigma}-\mathbf{X}), R, T\big)\,\frac{\partial q}{\partial \boldsymbol{\sigma}},$$

and coupled evolution

$$\dot{R} = h_R(R, \dot{\varepsilon}^{p}_{\mathrm{eq}}, T), \quad \dot{\mathbf{X}} = h_X(\mathbf{X}, \dot{\boldsymbol{\varepsilon}}^{\,p}, T), \quad \dot{D} = \mathcal{R}(D, q, \dot{\varepsilon}^{p}_{\mathrm{eq}}, T).$$

Fracture mechanics coupling uses crack growth laws with an effective stress intensity or notch-modified driving force $K_{\mathrm{eff}}(t)$ and Paris/Da/dN laws extended for creep:

$$\frac{da}{dt} = A_{\mathrm{cr}}(T)\,K_{\mathrm{eff}}^{p} + B_{\mathrm{fat}}\,(\Delta K)^{m},$$

where the first term captures time-dependent (creep) crack advance and the second cyclic fatigue contribution. Reliability is obtained by integrating the stochastic damage ODE ensemble or using first-passage time statistics for $D(t)$ exceeding D_c.

4.8.3 Solder joints and microelectronics — diffusion and grain-boundary controlled creep in small volumes

Microelectronic solder joints operate at low stresses but small geometrical scales; diffusional mechanisms dominate. Continuum representation couples viscoplasticity and diffusion by including vacancy concentration $c_v(\mathbf{x},t)$ and chemical potential μ:

$$\dot{\varepsilon}_{\mathrm{cr}} = \dot{\varepsilon}_{\mathrm{disl}}(\sigma, T) + \dot{\varepsilon}_{\mathrm{diff}}(c_v, \nabla c_v, T),$$

$$\frac{\partial c_v}{\partial t} + \nabla\cdot\mathbf{J} = S(\dot{\varepsilon}_{\mathrm{cr}}), \qquad \mathbf{J} = -M(c_v)\nabla\mu,$$

with diffusion contribution to strain rate linked to vacancy flux divergence. Grain-size scaling appears explicitly: Nabarro–Herring and Coble terms

$$\dot{\varepsilon}_{\mathrm{NH}} \propto \frac{D_L \sigma}{G a^2}, \qquad \dot{\varepsilon}_{\mathrm{Coble}} \propto \frac{D_{GB}\sigma}{G a^3},$$

so RVE or homogenized models must resolve a and boundary conditions. Thermo-mechanical cycling is modeled by time-periodic boundary loads and solved with adaptive timestepping to capture ratcheting and incremental creep.

4.8.4 Polycrystalline alloys with grain-boundary sliding — multiscale homogenization and RVE analyses

For polycrystals combine crystal-plasticity at grain scale with grain-boundary sliding (GBS) as an intergranular mechanism. At the RVE level enforce Hill–Mandel:

$$\langle \boldsymbol{\sigma} : \dot{\boldsymbol{\varepsilon}} \rangle = \langle \boldsymbol{\sigma} : \dot{\boldsymbol{\varepsilon}}^{e} \rangle + \langle \boldsymbol{\sigma} : \dot{\boldsymbol{\varepsilon}}^{p} \rangle + \langle \boldsymbol{\sigma} : \dot{\boldsymbol{\varepsilon}}^{GB} \rangle,$$

with homogenized creep rate

$$\dot{\bar{\varepsilon}}^{\,p} = \frac{1}{V}\int_V \sum_{\alpha} \dot{\gamma}^{\alpha}(\mathbf{x})\,\mathrm{sym}(\mathbf{s}^{\alpha}\otimes\mathbf{m}^{\alpha})\,dV + \frac{1}{V}\int_{\partial g} \dot{\gamma}_{GB}\,\mathbf{t}\otimes\mathbf{n}\,dS.$$

Self-consistent methods (VPSC) solve for grain response $\mathbf{E}^g$ and slip rates satisfying

$$\dot{\gamma}_g^\alpha = \dot{\gamma}_0^\alpha \Big\langle \frac{\tau_g^\alpha - \tau_c^\alpha(g)}{\tau_0^\alpha} \Big\rangle^{n^\alpha},$$

with compatibility via interaction tensors $\mathbb{P}^g$ such that

$$\mathbf{\Sigma} = \sum_g v_g \mathbb{M}^g : \mathbf{E}^g, \qquad \mathbf{E}^g = \mathbb{P}^g : \mathbf{\Sigma},$$

yielding an effective macroscopic Norton-type law $\dot{\bar{\varepsilon}}^p = A_{\text{eff}}(T)\,\bar{\sigma}^{\,n_{\text{eff}}}$ whose exponents depend on grain orientation distribution, GBS kinetics, and grain size.

4.8.5 Weldments, joints and notch effects — localization, mesh-objectivity and gradient regularization

Localized tertiary creep near welds and notches requires nonlocal/gradient regularization to obtain mesh-independent results. Augment free energy with gradient terms for damage or plastic strain:

$$\Psi = \Psi_0(\boldsymbol{\varepsilon}^e, \ldots) + (1-D)\,\psi_D^{\text{loc}}(D) + \tfrac{1}{2} a_\ell^2 |\nabla D|^2.$$

The local damage Euler–Lagrange equation in weak form becomes

$$\int_\Omega \big(Y\,\delta D + a_\ell^2 \nabla D \cdot \nabla \delta D \big)\, dV = \int_\Omega s(D, \dot{D}) \delta D \, dV,$$

where Y is the energy release rate. For finite elements this yields stable post-localization softening and allows accurate prediction of creep-rupture near weld toes with proper length-scale calibration from microstructural tests.

4.8.6 Life prediction, creep–fatigue interaction and probabilistic reliability

Life prediction integrates constitutive creep and damage ODEs under service loading histories. Under a constant stress path the coupled ODEs

$$\dot{\varepsilon}_{\text{cr}} = A(T)\big((1-D)^{-1} q(\sigma)\big)^n, \qquad \dot{D} = B(T)\big((1-D)^{-1} q(\sigma)\big)^m$$

are integrated to $D(t_r) = D_c$ to obtain deterministic t_r. For creep–fatigue interaction superpose cyclic damage via Miner-type rules generalized to time fraction or strain fraction:

$$\sum_i \frac{t_i}{t_{r,i}(\sigma_i, T_i)} \approx 1,$$

or use continuous damage accumulation

$$\dot{D} = B_c \sigma_{\text{eff}}^m + B_f (\Delta \varepsilon)^p,$$

and for probabilistic assessment model parameters as random variables $\boldsymbol{\theta}$ and compute failure probability

$$P_f(t) = \Pr\big(D(t;\boldsymbol{\theta}) \ge D_c\big) = \int I\{D(t;\boldsymbol{\theta}) \ge D_c\}\, p(\boldsymbol{\theta})\, d\boldsymbol{\theta}.$$

Monte-Carlo or surrogate models (PCE, Gaussian processes) accelerate evaluation; reliability sensitivity uses

$$\frac{\partial P_f}{\partial \mu_{\theta_i}} = \int I\{D \ge D_c\} \frac{\partial \log p(\boldsymbol{\theta})}{\partial \mu_{\theta_i}} p(\boldsymbol{\theta})\, d\boldsymbol{\theta}.$$

4.8.7 Integrated multi-physics examples and verification

Practical application couples thermo-mechanics (heat equation),

$$\rho c_p \dot{T} - \nabla \cdot (k \nabla T) = Q(\mathbf{x}, t),$$

with constitutive creep/damage and mass transport for oxidation or vacancy diffusion. Verification is performed by (i) reproducing canonical creep curves (primary–secondary–tertiary) from single-element tests, (ii) matching Paris-type crack growth under mixed creep–fatigue, and (iii) RVE homogenization convergence to effective Norton exponents. Convergence tests require temporal and spatial refinement such that

$$\lim_{\Delta t,\, h \to 0} \|\mathbf{u}_{h,\Delta t} - \mathbf{u}\|_{H^1(\Omega)} = 0,$$

and validation uses experimental observables: minimum creep rate $\dot{\varepsilon}_{\min}$, rupture time t_r, and strain accumulation maps.

Collectively these case studies demonstrate the transfer of mathematically rigorous creep–plasticity–damage models to real engineering problems through appropriate microstructural closures, multiscale homogenization, damage regularization, and coupled multiphysics integration; in each application the same thermodynamic and numerical principles—Clausius–Duhem admissibility, consistent linearization, and well-posed nonlocal regularization—provide the foundation for predictive analysis.

4.8.8 Future Directions

Advances in multiscale and concurrent coupling aim to derive predictive creep–plasticity laws from atomistic and mesoscale physics while retaining computational tractability at the structural scale. A formal asymptotic homogenization starting from a microstructural RVE with fast microscale coordinate $y = x/\varepsilon$ and slow macroscopic coordinate x yields the two-scale expansion

$$\mathbf{u}^{\varepsilon}(x,t) = \mathbf{u}^0(x,t) + \varepsilon\, \mathbf{u}^1(x,y,t) + \varepsilon^2 \mathbf{u}^2 + \cdots,$$

and the homogenized constitutive relation is obtained by solving the cell problem for $\mathbf{u}^1$ and averaging:

$$\overline{\mathbb{C}}_{ijkl}(x,t) = \frac{1}{|Y|} \int_Y \mathbb{C}_{ijkl}(y) \left(I + \nabla_y \boldsymbol{\chi}(y,x,t) \right) dy,$$

with $\boldsymbol{\chi}$ the corrector field satisfying microscale equilibrium including creep/plastic kinetics. Concurrent multiscale schemes impose consistency conditions between scales (e.g. energy and dissipation matching)

$$\int_\Omega \boldsymbol{\sigma} : \dot{\boldsymbol{\varepsilon}}\, dV = \int_{\Omega_{\text{macro}}} \overline{\boldsymbol{\sigma}} : \dot{\overline{\boldsymbol{\varepsilon}}}\, dV + \int_{\Omega_{\text{micro}}} \mathcal{D}_{\text{micro}}\, dV,$$

ensuring that mesoscale dissipation $\mathcal{D}_{\text{micro}}$ correctly projects to macroscopic viscoplastic mobilities. Development of physics-aware data-driven constitutive surrogates (reduced-order and operator-learning approaches) seeks to replace expensive microscale closures by learned operators while preserving thermodynamic constraints. Let $\mathcal{G} : \mathcal{H}_{\text{hist}} \mapsto \dot{\varepsilon}^p$ denote the history-to-rate operator; operator learning learns $\mathcal{G}_\theta$ parameterized by θ via minimizing loss subject to dissipation constraints:

$$\min_\theta \ \mathbb{E}_{\mathcal{D}}\big[\|\mathcal{G}_\theta(\mathcal{H}) - \dot{\varepsilon}^p_{\text{obs}}\|^2\big] \quad \text{s.t.} \quad \mathcal{D}(\mathcal{G}_\theta) \geq 0 \text{ a.e.}$$

Enforcing the Clausius–Duhem inequality during training is accomplished by penalty or constrained optimization:

$$\mathcal{L}(\theta) = \mathbb{E}\big[\|\cdot\|^2\big] + \lambda\, \mathbb{E}\big[\langle -\mathcal{D}(\mathcal{G}_\theta), 0 \rangle\big],$$

so that the learned surrogate is provably dissipative. Uncertainty quantification and Bayesian model calibration for creep–damage models must treat material, microstructural and loading uncertainty. Represent random fields (e.g. spatially varying yield $R(x,\omega)$) via Karhunen–Loève expansion:

$$R(x,\omega) = \bar{R}(x) + \sum_{i=1}^{\infty} \sqrt{\lambda_i}\phi_i(x)\xi_i(\omega),$$

truncate to N terms and propagate uncertainty by stochastic Galerkin or polynomial chaos (PC):

$$\dot{\mathbf{u}}(x,t,\omega) \approx \sum_{|\alpha|\le p} \hat{\mathbf{u}}_\alpha(x,t)\Psi_\alpha(\boldsymbol{\xi}(\omega)),$$

with PC coefficients $\hat{\mathbf{u}}_\alpha$ solved from deterministic coupled systems. Bayesian calibration of model parameters θ uses posterior

$$\pi(\theta \mid \mathcal{D}) \propto \pi(\mathcal{D} \mid \theta)\pi(\theta),$$

where the likelihood $\pi(\mathcal{D} \mid \theta)$ accounts for model discrepancy and experimental noise; efficient sampling employs surrogate-accelerated MCMC or sequential Monte-Carlo with likelihood evaluation via reduced-order models. A major direction is coupled chemo-thermo-mechanical and irradiation effects where mass transport, oxidation and radiation defect kinetics alter creep behavior. A unified free energy including chemical concentration c and damage D reads

$$\Psi(\boldsymbol{\varepsilon}^e, \boldsymbol{\alpha}, c, D, T) = (1-D)\,\Psi_e(\boldsymbol{\varepsilon}^e) + \Psi_{\text{int}}(\boldsymbol{\alpha}, c) + \Psi_c(c) + \Psi_D(D),$$

and the coupled evolution equations are

$$\begin{aligned}
&\rho\dot{\mathbf{u}} = \nabla\cdot\big((1-D)\,\mathbb{C} : \boldsymbol{\varepsilon}^e\big) + \mathbf{b},\\
&\dot{c} + \nabla\cdot\mathbf{J} = S(\boldsymbol{\varepsilon}^p, c, T), \quad \mathbf{J} = -M(c)\nabla\mu, \quad \mu = \partial_c\Psi,\\
&\dot{D} = \mathcal{R}(Y, c, \dot{\varepsilon}^p, T),\\
&\dot{\boldsymbol{\alpha}} = \mathcal{H}(\boldsymbol{\alpha}, \dot{\varepsilon}^p, c, T),
\end{aligned}$$

so that diffusion, defect production (e.g. irradiation) and plasticity are coupled through chemical potentials and damage driving forces.

Variational and structure-preserving formulations (energy–dissipation principles) are being extended to creep–damage to provide robust numerical schemes and existence theory. Seek $(\mathbf{u}, \boldsymbol{\alpha}, D)$ minimizing incremental potential

$$\mathcal{I}_{\Delta t}(\mathbf{u}, \boldsymbol{\alpha}, D) = \frac{1}{\Delta t}\mathcal{D}(\boldsymbol{\alpha}, D; \Delta\mathbf{y}) + \mathcal{E}(\mathbf{u}, \boldsymbol{\alpha}, D),$$

with energy $\mathcal{E} = \int_\Omega \Psi\, dV - \langle \mathbf{f}, \mathbf{u}\rangle$ and dissipation functional $\mathcal{D}$ convex in rates; time-incremental minimization yields stable algorithmic schemes and a posteriori error bounds. For phase-field fracture/creep combine phase-field ϕ with damage:

$$\mathcal{E} = \int_\Omega \big((1-\phi)^2\Psi_e(\boldsymbol{\varepsilon}^e) + G_c\big(\tfrac{\phi^2}{2\ell} + \tfrac{\ell}{2}|\nabla\phi|^2\big)\big)\, dV,$$

and evolve ϕ by variational inequalities ensuring irreversibility $\dot{\phi} \ge 0$.

Reduced-order, adaptive and real-time (digital twin) strategies are crucial for industrial prediction. Proper Orthogonal Decomposition (POD)/Galerkin ROMs derive basis $\{\boldsymbol{\varphi}_i\}$ from snapshots and solve projected dynamics:

$$\mathbf{u}(x,t) \approx \sum_{i=1}^{r} a_i(t)\boldsymbol{\varphi}_i(x), \qquad \mathbf{M}_r\dot{\mathbf{a}} + \mathbf{K}_r(\mathbf{a})\mathbf{a} = \mathbf{F}_r,$$

with hyper-reduction (DEIM, GNAT) for nonlinear viscoplastic operators. Error estimators and adaptive enrichment select when to query high-fidelity models:

$$\eta_{\mathrm{ROM}} = \|\mathbf{R}_{\mathrm{HF}}(\mathbf{u}_{\mathrm{ROM}})\|_{W^{-1}} \ ; \quad \eta_{\mathrm{ROM}} > \epsilon \Rightarrow \text{enrich basis.}$$

Mathematical analysis, well-posedness and regularization remain open for coupled softening systems. Address existence and uniqueness by enforcing gradient regularization and convexity of dissipation; prove under suitable hypotheses that for given loading the incremental variational problem admits a minimizer:

$$\exists\ (\mathbf{u}^{n+1}, \boldsymbol{\alpha}^{n+1}, D^{n+1}) \text{ s.t. } \mathcal{I}_{\Delta t}(\cdot) \text{ is minimized,}$$

and obtain a priori estimates of the form

$$\|\mathbf{u}^{n+1}\|_{H^1} + \|D^{n+1}\|_{H^1} \leq C(\|\mathbf{u}^{n}\|_{H^1}, \Delta t).$$

Finally, experimental–computational integration and active learning will accelerate model discovery and calibration by targeted experiments. Formulate optimal experiment design by maximizing information gain (Kullback–Leibler divergence) with respect to parameters θ:

$$\mathbf{q}^{*} = \arg\max_{\mathbf{q}\in\mathcal{Q}} \ \mathbb{E}_{\mathcal{D}|\mathbf{q}}\big[\,\mathrm{KL}\big(\pi(\theta \mid \mathcal{D}) \,\|\, \pi(\theta)\big)\big],$$

and employ sequential Bayesian updates to reduce uncertainty in the most influential parameters for creep and damage kinetics. Coupling these experimental design principles with physics-constrained learning, multiscale homogenization, stochastic model reduction, and structure-preserving numerics provides a coherent roadmap toward predictive, computationally efficient, and uncertainty-aware creep–plasticity–damage models for next-generation materials and high-temperature structures.

4.8.9 Conclusion

The study of creep deformation through the lens of plasticity unifies phenomenology, microscale mechanisms and thermodynamics into a single constitutive architecture: kinematically by an elastic–inelastic split (additive in small strains, multiplicative at finite strains), thermodynamically by a free energy and dissipation inequality, and mechanically by flow rules that map stresses and internal states to inelastic rates. In small strain form the kinematic and constitutive skeleton reads

$$\boldsymbol{\varepsilon} = \boldsymbol{\varepsilon}^{e} + \boldsymbol{\varepsilon}^{p}, \qquad \boldsymbol{\sigma} = \mathbb{C} : \boldsymbol{\varepsilon}^{e},$$

and in finite strain the corresponding multiplicative decomposition is

$$\mathbf{F} = \mathbf{F}^{e}\mathbf{F}^{p}, \qquad \mathbf{L}^{p} = (\dot{\mathbf{F}}^{p})\mathbf{F}^{p-1},$$

so that objective stress and strain measures (Mandel stress, Kirchhoff stress, elastic stretches) enter the constitutive statements. These kinematic relations are the necessary geometric backbone on which rate-dependent constitutive rules are posed.

Thermodynamic admissibility, expressed by the Clausius–Duhem inequality, constrains permissible kinetics and couples stored energy to dissipative rates. For isothermal processes one adopts a free-energy density $\psi(\boldsymbol{\varepsilon}^{e}, \boldsymbol{\alpha}, D, T)$ and requires

$$\mathcal{D} = \boldsymbol{\sigma} : \dot{\boldsymbol{\varepsilon}} - \rho\,\dot{\psi} \geq 0,$$

which, using $\boldsymbol{\sigma} = \rho\,\partial_{\boldsymbol{\varepsilon}^{e}}\psi$, reduces to the local dissipation statement

$$\mathcal{D} = \boldsymbol{\sigma} : \dot{\boldsymbol{\varepsilon}}^{\,p} - \rho\,\partial_{\boldsymbol{\alpha}}\psi \cdot \dot{\boldsymbol{\alpha}} + Y\dot{D} \geq 0,$$

with $Y = -\rho\,\partial_{D}\psi$ the damage energy release rate. The dissipation inequality is both a judge (for admissibility) and a guide (for constructing convex dissipation potentials or overstress kinetics that

guarantee $\mathcal{D} \geq 0$). Mechanically predictive models of creep arise from specifying flow rules and internal-variable kinetics consistent with the thermodynamic constraint and motivated by physical mechanisms. A compact general form is

$$\dot{\boldsymbol{\varepsilon}}^{\,p} = \Gamma\big(q(\boldsymbol{\sigma}, \mathbf{X}, D), \boldsymbol{\alpha}, T\big)\, \frac{\partial q}{\partial \boldsymbol{\sigma}}, \qquad \dot{\boldsymbol{\alpha}} = \mathcal{H}(\boldsymbol{\alpha}, \dot{\boldsymbol{\varepsilon}}^{\,p}, T), \qquad \dot{D} = \mathcal{R}(D, q, \dot{\boldsymbol{\varepsilon}}^{\,p}, T),$$

where $\Gamma \geq 0$ encodes rate sensitivity (Perzyna, Norton, sinh/Arrhenius forms), q is an equivalent stress, $\mathbf{X}$ kinematic resistance, and $\boldsymbol{\alpha}$ microstructural state (dislocation densities, grain-size indicators). Representative specializations include Norton's law

$$\dot{\varepsilon}^{\,p}_{\mathrm{eq}} = A(T)\, q^{\,n}, \qquad A(T) = A_0 \exp\big(-Q/(RT)\big),$$

Orowan's mesoscale relation

$$\dot{\varepsilon}^{\,p}_{\mathrm{eq}} = \rho_m b v_d(\tau, T),$$

and damage-coupled kinetics (Kachanov–Rabotnov)

$$\dot{D} = B(T)\, \big((1-D)^{-1} q\big)^m, \qquad \dot{\varepsilon}^{\,p}_{\mathrm{eq}} = A(T)\, \big((1-D)^{-1} q\big)^n,$$

which together capture steady secondary creep and accelerating tertiary rupture.

For predictive computation the constitutive model must be rendered into robust numerical form: implicit time discretization (backward Euler), local nonlinear solves for flow/internal variable increments, and exact consistent linearization for the global Newton iteration. The local residual system

$$\mathbf{R}_\ell(\Delta \mathbf{y}) = \mathbf{0}, \quad \Delta \mathbf{y} = [\Delta\gamma, \Delta\boldsymbol{\alpha}, \Delta D]^T,$$

is solved by Newton with Jacobian $\partial_{\Delta \mathbf{y}} \mathbf{R}_\ell$, and the algorithmic tangent

$$\mathbb{C}_{\mathrm{tan}} = \frac{\partial \boldsymbol{\sigma}^{n+1}}{\partial \boldsymbol{\varepsilon}^{n+1}}$$

is computed via implicit differentiation (or monolithic inversion when variables are strongly coupled) to ensure quadratic convergence of the global finite-element scheme. Regularization (gradient damage, nonlocal hardening) is essential to restore well-posedness when softening mechanisms produce localization. Synthesis of mechanisms and scales—crystal plasticity for lattice-controlled creep, diffusional laws for grain-boundary processes, and continuum damage for voiding and cavitation—provides mechanistic closure and explains empirical observations (stress exponents, grain-size scalings, Monkman–Grant relations). Homogenization and RVE averaging link microscale kinetics to macroscopic mobilities:

$$\overline{\dot{\boldsymbol{\varepsilon}}^{\,p}} = \frac{1}{|Y|} \int_Y \sum_\alpha \dot{\gamma}^\alpha(y)\, \mathrm{sym}(\mathbf{s}^\alpha \otimes \mathbf{m}^\alpha)\, dy,$$

so that emergent macroscopic laws inherit temperature, stress and microstructural dependence from the lower-scale physics.

Thus, the plasticity-based approach to creep yields a unified, thermodynamically consistent, and mechanistically interpretable framework that (i) captures primary, secondary and tertiary creep via internal-variable kinetics, (ii) accounts for microstructural controls through explicit state variables and homogenization, (iii) couples naturally to damage and fracture mechanics for life prediction, and (iv) admits stable numerical realization through implicit integration and consistent tangents. The canonical equations—kinematic decomposition, Clausius–Duhem dissipation, flow rules of the form $\dot{\boldsymbol{\varepsilon}}^{\,p} = \Gamma \partial_{\boldsymbol{\sigma}} q$, mesoscale Orowan relations, and damage–flow coupling—constitute the minimal, mathematically rigorous core from which applied creep–plasticity models are constructed, calibrated, and deployed in engineering analysis.

5 Sintering

At high temperatures, the interaction between thermodynamic forces, mechanical stresses, and atomic diffusion mechanisms in materials undergoing creep is a profoundly intricate phenomenon, particularly concerning the behavior of voids—microscopic cavities within the material. These voids

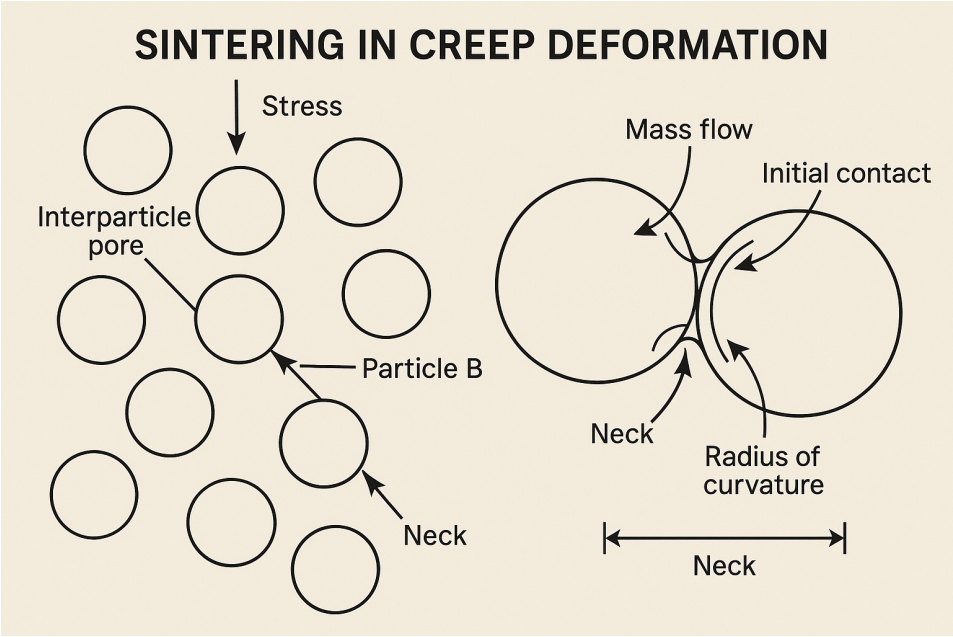

Figure 39: Sintering in Creep Deformation

play a pivotal role in determining whether a material succumbs to creep fracture. At elevated temperatures, voids tend to shrink due to the thermodynamic principle of energy minimization, wherein the system reduces its surface free energy. The surface energy E_s of a void is proportional to its surface area A, given by $E_s = \gamma A$, where γ is the surface energy per unit area. For a spherical void of radius r, the surface area is $A = 4\pi r^2$, making the surface energy:

$$E_s = \gamma(4\pi r^2).$$

As temperature increases, atomic diffusion becomes significant, facilitating the migration of atoms that effectively reduces the surface area A, thereby decreasing E_s. This diffusion process is thermally activated and described by the diffusion coefficient D, which follows an Arrhenius relationship:

$$D = D_0 e^{-\frac{Q}{kT}},$$

where D_0 is the pre-exponential factor, Q is the activation energy for diffusion, k is Boltzmann's constant, and T is the absolute temperature. This dependence underscores the criticality of temperature in enabling void shrinkage.

However, the application of tensile stress σ introduces a competing mechanical energy term that opposes void shrinkage and can promote void growth. The mechanical energy associated with void growth is given by:

$$W = \sigma V,$$

where V is the volume of the void. For a spherical void, $V = \frac{4}{3}\pi r^3$, leading to:

$$W = \sigma \left(\frac{4}{3}\pi r^3 \right).$$

The net energetics of void behavior result from the balance between the reduction in surface energy ΔE_s due to shrinkage and the mechanical energy W opposing this reduction. For void growth to

occur, the mechanical energy must exceed the reduction in surface energy, leading to the critical condition:

$$\sigma V > \Delta E_s.$$

Substituting the expressions for E_s and V, we find that void growth occurs if:

$$\sigma \left(\frac{4}{3} \pi r^3 \right) > \gamma (4\pi r^2).$$

Simplifying this inequality yields:

$$\sigma > \frac{3\gamma}{r}.$$

This threshold stress, $\sigma_c = \frac{3\gamma}{r}$, is known as the **sintering limit** of the system [16], representing the minimum tensile stress required to counteract the thermodynamic drive for void shrinkage and initiate void growth. Notably, σ_c is inversely proportional to the void radius r, implying that smaller voids require significantly higher stresses to grow, whereas larger voids are more susceptible to growth under lower stresses. When the applied tensile stress σ exceeds σ_c, voids begin to expand through diffusion-driven processes. These include **lattice diffusion** (Nabarro-Herring creep) and **grain boundary diffusion** (Coble creep), both of which are governed by Fick's first law:

$$J = -D \frac{\partial C}{\partial x},$$

where J is the diffusion flux, D is the diffusion coefficient, C is the atomic concentration, and $\frac{\partial C}{\partial x}$ is the concentration gradient. The rate of material transport, and hence the rate of void growth, is strongly temperature-dependent, as reflected by the Arrhenius dependence of D. Furthermore, the volumetric rate of void growth can be expressed as:

$$\dot{V} = \alpha D \sigma,$$

where α is a geometric factor determined by the void shape and stress distribution. This rate accelerates significantly with increasing temperature and stress. As voids grow and coalesce, the material loses its load-bearing capacity, leading to the onset of macroscopic cracks and ultimately creep fracture. The time to failure in creep-dominated scenarios is thus intricately linked to the kinetics of void growth, which can be modeled using constitutive laws for creep deformation, such as:

$$\dot{\varepsilon} = A \sigma^n e^{-\frac{Q}{kT}},$$

where $\dot{\varepsilon}$ is the creep strain rate, A is a material constant, σ is the applied stress, n is the stress exponent, Q is the activation energy, k is Boltzmann's constant, and T is the absolute temperature. This equation underscores the exponential sensitivity of creep processes to temperature. In summary, the phenomenon of void shrinkage and growth in high-temperature creep is governed by a delicate balance of thermodynamic, mechanical, and kinetic factors. The sintering limit σ_c serves as the critical stress threshold, below which voids shrink and above which voids grow, leading to creep fracture. The interplay of atomic diffusion mechanisms and the temperature-dependent energetics elucidates the complex behavior of materials under high-temperature tensile stresses, highlighting the critical importance of understanding these principles to mitigate creep-induced failures in structural applications.

Ghosh (2024) [86] presented a comprehensive and rigorous examination of Eshelby's solution for ellipsoidal inclusions in elastic media, extending classical elasticity theory by systematically exploring both foundational principles and diverse practical applications. The manuscript revisits the seminal Eshelby tensor, elucidating its mathematical derivation for stress and strain fields within and outside ellipsoidal inclusions, and elaborates on its pivotal role in micromechanical modeling of composite materials and homogenization techniques. By bridging theoretical elegance with applied relevance, this work provides an essential reference for researchers investigating inhomogeneity-driven field interactions and multiscale material behavior in continuum mechanics.

6 Examples of Creep Deformation

6.1 Surface materials

The application of fractal geometry, particularly employing a deterministic Cantor structure, to model surface topography represents a significant advancement in understanding and predicting the behavior of rough surfaces under conditions of thermoviscoelastic creep. Fractal geometry, characterized by its ability to describe complex and irregular patterns that exhibit self-similarity across different scales, provides a powerful mathematical framework for representing the intricate and hierarchical nature of surface roughness. The deterministic Cantor structure, a specific fractal construct, is instrumental in capturing the multi-scale distribution of asperities—microscopic peaks and valleys—that define the topography of rough surfaces. This level of detail is essential when studying thermoviscoelastic creep, as the interaction between these asperities under sustained stress and elevated temperatures significantly influences the material's long-term deformation behavior. Recent advancements in this domain have introduced sophisticated models that account for the thermomechanical and time-dependent characteristics of such interactions, enabling more accurate predictions of contact mechanics for rough surfaces.

To achieve this, various viscoelastic idealizations are employed to model the surface materials, each offering distinct approaches to capturing the complex interplay between elastic and viscous responses, for example: Maxwell, Kelvin–Voigt, standard linear solid and Jeffrey models [112]. The Maxwell model, for instance, represents a viscoelastic material as a combination of a spring and a dashpot in series, effectively modeling stress relaxation but lacking the ability to predict long-term elastic recovery. Conversely, the Kelvin–Voigt model, which combines a spring and dashpot in parallel, excels at describing immediate elastic deformation and steady-state creep but cannot account for stress relaxation. The standard linear solid model, a more sophisticated combination of these two configurations, provides a more comprehensive representation by capturing both transient and steady-state viscoelastic responses. The Jeffrey model further extends these capabilities by incorporating additional dashpots to simulate complex relaxation mechanisms observed in certain materials. Each of these models plays a critical role in simulating the behavior of rough surfaces under thermoviscoelastic creep conditions, allowing researchers to account for diverse material behaviors and operational conditions.

The integration of these viscoelastic models with fractal-based surface representations offers unparalleled insights into the thermoviscoelastic behavior of rough surfaces. For example, by using the deterministic Cantor structure to model the asperity distribution and applying viscoelastic idealizations to represent the material properties, it becomes possible to predict how surfaces will deform over time under sustained loads and varying thermal conditions. This approach not only enhances our understanding of material behavior but also informs the design and optimization of engineering systems where surface contact under high stress and temperature is critical, such as in tribology, microelectromechanical systems (MEMS), and advanced manufacturing processes. These advancements demonstrate the profound impact of combining mathematical rigor with physical modeling to address complex, multi-scale phenomena in materials science and engineering.

6.2 Metals

Creep in metals primarily manifests as movement within their microstructures, fundamentally governed by processes such as dislocation motion, grain boundary sliding, and atomic diffusion. These mechanisms are deeply rooted in the crystalline nature of metals, which consist of highly ordered atomic arrangements with imperfections called dislocations. Under sustained stress and elevated temperatures, these dislocations move through slip or climb processes, causing irreversible deformation over time. Additionally, the polycrystalline structure of metals, composed of numerous

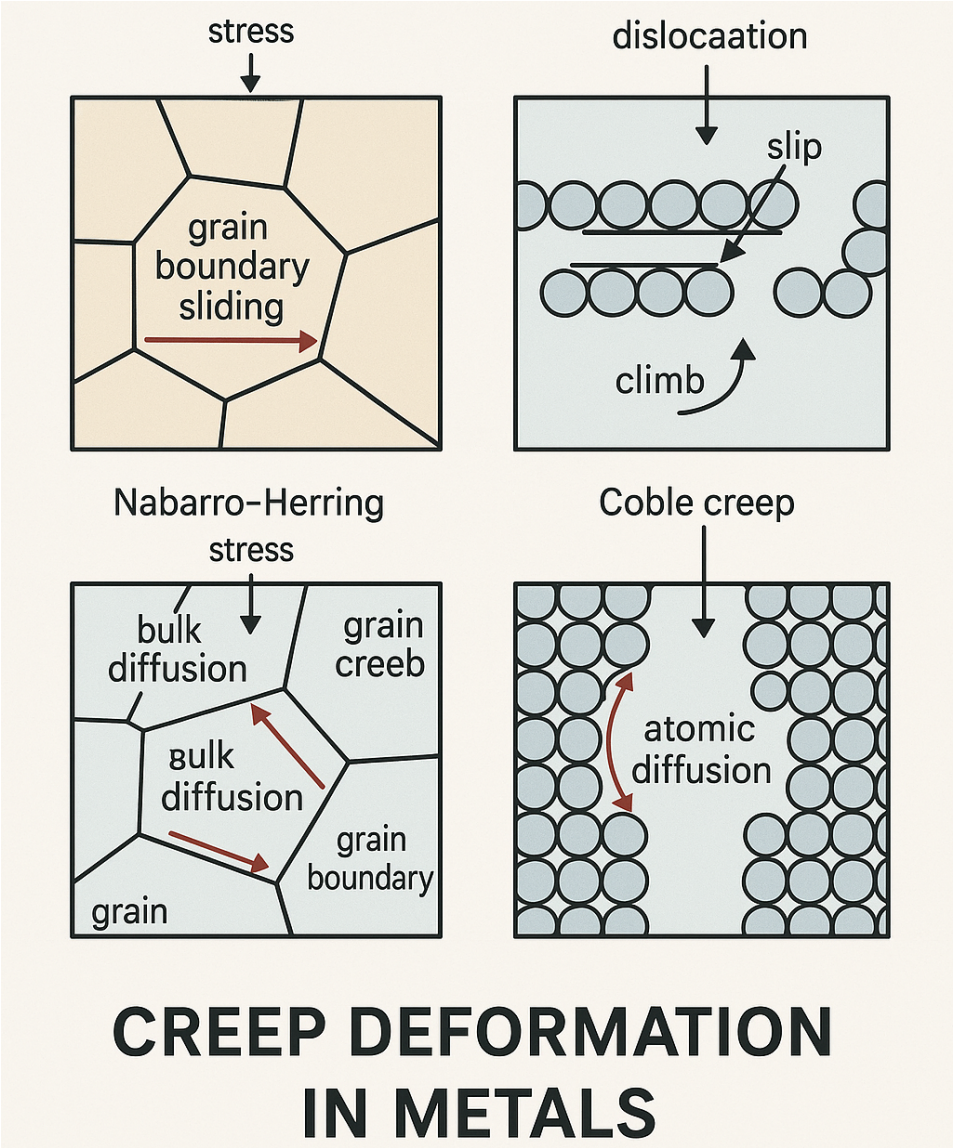

Figure 40: Creep Deformation in Metals

grains, facilitates grain boundary sliding, where adjacent grains shift relative to one another, further contributing to creep. Atoms also diffuse either through the bulk crystal lattice or along grain boundaries, resulting in Nabarro-Herring and Coble creep mechanisms, respectively. While polymers also exhibit creep, the underlying phenomena differ substantially due to their molecular structure. Polymers consist of long-chain molecules that can realign and slide past one another, often displaying a viscoelastic response characterized by both recoverable (elastic) and permanent (viscous) deformation. This viscoelastic behavior leads to a significantly different mechanical response from metals, where creep is largely plastic once the elastic limit is exceeded. The stress-strain relationship and time-dependence in polymers often necessitate models like the Maxwell or Kelvin-Voigt models, which account for time-dependent compliance due to molecular chain reorientation. In contrast, metals require thermally activated creep models that incorporate stress-driven mechanisms, such as $\dot{\varepsilon} = A\sigma^n \exp\left(-\frac{Q}{RT}\right)$, where the strain rate depends on stress, temperature, and the activation energy of the controlling mechanism. This distinction is critical because metals exhibit well-defined stages of creep—primary (decelerating rate), secondary (steady rate), and tertiary (accelerating rate leading to failure)—driven by their microstructural dynamics, while polymers respond differently across their amorphous or semi-crystalline regions. Consequently, the mathematical frameworks for modeling creep in metals focus on crystalline deformation physics, whereas polymer creep models emphasize molecular chain dynamics and viscoelastic effects. These differences highlight the necessity for distinct approaches in understanding and predicting creep behavior in metals and polymers,

as their mechanical responses are fundamentally tied to their unique microstructural characteristics [103] [104].

Metals, characterized by a crystalline structure composed of closely packed atoms arranged in regular patterns, exhibit a significant resistance to deformation at low temperatures compared to polymers due to the high energy barriers required for atomic diffusion and dislocation movement, the two primary mechanisms responsible for creep. Scenarios involving intense heat and mechanical stress, such as those found in turbine blades [106], engine components, and other structural applications [107], often rely on materials like intermetallic compounds and refractory metals. These processes are thermally activated, meaning that sufficient thermal energy is necessary to overcome the energy barriers associated with atomic migration and dislocation climb or slip. For most metals, this thermal energy becomes significant only at temperatures above approximately 0.4 times their melting temperature T_m, referred to as the homologous temperature. At such elevated temperatures, the increased atomic vibrations enable the migration of atoms along grain boundaries (Coble creep) or through the lattice (Nabarro-Herring creep) and facilitate the movement of dislocations, which collectively drive the time-dependent deformation associated with creep. In stark contrast, polymers, which consist of long-chain molecules with relatively weak intermolecular forces, are much more susceptible to deformation at low temperatures because their molecular chains can slide or rearrange even when relatively little thermal energy is available. Unlike metals, polymers often exhibit viscoelastic behavior, where deformation arises from a combination of elastic stretching of the chains and viscous flow due to molecular slippage. The low energy requirements for these processes allow polymers to experience creep at temperatures much closer to ambient conditions, often significantly below their glass transition temperature T_g, depending on their molecular structure and composition. This behavior is further exacerbated in amorphous or semi-crystalline polymers, where the lack of a rigid crystalline lattice permits substantial molecular mobility under even modest thermal conditions. Thus, while metals require high temperatures to activate their creep mechanisms due to their atomic-scale rigidity and the need for thermal energy to facilitate atomic motion and dislocation activity, polymers, with their fundamentally different molecular structure and deformation mechanisms, can undergo creep at much lower temperatures, making the two materials exhibit distinctly different thermal thresholds for creep deformation [105]. Creep in metals is characterized by not displaying linear viscoelastic behavior, lacking recoverability, and only occurring at high temperatures [100].

6.3 Polymers

Viscoelastic creep data can be effectively represented in two primary graphical forms to reveal the material's behavior under sustained loading over time. The first method involves plotting the total strain against time for a specific temperature or a range of temperatures. This representation provides insights into how the material deforms under a constant load at different thermal conditions. At lower levels of applied stress, the material may exhibit linear viscoelastic behavior, where the strain increases proportionally with time, indicating a direct relationship between stress and strain within the elastic region. This behavior is characterized by a stress-independent compliance, where the creep strain follows Hooke's Law, and the creep rate remains constant with time. However, as the applied stress exceeds a critical value, the material's response becomes non-linear. Above this threshold, the creep rate accelerates disproportionately with time. This phenomenon is indicative of the transition from linear viscoelasticity to a regime where the material undergoes time-dependent, irreversible deformation at an increasingly rapid rate. The increased creep rate above the critical stress is attributed to enhanced mechanisms such as dislocation movement, grain boundary sliding, and atomic diffusion, which become more prominent under higher stress conditions, leading to accelerated microstructural changes and deformation. The second method for presenting viscoelastic creep involves plotting the creep modulus, defined as the ratio of the applied stress to the corresponding total strain at a given time [99]. This graphical presentation effectively captures how

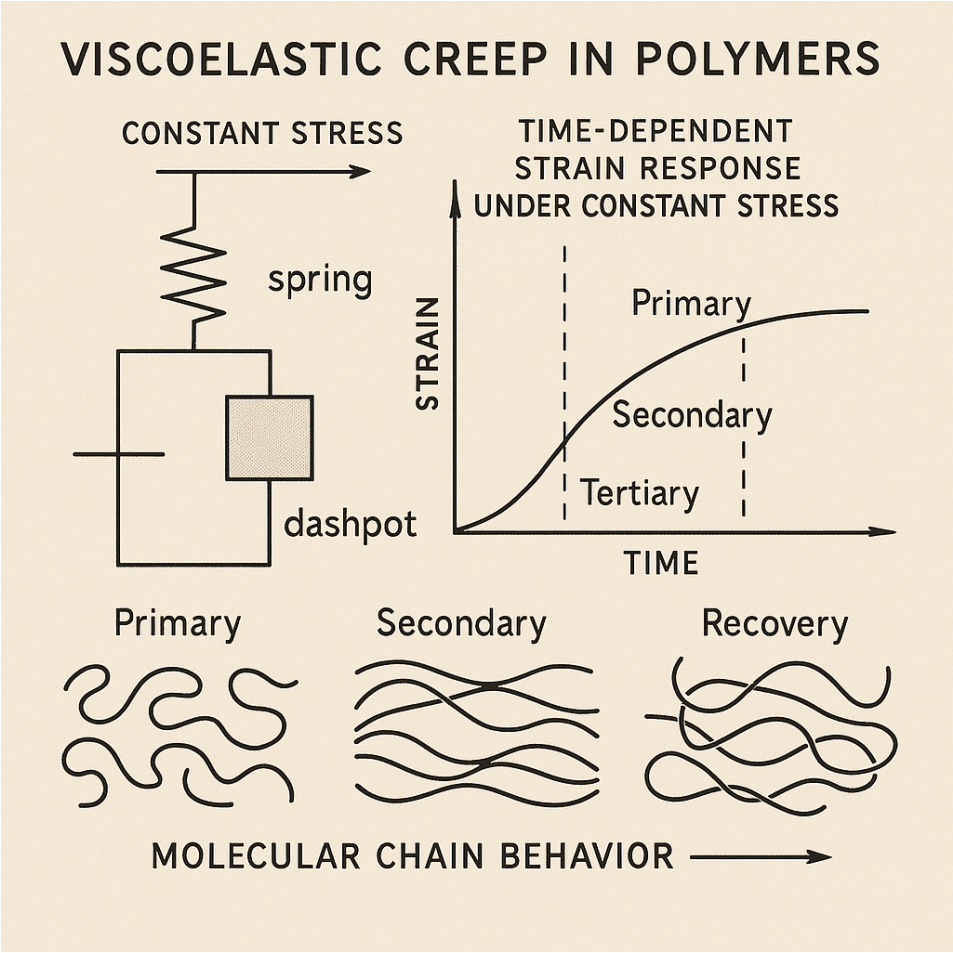

Figure 41: Viscoelastic Creep in Polymers

the material's stiffness evolves over time under sustained loading. The creep modulus provides a measure of the material's resistance to deformation at a particular stage of creep, indicating how much stress is required to maintain a unit of strain. As the material deforms under stress, the creep modulus typically decreases over time, reflecting the progressive softening of the material due to the accumulation of internal damage and microstructural changes. This decrease signifies the material's transition from a relatively elastic to a more viscous state, where the modulus diminishes due to dislocation movements, the growth of voids, and grain boundary sliding. By plotting the creep modulus against time, it becomes evident how the material's mechanical properties evolve during the creep process. These graphical representations are crucial for understanding and predicting the long-term performance of materials in high-temperature applications, such as turbine blades, where both the stress and temperature are sustained over long periods. They allow engineers and materials scientists to assess the material's creep resistance, determine suitable operating conditions, and design components that will maintain their structural integrity and performance over their intended service lifetimes.

The molecular weight of the polymer of interest plays a significant role in its creep behavior, influencing how the material deforms under sustained load over time. An increase in molecular weight tends to enhance the degree of entanglement between polymer chains, which strengthens the secondary bonding interactions within the polymer matrix. These interactions, such as van der Waals forces and hydrogen bonding, become more pronounced with higher molecular weight, thereby increasing the polymer's resistance to creep. As the molecular weight increases, the chains are less able to slide past one another easily under stress, leading to a more pronounced load-bearing capability. This added resistance is due to the greater inter-chain friction and the physical hindrance posed by the increased number of entanglements. Aromatic polymers, which contain additional stiffness due

to the presence of aromatic rings in their chemical structure, exhibit even greater creep resistance. The aromatic rings contribute rigidity to the polymer backbone, making it less flexible and more resistant to deformation under stress. The benzene ring's structure imparts additional stability to the polymer chains by restricting their mobility, thereby reducing the rate of creep. These polymers possess a higher thermal stability compared to their aliphatic counterparts, which is another critical factor in enhancing their creep resistance. The combination of increased molecular weight and the incorporation of aromatic rings significantly contributes to the overall creep resistance of the polymer. The increased thermal stability, due to the higher glass transition temperature (T_g) associated with aromatic polymers, means that they can maintain their mechanical properties over a broader temperature range. This stability allows these polymers to better withstand elevated temperatures without undergoing substantial plastic deformation or loss of mechanical properties. In applications where polymers are exposed to prolonged high-temperature conditions, such as in automotive under-the-hood components or aerospace parts, the increased molecular weight and the presence of aromatic structures are crucial for maintaining structural integrity. These features help ensure that the polymer maintains its shape and mechanical properties over time, reducing the rate of creep and enhancing the material's service life. Thus, understanding the impact of molecular weight and aromatic content on polymer creep behavior is essential for selecting appropriate materials for high-performance applications where long-term thermal and mechanical stability is critical [21].

6.4 Glass

The phenomenon of creep in glass, while valid under specific conditions, is frequently misunderstood and misrepresented in popular discourse, particularly in the context of aging glass windows. A

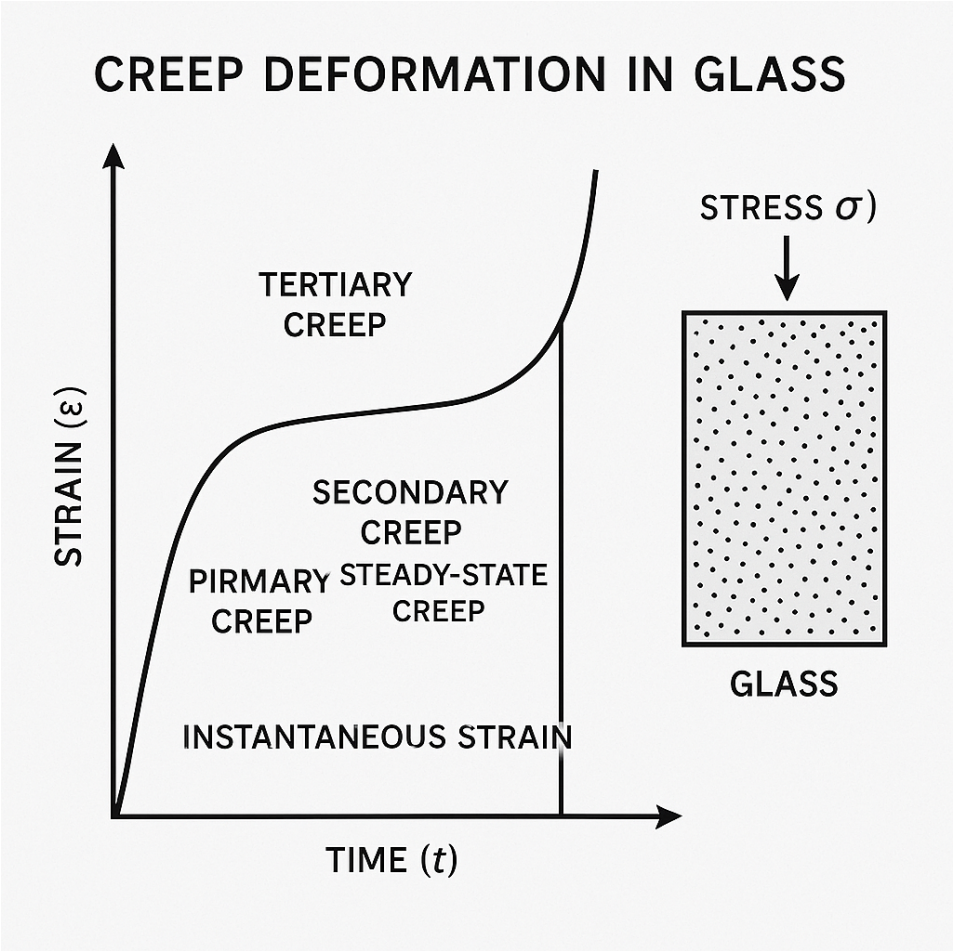

Figure 42: Creep Deformation in Glass

common misconception is that the sagging or apparent deformation observed in old glass windows is due to the slow, time-dependent flow of glass under its own weight, a process often mistakenly attributed to creep. However, this claim does not align with the fundamental thermomechanical properties of glass or the environmental conditions in which these windows exist. Creep in glass, like in other materials, is a time-dependent deformation that occurs when the material is subjected to a sustained stress, provided that it is also maintained at a temperature sufficiently high to enable atomic or molecular mobility. In the case of glass, the temperature at which significant molecular mobility can occur is the glass transition temperature, typically around 500°C (932°F) or higher, depending on the specific chemical composition of the glass. Below this temperature, glass exists in an amorphous, solid-like state with negligible molecular rearrangement, rendering measurable creep virtually impossible at ambient room temperatures, even over extended periods of time. The suggestion that ancient glass windows sag due to creep at room temperature is therefore fundamentally incorrect from a materials science perspective. Instead, the observable sagging in such windows is more plausibly attributed to the methods employed in their historical manufacture. One prominent technique used during earlier centuries, particularly in the production of crown glass, involved spinning molten glass into a disc. This process inherently produced glass panes with varying thicknesses, as centrifugal forces caused the molten material to distribute unevenly across the disc. When such panes were installed in windows, the thicker portions were often oriented at the bottom, either intentionally by craftsmen to provide greater stability or as a natural consequence of handling and installation practices. Over time, this uneven thickness gave rise to the misconception that the glass had flowed downward due to its own weight. While glass does exhibit genuine creep under conditions of sustained stress at high temperatures—such as in industrial processes like glassblowing or when exposed to extreme environmental conditions—these scenarios bear no resemblance to the ambient conditions surrounding aging windows [110] [111]. The perpetuation of this myth about glass creep highlights the importance of distinguishing between observable phenomena and their scientifically accurate explanations. Moreover, it underscores the necessity for critical analysis and accurate communication of material behavior, particularly when discussing the intersection of historical artifacts and materials science. By recognizing that the sagging of old glass windows is a vestige of historical manufacturing techniques rather than a manifestation of creep, we gain a deeper appreciation for the interplay between technology, craftsmanship, and the physical properties of materials. This understanding also serves as a valuable reminder of the need to contextualize scientific principles within the specific conditions under which they apply, ensuring that misconceptions are addressed with clarity and rigor.

6.5 Concrete

Creep in concrete refers to the time-dependent deformation that occurs when a sustained load is applied to the material. It is a significant and complex phenomenon influenced by the material's composition, the ambient environmental conditions, and the properties of the concrete itself. Some very good references for Creep in Concrete are Bazant and Osman 1976 [122], Yu et. al. 2012 [123], Neville 1971 [120] and 1964 [121], Ross 1958 [124], Bissonnette et.al. 2007 [125] and Ranaivomanana 2013 [126]. When a concrete structure, such as a beam or slab, is subjected to a sustained load, the individual cementitious particles, including the hydration products and the aggregate particles, experience gradual deformation over time. This deformation is a result of the internal stresses developed within the concrete matrix as water continues to diffuse through the structure, causing redistribution of internal forces. Creep in concrete is primarily governed by the diffusion and movement of water within the pore structure of the material. As water is absorbed by the concrete, it causes the cement paste to swell, which results in a gradual increase in the volume of the concrete and the deformation of the entire structure. The internal microstructure of concrete is composed of a network of interconnected pores and capillaries, which provide pathways for water to migrate. As water moves within these pores, it increases the internal pressure, leading to creep deformation. The rate of water movement is influenced by factors such as temperature, relative humidity, and

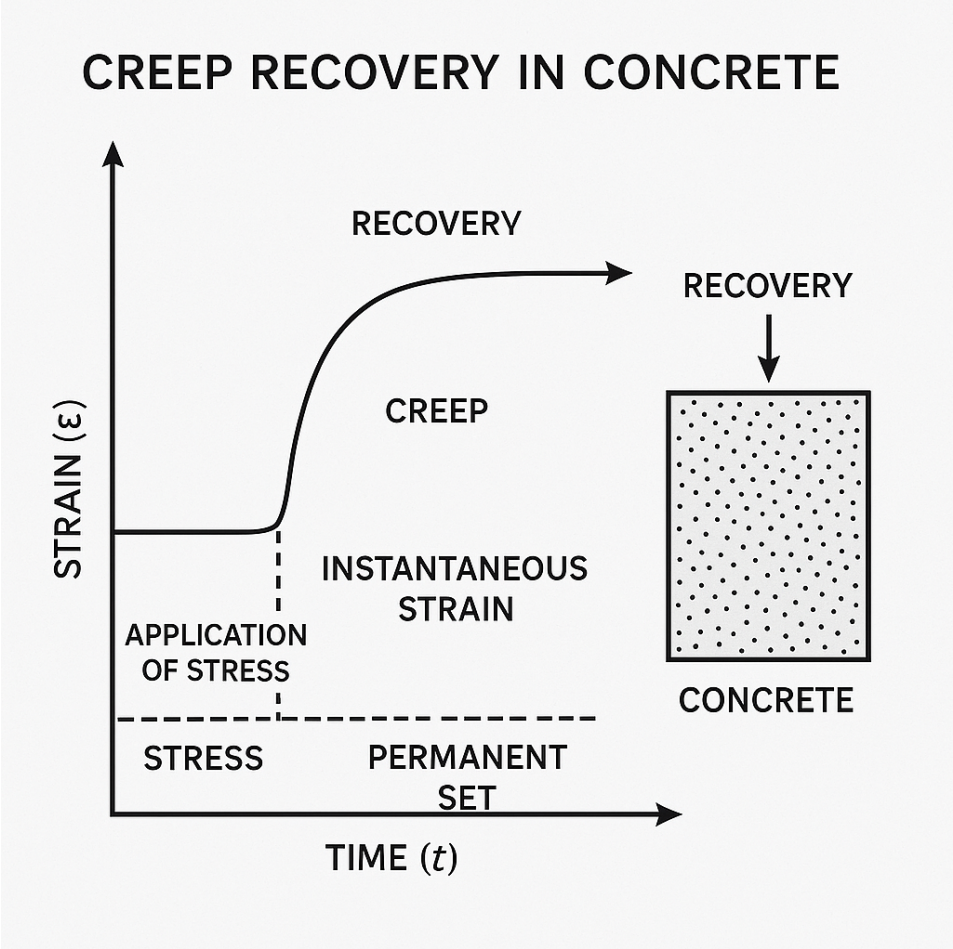

Figure 43: Creep Recovery in Concrete

the initial water-cement ratio used in the mix. Higher temperatures and lower relative humidity accelerate the rate of water diffusion, leading to faster creep rates. The chemical changes during hydration also contribute to creep; the ongoing chemical reactions between water and cementitious materials, such as the transformation of calcium silicate hydrates (C-S-H) into more compact crystalline forms, result in a continuous densification of the concrete matrix. This densification increases the stiffness of the concrete but also alters its internal stress distribution, contributing to creep. Over time, the concrete undergoes a process of "creep recovery" where some deformation is partially reversible when the load is removed. However, this recovery is not complete; the process leaves the concrete slightly deformed relative to its original shape due to the permanent rearrangement of particles within the cement paste and the continuing movement of water. The magnitude of creep is also influenced by the age of the concrete at the time of loading, the stress level applied, and the mix proportions of the concrete. For younger concrete, the creep deformation can be more significant because the hydration process and water movement are still ongoing. As concrete ages, its creep rate generally decreases, but it may never fully stop. The long-term effects of creep can lead to deflections and cracking in concrete structures, which are critical considerations in the design and analysis of concrete structures, especially for those subjected to sustained loads such as bridges, dams, and tall buildings. Understanding and accurately predicting creep behavior is essential for engineers to ensure that concrete structures will perform adequately over their intended service lives without excessive deformation or loss of strength. Effective mitigation strategies include using lower water-cement ratios, incorporating pozzolans to enhance the binding properties of the cement, and using higher-quality aggregates that influence the internal structure of the concrete to reduce its permeability and thus its susceptibility to creep.

6.6 Wood

Wood is classified as an orthotropic material due to its distinct mechanical properties that vary in three mutually perpendicular directions. Orthotropic materials exhibit different behavior in each

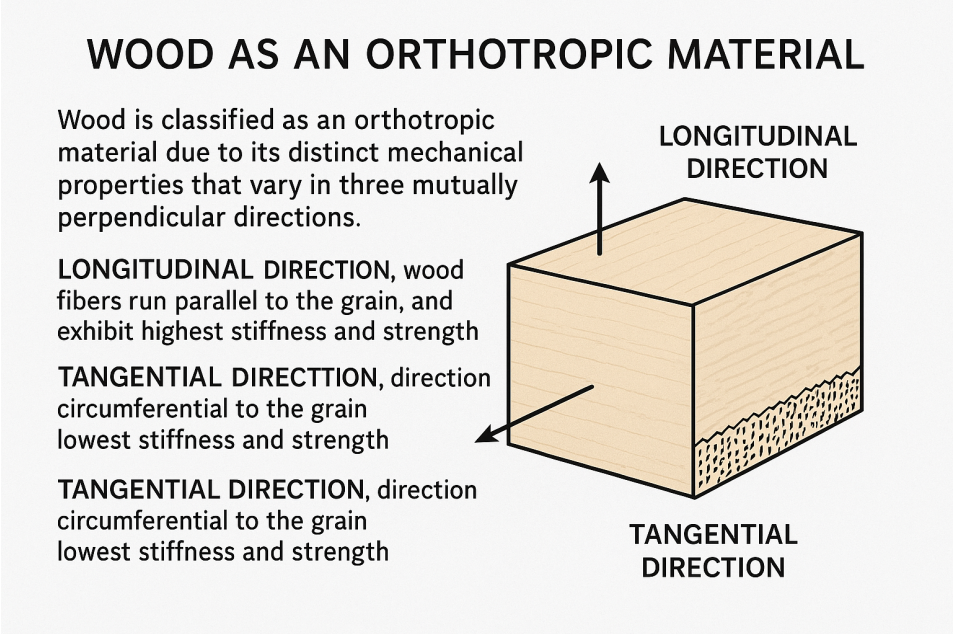

Figure 44: Wood as an Orthotropic Material

of these directions because of their complex, anisotropic structure. The three primary directions in which mechanical properties are evaluated in wood are the longitudinal, radial, and tangential directions. In the longitudinal direction, wood fibers run parallel to the grain, and its mechanical properties are primarily influenced by the alignment of cellulose fibers. This direction exhibits the highest stiffness and strength, as the fibers provide significant resistance to deformation. However, in the radial direction, which is perpendicular to the grain, the mechanical properties are affected by the arrangement of cells and the presence of the porous structure of the wood. Here, the properties are less pronounced compared to the longitudinal direction, but there is still considerable strength and stiffness due to the cellular structure. The tangential direction, which is circumferential to the grain, displays the lowest stiffness and strength among the three directions because it is subjected to the widest range of cell orientations and densities. It tends to show a slightly higher creep compliance compared to the radial direction, which means that under a constant load, wood in the tangential direction will experience more deformation over time relative to its initial shape compared to wood in the radial direction [101] [102]. This higher creep compliance in the tangential direction can be attributed to the inherent differences in the arrangement of cells and the alignment of the cellulose fibers, which are more dispersed and oriented differently in this direction compared to the other two. Experiments demonstrate this behavior by subjecting wood samples to sustained loading conditions and measuring the resulting strain over time. The tangential direction consistently exhibits greater strain, indicating a higher susceptibility to creep under the same conditions, primarily due to the weaker cell-wall structure and the higher mobility of water within the wood matrix in this direction. As the load is applied, the wood's cell walls in the tangential direction are more prone to deformation due to the disorganized alignment of fibers and the weaker hydrogen bonding between them. This behavior is crucial for understanding the long-term performance of wood in applications where it is used in structural components, such as beams or framing in construction, where the load may be sustained over extended periods. The differences in creep behavior across these directions must be accounted for in the design and selection of wood for various applications to ensure that the structural integrity is maintained over the intended service life.

7 Larson-Miller Parameter and Monkman Grant Rule

The Larson-Miller Parameter (LMP) is a widely used empirical tool in high-temperature materials science, serving as a method for estimating the creep life of materials under prolonged thermal exposure. It integrates temperature and time into a single parameter that encapsulates the complex interplay between these two variables in influencing the material's creep behavior. The derivation of the LMP is fundamentally rooted in the Arrhenius equation, which describes the temperature dependence of the creep rate:

$$\dot{\varepsilon} = A \exp\left(-\frac{Q}{RT}\right) \tag{211}$$

where $\dot{\varepsilon}$ is the creep rate, A is the pre-exponential factor, Q is the activation energy for creep, R is the universal gas constant, and T is the absolute temperature. The LMP combines this temperature-dependent creep rate with the logarithm of time to form a single composite index, given by:

$$P = T_m + \log t \tag{212}$$

Here, T_m is the temperature in Kelvin and $\log t$ represents the logarithm of the time in hours. This formulation reflects the exponential sensitivity of creep rate to temperature, highlighting that the rate of creep increases significantly with higher temperatures due to more available atomic energy for dislocation movement and defect creation. The inclusion of the logarithmic term for time, $\log t$,

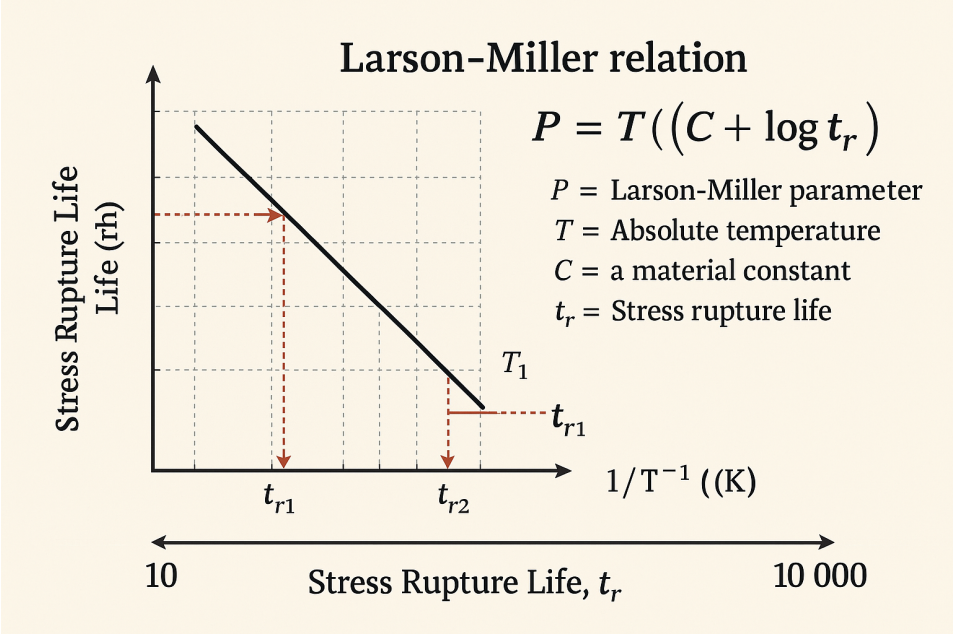

Figure 45: Larson Miller Relation

accounts for the accelerating effect of time on creep deformation, acknowledging that the likelihood of material failure shortens as the exposure time increases. By incorporating both variables into a single parameter, the LMP encapsulates the combined influence of time and temperature on the material's response to high-temperature stress, making it a powerful tool for engineers to predict the life of materials in applications like power plants, chemical processing, and aerospace components.

Empirical validation of the LMP has shown it to be an effective predictor of the time to failure across a broad range of metallic materials, including steels, superalloys, and aluminum alloys. This validation is based on extensive experimental data that aligns closely with the LMP, demonstrating its practical applicability in real-world engineering problems. The LMP's simplicity and empirical accuracy stem from its ability to condense the complex physical processes involved in creep deformation into a single, additive index. However, it should be noted that the LMP is an empirical tool

rather than a fundamental theoretical model. It does not explicitly account for all material-specific factors, such as microstructural changes, variations in impurity content, or differences in dislocation dynamics, which can influence the activation energy for creep. These factors can alter the material's response to high temperatures, potentially affecting the accuracy of LMP predictions in specific applications. Despite these limitations, the LMP remains a valuable tool due to its ability to provide quick and reliable estimates of the material's life under thermal exposure. Its empirical nature makes it a practical solution for managing the life and reliability of high-temperature materials, enabling engineers to optimize designs and predict the performance of components subjected to prolonged thermal stress efficiently.

The Monkman-Grant Rule is an empirical relationship that connects the fatigue life (N_f) of a material to the minimum stress (σ_{min}) it experiences during cyclic loading. This rule can be expressed as:

$$N_f \times \sigma_{min} = C \tag{213}$$

where C is a material-specific constant that embodies the material's intrinsic toughness and its resistance to fatigue damage. The derivation of this rule is deeply rooted in the mechanics of fatigue failure, which involves the progressive initiation and growth of microcracks within the material's microstructure under cyclic loading. The Monkman-Grant relationship is a manifestation of damage

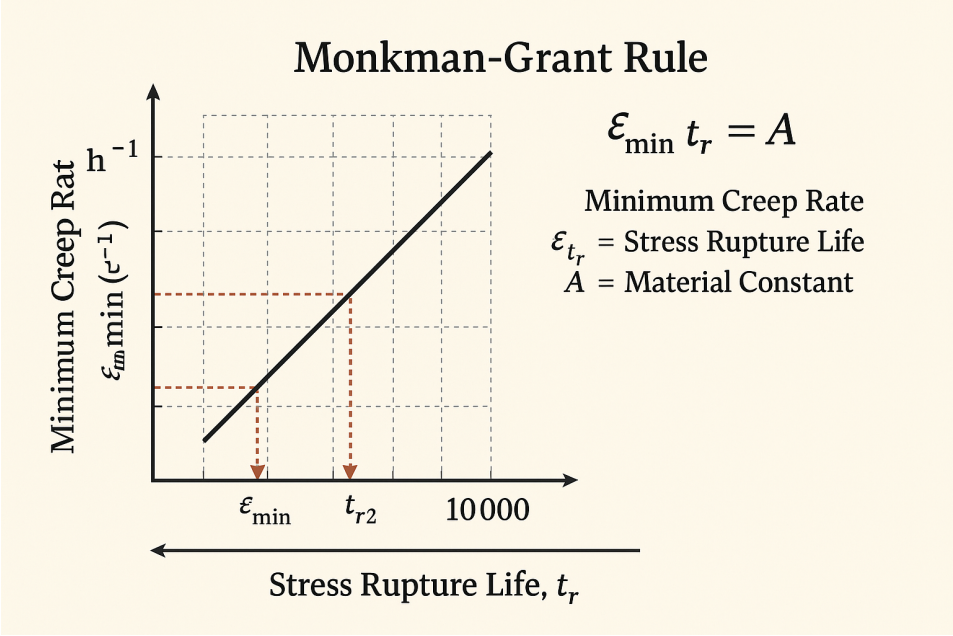

Figure 46: Monkman Grant Rule

accumulation over cycles of stress. As each stress cycle induces microcracks within the material, the cumulative fatigue damage is a function of the number of cycles and the stress amplitude. This relationship can be rigorously framed within the context of damage mechanics, where the damage variable D is defined as:

$$D = \frac{\Delta N}{N_f} \tag{214}$$

Here, ΔN is the number of cycles to failure, and N_f is the total number of cycles to failure at a given stress level. The rule indicates an inverse proportionality between fatigue life (N_f) and the minimum stress (σ_{min}), such that as σ_{min} decreases, N_f increases. Mathematically, this inverse relationship can be expressed as:

$$D \propto \sigma_{min}^{-1} \tag{215}$$

indicating that the damage or the fatigue life increases with decreasing stress amplitude. The material constant C is empirically derived from fatigue test data and reflects the material's resistance to

fatigue damage. For instance, a material with a higher C value indicates a greater ability to resist fatigue, often attributed to its finer grain structure and the distribution of precipitates that hinder the initiation and growth of microcracks. The inverse relationship of the Monkman-Grant Rule is further elucidated through the probabilistic approach such as Weibull distribution, commonly used in fatigue analysis. The Weibull distribution $F(N)$ for fatigue life can be expressed as:

$$F(N) = 1 - e^{-(N/\beta)^k} \tag{216}$$

where β is the characteristic life, and k is the shape parameter indicative of the material's resistance to fatigue damage. The material constant C correlates with these Weibull parameters, linking the material's fatigue properties directly to its microstructural integrity. The rigorous derivation of C involves statistical fitting of fatigue data across multiple stress levels, often requiring at least three distinct stress conditions to derive a reliable estimate of C. The linear relationship of $\log N_f$ versus $\log \sigma_{min}$ on a log-log plot provides a rigorous validation of the Monkman-Grant Rule. The material constant C is determined from the intercept of this linear fit, reflecting the material's consistent fatigue behavior under varying stress amplitudes. The theory behind the Monkman-Grant Rule also incorporates the concept of the endurance limit, which is the stress level below which a material can theoretically endure an infinite number of loading cycles without failure. The rule extends this endurance limit concept to low-stress ranges where the relationship $N_f \sigma_{min} = C$ still holds, but with a reduced C. The rigorous approach involves examining the damage rate under different stress conditions, leading to a deeper understanding of how the material's microstructure influences its fatigue life. The Monkman-Grant Rule serves as a powerful tool for engineers, providing a predictive model for fatigue life based on the material's microstructural properties. It not only informs decisions regarding material selection and component design but also enhances the understanding of how different microstructural features affect a material's resistance to cyclic loading. This rule integrates material science principles with empirical data, offering a scientifically and mathematically rigorous framework for assessing and predicting the fatigue behavior of materials, ultimately contributing to safer and more reliable engineering designs. The relationship encapsulated by the Monkman-Grant Rule can be further justified through advanced models such as linear elastic fracture mechanics, where the stress intensity factor K and the Paris law for fatigue crack growth can be employed. For instance, if we consider a crack of length a under cyclic loading, the fatigue crack growth rate $\frac{da}{dN}$ can be expressed using Paris' law:

$$\frac{da}{dN} = A(\Delta K)^m \tag{217}$$

where A and m are material constants, and ΔK is the range of stress intensity factor. Integrating this fatigue crack growth rate over the number of cycles, we obtain the Monkman-Grant relationship in a probabilistic sense, correlating N_f to σ_{min}. This approach illustrates the material's ability to absorb cyclic stress and the role of microstructural features in delaying crack initiation and propagation. The Monkman-Grant Rule, therefore, embodies a comprehensive framework linking material properties, damage mechanics, and probabilistic models, providing a mathematically rigorous basis for fatigue life prediction across a range of stress conditions.

8 Multi-Axial Creep and Damage Mechanics

8.1 Analysis of Multi-Axial Creep and Damage Mechanics

Multi-axial creep and damage mechanics delve into the complex interplay between time-dependent deformation (creep) and the progressive deterioration of material integrity (damage) under the influence of stress states that are multi-dimensional in nature. Creep deformation in materials occurs when a solid is subjected to sustained loads at elevated temperatures. Fundamentally, creep is driven by the thermally activated motion of defects, such as dislocations and vacancies, within the material's crystalline lattice. From a macroscopic continuum mechanics perspective, creep deformation is

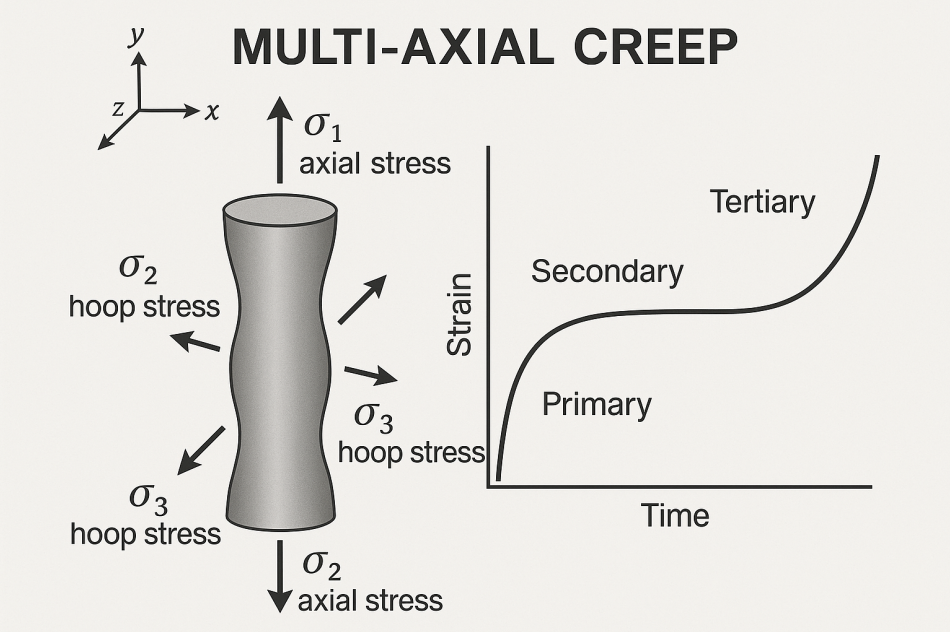

Figure 47: Multi Axial Creep

described by the evolution of the creep strain tensor $\boldsymbol{\epsilon}^c$, which quantifies the irreversible deformation occurring as a function of time. In multi-axial stress states, the stress tensor $\boldsymbol{\sigma}$ is decomposed into deviatoric ($\boldsymbol{s}$) and volumetric components to account for the directional nature of creep:

$$\boldsymbol{\sigma} = \boldsymbol{s} + \frac{1}{3}\,\mathrm{tr}(\boldsymbol{\sigma})\boldsymbol{I}, \tag{218}$$

where $\boldsymbol{s}$ is the deviatoric stress tensor and $\boldsymbol{I}$ is the second-order identity tensor. The equivalent stress σ_{eq}, often used as a scalar measure of stress intensity in isotropic materials, is rigorously defined as:

$$\sigma_{eq} = \sqrt{\frac{3}{2}\boldsymbol{s} : \boldsymbol{s}}, \tag{219}$$

where $\boldsymbol{s} : \boldsymbol{s}$ denotes the tensorial inner product. The equivalent stress forms the basis for creep constitutive models under multi-axial loading, ensuring invariance under coordinate transformations. The tensorial nature of creep deformation necessitates constitutive equations that respect material symmetries and thermodynamic principles. The creep strain rate tensor $\dot{\boldsymbol{\epsilon}}^c$ is generally expressed as a function of the deviatoric stress tensor $\boldsymbol{s}$ and the equivalent stress σ_{eq}. A typical tensorial formulation is:

$$\dot{\boldsymbol{\epsilon}}^c = \frac{3}{2}\frac{\dot{\epsilon}_s}{\sigma_{eq}}\boldsymbol{s}, \tag{220}$$

where $\dot{\epsilon}_s$ represents the scalar creep strain rate, often modeled using the **Norton-Bailey law**:

$$\dot{\epsilon}_s = A\sigma_{eq}^n \exp\left(-\frac{Q_c}{RT}\right). \tag{221}$$

This constitutive model, while phenomenological, is derived from considerations of dislocation motion and diffusion processes, providing a physical basis for the empirical parameters. The representation of material damage under multi-axial stress states requires the use of second- or higher-order tensors to capture the anisotropic nature of degradation. Damage is mathematically quantified using a scalar variable ω for isotropic damage or a second-order damage tensor $\boldsymbol{\Omega}$ for anisotropic damage. The effective stress concept, introduced by Kachanov and Lemaitre, modifies the nominal stress tensor $\boldsymbol{\sigma}$ to account for the loss of load-bearing capacity due to damage:

$$\tilde{\boldsymbol{\sigma}} = \boldsymbol{\sigma} : \boldsymbol{M}^{-1}, \quad \boldsymbol{M} = \boldsymbol{I} - \boldsymbol{\Omega}, \tag{222}$$

where $\boldsymbol{M}$ is the integrity tensor, describing the undamaged fraction of the material. For isotropic damage, this simplifies to:

$$\tilde{\sigma} = \frac{\sigma}{1-\omega}. \tag{223}$$

The evolution of damage is governed by thermodynamically consistent laws derived from the Helmholtz free energy ψ:

$$\psi = \psi(\boldsymbol{\epsilon}^e, \boldsymbol{\epsilon}^c, \boldsymbol{\Omega}, T). \tag{224}$$

The Clausius-Duhem inequality ensures that the rate of energy dissipation due to creep and damage remains non-negative:

$$\mathcal{D} = \boldsymbol{\sigma} : \dot{\boldsymbol{\epsilon}}^c - \frac{\partial \psi}{\partial \boldsymbol{\Omega}} : \dot{\boldsymbol{\Omega}} \geq 0. \tag{225}$$

Regarding the Coupled Creep-Damage Models, The interaction between creep and damage necessitates coupled models that simultaneously account for the evolution of $\boldsymbol{\epsilon}^c$ and $\boldsymbol{\Omega}$. These models integrate the creep strain rate and damage evolution equations:

$$\begin{aligned} \dot{\boldsymbol{\epsilon}}^c &= \mathcal{C}(\tilde{\boldsymbol{\sigma}}, T, \boldsymbol{\alpha}), \\ \dot{\boldsymbol{\Omega}} &= \mathcal{D}(\tilde{\boldsymbol{\sigma}}, \boldsymbol{\epsilon}^c, T, t), \end{aligned} \tag{226}$$

where $\mathcal{C}$ is the creep compliance tensor, and $\mathcal{D}$ is the damage evolution functional. For isotropic damage, $\mathcal{D}$ reduces to:

$$\dot{\omega} = B\sigma_{eq}^m (1-\omega)^n \exp\left(-\frac{Q_d}{RT}\right). \tag{227}$$

Regarding the Thermodynamics of Irreversible Processes, A rigorous thermodynamic framework for multi-axial creep and damage mechanics is established using the principles of **non-equilibrium thermodynamics**. The Helmholtz free energy ψ and the entropy production σ_s are expressed as:

$$\psi = \psi(\boldsymbol{\epsilon}^e, \boldsymbol{\Omega}, T), \quad \sigma_s = -\frac{\partial \psi}{\partial T}\dot{T} + \mathcal{D}. \tag{228}$$

The entropy production must satisfy the second law of thermodynamics:

$$\sigma_s \geq 0, \tag{229}$$

implying constraints on the constitutive relationships and evolution equations for $\boldsymbol{\epsilon}^c$ and $\boldsymbol{\Omega}$. Regarding the Variational Principles and Numerical Implementation, The governing equations of multi-axial creep and damage mechanics are formulated as a variational problem, minimizing the total potential energy Π:

$$\Pi = \int_\Omega \psi \, d\Omega - \int_\Omega \boldsymbol{f} \cdot \boldsymbol{u} \, d\Omega, \tag{230}$$

subject to compatibility and equilibrium constraints:

$$\nabla \cdot \boldsymbol{\sigma} + \boldsymbol{f} = 0, \quad \boldsymbol{\epsilon} = \nabla_s \boldsymbol{u}. \tag{231}$$

Numerical solutions are obtained using finite element methods (FEM), incorporating time-dependent creep and damage evolution. Temporal discretization uses backward Euler schemes for stability:

$$\boldsymbol{\epsilon}^{c,n+1} = \boldsymbol{\epsilon}^{c,n} + \Delta t \, \mathcal{C}(\tilde{\boldsymbol{\sigma}}^{n+1}, T^{n+1}). \tag{232}$$

Micromechanical models resolve the behavior of individual grains, dislocations, and voids, while statistical models describe damage as a probabilistic process. The void volume fraction ω is statistically defined as:

$$\omega = \int_0^\infty P(V,t) \, dV, \tag{233}$$

where $P(V,t)$ is the probability density function of void volume V over time t. Creep under complex loading conditions is analyzed using the von Mises equivalent stress:

$$\sigma_{\text{eq}} = \sqrt{\frac{3}{2}\boldsymbol{\sigma}' : \boldsymbol{\sigma}'}, \tag{234}$$

where $\boldsymbol{\sigma}'$ is the deviatoric stress tensor. The effective strain rate is then given by:

$$\dot{\varepsilon}_{\text{eq}} = A\sigma_{\text{eq}}^{n} \exp\left(-\frac{Q}{RT}\right). \tag{235}$$

The degradation of material properties during creep is modeled using a damage variable ω with the equation $\dot{\omega} = f(\sigma, \omega, t)$ with the creep strain rate modified as:

$$\dot{\varepsilon} = \frac{\sigma}{E(1-\omega)}, \tag{236}$$

where E is the elastic modulus.

8.2 Literature Review of Multi-Axial Creep and Damage Mechanics

The modern understanding of creep rupture under complex loading conditions traces its origins to the pioneering works of Kachanov (1958) [218] and Rabotnov (1969) [217], who proposed that material degradation could be represented by a scalar internal variable D that grows with time, thereby reducing the effective load-bearing area and accelerating creep towards rupture. In its simplest form, the effective stress relation reads

$$\sigma_{ij}^{\text{eff}} = \frac{\sigma_{ij}}{1-D}, \qquad \dot{D} = B\sigma^{n}(1-D)^{m},$$

where B, n, m are material constants calibrated from creep tests. This formulation underlies the Kachanov–Rabotnov model, still widely used in engineering practice for life prediction (Kachanov, 1958 [218]; Rabotnov, 1969 [217]).

The consolidation of continuum damage mechanics (CDM) as a formal thermodynamically consistent theory was carried out extensively by Lemaitre (1985) [220] and Chaboche (1981) [221]. In their treatments, the Helmholtz free energy is augmented by a damage variable, leading to consistent stress–strain–damage coupling and evolution equations of the form

$$Y = \frac{1}{2}\sigma : \frac{\partial \mathbf{C}^{-1}}{\partial D} : \sigma, \qquad \dot{D} = f(Y),$$

where Y is the energy release rate and $\mathbf{C}$ the damaged compliance tensor. These rigorous frameworks permit generalization to multiaxial states by using either isotropic scalar damage or anisotropic tensorial damage variables (Lemaitre, 1985 [220]; Chaboche, 1981 [221]). The problem of choosing a representative stress in multiaxial creep is central. While uniaxial creep is well captured by power-law relations of the form

$$\dot{\varepsilon} = A\sigma^{n} \exp\left(-\frac{Q}{RT}\right),$$

the multiaxial case requires a definition of σ_{rep}. Commonly, the von Mises equivalent stress

$$\sigma_{\text{eq}} = \sqrt{\tfrac{3}{2} s_{ij} s_{ij}}$$

is employed, but experimental evidence shows that hydrostatic stress strongly influences cavitation-controlled creep rupture. Thus combined measures such as

$$\sigma_{\text{rep}} = \sigma_{\text{eq}} + \alpha\sigma_{m},$$

where $\sigma_m = \frac{1}{3}\mathrm{tr}(\sigma_{ij})$ and α is a fitting parameter, have been proposed to capture observed multiaxial rupture behavior (Hayhurst, 1972 [223]; Dyson, 1983 [219]).

Micromechanical approaches provide further insight by explicitly modeling void nucleation, growth, and coalescence. The Gurson (1977) [230] porous plasticity model introduced a yield function for a voided solid as

$$\Phi = \left(\frac{\sigma_{\mathrm{eq}}}{\sigma_Y}\right)^2 + 2f\cosh\left(\frac{3\sigma_m}{2\sigma_Y}\right) - (1+f^2) = 0,$$

where f is the void volume fraction. Extensions by Tvergaard and Needleman (1984) [224] modified this yield surface with fitting constants q_1, q_2, q_3 to better capture void interaction and coalescence. This GTN model, when coupled with creep laws, has been shown to predict tertiary creep dominated by intergranular cavitation (Needleman, 1987 [225]). The transition from isotropic to anisotropic damage formulations became essential when experiments revealed directional growth of cavities under multiaxial stress. Anisotropic CDM models introduce a second-order damage tensor D_{ij}, modifying the compliance as

$$\mathbf{C}(D_{ij}) = \mathbf{C}_0 + \Delta\mathbf{C}(D_{ij}),$$

so that stiffness degradation reflects the orientation of damage (Murakami, 1988 [226]; Hayhurst, 1990 [238]). These models allow for more accurate prediction of crack initiation and growth in welded components where damage is strongly orientation dependent. Coupling of creep and fatigue within CDM frameworks is crucial for real service conditions. A typical approach superposes fatigue damage D_f and creep damage D_c into a cumulative variable

$$D = D_c + D_f, \qquad D_c = \int \dot{D}_c\, dt, \quad D_f = \sum \Delta D_f,$$

with interaction rules calibrated from combined creep–fatigue tests (Skelton, 1987 [231]; Chaboche, 1988 [222]). More sophisticated formulations introduce coupled evolution equations that allow interaction terms between cyclic plastic strain and creep strain rate, reflecting the observed synergy in crack growth rates (Miller, 1992 [232]). Finite element implementations of multiaxial creep-damage models are well established, often relying on implicit time-integration and regularization to avoid mesh dependence due to strain localization. For instance, gradient-enhanced damage models introduce higher-order terms of the form

$$\dot{D} = f(Y, \nabla D),$$

which provides a length scale and removes pathological mesh sensitivity (de Borst, 1996 [233]). Validation studies on biaxially loaded tubes, notched bars, and welded P91 steel joints confirm both the strengths and limitations of current CDM models (Ainsworth, 2003 [234]; Hyde, 2010 [235]).

Probabilistic extensions have been introduced to account for the large scatter observed in creep rupture data. By considering parameters in the KR model as random variables, one may define a stochastic damage evolution

$$\dot{D} = B(\omega)\sigma^{n(\omega)}(1-D)^{m(\omega)},$$

with ω denoting a probabilistic state. Reliability-based methods then predict a rupture time distribution rather than a deterministic value (Gonzalez, 2004 [236]; Rao, 2011 [237]). Such approaches are increasingly important for safety-critical components in power plants and aerospace engines. Recent developments emphasize multiscale integration, where void kinetics at the microscale are homogenized to macroscale constitutive behavior using computational homogenization. For example, crystal plasticity combined with grain-boundary cavitation models produces effective anisotropic creep-damage constitutive laws (Shenoy, 2010 [227]; Cailletaud, 2012 [228]). These models bridge the gap between mechanistic microstructural damage and macroscopic life prediction, offering improved transferability across stress states. Ghosh (2025) [175] developed a probabilistic framework to model fatigue damage evolution in reactor steels. Its contribution aligns with damage mechanics by quantifying time-dependent material degradation under complex loading, thereby enhancing

predictive reliability assessments. Ghosh (2025) [195] developed a rigorous mathematical framework for deep learning, grounding neural networks in functional analysis and variational methods. Such formulations are valuable for extending data-driven modeling in multi-axial creep and damage mechanics. They enable the construction of physics-informed surrogates to capture complex degradation under coupled loading. Sousa and Ghosh (2025) [38] presented a novel generalization of classical functional equations in analytic number theory. The underlying mathematical structures, particularly integral representations and symmetry relations, suggest powerful analogies for modeling path-dependent processes. Such abstractions can inspire new formulations in multi-axial creep and damage mechanics, where complex stress–strain evolutions require advanced functional frameworks. Maji et. al. (2023) [166] established the statistical equivalence of nonequilibrium ensembles under conserved quantities such as energy and enstrophy. The framework illustrates how global invariants can reproduce irreversible dynamics within reversible formulations. Such ideas can inspire constitutive modeling in multi-axial creep and damage mechanics, where enforcing macroscopic constraints enhances predictive fidelity.

Despite progress, major challenges remain. Representative stress definitions remain contested, parameter calibration under true multiaxial conditions is hampered by limited experimental data, and robust nonlocal formulations are needed to regularize softening responses. Moreover, coupling of creep with environmental degradation such as oxidation or corrosion is only beginning to be systematically incorporated (Pettinari-Sturmel, 2016 [229]). Future research must focus on carefully designed multiaxial experiments, integration of micromechanics with CDM, and probabilistic frameworks that unify deterministic life prediction with uncertainty quantification.

9 Creep Testing

Creep testing is a sophisticated experimental technique designed to investigate the time-dependent deformation and failure behavior of materials when subjected to a constant stress or load at elevated temperatures. This testing method is essential for understanding how materials behave over long periods under high-temperature conditions, which is critical for components used in power generation, aerospace, and nuclear industries. The theory behind creep testing involves intricate interactions between atomic diffusion, dislocation movement, and microstructural evolution, all of which dictate the material's response to sustained loading over time. These processes are driven by the thermal energy available, which allows atoms to migrate and rearrange themselves, and by the stress applied to the material, which accelerates the movement of dislocations and other defects within the microstructure.

The primary stages of creep include the initial primary stage where the creep rate decreases due to work hardening effects; the secondary, or steady-state, stage characterized by a constant creep rate that reflects a balance between recovery processes (such as dislocation climb and annihilation) and ongoing deformation; and the tertiary stage, which is marked by an accelerating creep rate leading towards eventual rupture due to microstructural instability. The steady-state creep rate, $\dot{\varepsilon}_c$, can be empirically described by the Norton-Bailey power law:

$$\dot{\varepsilon}_c = A\sigma^n \tag{237}$$

where A is a material constant, σ is the applied stress, and n is the stress exponent. The stress exponent n provides insight into the dominant creep mechanism. For diffusional creep, n tends to be higher, around 3 to 10, indicating a strong dependency on stress. For dislocation creep, n is lower, typically ranging from 1 to 4, reflecting a less direct relationship with applied stress. This law encapsulates the material's resistance to creep, highlighting how the deformation rate depends on the applied stress and the microstructural features of the material such as grain size, precipitate distribution, and phase transformations. Mathematically, the creep compliance J, which is the

inverse of the material's stiffness under constant stress, is defined as:

$$J = \frac{\varepsilon_c}{\sigma} \tag{238}$$

where ε_c is the creep strain and σ is the applied stress. This compliance is temperature-sensitive, with higher temperatures accelerating atomic diffusion and dislocation activity. The relationship between J and temperature can be modeled using the Arrhenius equation:

$$J = A_T \exp\left(\frac{-Q}{RT}\right) \tag{239}$$

Here, A_T is a temperature-dependent material constant, R is the universal gas constant, T is the absolute temperature, and Q is the activation energy for creep. The activation energy Q is indicative of the energy barriers that atoms must overcome to move, influenced by the material's microstructure, such as the presence of precipitates and the size of grains. This relationship highlights the profound impact of temperature on creep behavior, where elevated temperatures enhance atomic mobility, facilitating dislocation movement and phase changes within the material.

Different creep mechanisms can be quantitatively characterized using models that link the material's deformation rate to stress and temperature. For diffusional creep, the strain rate, $\dot{\varepsilon}_{diff}$, can be expressed as:

$$\dot{\varepsilon}_{diff} = A\sigma^2 \exp\left(\frac{-Q}{RT}\right) \tag{240}$$

where A is a material-specific constant, σ is the applied stress, Q is the activation energy for diffusion, and R is the gas constant. This equation demonstrates how stress and temperature influence the rate of diffusion-controlled creep, where the deformation occurs predominantly through the movement of atoms along grain boundaries. In contrast, dislocation creep is described by:

$$\dot{\varepsilon}_{disloc} = A_d\sigma^2 \exp\left(\frac{-Q_d}{RT}\right) \tag{241}$$

where A_d is a material constant specific to dislocation creep and Q_d is the activation energy for dislocation motion. These models indicate how different deformation mechanisms dominate depending on the material's temperature and stress conditions. For instance, at lower temperatures, dislocation creep may dominate, whereas at higher temperatures, diffusional creep becomes more significant due to enhanced atomic mobility. Creep rupture testing involves holding a material under a constant load until failure occurs, providing critical data on the material's resistance to creep deformation over time. The Larson-Miller parameter helps predict the service life of materials under high-temperature conditions:

$$LMP = T \log t_r + C \tag{242}$$

where T is the absolute temperature, t_r is the rupture time, and C is a material-specific constant. This parameter enables engineers to extrapolate creep rupture data across different temperatures, thus informing the design and selection of materials for high-temperature applications. The relationship illustrates the cumulative effect of stress and temperature on the material's service life, allowing for predictive modeling of material performance under real-world conditions.

Understanding these complex mechanisms through creep testing allows materials scientists to design and select materials with enhanced resistance to high-temperature deformation, improving their durability and reliability in demanding applications. The sophisticated mathematical models and empirical equations used in creep testing provide crucial insights into the underlying processes that control a material's long-term behavior, aiding in the development of new materials and the optimization of existing ones for high-performance applications. These equations and models are fundamental tools for advancing materials science, enabling the prediction of material behavior and the informed design of structural components that must endure extreme environmental conditions over long periods.

10 Environmental Effects on Creep: Oxidation and Irradiation

Creep, the time-dependent plastic deformation of materials under constant stress, is a highly complex phenomenon influenced by intrinsic material properties and external environmental factors such as oxidation and irradiation. These environmental effects not only alter the microstructural and chem-

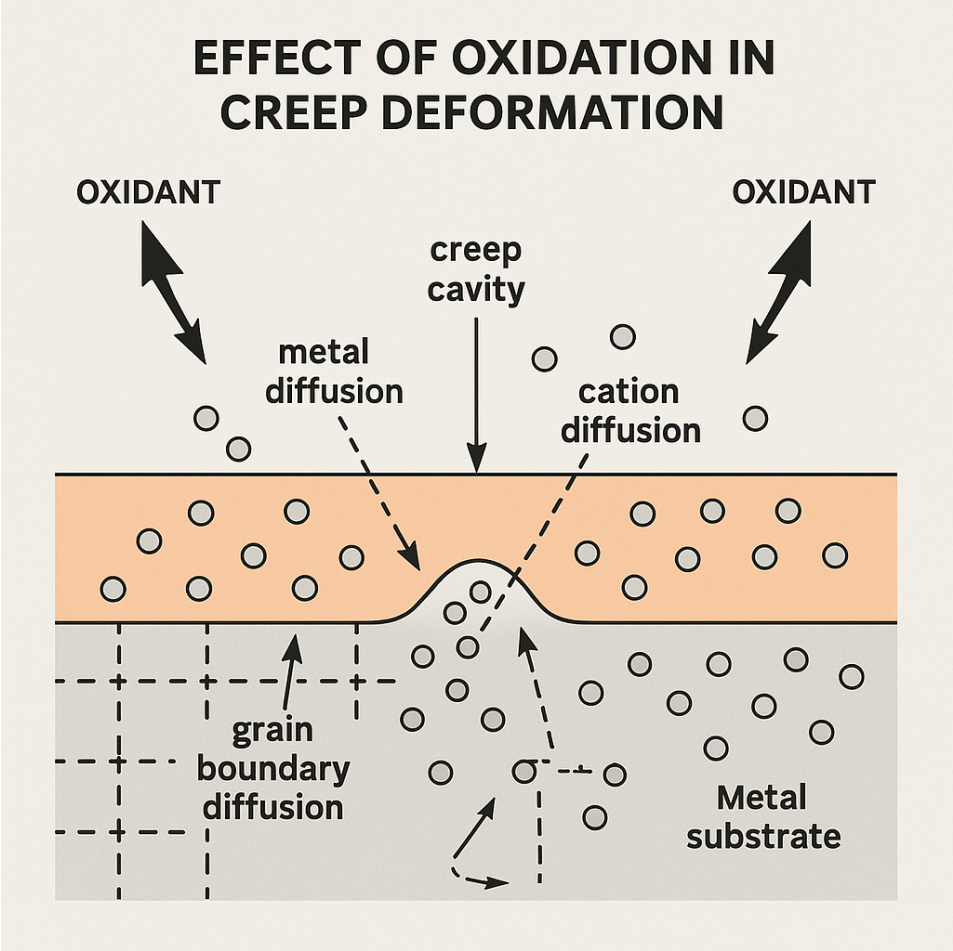

Figure 48: Effect of Oxidation in Creep Deformation

ical characteristics of the material but also significantly affect the underlying mechanisms driving creep deformation, often accelerating the damage progression. To rigorously understand these effects, it is necessary to delve into the thermodynamics, kinetics, and physical processes governing oxidation and irradiation and their interaction with the creep process. The effect of oxidation on Creep is very rigorously described by Neu and Sehitoglu [19] [20]. Oxidation occurs when a material, typically a metal, reacts with oxygen in the environment to form a stable oxide layer on its surface. This is a thermodynamically driven process that minimizes the free energy of the system. The formation and growth of oxide layers are controlled by diffusion processes, which are described by Fick's laws. The parabolic growth law,

$$\frac{dx}{dt} \propto \frac{1}{x} \quad \text{and} \quad x^2 \propto kt \tag{243}$$

where x is the oxide thickness, t is time, and k is the parabolic rate constant, emerges from the fact that oxide growth is diffusion-limited. At high temperatures, the activation energy for diffusion, expressed by

$$D = D_0 e^{-\frac{Q}{RT}} \tag{244}$$

where Q is the activation energy for diffusion, R is the universal gas constant, and T is the absolute temperature, governs the rate at which oxygen or metal ions diffuse through the oxide layer. As the

oxide layer grows, it exerts significant mechanical and chemical effects on the substrate material. Differential thermal expansion between the oxide scale and the underlying material leads to residual stresses in the scale, which can cause cracking or spallation. This exposes fresh surfaces to further oxidation, creating a self-sustaining damage mechanism. The reduction in effective load-bearing cross-section due to oxidation is a critical factor in creep, as described by

$$\sigma_{\text{eff}} = \frac{\sigma_{\text{applied}}}{(1 - \frac{\Delta A}{A})} \tag{245}$$

where ΔA is the area lost to oxidation. Subsurface oxidation, wherein oxygen diffuses into the material, further compromises the microstructure by forming brittle oxides and voids. These voids act as stress concentrators, enhancing grain boundary sliding and intergranular creep deformation. Oxidation also modifies the material's creep behavior through its interaction with diffusion-controlled mechanisms. Grain boundary diffusion is particularly significant, as it facilitates grain boundary

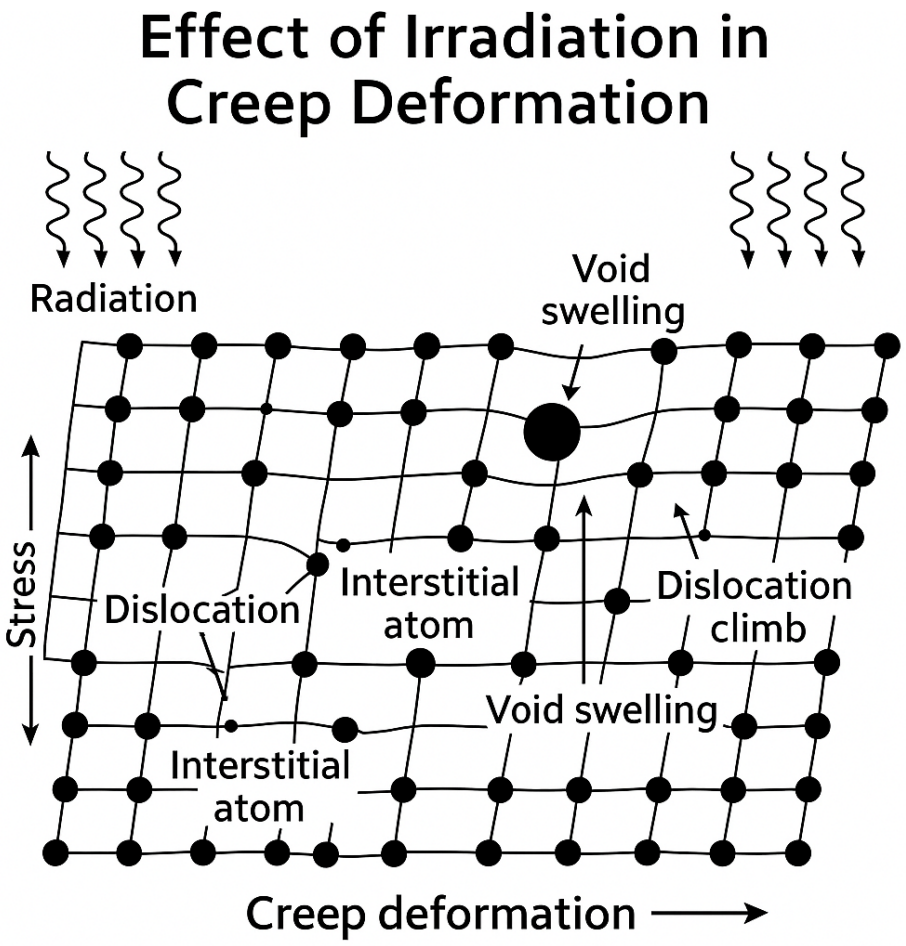

Figure 49: Effect of Irradiation in Creep Deformation

sliding, one of the dominant creep mechanisms at elevated temperatures. The oxide layer can serve as a pathway for vacancy diffusion, accelerating creep rates. This interaction between oxidation and creep is a classic example of environmentally assisted damage, where chemical and mechanical processes are tightly coupled. Irradiation, another critical environmental factor, involves the interaction of materials with high-energy particles such as neutrons, ions, or gamma rays. These particles impart sufficient energy to displace atoms from their lattice sites, creating vacancies and interstitials. These defects, collectively referred to as Frenkel pairs, significantly alter the diffusion properties of the material. Irradiation-enhanced diffusion is a key phenomenon, where defect mobility increases under irradiation, described by

$$D_{\text{irr}} = D_0 + \alpha\phi \tag{246}$$

where ϕ is the radiation flux, and α is a proportionality constant. This increased diffusivity facilitates dislocation climb and vacancy migration, both of which are critical to creep deformation. The introduction of point defects under irradiation also affects the dislocation dynamics. Dislocations, which are line defects in the crystal structure, are the primary carriers of plastic deformation. Under irradiation, dislocations become pinned by defects, altering their mobility. This interplay between pinning and unpinning modifies the strain hardening behavior of the material. At the same time, irradiation-induced swelling, caused by the aggregation of vacancies into voids, introduces internal stresses. These stresses interact with the applied stresses, further accelerating creep deformation.

Grain boundaries are particularly vulnerable to irradiation damage. The accumulation of radiation-induced defects at grain boundaries weakens their cohesion, facilitating grain boundary sliding. Additionally, voids formed at grain boundaries exacerbate stress concentrations, promoting localized deformation. Stress-assisted void growth, where voids grow preferentially in regions of high stress, is another significant mechanism by which irradiation accelerates creep. The nucleation and growth of these voids are governed by the competition between vacancy diffusion and stress relaxation mechanisms. The combined effects of oxidation and irradiation often result in synergistic damage mechanisms. For instance, irradiation can enhance oxidation rates by increasing the diffusivity of oxygen and metal ions through the oxide layer. Simultaneously, the weakening of grain boundaries by irradiation makes them more susceptible to the deleterious effects of oxidation. These combined effects lead to a rapid degradation of material properties, particularly in high-temperature and high-radiation environments, such as those found in nuclear reactors or aerospace applications. Mathematically, the total creep strain rate in such environments can be expressed as

$$\dot{\epsilon}_{\text{total}} = \dot{\epsilon}_{\text{thermal}} + \dot{\epsilon}_{\text{oxidation}} + \dot{\epsilon}_{\text{irradiation}} \tag{247}$$

where $\dot{\epsilon}_{\text{thermal}}$ is the thermally activated creep strain rate, and $\dot{\epsilon}_{\text{oxidation}}$ and $\dot{\epsilon}_{\text{irradiation}}$ represent the contributions from oxidation and irradiation, respectively. The Norton creep law,

$$\dot{\epsilon} = A\sigma^n e^{-\frac{Q_{\text{eff}}}{RT}} \tag{248}$$

is often modified to account for environmental effects, where

$$Q_{\text{eff}} = Q + Q_{\text{oxidation}} + Q_{\text{irradiation}} \tag{249}$$

includes the effective activation energy contributions from both oxidation and irradiation.

In conclusion, oxidation and irradiation fundamentally alter the microstructural and chemical characteristics of materials, accelerating creep deformation through a variety of coupled physical and chemical processes. Understanding these mechanisms requires a multidisciplinary approach that integrates thermodynamics, kinetics, and materials science. Such knowledge is essential for predicting and mitigating creep damage in high-temperature, high-radiation environments, thereby ensuring the reliability and longevity of critical components in applications such as nuclear reactors, power plants, and aerospace structures. This rigorous understanding is the foundation for developing advanced materials and protective strategies to counteract these environmental effects.

11 Increasing Creep Resistance

Increasing creep resistance is a cornerstone of material design for applications demanding long-term mechanical stability at elevated temperatures and stresses. Increasing creep resistance has been done for steels for power plant applications [59], magnesium alloys [60], magnesium cast alloys [61], microstructurally stable nanocrystalline alloy [62], and polymer nanocomposites reinforced with multiwalled carbon nanotubes [63]. At its core, creep deformation arises from time-dependent plastic strain mechanisms driven by applied stresses and thermally activated atomic or microstructural

processes. The theory of creep behavior is framed by the mathematical description of steady-state strain rate, as encapsulated in the Norton-Bailey equation:

$$\epsilon_{ss} = A\sigma^n \exp\left(-\frac{Q}{RT}\right), \tag{250}$$

where A is a material-dependent constant, σ the applied stress, n the stress exponent, Q the activation energy associated with the controlling creep mechanism, R the gas constant, and T the absolute temperature. Increasing creep resistance involves reducing ϵ_{ss} by systematically tailoring the microstructural features and material properties to optimize Q, n, and other parameters. The strategies to achieve this are deeply rooted in the thermodynamics of deformation, dislocation dynamics, and diffusion theories, each contributing to a rigorous scientific framework for understanding and enhancing creep resistance. Creep deformation operates through several mechanisms, each dominating in specific stress-temperature regimes. At high stresses and moderate to high temperatures, dislocation creep predominates, with deformation mediated by the glide and climb of dislocations. Glide refers to the lateral motion of dislocations through the crystal lattice, driven by the applied stress, while climb involves the migration of dislocations out of their slip planes, facilitated by the diffusion of vacancies. The rate of dislocation creep depends on the dislocation density ρ, Burgers vector b, applied stress σ, and drag coefficient B, described mathematically by the Orowan relation:

$$\epsilon_d = \rho b v, \tag{251}$$

where v, the dislocation velocity, is proportional to the stress and inversely proportional to the drag force. Strengthening mechanisms that impede dislocation motion—such as solid solution strengthening, precipitation hardening, and work hardening—directly enhance creep resistance by increasing the effective drag on dislocations.

11.1 Solid solution strengthening

Solid solution strengthening leverages the introduction of solute atoms into the crystal lattice, which generate localized lattice distortions due to size mismatch and elastic modulus differences with the host atoms. These distortions create stress fields that interact with moving dislocations, effectively pinning them and increasing the energy required for glide or climb. The strength of this interaction depends on the solute concentration and the magnitude of the size and modulus mismatch, contributing to a higher creep activation energy Q. Solid solution strengthening enhances creep resistance by introducing **substitutional** or **interstitial solute atoms** into a host metal matrix, leading to **lattice distortion**, which in turn impedes **dislocation motion**—the primary mechanism of plastic deformation during creep. The strain field around these solute atoms interacts with the stress field of moving dislocations, thereby increasing the **critical resolved shear stress (CRSS)** needed for dislocation glide. Mathematically, for substitutional solutes, the increase in shear yield strength $\Delta\tau$ due to solid solution strengthening can be expressed as:

$$\Delta\tau \propto G \cdot \varepsilon^{3/2} \cdot c^{1/2} \tag{252}$$

where G = shear modulus of the solvent, $\varepsilon = \dfrac{r_s - r_m}{r_m}$ = size misfit parameter, r_s = solute atomic radius, r_m = matrix atomic radius, and c = atomic concentration of solute. Additionally, the **elastic modulus misfit** contributes to strengthening, leading to a combined effect expressed by Labusch's model:

$$\Delta\tau = AG\left(\varepsilon^2 + \delta^2\right)^{3/4} c^{1/2} \tag{253}$$

where $\delta = \dfrac{G_s - G_m}{G_m}$ is the modulus mismatch, and A is a dimensionless constant. These strain fields hinder dislocation climb and glide, crucial during the **secondary (steady-state) creep** phase, effectively raising the **activation energy** for creep deformation.

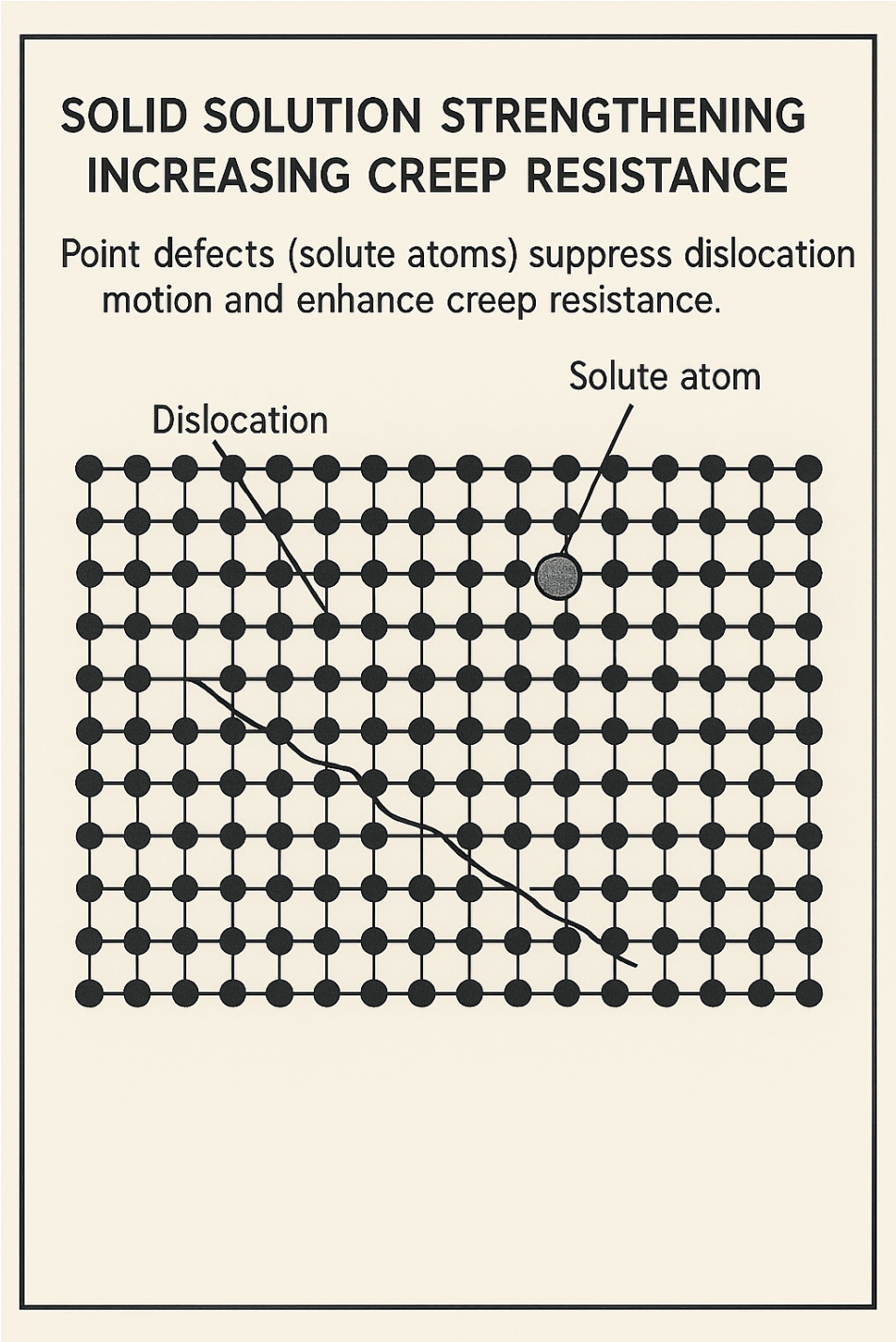

Figure 50: Solid solution strengthening in Creep Resistance

The **steady-state creep rate** $\dot{\varepsilon}_{ss}$ is governed by **dislocation motion**, particularly **climb**, which is thermally activated. Solid solution atoms impede this motion, and the net effect is a **reduction in creep rate**. The classical Norton's Law for steady-state creep is:

$$\dot{\varepsilon}_{ss} = A \cdot \sigma^n \cdot \exp\left(-\frac{Q_c}{RT}\right) \tag{254}$$

where $\dot{\varepsilon}_{ss}$ = steady-state creep rate, A = material constant, σ = applied stress, n = stress exponent (typically 3–8), Q_c = activation energy for creep, R = universal gas constant, and T = absolute temperature. In presence of solid solution strengthening, Q_c effectively increases due to the **solute drag** on dislocations, leading to a **lower** $\dot{\varepsilon}_{ss}$. The drag force F_{drag} experienced by a dislocation from

a solute atom is derived from the interaction energy U as:

$$F_{\text{drag}} = -\frac{dU}{dx} \approx -\frac{d}{dx}\left[\frac{Gb^3\varepsilon}{r}\right] \propto \frac{Gb^3\varepsilon}{r^2} \tag{255}$$

where b = Burgers vector and r = radial distance from solute atom. This interaction energy creates a **solute atmosphere** around dislocations, described by the **Cottrell atmosphere model**, and dislocations require higher energy to escape from this cloud:

$$E_{\text{binding}} = \frac{1}{2}Gb^3\varepsilon^2 \tag{256}$$

At high temperatures, where creep is active, solute atoms reduce **diffusional creep** (Nabarro-Herring and Coble creep) by decreasing **vacancy mobility** due to solute-vacancy binding energies, further resisting time-dependent plastic deformation.

From a fundamental standpoint, the effectiveness of solid solution strengthening in creep resistance can be directly quantified by considering its impact on **diffusivity** and **climb-controlled creep**. For example, in dislocation climb-limited creep, the creep rate is given by:

$$\dot{\varepsilon}_{climb} = \frac{AD_{\text{eff}}\sigma\Omega}{kTb^2} \tag{257}$$

where D_{eff} = effective diffusion coefficient in the presence of solutes, Ω = atomic volume, and k = Boltzmann constant. Solutes reduce D_{eff} by forming **solute-vacancy complexes**, so:

$$D_{\text{eff}} = D_0 \cdot \exp\left(-\frac{Q_{\text{eff}}}{kT}\right), \qquad Q_{\text{eff}} = Q_{\text{lattice}} + Q_{\text{binding}} \tag{258}$$

Moreover, the **threshold stress** σ_{th}, below which creep is negligible, increases with solute addition:

$$\sigma_{\text{eff}} = \sigma - \sigma_{\text{th}} \quad \Rightarrow \quad \dot{\varepsilon} = B(\sigma - \sigma_{\text{th}})^n \exp\left(-\frac{Q_c}{RT}\right) \tag{259}$$

Thus, the effective stress available for creep is reduced. In modern alloy design (e.g., Ni-base superalloys, ferritic steels), **optimized solid solution chemistry** ensures solute drag effects are maximized without compromising ductility. Alloys such as Ni-Cr, Fe-Mo, or Fe-Si show enhanced creep rupture life due to solid solution effects, often following the **Larson-Miller Parameter (LMP)** trend:

$$\text{LMP} = T(C + \log t_r) \qquad \text{where } C \approx 20 \tag{260}$$

An increase in LMP reflects the **delay in tertiary creep onset** and enhanced **creep strength**, both rooted in solid solution strengthening mechanisms that resist dislocation mobility and atomic diffusion, thus scientifically and mathematically increasing creep resistance.

11.2 Precipitation strengthening

11.2.1 Analysis of Precipitation strengthening

Precipitation hardening offers another pivotal approach. Fine, coherent precipitates, such as γ'-phase particles in nickel-based superalloys, act as obstacles to dislocation motion. The resistance provided by these precipitates depends on their size, distribution, and thermal stability, encapsulated by the equation:

$$\tau_{precipitate} = LGb \tag{261}$$

where G is the shear modulus, b is the Burgers vector, and L is the spacing between precipitates. Coherent precipitates distort the lattice, further impeding dislocations, while incoherent precipitates

block dislocations purely through their physical presence. However, at high temperatures, precipitate coarsening driven by Ostwald ripening can degrade their effectiveness, necessitating careful alloy design to maintain thermal stability. In diffusional creep, strain arises from the diffusion of atoms under stress gradients, either through the crystal lattice (Nabarro-Herring creep) or along grain boundaries (Coble creep). The strain rate for diffusional creep follows:

$$\epsilon_d \propto D\sigma d^2 \tag{262}$$

where D is the diffusion coefficient and d the grain size. The diffusion coefficient itself is temperature-dependent, given by:

$$D = D_0 \exp\left(-\frac{Q_d}{RT}\right) \tag{263}$$

with Q_d representing the activation energy for diffusion. Strategies to reduce diffusional creep include increasing Q_d through alloying with elements that impede atomic diffusion pathways or introducing barriers like grain boundary pinning agents. The Hall-Petch relationship, which correlates grain

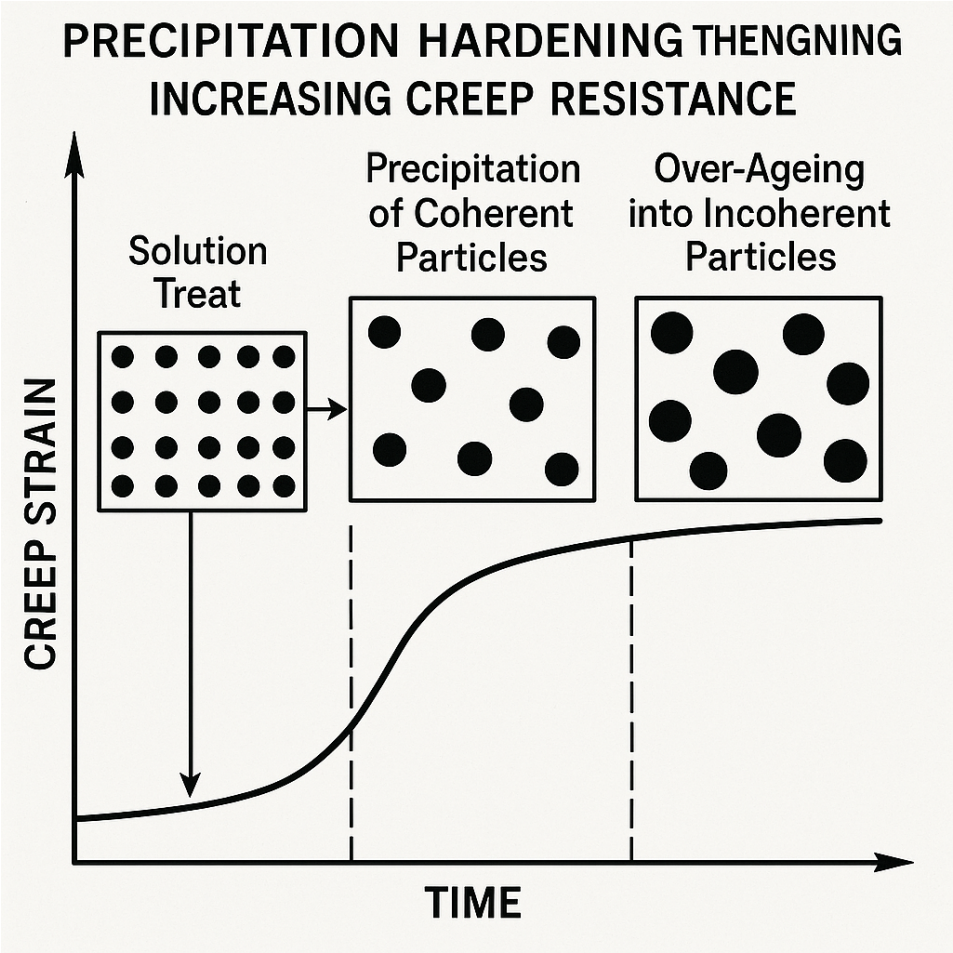

Figure 51: Precipitation hardening in increasing Creep Resistance

size with material strength, is particularly relevant here, as smaller grains enhance diffusional creep rates but suppress dislocation creep. Optimizing grain size is thus a delicate balance between these competing effects. Grain boundary sliding, another deformation mechanism, involves the relative motion of adjacent grains, facilitated by high mobility at grain boundaries. In materials like oxide dispersion-strengthened (ODS) alloys, nanoscale dispersoids such as yttria (Y_2O_3) are introduced to stabilize grain boundaries and impede sliding. These particles anchor the boundaries, enhancing resistance against both sliding and diffusional creep. From a thermodynamic perspective, the driving force for creep deformation is the reduction of the system's free energy, governed by the interplay of elastic strain energy, surface energy, and thermal vibrations. Alloy design strategies aim

to stabilize microstructures that minimize energy dissipation during deformation. High-temperature phases such as γ' in superalloys provide thermal stability due to their low diffusivity and resistance to coarsening. Computational thermodynamics tools, such as CALPHAD, predict phase stability and guide alloy compositions, while atomic-scale simulations like Density Functional Theory (DFT) reveal the fundamental interactions governing diffusion and dislocation behavior.

Precipitation strengthening, also known as **age hardening**, is a key mechanism by which the creep resistance of metallic alloys is enhanced, particularly in **nickel-based superalloys**, aluminum alloys, and steels. The underlying principle is to introduce a dense distribution of fine, coherent or semi-coherent precipitates into the matrix that **impede dislocation motion**, thereby raising the **creep rupture life** and **steady-state creep resistance**. Under steady-state creep, the total creep strain rate $\dot{\varepsilon}_{\text{creep}}$ is governed by the Orowan bowing mechanism, when dislocations bypass precipitates via looping:

$$\dot{\varepsilon}_{\text{creep}} = A \left(\frac{\sigma - \sigma_0}{G} \right)^n \exp\left(-\frac{Q_c}{RT} \right) \tag{264}$$

where A is a material-dependent constant, σ is the applied stress, σ_0 is the **threshold stress** (resistance due to precipitates), G is the shear modulus, n is the **stress exponent** (typically $4 < n < 8$), Q_c is the **activation energy for creep**, R is the gas constant, and T is absolute temperature. Precipitates such as γ' (Ni_3Al) in Ni-superalloys contribute a non-shearable barrier, increasing σ_0. The effective stress for dislocation motion is reduced, thereby reducing $\dot{\varepsilon}_{\text{creep}}$. This is crucial for long-term high-temperature applications like turbines and reactors.

When the precipitate size exceeds a critical radius r_c, dislocations cannot shear them and must **bypass via the Orowan looping mechanism**. The **Orowan stress** τ_{Orowan} is given by:

$$\tau_{\text{Orowan}} = \frac{Gb}{\lambda - 2r_p} \tag{265}$$

where G is the shear modulus, b is the Burgers vector magnitude, λ is the inter-precipitate spacing, and r_p is the precipitate radius. The corresponding **Orowan strain rate** contribution during creep is:

$$\dot{\varepsilon}_{\text{Orowan}} = \rho_m b v_d \tag{266}$$

where ρ_m is the mobile dislocation density and v_d is the dislocation velocity. The dislocation velocity is related to the effective stress by:

$$v_d = v_0 \exp\left(-\frac{\Delta F - \tau b L}{k_B T} \right) \tag{267}$$

where ΔF is the activation energy for dislocation motion, L is the dislocation segment length, and τ is the resolved shear stress. Precipitate shearing, by contrast, occurs if particles are small and coherent. The shearing stress τ_{shear} for ordered precipitates is given by:

$$\tau_{\text{shear}} = \frac{0.7\gamma'}{b} \tag{268}$$

where γ' is the antiphase boundary energy. Since coherent particles generate local strain fields, they also resist climb and glide by elastic interactions, increasing the creep threshold.

In creep-resistant alloys, precipitates also inhibit **dislocation climb**, particularly at high temperatures. Climb is thermally activated and governed by diffusion. The climb velocity v_{climb} in the presence of a precipitate barrier is:

$$v_{\text{climb}} = \frac{D_v \sigma b^2}{k_B T} \tag{269}$$

where D_v is the vacancy diffusion coefficient, σ is the stress acting normal to the glide plane, b is the Burgers vector. But precipitate-induced elastic fields create a **threshold climb stress** σ_{th}, below which dislocations cannot climb:

$$\sigma_{\text{eff}} = \sigma - \sigma_{\text{th}}, \quad \text{where} \quad \sigma_{\text{th}} \propto \frac{Gb}{L} \tag{270}$$

The **creep rate** then becomes **non-linear** and **strongly temperature dependent**:

$$\dot{\varepsilon}_{\text{creep}} \propto (\sigma - \sigma_{\text{th}})^n \exp\left(-\frac{Q}{RT}\right) \tag{271}$$

Thus, fine precipitates provide both **kinetic (diffusion/climb resistance)** and **mechanical (barrier to glide/bypass)** impediments to dislocation motion. Additionally, coarsening of precipitates over time (Ostwald ripening) reduces effectiveness, so **thermal stability** of precipitates is critical. The coarsening rate follows Lifshitz–Slyozov–Wagner (LSW) theory:

$$r(t)^3 - r_0^3 = Kt, \quad \text{where} \quad K \propto \frac{D_v \gamma V_m}{RTC} \tag{272}$$

where γ is the interfacial energy, V_m is the molar volume, C is the solubility of solute in the matrix. Alloys designed with **stable, fine, coherent precipitates** such as Ni_3(Al,Ti) in superalloys significantly delay creep deformation, enhancing both the **creep rupture life** and **steady-state creep resistance**, which are essential for high-performance structural components operating at elevated temperatures.

11.2.2 Literature Review of Precipitation strengthening

Kassner (2015) [1] remains a rigorous, mechanism-centered monograph that synthesizes diffusion, climb, and glide processes with constitutive creep laws, and it frames precipitate–dislocation interactions as rate controllers through cutting, Orowan bypass, and climb-assisted bypass at elevated temperature, offering quantitative links between microstructure and creep rate. Frost and Ashby (1982) [7] deformation-mechanism maps give a quantitative atlas for where precipitation hardening is effective in the stress–temperature space; their maps, combined with typical precipitate spacings and strengths, let one predict when a particle field will shift the operative creep mechanism or change the stress exponent by moving the alloy from glide- to climb-control.

Nembach (1997) [199] provides the most systematic derivation of strength increments from coherent and incoherent particles, extending to high-temperature conditions by including climb and modulus-mismatch/chemical-ordering terms; it also clarifies how particle size distributions and volume fraction govern both threshold stresses and the evolution of creep rate with time. Ardell (1985) [200] gives a comprehensive review of precipitation hardening that reconciles order-strengthening, coherency, and modulus-mismatch contributions with experimentally observed coarsening kinetics, showing how the time dependence of precipitate size and spacing feeds directly into tertiary-stage creep acceleration once cutting gives way to bypass. Reed (2008) [201] establishes γ/γ' microstructural design—volume fraction, lattice misfit, anti-phase boundary energies, and γ' size—as the central levers for creep resistance in Ni-base single crystals, and develops the physics of directional coarsening (rafting) that biases dislocation motion and reduces the effective resolved shear stress on creep systems.

Tin and Pollock (2014) [202] gave a review of nickel-base superalloys quantifies how γ' size, topology, and misfit set the creep rate by mediating dislocation shearing versus climb-bypass and by controlling rafting kinetics under load; the article also collates stress exponents and activation energies that distinguish precipitate-strengthened creep from solid-solution creep. The analytical rafting model developed for γ/γ' superalloys by Kamaraj (2003) [203] demonstrates how elastic energy minimization under applied stress drives γ' plates to align into rafts, and it connects the sign and magnitude

of misfit to raft morphology, linking directional coarsening directly to creep anisotropy and life. A rigorous overview by Abe (2008) [204] of high-temperature deformation in γ/γ' superalloys emphasizes how precipitate-controlled mechanisms—shearing via paired a/2 $\langle 110 \rangle$ superpartials at smaller γ', transition to Kear–Wilsdorf locks, and then climb-bypass at larger γ'—map onto the observed creep exponents and microstructural evolution during long holds. A complementary treatment by Danielsen (2016) [205] on superalloy directional coarsening provides a thermodynamic driving-force formalism and shows how rafting modifies channel widths for dislocation motion, thereby lowering effective creep rates when raft orientation reduces slip transmission and raising them when channeling is enhanced.

Modern synthesis of γ' rafting behavior by Tkachev et. al. (2020) [206] collates in situ and ex situ observations to show how precipitate shape factors, misfit, and applied stress set raft formation and coarsening rates, with direct implications for the onset of tertiary creep through channel widening and localized dislocation flux. Detailed experimental–computational work by Abe et. al. (2007) [207] on rafting in single-crystal superalloys demonstrates the coupling between creep strain, precipitate re-shaping, and dislocation substructure evolution, revealing that precipitate realignment can both shield and channel dislocations depending on orientation, thus modulating the creep rate. For age-hardenable Ni alloys such as 718, precipitation of γ' and γ'' and their subsequent coarsening under service temperatures determine whether creep proceeds by shearing or by climb-bypass; calibrated Kampmann–Wagner-type (KWN) precipitation models by Balan et. al. (2021) [208] now predict time-dependent strengthening during holds that feed directly into multi-stage creep curves.

Work on coherent Al3Sc precipitates by Karnesky et. al. (2007) [209] establishes a true threshold stress for creep in Al-based alloys despite precipitate coherency, ruling out cutting and pointing to climb-controlled bypass and elastic-interaction detachment as the governing processes; the magnitude and temperature dependence of the threshold can be tuned via Zr additions that suppress coarsening. A dislocation-climb model for coherent-particle by Krug and Dunand (2011) [210] bypass extends the classical Rösler–Arzt framework (Developed by Rösler and Arzt (1988) [211] & Arzt and Rösler (1988) [212]) by incorporating misfit strains and interface energetics, deriving a quantitative threshold stress that scales with precipitate size, spacing, and elastic mismatch, and reproducing the low-stress, high-exponent creep signatures of particle-strengthened alloys. The original threshold-stress formulation by Rösler and Arzt (1988) [211] & Arzt and Rösler (1988) [212] for dislocation climb over hard particles shows that an attractive particle–dislocation interaction creates a finite stress below which creep is immeasurably slow, thereby explaining anomalously high apparent stress exponents and activation energies in dispersion- and precipitate-strengthened systems.

The model-based creep equation for dispersion-strengthened alloys developed by Rösler and Arzt (1990) [213] recasts steady creep as a sequence of thermally activated detachment events from particles, predicting a true threshold and giving explicit temperature and particle-size dependences that have been validated across ODS and precipitate-hardened matrices. In situ TEM studies of threshold stress by Deshmukh et. al. (2010) [214] directly correlate dislocation pinning/detachment at particle interfaces with macroscopic creep thresholds, showing that the measured detachment stress matches the back-extrapolated threshold from creep curves and confirming the detachment-controlled kinetics posited by climb models. A broad review of creep and fracture in dispersion-strengthened materials by Arzt (1991) [215] compiled stress exponents far exceeding classical values, attributes them to threshold stress effects tied to interparticle spacing and interface structure, and highlights the microstructural stability of the dispersoid field as central to sustained creep resistance.

For tempered-martensitic 9–12%Cr ferritic steels, a critical review by Maruyama (2001) [216] demonstrates that creep resistance rests on a hierarchy of obstacles—lath/subgrain boundaries, high dislocation density, and a stable dispersion of MX carbonitrides and M23C6/Laves phases—where precipitation strengthening offsets recovery but long-term coarsening and boundary denudation de-

grade strength. Interrupted-creep experiments on 9%Cr steels quantify the time-resolved coarsening of precipitates and substructure, showing an early strengthening contribution from Laves precipitation, a mid-life plateau as lath coarsening and precipitate growth compensate, and late-stage acceleration as particle coarsening undermines dislocation storage. A recent dislocation-based model for long-term creep in ferritic steels incorporates local climb-around-particle physics with threshold stress terms, capturing the transition from precipitate-controlled to recovery-controlled creep and providing a microstructure-sensitive extrapolation to service lifetimes.

11.3 Particle dispersion strengthening

Creep in crystalline materials is the time-dependent plastic deformation occurring at elevated temperatures, typically $T > 0.4T_m$, where T_m is the melting temperature. Creep is governed by dislocation motion, diffusional flow, and grain boundary sliding. Particle dispersion strengthening impedes dis-

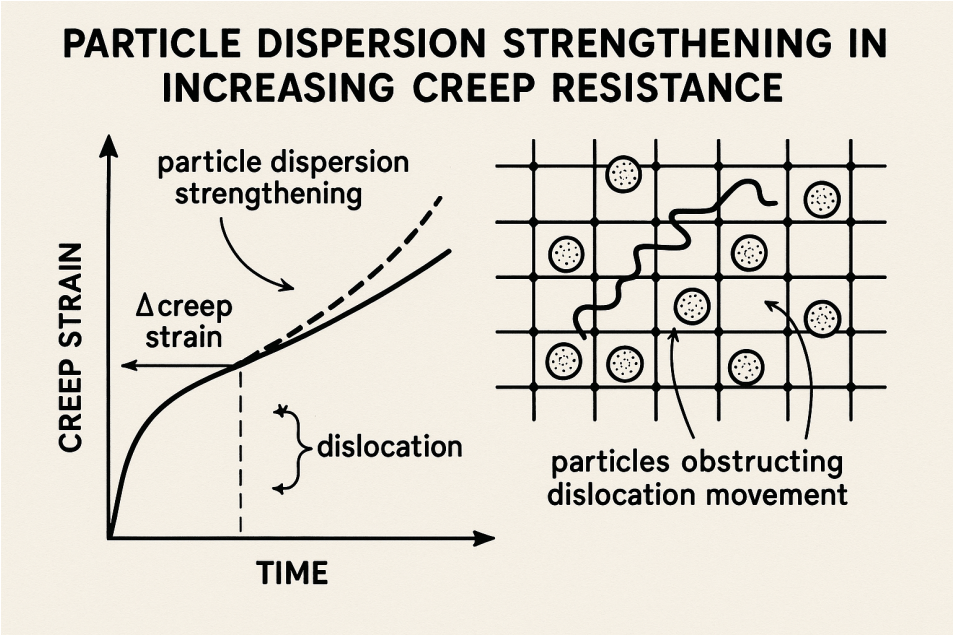

Figure 52: Particle Dispersion Strengthening in increasing Creep Resistance

location motion by introducing a high density of fine, thermally stable particles—typically oxides like Y_2O_3, Al_2O_3, or carbides—into the metal matrix. These particles obstruct dislocation glide and climb, two key creep mechanisms. The dislocations bow around the particles via the *Orowan mechanism*, forming loops and thus increasing the material's resistance to plastic strain under sustained load. The critical shear stress τ_{Orowan} required for bypassing non-shearable particles is given by:

$$\tau_{\text{Orowan}} = \frac{Gb}{L}\left[\frac{1}{2\pi}\ln\left(\frac{r}{b}\right)\right], \tag{273}$$

$$\sigma_{\text{Orowan}} = M\tau_{\text{Orowan}}, \tag{274}$$

where G is the shear modulus, b is the Burgers vector, L is the inter-particle spacing, r is the particle radius, and M is the Taylor factor (typically ~ 3) for converting shear to tensile stress. This impeding of dislocations adds a mechanical threshold that must be overcome before creep deformation can proceed, effectively raising the creep strength.

The steady-state (secondary) creep rate is generally described by *Norton's Law*:

$$\dot{\varepsilon}_{\text{ss}} = A\sigma^n \exp\left(-\frac{Q_c}{RT}\right), \tag{275}$$

where $\dot{\varepsilon}_{\text{ss}}$ is the steady-state creep strain rate, σ is the applied stress, n is the stress exponent (typically 3–10), Q_c is the activation energy for creep, R is the universal gas constant, T is absolute temperature, and A is a material-specific constant. For dispersion-strengthened alloys, the effective stress σ_{eff} available for dislocation motion is reduced by the Orowan stress:

$$\sigma_{\text{eff}} = \sigma_{\text{applied}} - \sigma_{\text{Orowan}}, \tag{276}$$

so the modified creep rate becomes:

$$\dot{\varepsilon}_{\text{ss}} = A\left(\sigma - \sigma_{\text{Orowan}}\right)^n \exp\left(-\frac{Q_c}{RT}\right). \tag{277}$$

At high temperatures, *dislocation climb* becomes the rate-controlling mechanism, enabled by vacancy diffusion. The time for a dislocation to climb past an obstacle of height h is:

$$t_{\text{climb}} \sim \frac{h^2}{D_v}, \tag{278}$$

where D_v is the vacancy diffusion coefficient, given by:

$$D_v = D_0 \exp\left(-\frac{Q_v}{RT}\right), \tag{279}$$

with Q_v as the activation energy for vacancy diffusion. Dispersion particles reduce effective climb rates by increasing the local climb distance and altering vacancy paths, thereby increasing t_{climb}, and hence reducing $\dot{\varepsilon}_{\text{ss}}$. The volume fraction f, particle size r, and inter-particle spacing λ play critical roles in determining strengthening effectiveness. For spherical particles with uniform distribution:

$$\lambda \approx r\left(\frac{\pi}{6f}\right)^{1/3} - 2r, \tag{280}$$

Smaller λ (i.e., closer spacing) increases the frequency of dislocation-particle interactions, which raises the Orowan stress and hence the creep resistance. The Orowan stress may also be written as:

$$\sigma_{\text{Orowan}} = \frac{0.13Gb}{\lambda} \ln\left(\frac{2r}{b}\right). \tag{281}$$

Thus, high f, small r, and large G maximize the creep strength. Furthermore, the threshold stress σ_{th}—below which creep is negligible—can be defined as the stress required to activate dislocation climb:

$$\sigma_{\text{th}} = \frac{Gb}{\lambda}\left(\ln\left(\frac{r}{b}\right) + C\right), \tag{282}$$

with $C \sim 1$–3 depending on the shape and distribution. For long-term creep life predictions, the Larson–Miller Parameter (LMP) is often used:

$$\text{LMP} = T(C + \log t_r), \tag{283}$$

where t_r is the rupture time. Dispersion strengthening improves creep life t_r by orders of magnitude at fixed stress and temperature. Hence, through rigorous control of particle dispersion characteristics, microstructure optimization leads to substantial improvements in creep resistance, verified both experimentally and via the above constitutive equations.

The intricate relationship between theory and practice in enhancing creep resistance underscores the necessity for a scientifically rigorous approach. By integrating principles of deformation mechanics, materials thermodynamics, and advanced computational tools, engineers can design materials that withstand the most demanding operational conditions, ensuring safety and longevity in applications from jet engines to nuclear reactors. This synthesis of theory and innovation exemplifies the profound depth of scientific inquiry required to push the boundaries of material performance.

11.4 Working Conditions

Creep that initiates below or at 0.5 times the melting temperature, T_m, is characterized as "low temperature creep" due to the significant reduction in atomic mobility required for diffusion-based mechanisms. At these temperatures, the thermal energy available for atomic movement is insufficient to drive diffusion processes such as vacancy diffusion, which is the primary creep mechanism at higher temperatures. This limitation significantly alters the dominant creep mechanisms, shifting from diffusion-dominated to dislocation mechanisms [117]. The onset of creep at temperatures below 0.5 T_m is marked by a transition from the high-temperature diffusion-based creep mechanisms, such as Nabarro-Herring creep and Coble creep, to more dislocation-based mechanisms like dislocation glide and climb. At low temperatures, dislocation glide becomes the dominant creep mechanism. The flow stress, σ_f, required for dislocation movement is primarily governed by the dislocation line tension and the resistance of the dislocation to move through the crystal lattice. The dislocation motion in this regime is primarily limited by the Peierls-Nabarro stress, τ_{PN}, which represents the stress required to initiate dislocation motion due to the periodic lattice resistance:

$$\sigma_f \sim \tau_{PN} = Gb\sqrt{\frac{\alpha}{\rho}} \tag{284}$$

where G is the shear modulus, b is the magnitude of the Burgers vector, α is a numerical factor related to the dislocation interaction, and ρ is the dislocation density. The expression τ_{PN} indicates that the flow stress required for dislocation motion at low temperatures is primarily a function of the dislocation interaction and the lattice resistance. In addition to dislocation glide, dislocation climb becomes significant at low temperatures, especially in the presence of obstacles such as precipitates or fine-grained microstructures that impede dislocation movement. Dislocation climb involves the exchange of atoms around the dislocation core, allowing dislocations to bypass obstacles. The activation energy for dislocation climb, Q_c, can be expressed as:

$$Q_c \approx Gb\frac{\rho}{2} \tag{285}$$

where ρ is the density of obstacles (e.g., precipitates or grain boundaries) hindering dislocation movement. This expression indicates that the activation energy for dislocation climb is directly proportional to the obstacle density, emphasizing the role of the microstructure in controlling low-temperature creep. The creep rate, $\dot{\epsilon}$, in this regime can be described by a power-law relationship:

$$\dot{\epsilon} = A\exp\left(-\frac{Q}{RT}\right)\sigma^n \tag{286}$$

where A is a material constant, Q is the activation energy for the creep process, R is the gas constant, T is the absolute temperature, and n is the stress exponent. For low-temperature creep, Q is typically lower compared to high-temperature creep because it is not dominated by vacancy diffusion but rather by dislocation mechanisms like climb and glide. Experimental observations reveal that the stress exponent n for low-temperature creep is typically greater than 3, indicating a more significant sensitivity of the creep rate to applied stress. This high stress exponent suggests that dislocation mechanisms, rather than diffusion processes, dominate the creep behavior at low temperatures. Additionally, the activation energy for creep is lower in this regime, which aligns with the notion that creep is not diffusion-controlled at these temperatures. The activation energy is primarily influenced by the interaction between dislocations and obstacles, such as precipitates or grain boundaries, which impede dislocation motion and contribute to the overall creep resistance. The flow stress σ_f in low-temperature creep also incorporates contributions from the stress due to obstacles. A modified expression for the flow stress that accounts for obstacle hardening can be given by:

$$\sigma_f = \tau_{obstacle} + Gb \tag{287}$$

where $\tau_{obstacle}$ represents the stress due to obstacles like precipitates or grain boundaries. This form shows that the creep resistance is significantly enhanced by the presence of these obstacles, requiring a higher applied stress to initiate dislocation motion. The microstructural evolution during low-temperature creep is fundamentally different from that during high-temperature creep. At low temperatures, the material's microstructure evolves mainly through the growth and interaction of obstacles such as precipitates and grain boundaries rather than through diffusional processes. These obstacles serve as barriers to dislocation motion, increasing the material's creep resistance. For example, precipitates can pin dislocations, leading to an increase in the flow stress and making dislocation glide more difficult. The interaction of dislocations with these obstacles can be described by a drag force:

$$F_d = Gb\rho \tag{288}$$

where ρ is the obstacle density, and b is the Burgers vector. This drag force increases with obstacle density, resulting in a higher flow stress and thus a slower creep rate.

In summary, low-temperature creep, which occurs below or at 0.5 T_m, is fundamentally different from high-temperature creep due to the dominance of dislocation mechanisms over atomic diffusion. The primary creep mechanisms at low temperatures are dislocation glide and climb, which are significantly influenced by the material's microstructure, such as the presence of obstacles like precipitates and grain boundaries. The resulting flow stress and creep rate are highly sensitive to applied stress, with a higher stress exponent and lower activation energy compared to high-temperature creep. These mechanisms lead to a different microstructural evolution, characterized by the growth and interaction of obstacles rather than diffusion-driven changes. The rigorous mathematical description of low-temperature creep and its mechanisms provides critical insights into the material behavior at these temperatures, emphasizing the importance of microstructural features in determining the creep resistance of materials.

11.4.1 Time

The concept of time in creep deformation is fundamental because creep strain accumulates progressively over time. The mathematical description of creep can be expressed using a power-law creep model, which describes the strain rate as a function of time, stress, and temperature. The basic creep equation is given by:

$$\dot{\epsilon}_c(t) = K\sigma^n \exp\left(-\frac{Q}{RT}\right) t^{-m} \tag{289}$$

where $\dot{\epsilon}_c(t)$ is the creep strain rate, K is a material constant, σ is the applied stress, n is the stress exponent, Q is the activation energy for creep, R is the universal gas constant, T is the absolute temperature, t is time, m is a material-specific exponent related to the strain hardening during creep. Stress exponent n and activation energy Q are critical parameters that vary with temperature and are influenced by microstructural features such as dislocation density and precipitate strengthening.m in the time exponent t^{-m} accounts for the hardening effect, where $m < 1$ typically represents the steady-state creep (secondary creep) phase where the strain rate becomes constant. The exponential dependence on stress and temperature reflects the thermally activated process of dislocation movement and vacancy diffusion, which are critical mechanisms in creep.

11.4.2 Temperature

Temperature profoundly affects creep behavior by increasing the rate of thermally activated processes such as atomic diffusion and dislocation motion. The Arrhenius relationship characterizes this temperature dependence:

$$\dot{\epsilon}_c = A \exp\left(-\frac{Q}{RT}\right) \sigma^n \tag{290}$$

where A is a pre-exponential factor, Q is the activation energy for creep, R is the universal gas constant, T is the absolute temperature, σ is the applied stress, n is the stress exponent. The Arrhenius equation describes the exponential increase in creep rate with temperature, which is a consequence of increased atomic mobility and reduced activation energy barriers for dislocation movement. The Q represents the energy required for the activation of processes like dislocation climb and vacancy diffusion, which control creep rates at high temperatures. The pre-exponential factor A incorporates the microstructural properties and the frequency of atomic events, which are influenced by the material's dislocation structure and grain boundaries.

11.4.3 Applied stress

The applied stress significantly influences the creep rate. Creep strain rate increases with stress, primarily due to enhanced dislocation movement under a greater applied load. The stress dependence can be modeled by a power-law relationship:

$$\dot{\epsilon}_c = A\sigma^n \exp\left(-\frac{Q}{RT}\right) \tag{291}$$

This model reflects the relationship between stress and creep rate. n (the stress exponent) reflects how the strain rate increases with stress. For materials with lower n, the creep rate is less sensitive to stress changes, indicating a greater resistance to creep. Higher stress increases the driving force for dislocation movement, which accelerates the creep rate. The power-law dependence on stress σ^n indicates that a higher stress leads to a significant increase in creep rate due to greater dislocation velocity and the easier movement of dislocations. The stress exponent n varies between different materials depending on their creep mechanisms (e.g., dislocation creep or diffusion creep).

All three parameters—time, temperature, and stress—interact to determine the creep strain rate. The comprehensive mathematical expression for creep strain rate incorporates the simultaneous effects of these parameters:

$$\dot{\epsilon}_c = A\sigma^n \exp\left(-\frac{Q}{RT}\right) t^{-m} \tag{292}$$

where A, Q, n, and m are material-specific constants, t is time, T is the temperature, σ is the applied stress. This equation illustrates the fundamental coupling between the time-dependent process of creep, the temperature-dependent activation energy, and the stress-dependent dislocation movement. The material's response to these parameters is highly sensitive to its microstructure and previous history, such as work hardening and phase transformations.

Creep resistance also depends on the microstructural stability of the material. The evolution of grain size, precipitate coarsening, and phase stability can significantly affect the creep rate. For example, fine-grained materials or those with precipitates that impede dislocation movement are more resistant to creep. These microstructural features can be modeled using the concept of effective grain boundary strengthening, which can be incorporated into the creep equation:

$$\sigma_{\text{eff}} = \sigma\left(1 + \frac{d}{\lambda}\right) \tag{293}$$

where d is the grain size and λ is the precipitate spacing. The effective stress σ_{eff} captures the strengthening effect of the microstructure.

Understanding the interplay between time, temperature, and stress allows engineers to design components that resist creep. For instance, selecting materials with higher Q values or fine microstructures can enhance resistance to creep. The Larson-Miller parameter, $\text{LMP} = T\log t + C$, is a practical tool for predicting creep rupture life, incorporating the effects of temperature, time, and stress on the material's resistance to creep. Designing a component with optimal creep resistance involves a multi-faceted approach:

1. **Material Selection**: Choosing materials with high Q and low A values for the creep-resistant phase.
2. **Microstructural Design**: Optimizing grain size and precipitate distribution to strengthen the material.
3. **Stress Management**: Minimizing stress through design to reduce the creep rate.
4. **Thermal Control**: Controlling temperature to lower the activation energy for creep processes.

All three parameters—time, temperature, and stress—must be rigorously considered together to design materials and components with effective creep resistance [119]. The interplay between these factors is mathematically complex but can be accurately modeled to provide predictive tools for designing materials with optimal creep properties. The mathematical models discussed provide a framework for understanding and predicting creep behavior, essential for ensuring the reliability and safety of high-temperature components in engineering applications. These models capture the fundamental mechanisms of creep, such as dislocation movement, diffusion, and phase stability, which are influenced by time, temperature, and stress, making them indispensable tools for material selection and component design in high-stress and high-temperature applications.

11.5 Material Selection

Ceramics are characterized by their high melting points T_m, which arise from their strong ionic or covalent bonds. The cohesive energy U_c, quantifying the total energy required to separate all constituent atoms, can be derived as:

$$U_c = \int_0^\infty -\frac{A}{r^m} + \frac{B}{r^n}\, dr, \tag{294}$$

where A and B are material-specific constants, r is the interatomic distance, and m, n are bond exponents related to the nature of ionic and covalent interactions. The high U_c ensures thermal stability, as the thermal energy per atom, proportional to $k_B T$ (where k_B is Boltzmann's constant), remains insufficient to disrupt bonding at high temperatures.

The melting point T_m is estimated via Lindemann's criterion, which states that melting occurs when the root-mean-square atomic displacement $\langle u^2 \rangle^{1/2}$ reaches a critical fraction of the interatomic spacing r_0. Mathematically:

$$\langle u^2 \rangle = \frac{3k_B T}{M\omega^2}, \quad T_m \propto \frac{M\omega^2 r_0^2}{k_B}, \tag{295}$$

where M is atomic mass and ω is vibrational frequency. For ceramics, the high values of M, r_0, and ω contribute to a higher T_m, ensuring operability under elevated temperatures. The ability of ceramics to resist creep deformation—time-dependent strain under constant stress—is governed by diffusion-controlled mechanisms, including Nabarro-Herring and Coble creep. The steady-state creep rate $\dot{\varepsilon}$ is often expressed by Norton's law:

$$\dot{\varepsilon} = A\sigma^n \exp\left(-\frac{Q}{RT}\right) \tag{296}$$

For diffusion-controlled creep, Q corresponds to the activation energy for atomic diffusion (Q_D), which is derived from:

$$D = D_0 \exp\left(-\frac{Q_D}{RT}\right), \tag{297}$$

where D_0 is the diffusion coefficient. For Coble creep, driven by grain boundary diffusion, the rate depends on grain size d as:

$$\dot{\varepsilon}_{\text{Coble}} = \frac{D_g \sigma \Omega}{k_B T d^3} \tag{298}$$

where D_g is the grain boundary diffusion coefficient, Ω is the atomic volume, k_B is Boltzmann's constant. For Nabarro-Herring creep, which involves lattice diffusion:

$$\dot{\varepsilon}_{\text{N-H}} = \frac{D_v \sigma \Omega}{k_B T d^2}, \tag{299}$$

where D_v is the volumetric diffusion coefficient. Comparing these equations shows the critical role of grain size d, with finer grains favoring Coble creep due to the larger grain boundary area, while coarser grains suppress diffusion pathways, reducing creep rates. Thermal conductivity k, governing heat dissipation, is critical for high-temperature applications. From Fourier's law:

$$q = -k \nabla T \tag{300}$$

where q is the heat flux and ∇T is the temperature gradient. A high k prevents localized overheating, reducing thermal gradients that induce thermal stress. Thermal stress σ_t arises due to thermal expansion mismatches and can be approximated by:

$$\sigma_t = \frac{\alpha E \Delta T}{1 - \nu}, \tag{301}$$

where α is the coefficient of thermal expansion, E is Young's modulus, ν is Poisson's ratio, ΔT is the temperature change. Minimizing α and maximizing k are essential to mitigate stress-induced failure in ceramics. The microstructure, characterized by grain size d, porosity P, and phase distribution, influences both strength and creep resistance. The Hall-Petch relationship:

$$\sigma_y = \sigma_0 + k_y d^{-1/2}, \tag{302}$$

where σ_0 is the intrinsic lattice strength and k_y is a strengthening coefficient, describes the strengthening effect of smaller grains. However, at high temperatures, grain boundaries facilitate creep through diffusion. Thus, balancing grain size becomes critical for optimizing both strength and creep resistance. Porosity P affects the effective modulus E_{eff} and strength σ_{eff} as:

$$E_{\text{eff}} = E(1 - P), \quad \sigma_{\text{eff}} = \sigma(1 - P)^2, \tag{303}$$

where E and σ are the modulus and strength of the fully dense material. High porosity reduces mechanical properties, necessitating densification during fabrication. At high temperatures, chemical stability against oxidation or reduction is governed by the Gibbs free energy change:

$$\Delta G = \Delta H - T \Delta S, \tag{304}$$

where ΔH is the enthalpy change and ΔS is the entropy change. For a reaction such as oxidation:

$$\text{M} + \frac{1}{2}\text{O}_2 \rightarrow \text{MO}, \tag{305}$$

ΔG must be negative to ensure thermodynamic stability. The rate of reaction is determined by the Arrhenius equation:

$$k = k_0 \exp\left(-\frac{E_a}{RT}\right), \tag{306}$$

where k_0 is the pre-exponential factor and E_a is the activation energy. A ceramic's resistance to oxidation depends on the stability of its oxide layer, which must be dense and adherent to prevent further degradation. Thus, the selection of suitable ceramic components for high-temperature and creep deformation conditions involves a multi-faceted approach grounded in material science principles. The interplay of thermal, mechanical, and chemical properties, quantified by equations like Fourier's law, Norton's creep law, and Gibbs free energy, dictates the optimal material design. Ceramics with high melting points, low thermal expansion coefficients, high thermal conductivity, and

finely tuned microstructures can achieve the desired performance, ensuring reliability under extreme operating conditions [115].

The importance of minimizing the dislocation and vacancy defects in enhancing the creep resistance of materials is huge. Creep is a critical factor influencing the performance of materials under high-temperature conditions, and the presence of dislocations and vacancies directly impacts the creep behavior. Dislocations are one-dimensional line defects in a crystal structure that allow plastic deformation to occur. The movement of dislocations under an applied stress is a primary mechanism of creep. Dislocations can move more easily at elevated temperatures due to the thermal activation of slip systems. The resistance to this movement, and hence the material's creep resistance, is determined by the obstacles to dislocation motion, which include other dislocations, solute atoms, grain boundaries, and precipitates.

The relationship between the applied stress and the dislocation movement can be captured through the Peierls-Nabarro model, which describes the energy required to move a dislocation across an array of obstacles:

$$E_d = G \cdot b \cdot \lambda \tag{307}$$

where E_d is the energy for dislocation movement, G is the shear modulus of the material, b is the magnitude of the Burgers vector, λ is the distance between obstacles (such as dislocations).A lower dislocation density increases the spacing λ, thereby increasing the energy E_d, which strengthens the material and improves its creep resistance. The stress-strain relationship during creep can be modeled by the Power-Law Creep Equation:

$$\dot{\epsilon} = A\sigma^n e^{-Q/RT} \tag{308}$$

where $\dot{\epsilon}$ is the creep strain rate, σ is the applied stress, A is a material constant, n is the stress exponent, Q is the activation energy for creep, R is the gas constant, T is the absolute temperature. A lower dislocation density results in a lower stress exponent n, indicating reduced sensitivity of the creep rate to the applied stress, thus better creep resistance.

Vacancies are point defects within a crystal structure where an atom is missing from its lattice site. These defects can move easily under thermal activation, leading to enhanced diffusion at elevated temperatures. The presence of vacancies accelerates creep deformation by facilitating atomic movement, leading to grain boundary sliding and enhanced diffusional creep. The formation of vacancies can be described by the Arrhenius equation:

$$N_v = N_0 \exp\left(-\frac{Q_v}{RT}\right) \tag{309}$$

where N_v is the number of vacancies per unit volume, N_0 is a constant, Q_v is the activation energy for vacancy formation, R is the gas constant, T is the absolute temperature. A low vacancy concentration minimizes the number of vacancies, reducing the rate of diffusion and improving the creep resistance. The mobility of vacancies, characterized by their diffusion coefficient D_v, contributes to the overall creep rate:

$$D_v = D_0 \exp\left(-\frac{Q_v}{RT}\right) \tag{310}$$

where D_0 is the pre-exponential factor, Q_v is the activation energy for vacancy diffusion, R is the gas constant, T is the absolute temperature. A lower vacancy concentration reduces D_v, which decreases the atomic mobility and enhances creep resistance. The combined effect of dislocations and vacancies on creep resistance can be understood through their interaction in the material's microstructure. Dislocations and vacancies interact synergistically to influence the creep behavior. A low dislocation density reduces the resistance to dislocation movement, while a low vacancy concentration limits the rate of atomic diffusion. The competition between these two types of defects determines the

overall creep resistance. The stress-strain relationship during creep can be refined to include both dislocation and vacancy effects:

$$\dot{\epsilon} = A\sigma^n e^{-Q/RT} e^{-k_v N_v} \tag{311}$$

where k_v is a material constant related to vacancy mobility, N_v is the vacancy concentration. This equation reflects the dual impact of dislocation density and vacancy concentration on creep resistance. The exponential term $e^{-k_v N_v}$ represents the additional resistance to creep provided by a low vacancy concentration. Regarding the Dislocation Interaction Energy, The interaction of dislocations with obstacles (such as vacancies) can be modeled by the Orowan equation:

$$\Delta\tau = \frac{\sigma b}{2\pi\lambda} \exp\left(-\frac{Q}{RT}\right) \tag{312}$$

where $\Delta\tau$ is the additional stress required to move a dislocation, λ is the distance between obstacles, Q is the activation energy for overcoming these obstacles. A lower dislocation density increases λ, which increases $\Delta\tau$, thereby improving creep resistance. The influence of vacancies on dislocation movement can be described by the Coble creep mechanism, where the diffusion of atoms from a vacancy in one grain to another through grain boundaries reduces the stress on dislocations:

$$\dot{\epsilon}_{\text{Coble}} = \frac{D_v}{b^2} \frac{\sigma}{RT} e^{-Q_v/RT} \tag{313}$$

where $\dot{\epsilon}_{\text{Coble}}$ is the Coble creep rate, D_v is the vacancy diffusion coefficient, b is the Burgers vector, Q_v is the activation energy for vacancy diffusion. A lower vacancy concentration decreases D_v, thereby reducing the Coble creep rate and enhancing the creep resistance of the material.

The selection and development of materials with low dislocation and vacancy contents are crucial for enhancing their creep resistance. Mathematical models and equations such as the Power-Law Creep Equation, the Peierls-Nabarro model, and the Coble creep equation provide a rigorous framework to understand and quantify the influence of these defects on creep behavior. By managing dislocation and vacancy densities, materials can be designed to resist creep deformation more effectively, making them suitable for high-temperature applications where long-term durability is essential [115] [116].

12 Creep Prevention in Superalloys

Creep prevention in superalloys is a critical area of material science that focuses on enhancing the high-temperature strength and durability of materials used in demanding applications such as turbine engines, nuclear reactors, and other components subjected to prolonged mechanical stress at elevated temperatures. Superalloys are specifically designed alloys that exhibit exceptional creep resistance due to their advanced microstructures and compositional features. The primary mechanisms contributing to their enhanced creep resistance include solid solution strengthening, precipitation hardening, grain boundary strengthening, and the presence of multiple phases. Each of these mechanisms plays a crucial role in impeding dislocation movement, stabilizing the microstructure, and preventing the degradation of mechanical properties over time. Some very good articles on this subject are Long et.al. 2018 [113], Pollock and Sammy 2006 [106], Pollock and Argon 1992 [53], Suzuki et.al. 2015 [114], Kakehi 2000 [54], Sun et.al. 2016 [55], Zhang et. al. 2003 [58], Zhang et. al. 2004 [56].

Solid solution strengthening is a foundational mechanism in the development of creep-resistant superalloys. This method involves the addition of elements such as molybdenum, niobium, and titanium into the base metal, which disrupts the regular atomic arrangement of the lattice. In alloys like Inconel 625, molybdenum is added to form a solid solution that increases lattice friction and makes it more difficult for dislocations to glide. These solute atoms create obstacles to dislocation motion by interacting with the dislocations themselves, leading to an increase in lattice friction. Niobium in

alloys like Inconel 718 forms solid solutions that stabilize the γ' phase, which is crucial for enhancing high-temperature strength. The γ' phase, a nickel-aluminum compound, forms ordered precipitates that impede dislocation movement by acting as obstacles. These precipitates are coherent with the matrix and exhibit excellent thermal stability, meaning they resist coarsening even under prolonged thermal exposure. The alloy's ability to retain these finely dispersed γ' precipitates during thermal cycling is vital for maintaining its creep resistance. The presence of these particles prevents dislocations from bypassing them, ensuring that the material maintains its integrity under prolonged high-temperature exposure. The precise control of alloying elements and the aging process are critical to optimize the size and distribution of these precipitates, ensuring optimal creep resistance. For example, Inconel 718 is aged to develop γ' precipitates, which enhance its strength without losing its ductility. The aging process, involving specific temperature and time treatments, ensures the optimal formation of γ' precipitates, which are crucial for improving the alloy's resistance to creep. This process involves a controlled precipitation hardening treatment that optimizes the dispersion of γ' precipitates, which act as barriers to dislocation movement, thereby enhancing the alloy's creep resistance.

Precipitation hardening is another crucial mechanism in the design of superalloys, especially for enhancing their creep resistance. The aging process in these alloys induces the formation of fine, coherent precipitates within the matrix, which significantly strengthen the material. In Inconel 718, the presence of niobium and aluminum leads to the formation of γ' precipitates during aging. These ordered nickel-aluminum precipitates block dislocation movement by creating a barrier that prevents them from gliding through the matrix. The aging process in Inconel 718 stabilizes the γ' precipitates, making them more resistant to coarsening under thermal cycling. The formation of fine γ' precipitates is crucial for improving creep resistance. The size and distribution of these precipitates are tailored through aging treatments, which involve precise control over temperature and time. These precipitates not only increase the alloy's strength but also enhance its thermal stability, ensuring it can endure high-temperature exposure without losing its mechanical properties. The interaction between dislocations and these precipitates is such that they effectively block dislocations, thereby preventing them from moving through the crystal lattice. The control over aging processes is crucial for optimizing the formation of γ' precipitates, which is vital for maintaining the alloy's strength under long-term thermal exposure. The optimization of the aging treatment in Inconel 718 is achieved through controlled aging at temperatures that promote the formation of finely dispersed γ' precipitates, which are resistant to coarsening and contribute significantly to the alloy's creep resistance. These precipitates form a complex, three-dimensional network that blocks dislocation movement, making the alloy highly resistant to creep deformation under high temperatures.

Grain boundary strengthening is another essential mechanism that enhances the creep resistance of superalloys. The integrity of grain boundaries is critical for maintaining the material's strength at high temperatures. Alloying elements such as boron, zirconium, and titanium are added to form carbides and borides at grain boundaries. These particles pin the grain boundaries, making it more difficult for dislocations to move across them. In alloys like Haynes 230, boron and titanium are added to segregate at grain boundaries and form titanium-boride particles. These particles effectively immobilize dislocations, preventing them from moving along the grain boundaries—a significant creep mechanism at high temperatures. The presence of these grain boundary particles ensures the alloy maintains its strength over time, particularly under cyclic thermal conditions. These carbides and borides at grain boundaries serve as pinning points that prevent grain boundary sliding—a primary mechanism of creep deformation at high temperatures. The formation of these pinning particles significantly enhances the alloy's creep resistance by preventing dislocations from migrating along the grain boundaries, which is a critical feature for materials used in high-temperature applications. The Hall-Petch relationship describes the relationship between grain size and strength, showing that

the yield strength increases with a reduction in grain size due to grain boundary strengthening:

$$\sigma_y = \sigma_0 + \frac{K}{\sqrt{d}} \tag{314}$$

where σ_y is the yield strength, σ_0 is the frictional stress, K is a material constant, and d is the average grain size. This equation quantitatively explains the role of grain boundaries in strengthening the alloy, demonstrating the effectiveness of grain boundary strengthening in preventing creep deformation. The segregation of elements such as boron and titanium at grain boundaries forms stable pinning phases that prevent dislocations from moving across these boundaries, thereby enhancing the alloy's creep resistance. This segregation not only increases the diffusional path length for atoms but also stabilizes the microstructure during thermal exposure, contributing significantly to the alloy's long-term strength and stability under high temperatures.

The presence of multiple phases in superalloys further contributes to their creep resistance. Advanced superalloys, like PWA 1480, contain a complex microstructure with γ, γ', and γ'' phases. The γ'' phase, which is an ordered Ni3Nb phase, enhances the creep resistance by providing additional obstacles to dislocation motion. These γ'' precipitates act as barriers within the matrix, creating a more complex microstructure that enhances the alloy's high-temperature strength. The formation of these phases is controlled by alloy composition and heat treatment processes, which tailor the microstructure to optimize the alloy's creep resistance. The coherency strains introduced by γ'' precipitates are particularly effective at blocking dislocation movement, further stabilizing the microstructure during thermal cycling. These precipitates provide additional resistance to dislocation motion, thereby enhancing the creep strength of the superalloy, especially in applications requiring stable dimensional stability under thermal cycling.

To further justify these mechanisms, mathematical models and equations are employed to describe the creep behavior in superalloys. The Norton-Bailey creep law is one such model used to describe the creep strain rate:

$$\dot{\epsilon} = A\sigma^n \exp\left(-\frac{Q}{RT}\right) \tag{315}$$

where $\dot{\epsilon}$ is the creep strain rate, σ is the applied stress, A is a material constant related to the creep resistance, n is the stress exponent, Q is the activation energy for creep, R is the gas constant, and T is the absolute temperature. This equation encapsulates the combined effects of solid solution strengthening, precipitation hardening, and grain boundary strengthening. The stress exponent n typically ranges from 3 to 5 for creep in superalloys, indicative of the dominant creep mechanisms such as dislocation glide, dislocation climb, and grain boundary sliding. The activation energy Q reflects the energy barriers associated with dislocation movement and the stability of γ' precipitates. The effectiveness of superalloy compositions in enhancing creep resistance can be quantitatively described by these equations, providing a predictive tool for the development of new superalloys. The Norton-Bailey model effectively combines the effects of all the mechanisms discussed, illustrating how they contribute to the creep resistance of superalloys. These equations serve as a powerful tool for predicting the performance of superalloys under various service conditions, providing valuable insights into the development of advanced materials for high-temperature applications.

In conclusion, the prevention of creep in superalloys involves a complex interplay of mechanisms such as solid solution strengthening, precipitation hardening, grain boundary strengthening, and the presence of multiple phases. The precise control of alloy composition, microstructure, and heat treatment processes is critical for the development of superalloys that maintain their mechanical properties over extended periods at high temperatures. The ongoing research in this field aims to further refine these mechanisms, enabling the development of new superalloys with even higher creep resistance, improved thermal stability, and extended operational lifetimes. These advancements are

essential for high-performance applications in aerospace, power generation, and other industries requiring materials that can operate under extreme conditions.

13 Famous Accidents

13.1 Big Dig tunnel ceiling collapse in Boston on July 2006

The catastrophic collapse of the Big Dig tunnel ceiling in Boston, Massachusetts, in July 2006, has been attributed in significant part to the phenomenon of creep in the epoxy anchor adhesive used to secure the ceiling panels [108]. This tragic failure underscores the critical importance of understanding the time-dependent behavior of materials under sustained loads, particularly in safety-critical applications. Epoxy adhesives, while often chosen for their strong initial bonding properties and resistance to environmental degradation, are inherently viscoelastic materials. This viscoelasticity means they exhibit both elastic (recoverable) and viscous (time-dependent) deformation characteristics when subjected to stress. Under sustained loads, such as the weight of ceiling panels in the Big Dig tunnel, creep deformation can occur as the material undergoes gradual and irreversible elongation or deformation over time. In the case of the Big Dig, the epoxy adhesive was used to anchor bolts that supported the heavy concrete ceiling panels. Over time, and under the constant tensile load exerted by the weight of these panels, the adhesive likely experienced progressive creep, which diminished its load-carrying capacity. The viscoelastic nature of epoxy adhesives makes them particularly susceptible to creep at elevated temperatures, even within ranges considered normal for the operational environment. However, even in the absence of significant temperature fluctuations, the prolonged application of stress can lead to molecular reorganization within the adhesive, reducing its mechanical integrity. In this instance, the adhesive's gradual deformation under the sustained load may have resulted in the bolts slipping or detaching entirely, thereby undermining the overall structural stability of the ceiling. Compounding this issue is the possibility that the design and material selection did not fully account for the long-term creep behavior of the adhesive under the specific loading conditions. This failure to anticipate or mitigate creep may have been due to an underestimation of the stresses involved, a lack of rigorous long-term testing of the adhesive under simulated conditions, or an overreliance on the initial strength properties of the material without adequate consideration of its time-dependent degradation. The collapse of the ceiling panels, tragically resulting in loss of life and severe damage, illustrates the dire consequences of overlooking creep in the design and maintenance of critical infrastructure. This event has since prompted greater scrutiny of material selection, design practices, and quality control in construction projects, emphasizing the need for thorough testing and analysis of all materials used, particularly those subjected to sustained loads in safety-critical applications. Furthermore, it highlights the importance of incorporating redundancy and fail-safe mechanisms in structural designs to prevent catastrophic failures even in the event of material degradation. The Big Dig incident serves as a stark reminder of the complex interplay between material properties, environmental conditions, and structural demands, emphasizing the necessity for rigorous engineering practices to ensure long-term safety and reliability.

13.2 Collapse of the World Trade Center on September 11, 2001

The collapse of the World Trade Center, while primarily attributed to the significant reduction in yield strength of structural materials at elevated temperatures, also involved the critical contribution of creep deformation caused by the extreme thermal conditions during the event. The structural steel within the towers was subjected to extraordinarily high temperatures due to the intense and sustained fires following the impact of the airplanes. At these elevated temperatures, steel experiences a marked decline in its ability to withstand stress, as the temperature-induced softening reduces its yield strength, which is the stress level at which a material begins to deform plastically. Beyond this thermal softening, creep became a critical factor under these conditions because the steel components were subjected to both sustained mechanical loads from the weight of the building and the additional

thermal stress caused by the uneven heating. Creep in metals, including structural steel, is characterized by time-dependent plastic deformation under constant stress, and its effects become pronounced at high temperatures, particularly above approximately 0.4 times the material's melting temperature (in Kelvin). In the case of the World Trade Center, the extreme heat likely exceeded this threshold, accelerating creep deformation. The steel beams and columns, which were essential to maintaining the structural integrity of the towers, experienced gradual elongation and deformation due to creep. This deformation compromised the load-bearing capacity of the steel elements, leading to progressive failures within the structural framework. As the steel components deformed, the redistribution of loads caused additional stresses on already weakened elements, creating a cascade effect that further destabilized the structure. The combined effects of reduced yield strength and accelerated creep led to significant deformations, particularly in the connections between beams and columns, which were critical for structural stability. These deformations likely caused the misalignment of key load paths and the failure of essential joints, which are critical points in the structural network that rely on precise alignment and material strength to function effectively. As these elements failed under the combined effects of creep and thermal softening, the structural system of the towers could no longer support the immense gravitational forces of the upper floors. This ultimately led to the rapid and catastrophic collapse of the towers. The role of creep in this scenario underscores the importance of considering time-dependent deformation in the design and analysis of structures subjected to high-temperature conditions, especially in situations involving fire or other extreme heat sources. It also highlights the complex interplay between thermal effects, material behavior, and structural stability during high-temperature events, emphasizing the necessity for advanced modeling and simulation to predict and mitigate such catastrophic failures in future designs [109].

14 Conclusions

This rigorous analysis of creep deformation integrates mechanistic insights and phenomenological descriptions into a comprehensive framework. By coupling diffusion kinetics, dislocation motion, and damage mechanics, the models presented herein provide a robust foundation for predicting and mitigating time-dependent deformation.

15 Acknowledgments

The authors acknowledge the contributions of researchers whose foundational work has shaped our understanding of creep deformation.

References

[1] Kassner, M. E. (2015). Fundamentals of creep in metals and alloys. Butterworth-Heinemann. https://www.sciencedirect.com/book/9780080994277/fundamentals-of-creep-in-metals-and-alloys

[2] Poirier, J. P. (1985). Creep of crystals: high-temperature deformation processes in metals, ceramics and minerals. Cambridge University Press. https://www.cambridge.org/core/books/creep-of-crystals/6DAEE35A6BAD29EC9D067C4DAA48177B

[3] Penny, R. K., and Marriott, D. L. (2012). Design for creep. Springer Science and Business Media. https://link.springer.com/book/10.1007/978-94-011-0561-3

[4] Naumenko, K., and Altenbach, H. (2007). Modeling of creep for structural analysis. Springer Science and Business Media. https://link.springer.com/book/10.1007/978-3-540-70839-1

[5] Boyle, J. T., and Spence, J. (2013). Stress analysis for creep. Elsevier. https://www.sciencedirect.com/book/9780408011723/stress-analysis-for-creep

[6] Ashby, M. F., and Jones, D. R. (2012). Engineering materials 1: an introduction to properties, applications and design (Vol. 1). Elsevier. https://shop.elsevier.com/books/engineering-materials-1/jones/978-0-08-096665-6

[7] Frost, Harold J.; Ashby, Michael F. (1982). Deformation-Mechanism Maps: The Plasticity and Creep of Metals and Ceramics. Pergamon Press. ISBN 978-0-08-029337-0. https://defmech.engineering.dartmouth.edu/

[8] Turner, S. (2001). Creep of polymeric materials. Encyclopedia of materials: science and technology, 1813-1817. https://www.sciencedirect.com/science/article/abs/pii/B0080431526003284?via%3Dihub

[9] Passmore, E. M., Duff, R. H., and Vasilos, T. (1966). Creep of dense, polycrystalline magnesium oxide. Journal of the American Ceramic Society, 49(11), 594-600. https://ceramics.onlinelibrary.wiley.com/doi/abs/10.1111/j.1151-2916.1966.tb13175.x

[10] Tremper, R. T., and Gordon, R. S. (1971). Effect of nonstoichiometry on the viscous creep of iron-doped polycrystalline magnesia (No. COO-1591-15; UTEC-MSE-71-102; CONF-711030-8). Utah Univ., Salt Lake City. Div. of Materials Science and Engineering. https://www.osti.gov/servlets/purl/4717607

[11] Vandervoort, R. R., and Barmore, W. L. (1963). Compressive creep of polycrystalline beryllium oxide. Journal of the American Ceramic Society, 46(4), 180-184. https://ceramics.onlinelibrary.wiley.com/doi/abs/10.1111/j.1151-2916.1963.tb11711.x

[12] Hollenberg, G. W., and Gordon, R. S. (1973). Effect of oxygen partial pressure on the creep of polycrystalline Al2O3 doped with Cr, Fe, or Ti. Journal of the American Ceramic Society, 56(3), 140-147. https://ceramics.onlinelibrary.wiley.com/doi/abs/10.1111/j.1151-2916.1973.tb15430.x

[13] Ahres, T. J. (1995). Rock Physics and Phase Relations a handbook of physical constants: Washington. American Geophysical Union, 190-191. https://www.wiley.com/en-us/Rock+Physics+and+Phase+Relations%3A+A+Handbook+of+Physical+Constants-p-9781118668108

[14] Berry, J., Rottler, J., Sinclair, C. W., and Provatas, N. (2015). Atomistic study of diffusion-mediated plasticity and creep using phase field crystal methods. Physical Review B, 92(13), 134103. https://journals.aps.org/prb/abstract/10.1103/PhysRevB.92.134103

[15] Goldsby, D. L. (2006). Superplastic flow of ice relevant to glacier and ice-sheet mechanics. Glacier science and environmental change, 308-314. https://onlinelibrary.wiley.com/doi/abs/10.1002/9780470750636.ch60

[16] Courtney, T. H. (2005). Mechanical behavior of materials. Waveland Press. https://www.waveland.com/browse.php?t=394

[17] Nabarro, F. R. N. (1948). Deformation of crystals by the motion of single ions. Report of a Conference on Strength of Solids, Physical Society, London, 75–90. https://cir.nii.ac.jp/crid/1370004233292144776

[18] Herring, C. (1950). Diffusional viscosity of a polycrystalline solid. Journal of applied physics, 21(5), 437-445. https://pubs.aip.org/aip/jap/article/21/5/437/159377/Diffusional-Viscosity-of-a-Polycrystalline-Solid

[19] Neu, R. W., and Sehitoglu, H. (1989). Thermomechanical fatigue, oxidation, and creep: Part I. Damage mechanisms. Metallurgical transactions A, 20, 1755-1767. https://link.springer.com/article/10.1007/BF02663207

[20] Neu, R. W., and Sehitoglu, H. (1989). Thermomechanical fatigue, oxidation, and creep: Part II. Life prediction. Metallurgical transactions A, 20, 1769-1783. https://link.springer.com/article/10.1007/BF02663208

[21] Meyers, M. A., and Chawla, K. K. (2008). Mechanical behavior of materials. Cambridge university press. https://www.cambridge.org/highereducation/books/mechanical-behavior-of-materials/48AD6E15E989D76D5DAF9926123137CF?chapterId=CBO9780511810947A169

[22] Coble, R. L. (1963). A model for boundary diffusion controlled creep in polycrystalline materials. Journal of applied physics, 34(6), 1679-1682. https://pubs.aip.org/aip/jap/article/34/6/1679/362784/A-Model-for-Boundary-Diffusion-Controlled-Creep-in

[23] Cottrell, A. H., and Jaswon, M. A. (1949). Distribution of solute atoms round a slow dislocation. Proceedings of the Royal Society of London. Series A. Mathematical and Physical Sciences, 199(1056), 104-114. https://www.jstor.org/stable/98371

[24] Cottrell, A. H. (1953). LXXXVI. A note on the Portevin-Le Chatelier effect. The London, Edinburgh, and Dublin Philosophical Magazine and Journal of Science, 44(355), 829-832. https://www.tandfonline.com/doi/abs/10.1080/14786440808520347

[25] Gibbs, G.B. (1966), Grain Boundary Impurity Diffusion. phys. stat. sol. (b), 16: K27-K29. https://doi.org/10.1002/pssb.19660160143, https://onlinelibrary.wiley.com/doi/10.1002/pssb.19660160143

[26] Wei, Y., Bower, A. F., & Gao, H. (2010). Analytical model and molecular dynamics simulations of the size dependence of flow stress in amorphous intermetallic nanowires at temperatures near the glass transition. Physical Review B—Condensed Matter and Materials Physics, 81(12), 125402. https://journals.aps.org/prb/abstract/10.1103/PhysRevB.81.125402

[27] Penning, P. (1972). Mathematics of the portevin-le chatelier effect. Acta Metallurgica, 20(10), 1169-1175. https://www.sciencedirect.com/science/article/pii/0001616072901654

[28] Yilmaz, A. (2011). The Portevin–Le Chatelier effect: a review of experimental findings. Science and technology of advanced materials, 12(6), 063001. https://www.tandfonline.com/doi/full/10.1088/1468-6996/12/6/063001

[29] Rizzi, E., and Hähner, P. (2004). On the Portevin–Le Chatelier effect: theoretical modeling and numerical results. International Journal of Plasticity, 20(1), 121-165. https://www.sciencedirect.com/science/article/pii/S0749641903000354?via%3Dihub

[30] Jiang, H., Zhang, Q., Chen, X., Chen, Z., Jiang, Z., Wu, X., and Fan, J. (2007). Three types of Portevin–Le Chatelier effects: Experiment and modelling. Acta materialia, 55(7), 2219-2228. https://www.sciencedirect.com/science/article/pii/S1359645406007543?via%3Dihub

[31] Burton, B. (1982). The influence of solute drag on dislocation creep. Philosophical Magazine A, 46(4), 607-616. https://www.tandfonline.com/doi/abs/10.1080/01418618208236916

[32] Heald, P. T., and Harbottle, J. E. (1977). Irradiation creep due to dislocation climb and glide. Journal of Nuclear Materials, 67(1-2), 229-233. https://www.sciencedirect.com/science/article/pii/0022311577901775

[33] Mansur, L. K. (1979). Irradiation creep by climb-enabled glide of dislocations resulting from preferred absorption of point defects. Philosophical Magazine A, 39(4), 497-506. https://www.tandfonline.com/doi/abs/10.1080/01418617908239286

[34] Weertman, J. (1957). Steady-state creep of crystals. Journal of Applied Physics, 28(10), 1185-1189. https://pubs.aip.org/aip/jap/article/28/10/1185/161881/Steady-State-Creep-of-Crystals

[35] Mott, N. F. (1955). Dislocations, work-hardening and creep. Nature, 175, 365-367. https://doi.org/10.1038/175365a0, https://www.nature.com/articles/175365a0

[36] Harper, J., and Dorn, J. E. (1957). Viscous creep of aluminum near its melting temperature. Acta Metallurgica, 5(11), 654-665. https://www.sciencedirect.com/science/article/pii/0001616057901128

[37] Mohamed, F. A., Murty, K. L., and Morris, J. W. (1973). Harper-dorn creep in al, pb, and sn. Metallurgical Transactions, 4, 935-940. https://link.springer.com/article/10.1007/BF02645593

[38] Sousa, J. R., & Ghosh, S. (2025). A New Generalization of the Riemann Functional Equation.

[39] Barrett, C. R., Muehleisen, E. C., and Nix, W. D. (1972). High temperature-low stress creep of Al and Al+ 0.5 Fe. Materials Science and Engineering, 10, 33-42. https://www.sciencedirect.com/science/article/pii/0025541672900638

[40] Kassner, M. E., and Pérez-Prado, M. T. (2000). Five-power-law creep in single phase metals and alloys. Progress in materials science, 45(1), 1-102. https://www.sciencedirect.com/science/article/pii/S0079642599000067

[41] Singh, S. P., Kumar, P., and Kassner, M. E. (2020). The low-stress and high-temperature creep in LiF single crystals: An explanation for the So-called Harper-Dorn creep. Materialia, 13, 100864. https://www.sciencedirect.com/science/article/pii/S2589152920302805

[42] Srivastava, V., McNee, K. R., Jones, H., and Greenwood, G. W. (2005). Tensile creep behaviour of coarse grained copper foils at high homologous temperatures and low stresses. Materials science and technology, 21(6), 701-707. https://www.tandfonline.com/doi/abs/10.1179/174328405X46105

[43] Malakondaiah, G., and Rao, P. R. (1979). Grain size independent viscous creep in alpha titanium and beta cobalt. Scripta Metallurgica, 13(12), 1187-1190. https://www.sciencedirect.com/science/article/pii/0036974879902801

[44] Blum, W., and Maier, W. (1999). Harper-Dorn Creep—a Myth?. physica status solidi (a), 171(2), 467-474. https://onlinelibrary.wiley.com/doi/abs/10.1002/%28SICI%291521-396X%28199902%29171%3A2%3C467%3A%3AAID-PSSA467%3E3.0.CO%3B2-8

[45] Ginter, T. J., Chaudhury, P. K., and Mohamed, F. A. (2001). An investigation of Harper–Dorn creep at large strains. Acta materialia, 49(2), 263-272. https://www.sciencedirect.com/science/article/pii/S1359645400003165

[46] Ginter, T. J., and Mohamed, F. A. (2002). Evidence for dynamic recrystallization during Harper–Dorn creep. Materials Science and Engineering: A, 322(1-2), 148-152. https://www.sciencedirect.com/science/article/pii/S0921509301011273

[47] McClay, K. R. (1977). Pressure solution and Coble creep in rocks and minerals: a review. Journal of the Geological Society, 134(1), 57-70. https://www.lyellcollection.org/doi/abs/10.1144/gsjgs.134.1.0057

[48] Wheeler, J. (1992). Importance of pressure solution and coble creep in the deformation of polymineralic rocks. Journal of Geophysical Research: Solid Earth, 97(B4), 4579-4586. https://agupubs.onlinelibrary.wiley.com/doi/abs/10.1029/91JB02476

[49] Blum, W., and Eisenlohr, P. (2009). Dislocation mechanics of creep. Materials Science and Engineering: A, 510, 7-13. https://www.sciencedirect.com/science/article/pii/S0921509308014123

[50] Hirth, G., and Tullis, J. A. N. (1992). Dislocation creep regimes in quartz aggregates. Journal of structural geology, 14(2), 145-159. https://www.sciencedirect.com/science/article/abs/pii/019181419290053Y

[51] Somekawa, H., Hirai, K., Watanabe, H., Takigawa, Y., and Higashi, K. (2005). Dislocation creep behavior in Mg–Al–Zn alloys. Materials Science and Engineering: A, 407(1-2), 53-61. https://www.sciencedirect.com/science/article/pii/S0921509305006696

[52] Renner, J., Evans, B., and Siddiqi, G. (2002). Dislocation creep of calcite. Journal of Geophysical Research: Solid Earth, 107(B12), ECV-6. https://agupubs.onlinelibrary.wiley.com/doi/full/10.1029/2001JB001680

[53] Pollock, T. M., and Argon, A. S. (1992). Creep resistance of CMSX-3 nickel base superalloy single crystals. Acta Metallurgica et Materialia, 40(1), 1-30. https://www.sciencedirect.com/science/article/pii/095671519290195K

[54] Kakehi, K. (2000). Effect of primary and secondary precipitates on creep strength of Ni-base superalloy single crystals. Materials Science and Engineering: A, 278(1-2), 135-141. https://www.sciencedirect.com/science/article/pii/S0921509399005791

[55] Sun, F., Gu, Y. F., Yan, J. B., Xu, Y. X., Zhong, Z. H., and Yuyama, M. (2016). Creep deformation and rupture mechanism of an advanced wrought NiFe-based superalloy for 700° C class A-USC steam turbine rotor application. Journal of Alloys and Compounds, 687, 389-401. https://www.sciencedirect.com/science/article/pii/S0925838816318448

[56] Zhang, J. X., Murakumo, T., Harada, H., Koizumi, Y., and Kobayashi, T. (2004). Creep deformation mechanisms in some modern single-crystal superalloys. Superalloys, 2004, 189-195. https://www.tms.org/Superalloys/10.7449/2004/Superalloys_2004_189_195.pdf

[57] Ghosh, S. (2024). Tensor Derivative in Curvilinear Coordinates. https://engrxiv.org/preprint/view/4210

[58] Zhang, J. X., Murakumo, T., Harada, H., and Koizumi, Y. J. S. M. (2003). Dependence of creep strength on the interfacial dislocations in a fourth generation SC superalloy TMS-138. Scripta Materialia, 48(3), 287-293. https://www.sciencedirect.com/science/article/pii/S1359646202003792?via%3Dihub

[59] Ennis, P. J., and Czyrska-Filemonowicz, A. (2003). Recent advances in creep-resistant steels for power plant applications. Sadhana, 28, 709-730. https://link.springer.com/article/10.1007/BF02706455

[60] Pekguleryuz, M., and Celikin, M. (2010). Creep resistance in magnesium alloys. International Materials Reviews, 55(4), 197-217. https://www.tandfonline.com/doi/abs/10.1179/095066010X12646898728327

[61] Mo, N., Tan, Q., Bermingham, M., Huang, Y., Dieringa, H., Hort, N., and Zhang, M. X. (2018). Current development of creep-resistant magnesium cast alloys: A review. Materials and Design, 155, 422-442. https://www.sciencedirect.com/science/article/pii/S0264127518304982?via%3Dihub

[62] Darling, K. A., Rajagopalan, M., Komarasamy, M., Bhatia, M. A., Hornbuckle, B. C., Mishra, R. S., and Solanki, K. N. (2016). Extreme creep resistance in a microstructurally stable nanocrystalline alloy. Nature, 537(7620), 378-381. https://pubmed.ncbi.nlm.nih.gov/27629642/

[63] Yang, J., Zhang, Z., Friedrich, K., and Schlarb, A. K. (2007). Creep resistant polymer nanocomposites reinforced with multiwalled carbon nanotubes. Macromolecular rapid communications, 28(8), 955-961. https://onlinelibrary.wiley.com/doi/full/10.1002/marc.200600866

[64] Bell, R. L., and Langdon, T. G. (1967). An investigation of grain-boundary sliding during creep. Journal of Materials Science, 2, 313-323. https://link.springer.com/article/10.1007/BF00572414

[65] Rachinger, W. A. (1956). Glide in lead telluride. Acta Metallurgica, 4(6), 647-649. https://www.sciencedirect.com/science/article/pii/0001616056901699

[66] Lifshitz, I. M. (1963). On the theory of diffusion-viscous flow of polycrystalline bodies. Sov. Phys. Jetp-USSR, 17(4), 909. http://www.jetp.ras.ru/cgi-bin/dn/e_017_04_0909.pdf

[67] Raj, R., and Ashby, M. F. (1971). On grain boundary sliding and diffusional creep. Metallurgical transactions, 2, 1113-1127. https://link.springer.com/article/10.1007/BF02664244

[68] Kingery, W. D., & Berg, M. (1955). Study of initial stages of sintering solids by viscous flow, evaporation-condensation, and self-diffusion. Journal of Applied Physics, 26(10), 1205–1212. https://doi.org/10.1063/1.1721874, https://pubs.aip.org/aip/jap/article/26/10/1205/160664/Study-of-the-Initial-Stages-of-Sintering-Solids-by

[69] Ashby, M. F. (1972). A first report on deformation-mechanism maps. Acta Metallurgica, 20(7), 887–897. https://doi.org/10.1016/0001-6160(72)90082-X, https://www.sciencedirect.com/science/article/pii/000161607290082X

[70] Bhaduri, A. (2018). Mechanical properties and working of metals and alloys (Vol. 264). Singapore: Springer Singapore. https://link.springer.com/book/10.1007/978-981-10-7209-3

[71] Balluffi, R. W., Allen, S. M., & Carter, W. C. (2005). Kinetics of materials. John Wiley & Sons.

[72] Langdon, T. G. (2006). Grain boundary sliding revisited: Developments in sliding over four decades. Journal of Materials Science, 41, 597-609. https://link.springer.com/article/10.1007/s10853-006-6476-0

[73] Langdon, T. G. (2013). Twenty-five years of ultrafine-grained materials: Achieving exceptional properties through grain refinement. Acta Materialia, 61(19), 7035-7059. https://www.sciencedirect.com/science/article/pii/S1359645413006149

[74] Schiøtz, J., & Jacobsen, K. W. (2003). A maximum in the strength of nanocrystalline copper. Science, 301(5638), 1357-1359. https://www.science.org/doi/full/10.1126/science.1086636

[75] Yamakov, V., Wolf, D., Phillpot, S. R., & Gleiter, H. (2002). Grain-boundary diffusion creep in nanocrystalline palladium by molecular-dynamics simulation. Acta Materialia, 50(1), 61-73. https://www.sciencedirect.com/science/article/pii/S1359645401003299

[76] Caro, A., Farkas, D., Bringa, E. M., Gilmer, G. H., & Zepeda-Ruiz, L. A. (2010, February). Effects of microalloying on the mobility and mechanical response of interfaces in nanocrystalline Cu. In Materials Science Forum (Vol. 633, pp. 21-30). Trans Tech Publications Ltd. https://www.scientific.net/MSF.633-634.21

[77] Yang, X., Li, J., & Wang, P. (2020). Grain boundary migration in nanocrystalline Ni under constant shear strains and its mechanism. Computational Materials Science, 176, 109530. https://www.sciencedirect.com/science/article/pii/S0927025620300215

[78] Van Swygenhoven, H., Caro, A., & Farkas, D. (2001). A molecular dynamics study of polycrystalline fcc metals at the nanoscale: grain boundary structure and its influence on plastic deformation. Materials Science and Engineering: A, 309, 440-444. https://www.sciencedirect.com/science/article/pii/S0921509300017949

[79] Schiotz, J., Vegge, T., & Jacobsen, K. W. (1998). Atomic-scale modeling of the deformation of nanocrystalline metals. MRS Online Proceedings Library (OPL), 538, 299. https://www.cambridge.org/core/journals/mrs-online-proceedings-library-archive/article/atomicscale-modeling-of-the-deformation-of-nanocrystalline-metals/39D96AE2881B141C423617EA0EC45429

[80] Fiebig, J., Divinski, S., Rösner, H., Estrin, Y., & Wilde, G. (2011). Diffusion of Ag and Co in ultrafine-grained α-Ti deformed by equal channel angular pressing. Journal of Applied Physics, 110(8). https://pubs.aip.org/aip/jap/article/110/8/083514/954130

[81] Shousha, S., Kadambi, S. B., Beeler, B., & Kombaiah, B. (2024). Vacancy-mediated transport and segregation tendencies of solutes in fcc nickel under diffusional creep: A density functional theory study. Physical Review Materials, 8(8), 083605. https://journals.aps.org/prmaterials/abstract/10.1103/PhysRevMaterials.8.083605

[82] Morgado, F. F., Katnagallu, S., Freysoldt, C., Klaes, B., Vurpillot, F., Neugebauer, J., ... & Stephenson, L. T. (2021). Revealing atomic-scale vacancy-solute interaction in nickel. Scripta Materialia, 203, 114036. https://www.sciencedirect.com/science/article/pii/S135964622100316X

[83] Magri, M., Lemoine, G., Adam, L., & Segurado, J. (2020). A coupled model of diffusional creep of polycrystalline solids based on climb of dislocations at grain boundaries. Journal of the Mechanics and Physics of Solids, 135, 103786. https://www.sciencedirect.com/science/article/pii/S002250961930732X

[84] Zhang, X., Divinski, S. V., & Grabowski, B. (2022). Ab initio prediction of vacancy energetics in HCP Al-Hf-Sc-Ti-Zr high entropy alloys and the subsystems. Acta Materialia, 227, 117677. https://www.sciencedirect.com/science/article/pii/S1359645422000647

[85] Dobson, D. P., Lindsay-Scott, A., Hunt, S. A., Bailey, E., Wood, I. G., Brodholt, J. P., ... & Wheeler, J. (2019). Anisotropic diffusion creep in postperovskite provides a new model for deformation at the core - mantle boundary. Proceedings of the National Academy of Sciences, 116(52), 26389-26393. https://www.pnas.org/doi/abs/10.1073/pnas.1914826116

[86] Ghosh, S. (2024). Theory and Applications of the Eshelby Ellipsoidal Elastic Inclusion Problem. https://engrxiv.org/preprint/view/4198

[87] Rösler, J., Harders, H., and Bäker, M. (2007). Mechanical behaviour of engineering materials: metals, ceramics, polymers, and composites. Springer Science and Business Media. https://link.springer.com/book/10.1007/978-3-540-73448-2

[88] Ree, J. H. (1994). Grain boundary sliding and development of grain boundary openings in experimentally deformed octachloropropane. Journal of Structural Geology, 16(3), 403-418. https://www.sciencedirect.com/science/article/abs/pii/0191814194900442

[89] Gifkins, R. (1976). Grain-boundary sliding and its accommodation during creep and superplasticity. Metallurgical transactions a, 7, 1225-1232. https://link.springer.com/article/10.1007/BF02656607

[90] Yang, H., Gavras, S., and Dieringa, H. (2021). Creep characteristics of metal matrix composites. In Encyclopedia of Materials: Composites (Vol. 1, pp. 375-388). Elsevier. https://www.sciencedirect.com/science/article/abs/pii/B9780128035818118223?via%3Dihub

[91] Adams, M. A., and Murray, G. T. (1962). Direct Observations of Grain-Boundary Sliding in Bi-Crystals of Sodium Chloride and Magnesia. Journal of Applied Physics, 33(6), 2126-2131. https://pubs.aip.org/aip/jap/article/33/6/2126/163641/Direct-Observations-of-Grain-Boundary-Sliding-in

[92] Naziri, H., Pearce, R., Brown, M. H., and Hale, K. F. (1975). Microstructural-mechanism relationship in the zinc/aluminium eutectoid superplastic alloy. Acta Metallurgica, 23(4), 489-496. https://www.sciencedirect.com/science/article/pii/0001616075900887

[93] Sergueeva, A. V., Mara, N. A., and Mukherjee, A. K. (2007). Grain boundary sliding in nanomaterials at elevated temperatures. Journal of materials science, 42, 1433-1438. https://link.springer.com/article/10.1007/s10853-006-0697-0

[94] Zhang, X., Li, W., Ma, J., Li, Y., Zhang, X., and Zhang, X. (2021). Modeling the effects of grain boundary sliding and temperature on the yield strength of high strength steel. Journal of Alloys and Compounds, 851, 156747. https://www.sciencedirect.com/science/article/pii/S092583882033111X

[95] Mikhaylovskaya, A. V., Yakovtseva, O. A., and Irzhak, A. V. (2022). The role of grain boundary sliding and intragranular deformation mechanisms for a steady stage of superplastic flow for Al–Mg-based alloys. Materials Science and Engineering: A, 833, 142524. https://www.sciencedirect.com/science/article/pii/S0921509321017846

[96] Wright, P. K. (1978). The high temperature creep behavior of doped tungsten wire. Metallurgical Transactions A, 9, 955-963. https://link.springer.com/article/10.1007/BF02649840

[97] Raj, R., and King, G. W. (1978). Life prediction of tungsten filaments in incandescent lamps. Metallurgical Transactions A, 9, 941-946. https://link.springer.com/article/10.1007/BF02649838

[98] Schade, P. (2010). 100 years of doped tungsten wire. International Journal of Refractory Metals and Hard Materials, 28(6), 648-660. https://www.sciencedirect.com/science/article/pii/S0263436810000752

[99] Rosato, M. G., and Rosato, D. V. (Eds.). (2013). Plastics design handbook. Springer Science and Business Media. https://www.goodreads.com/book/show/6094734-plastics-design-handbook

[100] McCrum, N. G., Buckley, C. P., and Bucknall, C. B. (1997). Principles of polymer engineering. Oxford University Press. https://global.oup.com/academic/product/principles-of-polymer-engineering-9780198565260?cc=in&lang=en&

[101] Ozyhar, T., Hering, S., and Niemz, P. (2013). Viscoelastic characterization of wood: Time dependence of the orthotropic compliance in tension and compression. Journal of Rheology, 57(2), 699-717. https://pubs.aip.org/sor/jor/article/57/2/699/241100

[102] Jiang, J., Erik Valentine, B., Lu, J., and Niemz, P. (2016). Time dependence of the orthotropic compression Young's moduli and Poisson's ratios of Chinese fir wood. Holzforschung, 70(11), 1093-1101. https://www.degruyterbrill.com/document/doi/10.1515/hf-2016-0001/html

[103] McLean, D. (1966). The physics of high temperature creep in metals. Reports on Progress in Physics, 29(1), 1. https://iopscience.iop.org/article/10.1088/0034-4885/29/1/301

[104] Pineau, A., McDowell, D. L., Busso, E. P., and Antolovich, S. D. (2016). Failure of metals II: Fatigue. Acta Materialia, 107, 484-507. https://www.sciencedirect.com/science/article/pii/S135964541500381X?via%3Dihub

[105] Chen, Z., Yang, F., Liu, S., Hu, X., Liu, C., Zhou, Z., ... and Liu, L. (2022). Creep behavior of intermetallic compounds at elevated temperatures and its effect on fatigue life evaluation of Cu pillar bumps. Intermetallics, 144, 107526. https://www.sciencedirect.com/science/article/pii/S096697952200067X?via%3Dihub

[106] Pollock, T. M., and Tin, S. (2006). Nickel-based superalloys for advanced turbine engines: chemistry, microstructure and properties. Journal of propulsion and power, 22(2), 361-374. https://arc.aiaa.org/doi/10.2514/1.18239

[107] Clemens, H., and Mayer, S. (2013). Design, processing, microstructure, properties, and applications of advanced intermetallic TiAl alloys. Advanced engineering materials, 15(4), 191-215. https://advanced.onlinelibrary.wiley.com/doi/full/10.1002/adem.201200231

[108] "Ceiling Collapse in the Interstate 90 Connector Tunnel". National Transportation Safety Board. Washington, D.C.: NTSB. July 10, 2007. Retrieved 2 December 2016. https://www.ntsb.gov/investigations/AccidentReports/Reports/HAR0702.pdf

[109] Bažant, Z. P., and Zhou, Y. (2002). Why did the world trade center collapse?—Simple analysis. Journal of Engineering Mechanics, 128(1), 2-6. https://ascelibrary.org/doi/10.1061/%28ASCE%290733-9399%282002%29128%3A1%282%29

[110] Lakes, R. S. (2017). Viscoelastic Solids (1998). CRC press. https://www.taylorfrancis.com/books/mono/10.1201/9781315121369/viscoelastic-solids-1998-roderic-lakes-frank-kulacki

[111] "Is glass liquid or solid?". University of California, Riverside. Retrieved 2008-10-15. https://math.ucr.edu/home/baez/physics/General/Glass/glass.html

[112] Abuzeid, O. M., Al-Rabadi, A. N., and Alkhaldi, H. S. (2011). Recent Advancements in Fractal Geometric-Based Nonlinear Time Series Solutions to the Micro-Quasistatic Thermoviscoelastic Creep for Rough Surfaces in Contact. Mathematical Problems in Engineering, 2011(1), 691270. https://onlinelibrary.wiley.com/doi/10.1155/2011/691270

[113] Long, H., Mao, S., Liu, Y., Zhang, Z., and Han, X. (2018). Microstructural and compositional design of Ni-based single crystalline superalloys—A review. Journal of Alloys and Compounds, 743, 203-220. https://www.sciencedirect.com/science/article/pii/S0925838818302263?via%3Dihub

[114] Suzuki, A., Inui, H., Pollock, T.M. (2015). L12-Strengthened Cobalt-Base Superalloys, Annual Review of Materials Research, 45, 345-368, https://doi.org/10.1146/annurev-matsci-070214-021043, https://www.annualreviews.org/content/journals/10.1146/annurev-matsci-070214-021043

[115] Pelleg, J., and Pelleg, J. (2017). Creep in ceramics (pp. 41-61). Springer International Publishing. https://link.springer.com/book/10.1007/978-3-319-50826-9

[116] Bakunov, V. S., and Belyakov, A. V. (2000). Creep and structure of ceramics. Inorganic materials, 36, 1297-1301. https://link.springer.com/article/10.1023/A:1026658404494

[117] Duddu, R., and Waisman, H. (2012). A temperature dependent creep damage model for polycrystalline ice. Mechanics of Materials, 46, 23-41. https://www.sciencedirect.com/science/article/pii/S0167663611002122?via%3Dihub

[118] Ghosh, S. (2025). Rate-Dependent Plastic Deformation Model of Euler-Bernoulli Beams. https://engrxiv.org/preprint/view/4719

[119] Pandey, M. C., Taplin, D. M. R., Ashby, M. F., and Dyson, B. F. (1986). The effect of prior exposure-time on air-environment/creep interactions. Acta Metallurgica, 34(11), 2225-2233. https://www.sciencedirect.com/science/article/pii/0001616086901689

[120] Neville, A. M. (1971). Creep of concrete: plain, reinforced, and prestressed. https://trid.trb.org/View/99140

[121] Neville, A. M. (1964). Creep of concrete as a function of its cement paste content. Magazine of concrete Research, 16(46), 21-30. https://www.emerald.com/jmacr/article-abstract/16/46/21/414580/Creep-of-concrete-as-a-function-of-its-cement?redirectedFrom=fulltext

[122] Bažant, Z. P., and Osman, E. (1976). Double power law for basic creep of concrete. Matériaux et Construction, 9, 3-11. https://link.springer.com/article/10.1007/BF02478522

[123] Yu, Q., Bazant, Z. P., and Wendner, R. (2012). Improved algorithm for efficient and realistic creep analysis of large creep-sensitive concrete structures. ACI Structural Journal, 109(5), 665. http://cee.northwestern.edu/people/bazant/PDFs/Papers/515.pdf

[124] Ross, A. D. (1958, March). Creep of concrete under variable stress. In Journal Proceedings (Vol. 54, No. 3, pp. 739-758). https://www.concrete.org/publications/internationalconcreteabstractsportal.aspx?m=details&id=11466

[125] Bissonnette, B., Pigeon, M., and Vaysburd, A. M. (2007). Tensile creep of concrete: study of its sensitivity to basic parameters. ACI Materials journal, 104(4), 360. https://www.concrete.org/publications/internationalconcreteabstractsportal.aspx?m=details&ID=18825

[126] Ranaivomanana, N., Multon, S., and Turatsinze, A. (2013). Basic creep of concrete under compression, tension and bending. Construction and Building Materials, 38, 173-180. https://www.sciencedirect.com/science/article/pii/S0950061812006095

[127] Orozco-Caballero, A., Lunt, D., Robson, J. D., & Da Fonseca, J. Q. (2017). How magnesium accommodates local deformation incompatibility: a high-resolution digital image correlation study. Acta Materialia, 133, 367-379. https://www.sciencedirect.com/science/article/pii/S1359645417304275

[128] Orozco-Caballero, A., Jackson, T., & Da Fonseca, J. Q. (2021). High-resolution digital image correlation study of the strain localization during loading of a shot-peened RR1000 nickel-based superalloy. Acta Materialia, 220, 117306. https://www.sciencedirect.com/science/article/pii/S1359645421006868

[129] Singh, P. S., Liang, Z., Pharr, G. M., & de Boer, M. P. (2020). Creep of a thermally stable nanocrystalline nickel tungsten alloy as measured by high temperature nanoindentation. Materials Science and Engineering: A, 784, 139309. https://www.sciencedirect.com/science/article/pii/S0921509320303919

[130] Yagi, N., Rikukawa, A., Mizubayashi, H., & Tanimoto, H. (2006). Experimental tests of the elementary mechanism responsible for creep deformation in nanocrystalline gold. Physical Review B—Condensed Matter and Materials Physics, 74(14), 144105. https://journals.aps.org/prb/abstract/10.1103/PhysRevB.74.144105

[131] Rozman, K. A., Detrois, M., Liu, T., Gao, M. C., Jablonski, P. D., & Hawk, J. A. (2020). Long-term creep behavior of a CoCrFeNiMn high-entropy alloy. Journal of Materials Engineering and Performance, 29(9), 5822-5839. https://link.springer.com/article/10.1007/s11665-020-05103-2

[132] Xing, B., Zou, W., Rupert, T. J., & Cao, P. (2024). Vacancy diffusion barrier spectrum and diffusion correlation in multicomponent alloys. Acta Materialia, 266, 119653. https://www.sciencedirect.com/science/article/pii/S1359645424000065

[133] Xu, R., Chen, C. C., Wu, L., Scott, M. C., Theis, W., Ophus, C., ... & Miao, J. (2015). Three-dimensional coordinates of individual atoms in materials revealed by electron tomography. Nature materials, 14(11), 1099-1103. https://www.nature.com/articles/nmat4426

[134] Xu, C., & Was, G. S. (2013). In situ proton irradiation creep of ferritic–martensitic steel T91. Journal of nuclear materials, 441(1-3), 681-687. https://www.sciencedirect.com/science/article/pii/S0022311513005497

[135] Berry, J., Rottler, J., Sinclair, C. W., & Provatas, N. (2015). Atomistic study of diffusion-mediated plasticity and creep using phase field crystal methods. Physical Review B, 92(13), 134103. https://journals.aps.org/prb/abstract/10.1103/PhysRevB.92.134103

[136] Voyiadjis, G. Z., & Song, Y. (2019). Strain gradient continuum plasticity theories: theoretical, numerical and experimental investigations. International Journal of Plasticity, 121, 21-75. https://www.sciencedirect.com/science/article/pii/S0749641918307344

[137] Voyiadjis, G. Z., & Faghihi, D. (2012). Thermo-mechanical strain gradient plasticity with energetic and dissipative length scales. International Journal of Plasticity, 30, 218-247. https://www.sciencedirect.com/science/article/pii/S074964191100177X

[138] Khalajhedayati, A., & Rupert, T. J. (2015). High-temperature stability and grain boundary complexion formation in a nanocrystalline Cu-Zr alloy. Jom, 67(12), 2788-2801. https://link.springer.com/article/10.1007/s11837-015-1644-9

[139] Sendek, A. D., Cubuk, E. D., Antoniuk, E. R., Cheon, G., Cui, Y., & Reed, E. J. (2018). Machine learning-assisted discovery of many new solid li-ion conducting materials. arXiv preprint arXiv:1808.02470. https://arxiv.org/abs/1808.02470

[140] Ghosh, S. (2025). Rate-Independent Gradient-Enhanced Plastic Deformation Model of Euler-Bernoulli Beams. https://engrxiv.org/preprint/view/4718

[141] Gurtin, M. E. (1996). Generalized Ginzburg-Landau and Cahn-Hilliard equations based on a microforce balance. Physica D: Nonlinear Phenomena, 92(3-4), 178-192. https://www.sciencedirect.com/science/article/pii/0167278995001735

[142] Gurtin, M. E., Fried, E., & Anand, L. (2010). The mechanics and thermodynamics of continua. Cambridge university press. https://books.google.com/books?hl=en&lr=&id=eGUQQaDsTsQC&oi=fnd&pg=PR5&dq=Gurtin,+M.+E.,+Fried,+E.,+%5C%26+Anand,+L.+(2010).+The+mechanics+and+thermodynamics+of+continua.+Cambridge+university+press.&ots=2ct4rX-69r&sig=jSEjyBQm_AUAN3dRiICmPjgoTnw

[143] Geers, M. G. D., Cottura, M., Appolaire, B., Busso, E. P., Forest, S., & Villani, A. (2014). Coupled glide-climb diffusion-enhanced crystal plasticity. Journal of the Mechanics and Physics of Solids, 70, 136-153. https://www.sciencedirect.com/science/article/pii/S0022509614000908

[144] Gibson, J. S. L., Schröders, S., Zehnder, C., & Korte-Kerzel, S. (2017). On extracting mechanical properties from nanoindentation at temperatures up to 1000 C. Extreme Mechanics Letters, 17, 43-49. https://www.sciencedirect.com/science/article/pii/S2352431617300925

[145] Bergers, L. I. J. C., Hoefnagels, J. P. M., & Geers, M. G. D. (2011, May). Creep measurements in free-standing thin metal film micro-cantilever bending. In MEMS and Nanotechnology, Volume 4: Proceedings of the 2011 Annual Conference on Experimental and Applied Mechanics (pp. 167-171). New York, NY: Springer New York. https://link.springer.com/chapter/10.1007/978-1-4614-0210-7_24

[146] Petkov, M., Chevalier, M., Dean, D., & Cocks, A. C. (2021). Creep-fatigue interactions in a polycrystalline structural material under typical high-temperature power plant operating conditions. arXiv preprint arXiv:2103.00320. https://arxiv.org/abs/2103.00320

[147] Wallis, D., Hansen, L. N., Wilkinson, A. J., & Lebensohn, R. A. (2021). Dislocation interactions in olivine control postseismic creep of the upper mantle. Nature Communications, 12(1), 3496. https://www.nature.com/articles/s41467-021-23633-8

[148] Caillard, D., Rautenberg, M., & Feaugas, X. (2015). Dislocation mechanisms in a zirconium alloy in the high-temperature regime: An in situ TEM investigation. Acta Materialia, 87, 283-292. https://www.sciencedirect.com/science/article/pii/S1359645415000208

[149] Hirth, G. (2002). Laboratory constraints on the rheology of the upper mantle. Reviews in Mineralogy and Geochemistry, 51(1), 97-120. https://pubs.geoscienceworld.org/msa/rimg/article-abstract/51/1/97/87437

[150] Beyerlein, I. J., Li, Z., & Mara, N. A. (2022). Mechanical properties of metal nanolaminates. Annual Review of Materials Research, 52, 281-304. https://www.annualreviews.org/content/journals/10.1146/annurev-matsci-081320-031236

[151] Makineni, S. K., Kumar, A., Lenz, M., Kontis, P., Meiners, T., Zenk, C., ... & Gault, B. (2018). On the diffusive phase transformation mechanism assisted by extended dislocations during creep of a single crystal CoNi-based superalloy. Acta Materialia, 155, 362-371. https://www.sciencedirect.com/science/article/pii/S1359645418304713

[152] Lilensten, L., Antonov, S., Gault, B., Tin, S., & Kontis, P. (2021). Enhanced creep performance in a polycrystalline superalloy driven by atomic-scale phase transformation along planar faults. Acta Materialia, 202, 232-242. https://www.sciencedirect.com/science/article/pii/S1359645420308600

[153] Mosquera-Lois, I., Kavanagh, S. R., Klarbring, J., Tolborg, K., & Walsh, A. (2023). Imperfections are not 0 K: free energy of point defects in crystals. Chemical Society Reviews, 52(17), 5812-5826. https://pubs.rsc.org/en/content/articlehtml/2012/zp/d3cs00432e

[154] Paladino, A. E., & Coble, R. L. (1963). Effect of grain boundaries on diffusion-controlled processes in aluminum oxide. Journal of the American Ceramic Society, 46(3), 133-136. https://ceramics.onlinelibrary.wiley.com/doi/abs/10.1111/j.1151-2916.1963.tb11696.x

[155] Ashby, M. F., & Verrall, R. A. (1973). Diffusion-accommodated flow and superplasticity. Acta metallurgica, 21(2), 149-163. https://www.sciencedirect.com/science/article/pii/0001616073900576

[156] Langdon, T. G. (1994). A unified approach to grain boundary sliding in creep and superplasticity. Acta metallurgica et materialia, 42(7), 2437-2443. https://www.sciencedirect.com/science/article/pii/0956715194903220

[157] Yokogawa, K., Fukuyama, S., Kudo, K., & Shewmon, P. G. (1989). Effect of hydrogen attack on tensile and creep properties of low carbon steel. International journal of pressure vessels and piping, 37(5), 365-385. https://www.sciencedirect.com/science/article/pii/0308016189900306

[158] Shewmon, P. (2016). Thermo-and electro-transport in solids. In Diffusion in solids (pp. 223-241). Cham: Springer International Publishing. https://link.springer.com/content/pdf/10.1007/978-3-319-48206-4_7?pdf=chapter%20toc

[159] Ghahremani, F. (1980). Effect of grain boundary sliding on anelasticity of polycrystals. International Journal of Solids and Structures, 16(9), 825-845. https://www.sciencedirect.com/science/article/pii/0020768380900529

[160] Ruano, O. A., & Sherby, O. D. (1982). Low stress creep of fine-grained materials at intermediate temperatures: Diffusional creep or grain boundary sliding?. Materials Science and Engineering, 56(2), 167-175. https://www.sciencedirect.com/science/article/pii/0025541682901690

[161] Lessing, P. A., & Gordon, R. S. (1977). Creep of polycrystalline alumina, pure and doped with transition metal impurities. Journal of Materials Science, 12(11), 2291-2302. https://link.springer.com/article/10.1007/BF00552251

[162] Wakai, F., Nagano, T., & Iga, T. (1997). Hardening in creep of alumina by zirconium segregation at the grain boundary. Journal of the American Ceramic Society, 80(9), 2361-2366. https://ceramics.onlinelibrary.wiley.com/doi/abs/10.1111/j.1151-2916.1997.tb03128.x

[163] Nix, W. D. (1988). Mechanisms and controlling factors in creep fracture. Materials Science and Engineering: A, 103(1), 103-110. https://www.sciencedirect.com/science/article/pii/0025541688905563

[164] Kassner, M. E., & Pérez-Prado, M. T. (2000). Five-power-law creep in single phase metals and alloys. Progress in materials science, 45(1), 1-102. https://www.sciencedirect.com/science/article/pii/S0079642599000067

[165] Mohamed, F. A., & Langdon, T. G. (1974). The transition from dislocation climb to viscous glide in creep of solid solution alloys. Acta metallurgica, 22(6), 779-788. https://www.sciencedirect.com/science/article/pii/0001616074900881

[166] Maji, M., Eswaran, K. S., Ghosh, S., Seshasayanan, K., & Shukla, V. (2023). Equivalence of nonequilibrium ensembles: Two-dimensional turbulence with a dual cascade. Physical Review E, 108(1), 015102.

[167] Langdon, T. G. (1977). The relationship between strain rate sensitivity and ductility in superplastic materials. Scripta Metallurgica, 11(11), 997-1000. https://www.sciencedirect.com/science/article/pii/003697487790254X

[168] Mohamed, F. A., & Li, Y. (2001). Creep and superplasticity in nanocrystalline materials: current understanding and future prospects. Materials Science and Engineering: A, 298(1-2), 1-15. https://www.sciencedirect.com/science/article/pii/S0928493100001909

[169] Atkinson, A. (1988). Interfacial Diffusion. MRS Online Proceedings Library, 122(1), 183-192. https://link.springer.com/article/10.1557/PROC-122-183

[170] Herwegh, M., & Jenni, A. (2001). Granular flow in polymineralic rocks bearing sheet silicates: new evidence from natural examples. Tectonophysics, 332(3), 309-320. https://www.sciencedirect.com/science/article/pii/S0040195100002882

[171] Hirth, G., & Kohlstedf, D. (2003). Rheology of the upper mantle and the mantle wedge: A view from the experimentalists. Geophysical monograph-american geophysical union, 138, 83-106. http://www.soest.hawaii.edu/GG/FACULTY/smithkonter/GG631/other/HirthKohlstedt_2000.pdf

[172] Wang, Z., Gu, L., Zhang, Q., Yue, S., & Zhang, G. (2020). Creep characteristics and prediction of creep failure of rock discontinuities under shearing conditions. International Journal of Earth Sciences, 109(3), 945-958. https://link.springer.com/article/10.1007/s00531-020-01842-8

[173] Tasaka, M., Zimmerman, M. E., Kohlstedt, D. L., Stünitz, H., & Heilbronner, R. (2017). Rheological weakening of olivine+ orthopyroxene aggregates due to phase mixing: Part 2. Microstructural development. Journal of Geophysical Research: Solid Earth, 122(10), 7597-7612. https://agupubs.onlinelibrary.wiley.com/doi/abs/10.1002/2017jb014311

[174] Tasaka, M., Zimmerman, M. E., & Kohlstedt, D. L. (2017). Rheological weakening of olivine+ orthopyroxene aggregates due to phase mixing: 1. Mechanical behavior. Journal of Geophysical Research: Solid Earth, 122(10), 7584-7596. https://agupubs.onlinelibrary.wiley.com/doi/abs/10.1002/2017JB014333

[175] Ghosh, S., Kumawat, K., Sajish, S. D., Arul, J., & Bhattacharya, B. (2025). Time-dependent fatigue reliability of main vessel steel structural components in sodium cooled fast breeder reactors. Nuclear Engineering and Design, 433, 113820. https://www.sciencedirect.com/science/article/pii/S0029549324009208

[176] Hansen, L. N., Zimmerman, M. E., & Kohlstedt, D. L. (2011). Grain boundary sliding in San Carlos olivine: Flow law parameters and crystallographic-preferred orientation. Journal of Geophysical Research: Solid Earth, 116(B8). https://agupubs.onlinelibrary.wiley.com/doi/abs/10.1029/2011jb008220

[177] Goldsby, D. L., & Kohlstedt, D. L. (2001). Superplastic deformation of ice: Experimental observations. Journal of Geophysical Research: Solid Earth, 106(B6), 11017-11030. https://agupubs.onlinelibrary.wiley.com/doi/abs/10.1029/2000jb900336

[178] Goldsby, D. L., & Kohlstedt, D. L. (1997). Grain boundary sliding in fine-grained ice I. Scripta Materialia, 37(9), 1399-1406. https://citeseerx.ist.psu.edu/document?repid=rep1&type=pdf&doi=549d7611a760e4c4aa06b9180573bdf3accc32ca

[179] Bürgmann, R., & Dresen, G. (2008). Rheology of the lower crust and upper mantle: Evidence from rock mechanics, geodesy, and field observations. Annu. Rev. Earth Planet. Sci., 36(1), 531-567. https://www.annualreviews.org/content/journals/10.1146/annurev.earth.36.031207.124326

[180] Mocellin, A., & Kingery, W. D. (1971). Creep Deformation in MgO-Saturated Large-Grain-Size Al2O3. Journal of the American Ceramic Society, 54(7), 339-341. https://ceramics.onlinelibrary.wiley.com/doi/abs/10.1111/j.1151-2916.1971.tb12309.x

[181] Chokshi, A. H. (1990). An evaluation of the grain-boundary sliding contribution to creep deformation in polycrystalline alumina. Journal of materials science, 25(7), 3221-3228. https://link.springer.com/article/10.1007/BF00587678

[182] Heuer, A. H. (2008). Oxygen and aluminum diffusion in α-Al2O3: How much do we really understand?. Journal of the European Ceramic Society, 28(7), 1495-1507. https://www.sciencedirect.com/science/article/pii/S0955221907006097

[183] DIMOS, D., KOHLSTEDI, D., & SCHMALZRIED, H. (1988). High-temperature creep and kinetic demixing in (Co, Mg) O. Journal of the American Ceramic Society, 71(9), 732-741. https://ceramics.onlinelibrary.wiley.com/doi/abs/10.1111/j.1151-2916.1988.tb06406.x

[184] Gifkins, R. C. (1968). Diffusional creep mechanisms. Journal of the American Ceramic Society, 51(2), 69-72. https://ceramics.onlinelibrary.wiley.com/doi/abs/10.1111/j.1151-2916.1968.tb11838.x

[185] Koch, R. H., Lloyd, J. R., & Cronin, J. (1985). 1 f noise and grain-boundary diffusion in aluminum and aluminum alloys. Physical review letters, 55(22), 2487. https://journals.aps.org/prl/abstract/10.1103/PhysRevLett.55.2487

[186] Raj, R. (1975). Transient behavior of diffusion-induced creep and creep rupture. Metallurgical Transactions A, 6(8), 1499. https://link.springer.com/article/10.1007/BF02641961

[187] Raj, R., & Ashby, M. F. (1975). Intergranular fracture at elevated temperature. Acta metallurgica, 23(6), 653-666. https://www.sciencedirect.com/science/article/pii/0001616075900474

[188] Kassner, M. E., & Hayes, T. A. (2003). Creep cavitation in metals. International journal of plasticity, 19(10), 1715-1748. https://www.sciencedirect.com/science/article/pii/S0749641902001110

[189] Meixner, F., Ahmadi, M. R., & Sommitsch, C. (2022). Cavity nucleation and growth in nickel-based alloys during creep. Materials, 15(4), 1495.https://www.mdpi.com/1996-1944/15/4/1495

[190] Fuller Jr, E. R., Fields, R. J., Chuang, T. J., & Singhal, S. (1984). Characterization of creep damage in metals using small angle neutron scattering. JOURNAL OF RESEARCH of the National Bureau of Standards, 89(1), 35. https://pmc.ncbi.nlm.nih.gov/articles/PMC6768172/

[191] Kim, B. N., Morita, K., & Hiraga, K. (2003). Rate of diffusion creep accompanied by grain boundary sliding in elongated microstructures. Materials Science and Engineering: A, 363(1-2), 67-71. https://www.sciencedirect.com/science/article/pii/S0921509303005768

[192] Wang, C. (2010). Study of Deformation Behavior of Nanocrystalline Nickel using Nanoindentation Techniques. https://trace.tennessee.edu/utk_graddiss/862/

[193] Brassard, J. (2003). Deformation mechanisms during creep and cold rolling of nanocrystalline nickel. https://utoronto.scholaris.ca/items/f92e9166-1af4-408c-b8cb-3ada34a894a3

[194] Schiotz, J., Vegge, T., & Jacobsen, K. W. (1998). Atomic-scale modeling of the deformation of nanocrystalline metals. MRS Online Proceedings Library (OPL), 538, 299. https://www.cambridge.org/core/journals/mrs-online-proceedings-library-archive/article/atomicscale-modeling-of-the-deformation-of-nanocrystalline-metals/39D96AE2881B141C423617EA0EC45429

[195] Ghosh, S. (2025). Mathematical Foundations of Deep Learning. https://hal.science/hal-04928560/

[196] Zhang, B. B., Tang, Y. G., Mei, Q. S., Li, X. Y., & Lu, K. (2022). Inhibiting creep in nanograined alloys with stable grain boundary networks. Science, 378(6620), 659-663. https://www.science.org/doi/abs/10.1126/science.abq7739

[197] Carter, C. B., & Norton, M. G. (2007). Ceramic materials: science and engineering (Vol. 716). Springer. https://link.springer.com/book/10.1007/978-1-4614-3523-5

[198] Meyers, M. A., & Chawla, K. K. (2008). Mechanical behavior of materials. Cambridge university press. https://books.google.com/books?hl=en&lr=&id=v-_oAwAAQBAJ&oi=fnd&pg=PT19&dq=Meyers,+M.+A.,+%26+Chawla,+K.+K.+(2008).+Mechanical+behavior+of+materials.+Cambridge+univer-+sity+press.&ots=Kqraxbfqc9&sig=PXrjf2arGJX2qTUik4iQ3sw4egY

[199] Nembach, E. (1997). Particle strengthening of metals and alloys. https://cir.nii.ac.jp/crid/1130000795362721920

[200] Ardell, A. J. (1985). Precipitation hardening. Metallurgical Transactions A, 16(12), 2131-2165. https://link.springer.com/article/10.1007/BF02670416

[201] Reed, R. C. (2008). The superalloys: fundamentals and applications. Cambridge university press. https://dlib.scu.ac.ir/bitstream/Hannan/369808/2/9780521859042.pdf

[202] Tin, S., & Pollock, T. M. (2014). Nickel-Based Superalloys. Turbine Aerodynamics, Heat Transfer, Materials, and Mechanics; American Institute of Aeronautics and Astronautics, Inc.: Reston, VA, USA, 243, 423-466. https://www.academia.edu/download/63407285/Turbine_aerodynanics__Heat_transfer__Materials_and_Mechanics20200523-23383-107shcz.pdf#page=440

[203] Kamaraj, M. (2003). Rafting in single crystal nickel-base superalloys—An overview. Sadhana, 28(1), 115-128. https://link.springer.com/article/10.1007/BF02717129

[204] Abe, F. (2008). Precipitate design for creep strengthening of 9% Cr tempered martensitic steel for ultra-supercritical power plants. Science and Technology of Advanced Materials, 9(1), 013002. https://iopscience.iop.org/article/10.1088/1468-6996/9/1/013002/meta

[205] Danielsen, H. K. (2016). Review of Z phase precipitation in 9–12 wt-Cr steels. Materials Science and Technology, 32(2), 126-137. https://journals.sagepub.com/doi/abs/10.1179/1743284715Y.0000000066

[206] Tkachev, E., Belyakov, A., & Kaibyshev, R. (2020). Creep strength breakdown and microstructure in a 9% Cr steel with high B and low N contents. Materials Science and Engineering: A, 772, 138821. https://www.sciencedirect.com/science/article/pii/S0921509319316065

[207] Abe, F., Taneike, M., & Sawada, K. (2007). Alloy design of creep resistant 9Cr steel using a dispersion of nano-sized carbonitrides. International Journal of Pressure Vessels and Piping, 84(1-2), 3-12. https://www.sciencedirect.com/science/article/pii/S030801610600158X

[208] Balan, A., Perez, M., Chaise, T., Cazottes, S., Bardel, D., Corpace, F., ... & Nelias, D. (2021). Precipitation of γ'' in Inconel 718 alloy from microstructure to mechanical properties. Materialia, 20, 101187. https://www.sciencedirect.com/science/article/pii/S2589152921001903

[209] Karnesky, R. A., Meng, L., & Dunand, D. C. (2007). Strengthening mechanisms in aluminum containing coherent Al3Sc precipitates and incoherent Al2O3 dispersoids. Acta Materialia, 55(4), 1299-1308. https://www.sciencedirect.com/science/article/pii/S135964540600718X

[210] Krug, M. E., & Dunand, D. C. (2011). Modeling the creep threshold stress due to climb of a dislocation in the stress field of a misfitting precipitate. Acta materialia, 59(13), 5125-5134. https://www.sciencedirect.com/science/article/pii/S1359645411003004

[211] Rösler, J., & Arzt, E. (1988). The kinetics of dislocation climb over hard particles—I. Climb without attractive particle-dislocation interaction. Acta Metallurgica, 36(4), 1043-1051. https://www.sciencedirect.com/science/article/pii/0001616088901587

[212] Arzt, E., & Rösler, J. (1988). The kinetics of dislocation climb over hard particles—II. Effects of an attractive particle-dislocation interaction. Acta Metallurgica, 36(4), 1053-1060. https://www.sciencedirect.com/science/article/pii/0001616088901599

[213] Rösler, J., & Arzt, E. (1990). A new model-based creep equation for dispersion strengthened materials. Acta metallurgica et Materialia, 38(4), 671-683. https://www.sciencedirect.com/science/article/pii/0956715190902234

[214] Deshmukh, S. P., Mishra, R. S., & Robertson, I. M. (2010). Investigation of creep threshold stresses using in situ TEM straining experiment in an Al–5Y2O3–10SiC composite. Materials Science and Engineering: A, 527(9), 2390-2397. https://www.sciencedirect.com/science/article/pii/S0921509309013185

[215] Arzt, E. (1991). Creep of dispersion strengthened materials: a critical assessment. https://publikationen.sulb.uni-saarland.de/handle/20.500.11880/24031

[216] Maruyama, K., Sawada, K., & Koike, J. I. (2001). Strengthening mechanisms of creep resistant tempered martensitic steel. ISIJ international, 41(6), 641-653. https://www.jstage.jst.go.jp/article/isijinternational1989/41/6/41_6_641/_article/-char/ja/

[217] Rabotnov, Y. N. (1969). Creep rupture. In *Proceedings of the 12th International Congress on Applied Mechanics* (pp. 342–349).

[218] Kachanov, L. M. (1958). Time of rupture process under creep conditions. *Izv. Akad. Nauk SSSR. Otd. Tekh. Nauk*, 8, 26–31.

[219] Dyson, B. F. (1988). Continuum damage mechanics models for creep. *Metallurgical Transactions A*, 19(6), 1389–1395.

[220] Lemaitre, J. (1985). A continuous damage mechanics model for ductile fracture. *Journal of Engineering Materials and Technology*, 107(1), 83–89.

[221] Chaboche, J. L. (1981). Continuum damage mechanics: Part I–General concepts. *Journal of Applied Mechanics*, 48(2), 364–368.

[222] Chaboche, J. L. (1988). Continuum damage mechanics: Part II–Damage growth, crack initiation, and crack growth. *Journal of Applied Mechanics*, 55(1), 65–72.

[223] Hayhurst, D. R. (1972). Creep rupture under multi-axial states of stress. *Journal of the Mechanics and Physics of Solids*, 20(6), 381–382.

[224] Tvergaard, V., & Needleman, A. (1984). Analysis of the cup–cone fracture in a round tensile bar. *Acta Metallurgica*, 32(1), 157–169.

[225] Needleman, A. (1987). A continuum model for void nucleation by inclusion debonding. *Journal of Applied Mechanics*, 54(3), 525–531.

[226] Murakami, S. (1988). Mechanical modeling of material damage. *Journal of Applied Mechanics*, 55(2), 280–286.

[227] Shenoy, M., & McMeeking, R. J. (2010). Multiscale modeling of creep–damage by grain boundary cavitation. *Acta Materialia*, 58(13), 4424–4438.

[228] Cailletaud, G., & Sai, L. (2012). Multiscale approaches to creep and fatigue damage. *International Journal of Plasticity*, 32, 17–30.

[229] Pettinari-Sturmel, P., & Vincent, R. (2016). Oxidation–creep interactions in high-temperature alloys. *Corrosion Science*, 104, 52–61.

[230] Gurson, A. L. (1977). Continuum theory of ductile rupture by void nucleation and growth. *Journal of Engineering Materials and Technology*, 99(1), 2–15.

[231] Skelton, R. P., & Hayhurst, D. R. (1987). Creep damage mechanics: The effect of multiaxial stress states on the creep rupture of notched bars. *Journal of the Mechanics and Physics of Solids*, 35(4), 281–296.

[232] Miller, W. S., & McDowell, D. L. (1992). Creep damage mechanics: A review. *Journal of Engineering Materials and Technology*, 114(3), 257–265.

[233] de Borst, R., & Pamin, J. (1996). Gradient plasticity in numerical simulation of concrete cracking. *European Journal of Mechanics - A/Solids*, 15(3), 295–320.

[234] Ainsworth, R. A. (Ed.). (2003). *Assessment Procedure for the High Temperature Response of Structures*. Issue 3. Barnwood: BEGL Ltd.

[235] Hyde, C. J., Hyde, T. H., Sun, W., & Becker, A. A. (2010). Damage mechanics based predictions of creep crack growth in 316 stainless steel. *Engineering Fracture Mechanics*, 77(12), 1965–1982.

[236] Gonzalez, J. M., & Ruggieri, N. (2004). Micro–macro creep damage simulation for welded joints. *International Journal of Pressure Vessels and Piping*, 81(5), 353–363.

[237] Rao, P. S., & Reddy, B. V. (2011). Creep damage analysis of mod.9Cr-1Mo steel welds considering strain softening and damage due to void formation. *International Journal of Pressure Vessels and Piping*, 88(4), 201–210.

[238] Hayhurst, D. R. (1990). Multi-axial creep rupture of a model structure using a two-parameter material model. *International Journal of Mechanical Sciences*, 32(1), 35–48.